DIGITAL HOLOGRAPHY: TECHNIQUES AND APPLICATIONS

EDITED BY: Liangcai Cao, Zeev Zalevsky, Jianglei Di and Peng Gao

frontiers Research Topics

About Frontiers

Frontiers is more than just an open-access publisher of scholarly articles: it is a pioneering approach to the world of academia, radically improving the way scholarly research is managed. The grand vision of Frontiers is a world where all people have an equal opportunity to seek, share and generate knowledge. Frontiers provides immediate and permanent online open access to all its publications, but this alone is not enough to realize our grand goals.

Frontiers Journal Series

The Frontiers Journal Series is a multi-tier and interdisciplinary set of open-access, online journals, promising a paradigm shift from the current review, selection and dissemination processes in academic publishing. All Frontiers journals are driven by researchers for researchers; therefore, they constitute a service to the scholarly community. At the same time, the Frontiers Journal Series operates on a revolutionary invention, the tiered publishing system, initially addressing specific communities of scholars, and gradually climbing up to broader public understanding, thus serving the interests of the lay society, too.

Dedication to Quality

Each Frontiers article is a landmark of the highest quality, thanks to genuinely collaborative interactions between authors and review editors, who include some of the world's best academicians. Research must be certified by peers before entering a stream of knowledge that may eventually reach the public - and shape society; therefore, Frontiers only applies the most rigorous and unbiased reviews.
Frontiers revolutionizes research publishing by freely delivering the most outstanding research, evaluated with no bias from both the academic and social point of view. By applying the most advanced information technologies, Frontiers is catapulting scholarly publishing into a new generation.

What are Frontiers Research Topics?

Frontiers Research Topics are very popular trademarks of the Frontiers Journals Series: they are collections of at least ten articles, all centered on a particular subject. With their unique mix of varied contributions from Original Research to Review Articles, Frontiers Research Topics unify the most influential researchers, the latest key findings and historical advances in a hot research area! Find out more on how to host your own Frontiers Research Topic or contribute to one as an author by contacting the Frontiers Editorial Office: frontiersin.org/about/contact

DIGITAL HOLOGRAPHY: TECHNIQUES AND APPLICATIONS

Topic Editors:
Liangcai Cao, Tsinghua University, China
Zeev Zalevsky, Bar-Ilan University, Israel
Jianglei Di, Guangdong University of Technology, China
Peng Gao, Xidian University, China

Table of Contents

Fusion Coding of 3D Real and Virtual Scenes Information for Augmented Reality-Based Holographic Stereogram

Yunpeng Liu[1†], Xingpeng Yan[1*†], Xinlei Liu[1], Xi Wang[1], Tao Jing[1], Min Lin[2], Song Chen[1], Pei Li[3] and Xiaoyu Jiang[1]

[1]Department of Information Communication, Army Academy of Armored Forces, Beijing, China, [2]Department of Basic Education, Army Academy of Armored Forces, Beijing, China, [3]R & D Center for Intelligent Control and Advanced Manufacturing, Research Institute of Tsinghua University in Shen Zhen, Shen Zhen, China

In this paper, an optical field coding method for the fusion of real and virtual scenes is proposed to implement an augmented reality (AR)-based holographic stereogram. The occlusion relationship between the real and virtual scenes is analyzed, and a fusion strategy based on instance segmentation and depth determination is proposed. A real three-dimensional (3D) scene sampling system is built, and the foreground contour of the sampled perspective image is extracted by the Mask R-CNN instance segmentation algorithm. The virtual 3D scene is rendered by a computer to obtain the virtual sampled images as well as their depth maps. According to the occlusion relation of the fusion scenes, the pseudo-depth map of the real scene is derived, and the fusion coding of 3D real and virtual scenes information is implemented by the depth information comparison. The optical experiment indicates that AR-based holographic stereogram fabricated by our coding method can reconstruct real and virtual fused 3D scenes with correct occlusion and depth cues on full parallax.

Keywords: holographic stereogram, augmented reality, instance segmentation, 3D display, fusion of 3D real and virtual scenes

INTRODUCTION

A holographic stereogram [1–3] is an effective three-dimensional (3D) display technology. It combines traditional optical holography [4] with the parallax effect [5] and can realize high-resolution and wide-viewing-angle 3D naked eye display of 3D scenes, which is considered the ultimate form of 3D display technology [6, 7]. A holographic stereogram takes advantage of the limited resolution of human eyes, and it can express continuous and realistic 3D optical field information with a limited 2D perspective sequence, the parallax information of which is less than the resolving power of human eyes. The amount of data sampling and processing loss are small. 2D perspective images are not the only data source, but the reconstruction image and the formation of stereo vision also come from the difference of information received by human eyes. Therefore, the scene data source suitable for holographic stereogram is more universal and flexible, and the 3D optical field information it can express is more abundant and diverse. For real scenes, a camera array or motion camera can be used for capturing and sampling, which can realize the display of large-format scenes. For 3D models rendered by a computer, one can use software to realize 3D cues such

as occlusion, shadow, and transparency between scenes. It is worth mentioning that, on some occasions, the fusion of real and virtual scenes in 3D display may be more valuable. For example, in the exhibition of cultural relics, in order to display the 3D image and specific information of cultural relics while protecting cultural relics, some virtual introductory signs can be superimposed on the image of cultural relics. Obviously, this kind of holographic 3D display can enhance people's perception of the 3D world and achieve the effect of augmented reality (AR). In order to make this kind of holographic stereogram, the real and virtual scenes must be sampled separately, and the optical field information must be encoded and holographically printed according to the required spatial position relationship, so as to realize the AR display based on holographic stereo vision.

In traditional AR display, virtual information such as text, images, and 3D models generated by a computer is simulated and superimposed on the real world. The two kinds of information complement each other, so as to realize the "enhancement" of the real world. Generally, it does not need to encode and reconstruct the real scene. Deng et al. used a reflective polarizer (RP) to realize AR 3D display, which has potential applications in stomatology and vehicle AR display [8]. Shi et al. demonstrated a convolutional neural network (CNN)-based computer-generated holographic (CGH) pipeline capable of synthesizing a photorealistic color 3D hologram from a single RGBD image in real time [9]. Maimone et al. presented designs for virtual reality (VR) and AR near-eye displays based on phase-only holographic projection, which not only fix minor aberrations but also enable truly compact, eyeglass-like displays with wide fields of view (80°) [10]. Yang et al. proposed a fast CGH method with multiple projection images for a near-eye VR and AR 3D display by convoluting the projection images with the corresponding point spread function (PSF) [11]. In 2012, Google released Google Project Glass that can display an operation interface similar to smart phones, and people can operate it through sound or touch sensing devices [12]. In 2015, Microsoft released an AR head-mounted display that can interact with people through gestures and that is expected to realize the sense of technology visualized in some science fiction movies [13].
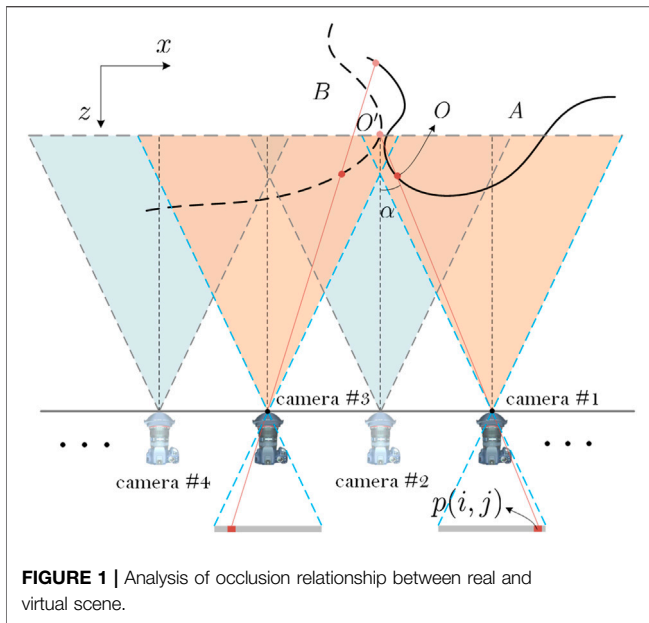
However, in the field of holographic stereograms, there is little research on the AR display of 3D scenes. Drawing on the experience of AR, the main task of AR 3D display of holographic stereograms is to implement the fusion coding of 3D real and virtual scenes information. Moreover, the key to fusion lies in the correct expression of the occlusion relationship between scenes. Three methods exist to deal with the problem of real and virtual scenes occlusion: model-based, depth-based, and image analysis-based methods.

The model-based method is used to reconstruct the 3D model of the real scene by a computer and then export the model data and render the virtual scene at the same time to achieve the fusion effect. This method was first proposed by Breen in 1996, but it was difficult to realize due to the technical conditions at that time [14]. Ong et al. presented a 3D reconstruction approach using a structure from motion (SFM) algorithm to obtain the real scene 3D model, avoiding the huge workload of traditional modeling [15]. Newcombe et al. designed a 3D reconstruction

system that can transmit 3D information accurately and in real time [16]. The system uses a Kinect sensor to obtain the depth information of the real scenes and uses GPU parallel computing for real-time reconstruction and fusion rendering. The depth-based method is used to determine the occlusion relationship according to the depth value of the object point and usually only displays the information of the near object point. Wloka et al. proposed a video see-through AR system capable of resolving occlusion between real and computer-generated objects, which calculates the pixel depth value through a stereo matching algorithm and compares the depth value to determine the position relationship between real and virtual scenes [17]. Some researchers use hardware devices to calculate depth. Jesus et al. introduced a depth-of-flight range sensor into AR to obtain the depth map and then judged the visibility of the fusion scene [18]. The method based on image analysis, which was proposed by Berger in 1997 [19], is to first detect the edge of the real scene image, draw an accurate contour, and then manually mark and complete the occlusion relationship between the real and virtual scenes. This method relies on the superiority of the edge detection algorithm, and each image must be marked manually; so, it cannot guarantee real-time performance. Many researchers have proposed background extraction and target contour fusion, but the results are not accurate [20–22]. Roxas et al. used a CNN-based semantic segmentation algorithm to obtain more accurate foreground segmentation results. Moreover, according to the complexity of object boundary and texture, labels are assigned to the real scene, which improves the automation performance [23].

The model-based method can better express the occlusion relationship by putting the real and virtual scenes into the same time and space, but there is a certain degree of information loss in using a 3D model to express the real light field, which will cause the real scene to be unreal. In theory, the depth-based method can effectively deal with more complex occlusion relationships, but, in practice, the accurate calculation of a depth map is not easy, and there are some other problems, such as limited range, dependence on lighting conditions, and sparsity of data points. The method based on image analysis not only keeps the authenticity of the real light field but also does not need to calculate the accurate depth value. However, it usually needs manual marking and has a low degree of automation.

In this paper, we reference the method based on image analysis and use the Mask R-CNN [24] instance segmentation algorithm to extract the contour of the real scene. To reduce the manual marking part and improve the automation of the image analysis-based method, we use the results of an instance segmentation algorithm to give a pseudo-depth-value to each instance according to the occlusion relationship, and then the depth-based method is applied to encode the optical field to achieve the effective fusion when the virtual scene and real scene have a mutual occlusion relationship. The principle and implementation details of the optical field coding method are introduced. The encoded images are processed by the effective perspective images' segmentation and mosaicking (EPISM) printing method [25, 26]. Optical experiments show that the method proposed in this paper can effectively realize AR 3D display of holographic stereogram.

FIGURE 1 | Analysis of occlusion relationship between real and virtual scene.

FIGURE 2 | Correspondence between pixels and points in optical field fusion.

Finally, we analyze and discuss the reconstructed optical field in detail.

BASIC PRINCIPLES AND METHOD

Real and Virtual Scenes Occlusion in Holographic Stereogram AR Display

The scene's information fusion coding of an AR-based holographic stereogram cannot be simply obtained by superimposing virtual 3D scenes onto the real scenes. The real and virtual scenes should have a reasonable or even complex occlusion relationship, so that the observer can have a good and real visual experience that can reconstruct the real and virtual fused 3D scenes correctly.

Figure 1, taking a simple real and virtual fused 3D scene as an example, shows a real 3D scene A and a virtual one B. For simplicity, the occlusion on the $x - z$ plane is analyzed. After image coding, the perspective seen at the camera #1 position should display part of the information of the two scenes at the same time. Taking pixel $p(i, j)$ [(i, j) is the pixel position index in the sampled image] as an example, when A and B are sampled, object points O on A and O' on B retain the optical information at pixel $p(i, j)$ of their respective sampled images. However, considering occlusion, O blocks O' at the camera #1 position. Therefore, pixel $p(i, j)$ of the encoded image should only retain the information of object point O of the virtual scene. The situation of camera #3 is contrary to that of camera #1.

The fused image from a certain perspective can be expressed as:

$$Q_{AR}(i, j) = \begin{cases} I[O(x, z, \alpha)], z < z' \\ I[O'(x', z', \alpha)], z > z'' \end{cases} \quad (1)$$

where $Q_{AR}(i, j)$ represents the fused image pixel information at pixel index positions (i, j). $O(x, z, \alpha)$ and $O'(x', z', \alpha)$ are the object
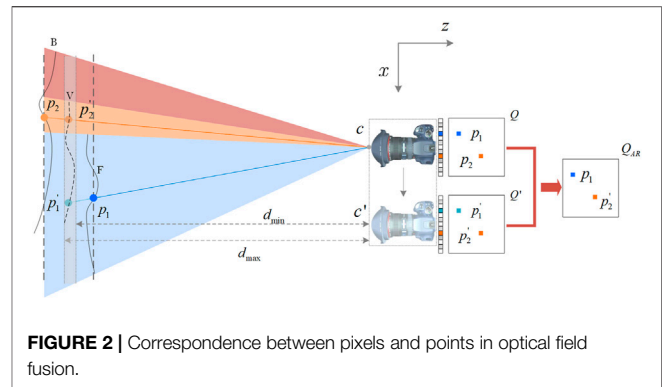
point information, and α is the projection angle. $I[\bullet]$denotes the optical intensity information. Because the object points of real and virtual scenes usually do not coincide, $z = z'$ is meaningless and need not be discussed. **Eq. 1** only gives the principle of depth determination in the case of occlusion, and it must be explained that there is no need for depth comparison in the case of no occlusion.

The above is the basic principle of the depth-based method, in which the process of solving the depth information z is the key but also the challenge. Depth estimation algorithms are usually used to calculate depth information, such as monocular depth estimation [27–29], stereo matching algorithms [30–32], and depth estimation based on deep learning [33–35]. However, it is difficult to obtain accurate depth values using these methods, and a good effect in estimating the depth of the scene over a long distance cannot be achieved. When the distance between the real and virtual scenes is large, the error caused by depth estimation is acceptable. However, when the depth difference is small, the error of depth estimation will result in an incorrect choice, which makes the original occlusion relationship completely contrary. This is not acceptable, and we have to find a new way to solve this problem.

Fusion Method Based on Instance Segmentation and Pseudo-depth

The principle of the depth-based method shows that the main reason for occlusion in the fusion images between the real and virtual 3D scenes is the difference of object point depth information in a certain ray. The point with a small depth blocks the point with a large depth and leaves the intensity information at the corresponding pixels of the fusion image. However, the decision condition is only to compare the value of the depth and does not require the specific depth value, which provides the opportunity to improve the depth-based method.

Referring to **Figure 2**, B and F are the projection curves of the background and foreground, respectively, of the real scene on the $x - z$ plane; V is the projection curve of the virtual scene, and its depth range is $(d_{\min}, d_{\max})$. c and c are the real and virtual sampling cameras, respectively, with the same spatial pose at a certain viewpoint. After sampling, perspectives Q and Q' are obtained separately. The intensity information of points p_1 and p_2
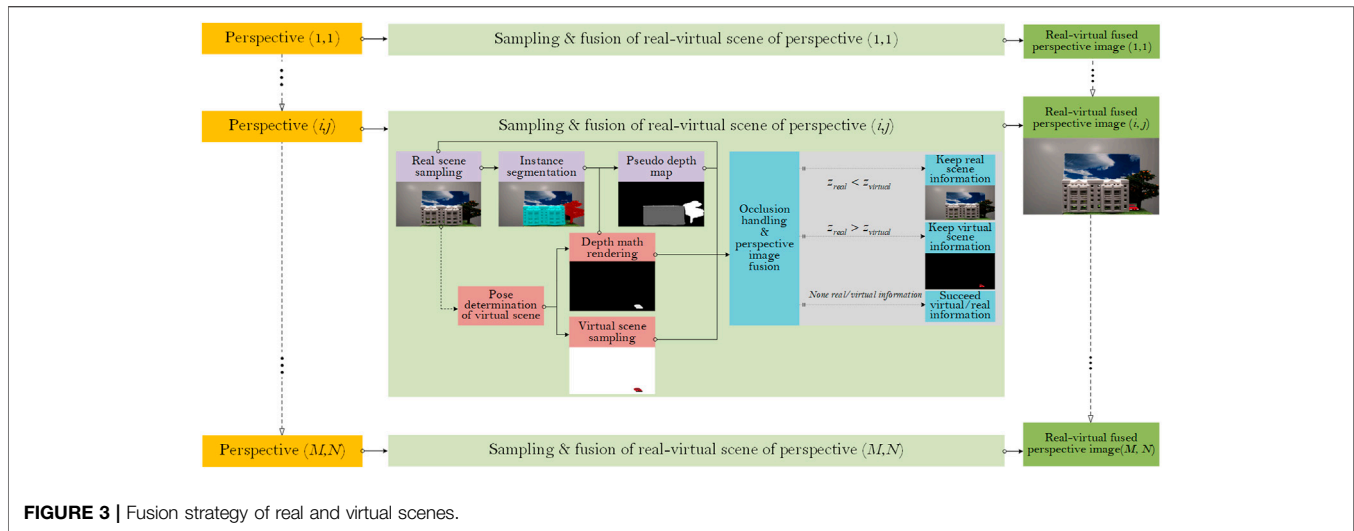
FIGURE 3 | Fusion strategy of real and virtual scenes.

are kept in Q and that of points p_1' and p_2' are kept in Q'. For the fused optical field to satisfy the occlusion relation depicted in **Figure 2**, it must be ensured that

$$\begin{cases} d_F < d_{\min} \\ d_B > d_{\max} \end{cases}, \tag{2}$$

where d_F and d_B are the depths of F and B, respectively. Here, we use the instance segmentation method [36, 37] to layer the foreground and background of the real scene, assign a pseudo-depth-value to each layer according to **Eq. 2**, and then use the depth-based method for image coding, as follows:

$$Q[p_1, p_2] + Q'[p_1', p_2'] = Q_{AR}[p_1, p_2'] \tag{3}$$

In terms of technical difficulty, instance segmentation is simpler than accurate depth calculation. Next, combined with the actual application of the scene in this paper, the real and virtual scene image fusion coding strategy is introduced in detail.

Fusion Strategy of Real and Virtual Scenes

Figure 3 shows the fusion strategy of real and virtual scenes for holographic stereogram AR 3D display. Taking the perspective (i, j) [(i, j) is the sequential index of perspectives, and the total number of images is $M \times N (1 \le i \le M, 1 \le j \le N)$] in the perspective sequence as an example, the basic principles and methods of the strategy are described in detail.

Step 1: Real scene sampling. Obtain the real scene sampling perspective sequence. The instance segmentation algorithm is used to segment different instances in the scene. Furthermore, the real scene sampling images $Q_R(s, t)$ [(s, t) is the pixel position index of the depth map] in **Figure 3** can be represented as

$$Q_R(s, t) = H + T + B, \tag{4}$$

where the three terms on the right-hand side of the equation represent the light field sampling information of the house, tree, and background in $Q_R(s, t)$, respectively.

Step 2: According to the scene space position and camera pose adjustment in Step 1, the virtual scene sampling parameters are set. The sampled image $Q_V(s, t)$ can be expressed as

$$Q_V(s, t) = C + B' \tag{5}$$

where C and B' represent the car and background of the image $Q_V(s, t)$, respectively. The depth map is rendered at the same time. The quantization method of depth map is given by

$$D_V(s, t) = D_V^{(C)} \cup D_V^{(B')} \begin{cases} 255 \times \dfrac{z^{(s,t)} - z_{\min}}{z_{\max} - z_{\min}}, & z_{\min} \le z^{(s,t)} \le z_{\max} \\ 255, & z^{(s,t)} > z_{\max} \\ 0, & z^{(s,t)} < z_{\min} \cup z \in B' \end{cases}, \tag{6}$$

where $D_V^{(\bullet)}$ represents the depth map of $\bullet$, $z^{(s,t)}$ is the depth of the corresponding object point, and $z_{\min}$ and $z_{\max}$ are the quantization ranges of the set depth value. In the pixel area without a scene, the value is 0.

Step 3: According to the occlusion relationship and the depth map of the virtual scene, the pseudo-depth-value is assigned to each instance after the instance segmentation, and the value of H occlusion C and C occlusion T is given as

$$\begin{cases} D_R^{(H)} \in (0, \min[D_V(s, t)]) \\ D_R^{(T)} \in (\max[D_V(s, t)], 255), \\ D_R^{(B)} = 0 \end{cases} \tag{7}$$

where $D_R^{(H)}$, $D_R^{(T)}$, and $D_R^{(B)}$ represent the values assigned to each instance and background, which are respectively H for house, T for tree, and B for background. Then, the pseudo-depth-map can be expressed as

$$D_R = D_R^{(H)} \cup D_R^{(T)} \cup D_R^{(B)}. \tag{8}$$

Step 4: The fusion of real and virtual optical fields. According to the depth-based method, the near information in the fusion scene is retained in the processed image, as shown in

FIGURE 4 | (A) Single camera timing sampling system **(B)** real scene image.

$$Q_F(s,t) = \begin{cases} Q_R(s,t), D_R(s,t) < D_v(s,t) \\ Q_V(s,t), D_R(s,t) > D_v(s,t) \\ Q_R(s,t), D_R(s,t) = D_v(s,t) = 0 \end{cases} . \qquad (9)$$

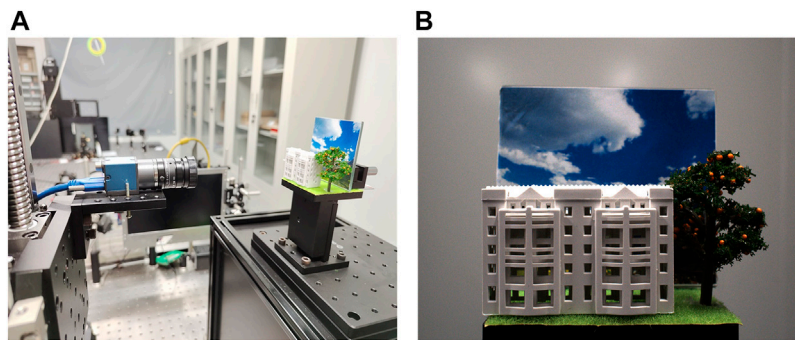Note that $D_R(s,t) = D_V(s,t) = 0$ above, indicating that the virtual depth map and real pseudo-depth-map are only 0 at the same time when the position value of a pixel is equal. This is because there is usually no point in space that belongs to both the real scene and virtual scene. The above-mentioned four steps can realize the fusion of real and virtual optical fields with a correct occlusion relationship in each image. It should be pointed out that, for the perspective sequence shown in **Figure 3**, each group of horizontal parallax image sequences is transformed from the real scene occlusion virtual scene to the virtual scene occlusion real scene, which allows us to not have to code the images one by one. In our work, we only coded the optical field twice—once to keep the foreground pixels of the real scene in the occluded area, and once to keep the pixels of the virtual scene—and then extracted the images with a correct occlusion relationship. However, although this process is more flexible than manually marking each image, it is still not fully automated. Of course, automation is not the main goal of this paper.

EXPERIMENT AND DISCUSSION

Implementation of Optical Field Coding

According to the above-mentioned four steps, we gradually realized the effective coding of real and virtual scene optical fields and carried out the detail display and result analysis.

Real Scene Sampling and Instance Segmentation

In our work, we used the "house and tree" model as the foreground objects of the real scene and the "sky" as the background (see **Figure 4B**). A single camera timing sampling system was built to sample the real scene's perspective information. A single MER2-502-79U3C CMOS digital camera was fixed on a Zolix KSA300 electronic control displacement platform. The stepper motor in the displacement platform was driven by a Zolix MC600 motion controller, which could realize

arbitrary interval shift sampling in both the horizontal and vertical directions, as shown in **Figure 4A**.

After comprehensive comparison of several instance segmentation methods, we used the better Mask R-CNN instance segmentation network architecture for processing. Mask R-CNN can realize target detection, semantic segmentation, and instance segmentation. Fast R-CNN (an excellent target detection network architecture) adds a full convolution network (FCN), realizes semantic segmentation on the basis of target detection, and then realizes instance segmentation [38]. It adds a layer of random color mask to the specified instance. Using the Windows operating system and the efficient computing power of an NVIDIA TITAN XP graphics card, we built a Mask R-CNN network architecture based on the Keras2.1.5 model library on the Tensorflow 1.13.2 deep-learning open-source framework. A dataset of 400 real scene images with mask labels was produced by using the "labelme" annotation tool (the total number of images to be encoded was 4,761), of which 350 were used for training and 50 for validation. We set the training times to 150 epochs. After the iterative optimization training of the multi-layer feature pyramid network, the training set loss was reduced to 0.017, the validation set loss was reduced to 0.016, and the confidence of the target detection accuracy was close to 1.0. **Figures 5A,B** show the sampled images and labeled masked label in the experiment respectively. The test effect on the self-made dataset is shown in **Figure 5C**. Details of the occlusion mask are shown. The main part of the house model was completely covered, but areas violating the mask coverage still remained at the four corners. This may be due to the small cardinality of self-made datasets. The edge of the house and tree trunk can be completely covered, which basically meets the requirements of stratification.

Virtual Scene Sampling and Depth Map Rendering

The virtual scene was rendered with 3D studio Max software, and its sampling was adopted to be consistent with the real scene sampling settings. In addition, the "Z depth" channel was rendered to obtain the "car" model's depth maps, where the front end of the car was 14.3 cm from the camera. The gray value of the depth map of the car area was between 139 and 232 (0–255 is used to represent the gray range of each gray image). **Figures 6A,B** show one of the sampled images and its depth map of the virtual scene.
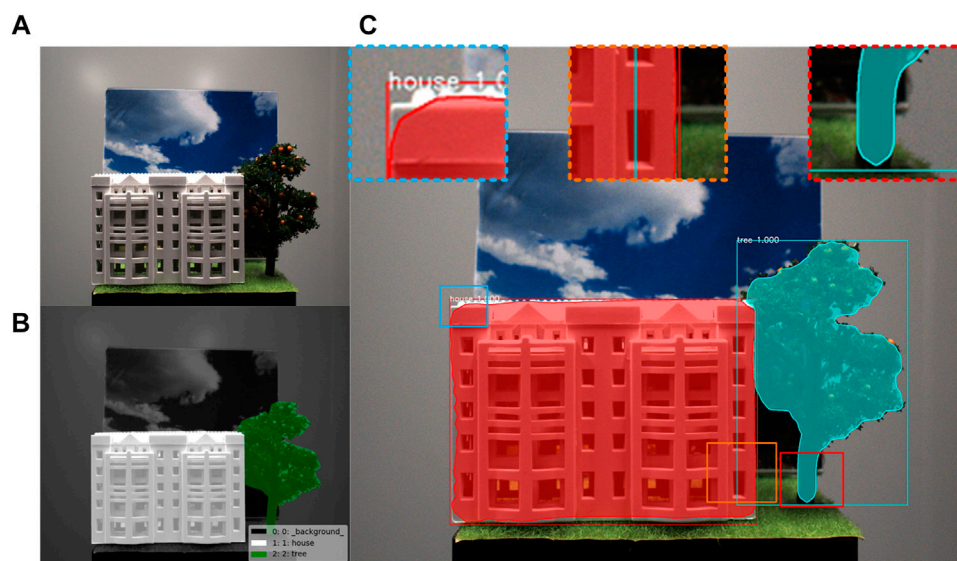
FIGURE 5 | **(A)** An real scene image and **(B)** its masked label files **(C)** Details display after instance segmentation.
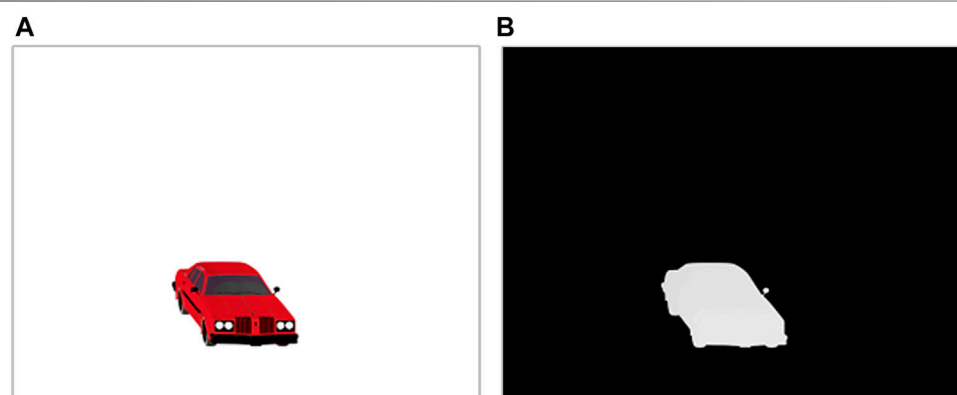
FIGURE 6 | **(A)** A virtual scene image and **(B)** its depth map.
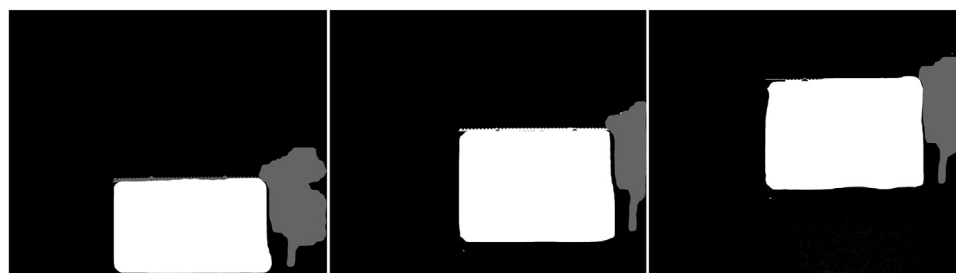
FIGURE 7 | Three gray images with pseudo-depth-values.

Generating Pseudo Depth Map

The trained model was used to predict all the real scene images to be encoded, and the corresponding images with masks were obtained. Digital image processing technology is used to assign pseudo-depth-values to the areas covered by each mask in each image. In order to ensure that the car stopped between the house
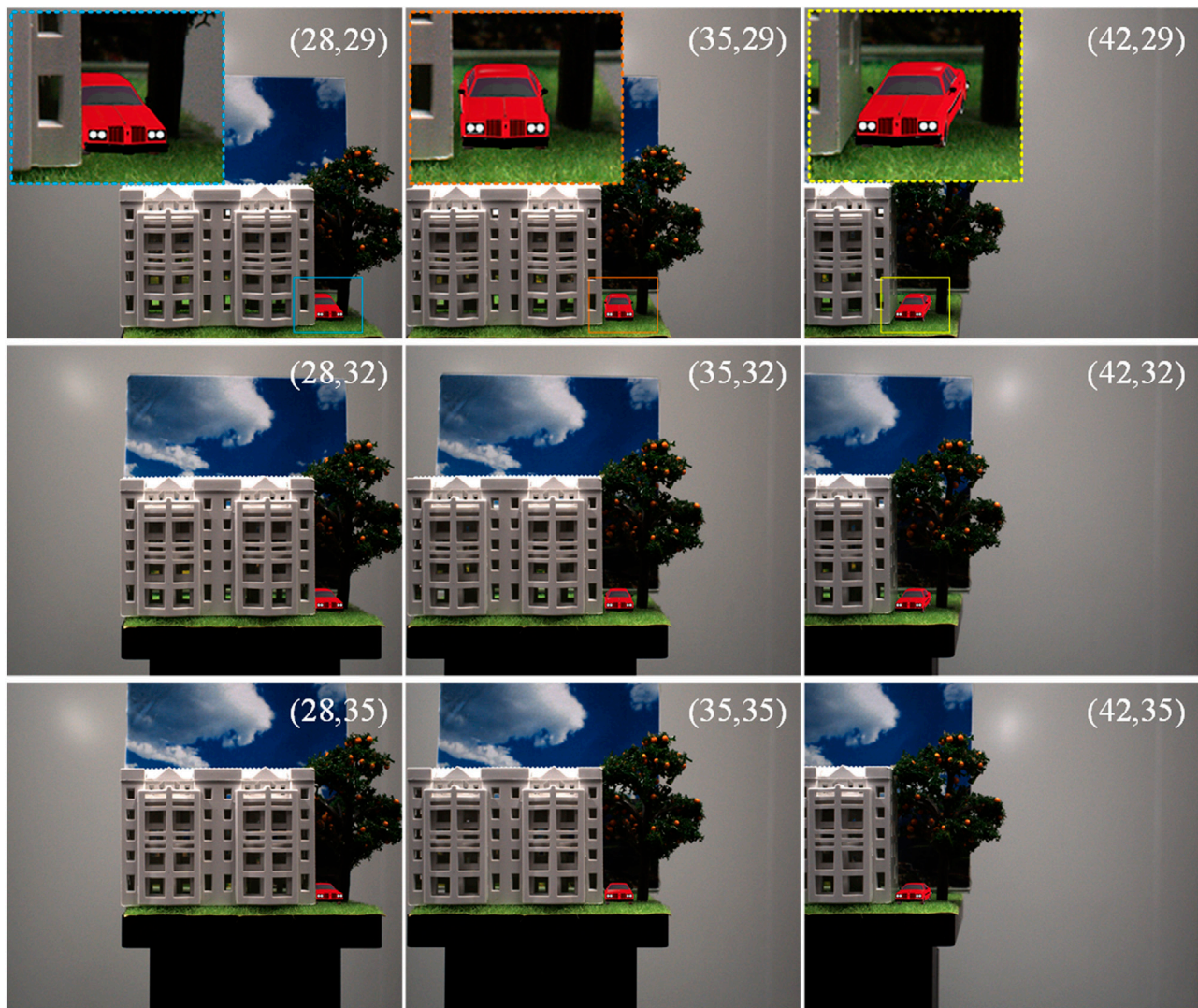
FIGURE 8 | Nine encoded perspectives.

and the tree, we assigned values to two groups of pseudo-depth-maps. In one group, the house was 100, the tree was 255, and the background was 0. In the other group, the house was 255, the tree was 100, and the background was 0 (corresponding to the principle). **Figure 7** shows three pseudo-depth-maps.

Optical Field Fusion Coding

Figure 8 shows some encoded perspectives, which are the images with the correct occlusion relationship selected from the results of the above-mentioned two groups of pseudo-depths. The number labels in the upper right-hand corner of the perspectives represent the ranking of these images in the sequence. We zoomed-in on some of the details of the first three images to show the coding effect. It can be seen that the information of the virtual scene has been integrated into the house and tree of the real scene. In perspective (28,29), the rear part of the car is blocked by the house, and the tree is blocked by the front of the car. In perspective (35,29), there is no occlusion relationship between the

car and the house. In perspective (42,29), the house is blocked by the front of the car. This further proves the effectiveness of the proposed method for the fusion of real and virtual occlusion. In addition, our optical field coding method only determines the position at which there is scene information in the virtual images and directly retains the real scene information of the position at which there is no scene information. Therefore, the encoded images are not affected by the incomplete coverage of the instance segmentation mask.

After the fusion perspectives of real and virtual scenes are obtained, the EPISM method can be used for the image process to generate the optical field information that can be directly used for holographic printing. For details of the EPISM printing method, please refer to Ref. [25].

Optical Experiment and Discussion

The EPISM holographic stereogram printing method proposed by our group is used for image pre-processing to

FIGURE 9 | Holographic printing optical scheme.
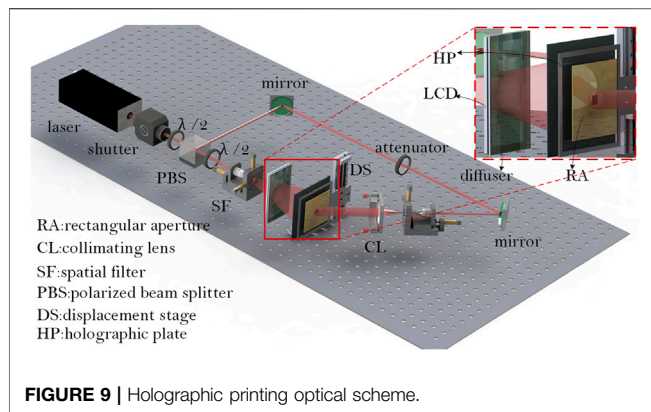
obtain the exposure images for holographic printing. The optical experimental scheme was set up as shown in **Figure 9**. A 400-MW/639-nm single longitudinal mode linearly polarized solid-state laser (CNI MSL-FN-639) was used as the light source, and an electronic shutter (Sigma Koki SSH-C2B) was used to control the exposure time. After passing through a $\lambda/2$-wave plate and a polarizing beam splitter (PBS), the laser beam divided into two beams, namely, the object beam and the reference beam. The polarization state of the object beam was adjusted by a $\lambda/2$-wave plate to be consistent with the reference beam. The attenuator of the reference beam was adjusted to attain an object reference energy ratio of 1:20. The object beam irradiated the LCD screen after being expanded and reached the holographic plane after being diffused by the scattering film. After filtering and collimating, the uniform plane wave reference beam was obtained. The object beam and reference beam interfered with each other after being incident from both sides, and the exposure image information was written. The holographic plate was fixed on the KSA300 X-Y linear displacement platform, and the positioning accuracy of the platform in the horizontal and vertical directions was 1 μm. The displacement platform was controlled by an MC600

programmable controller. In our work, the size of the hogel was 4 mm, and the size of the hologram was 8 cm.

After printing, the holographic plate can reconstruct 3D images in the conjugate of original reference light after developing and bleaching. As shown in **Figure 10**, the reconstructed image was taken with a Canon camera and a macro lens with a focal length of 100 mm, which was placed approximately 40 cm in front of the holographic plate.

As shown in **Figure 11**, the full parallax reconstruction effect of an AR 3D image in a holographic stereogram at different angles of view can be observed. It can be further observed that the fusion reconstruction images of real and virtual scenes are not only consistent with the original scene at the time of acquisition but the occlusion of a virtual scene to a real scene also conforms to the corresponding spatial position relationship, that is, at the left angle (−5°, +2.5°), the car is blocked by the house, and at the right angle (+5°, +2.5°), the house is blocked by the car, which shows the correctness of the optical field coding method. The holographic stereogram has smooth motion parallax and no visual jump effect. According to the printing principle of the EPISM method, the field of view of the holographic stereogram is determined by the field of view of the printing system and each hogel. In this experiment, the field of view is 39.8°. However, due to the large main part of the real scene, when the observer is located in the limited visual area ±19.9°, the foreground part of the entire real scene (houses, cars, and trees in the image) will not be observed in the reconstructed optical field. In order to capture the complete reproduction image of the real scene and to better display the AR 3D display effect, the shooting angle of the digital camera—that is, the horizontal and vertical viewing angles shown in **Figure 11**—is less than 19.9°. The horizontal observation angle is also slightly larger than the vertical observation angle.

In order to further test the ability of detail expression (see **Figure 12**) and the expressiveness of the scene depth (see **Figure 13**) of the AR hologram obtained by the proposed

FIGURE 10 | Holographic optical reconstruction scheme.
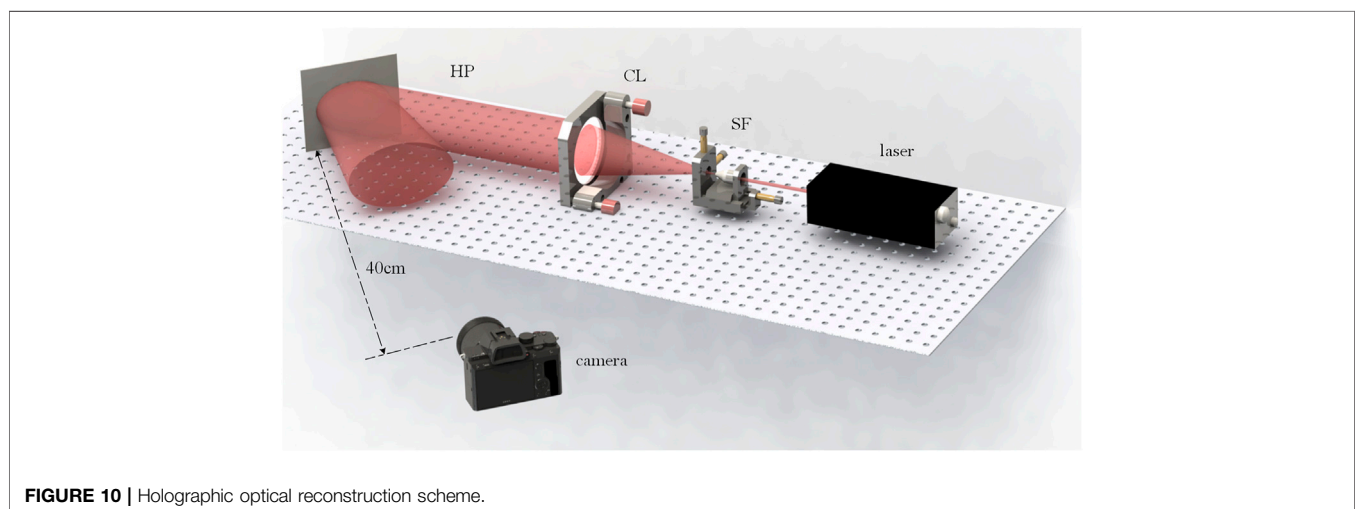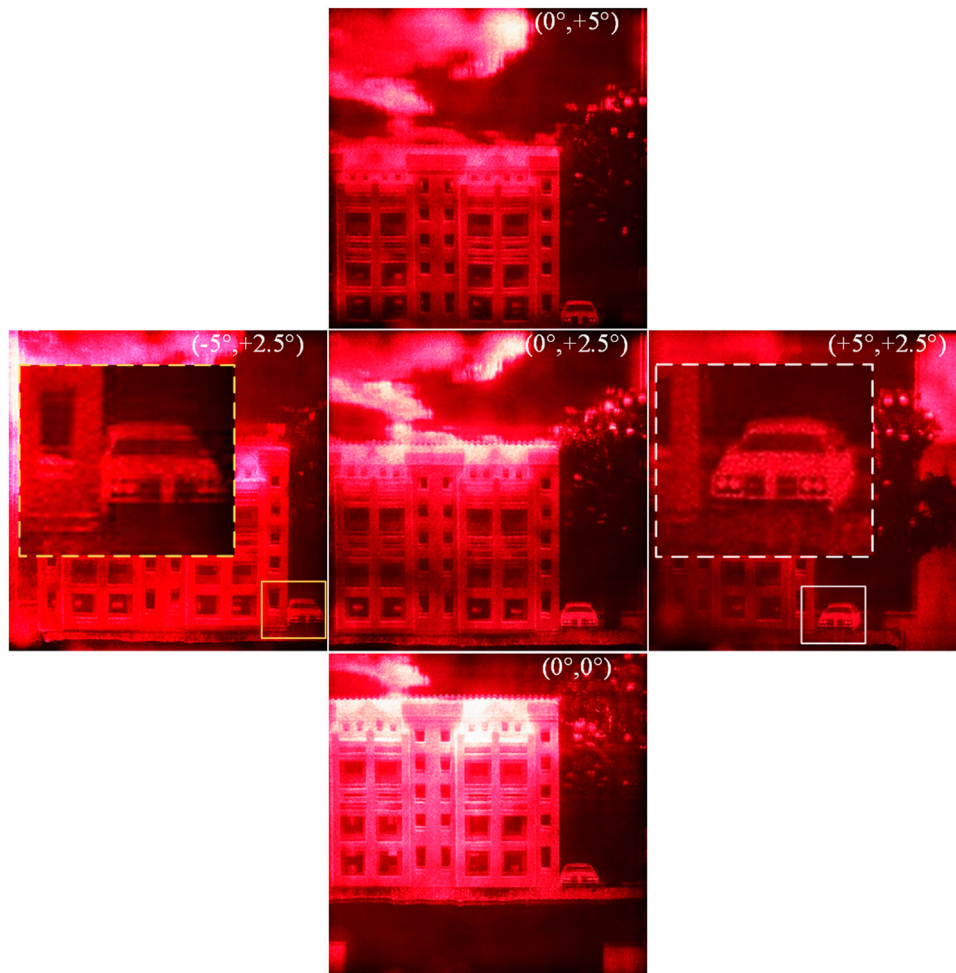
FIGURE 11 | Reproduction images of five viewpoints.

FIGURE 12 | Effect display of a new scene of augmented-reality display.
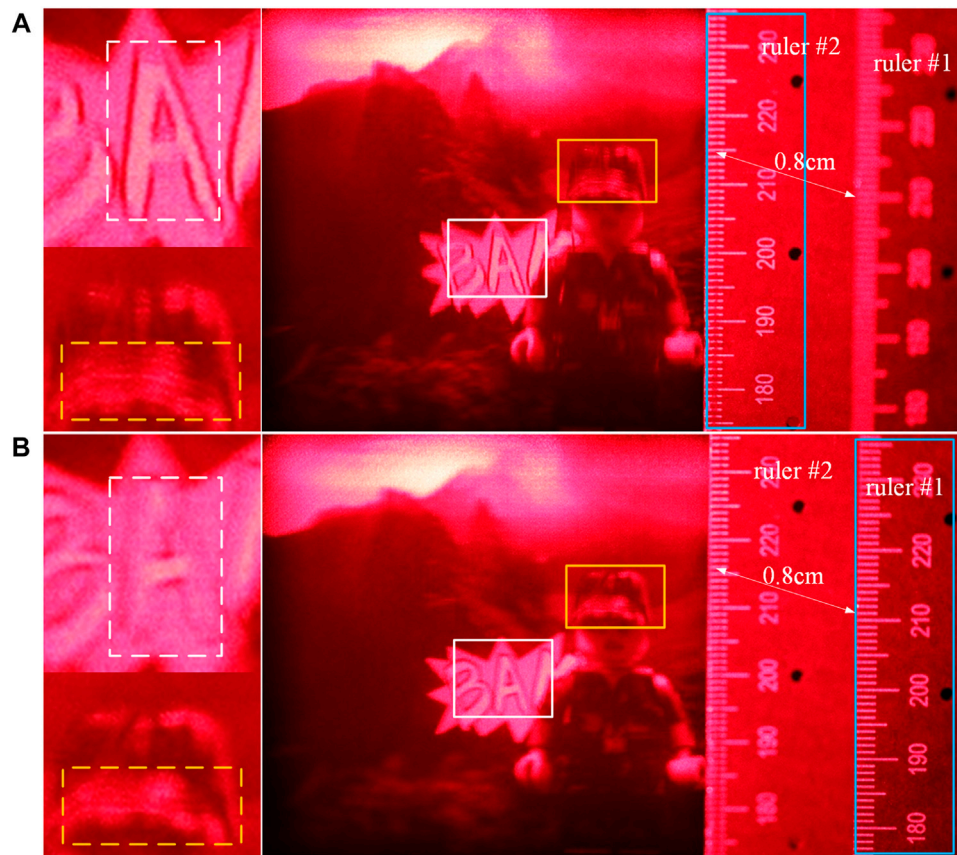
FIGURE 13 | Analysis of scene depth information.

method, we used the same printing system and selected a soldier model and a "BAM!" model as the real scene and the virtual scene, respectively; the holographic stereogram was printed again, and the reconstructed image was taken.

Figure 12 shows the sampled image and the reproduced image, which is successfully displayed by the fusion of real and virtual scenes and some details (from right to left). In the two detailed images on the left, the neck of the soldier can be well integrated with the virtual scene, but the arm is not as smooth as in the sampled image, which is due to the difference of coverage of different parts in the segmentation results of the instance. This shows that the proposed optical field coding method of a holographic stereogram AR display is greatly affected by the effect of instance segmentation. Therefore, in order to achieve high-quality display, the accuracy of instance segmentation must be improved.

Two rulers were placed to help display the comparison results, as shown in **Figure 13**. The distance between ruler #1 and the holographic plate is 14.3 cm and that between ruler #2 and the holographic plate is 13.5 cm, which are consistent with the sampling parameters. It can be seen that when the camera focuses on ruler #2, the letter "A" is displayed clearly. When ruler #1 is clear, the soldier is clearer than ruler #2. This not only means that there is a depth difference between the real

and virtual scenes in the reconstructed image but also indicates that the depth difference does not change with the pseudo-depth assignment. It should be pointed out that the real camera sampling effect is not as good as that of the virtual camera in the software; the contrast effect is not obvious, but we can see that the artifact of the hat is reduced.

CONCLUSION

In our work, a fusion coding method of 3D real and virtual scenes information is proposed to achieve an AR-based holographic stereogram. Theoretical analysis and experimental results show that the proposed coding method can effectively add some virtual 3D elements into the real scene to enhance the visual experience in the field of holographic stereogram 3D display. The combination of real and virtual scenes fully considers the occlusion relationship, which is not a simple scene superposition. The core is to assign and determine the pseudo-depth after instance segmentation. There is still a large gap between the AR 3D display mentioned in this paper and the latest work in the field of AR, but the proposed method provides a basic idea for the research direction of holographic stereogram AR 3D display, which can be further explored. For

example, by continuously improving the efficiency of instance segmentation, the scenes can be more accurately foreground-extracted. Moreover, if the accurate depth calculation method can be studied, then using the accurate depth value as the basic processing data can better present the effect of holographic stereogram AR 3D display. It should be pointed out that our work only discusses simple and small scenes that tend to be the ideal conditions. However, the related work of complex scenes still needs further analysis and research; for example, there are no obvious foreground objects and background objects in the scene, or the front and back objects belong to the same instance. Taking our experiment as an example, if the car is located inside of the garage, only a part of the garage needs to be separated in the instance segmentation, which violates the original intention of the instance segmentation algorithm. Therefore, the methods mentioned in this paper have some limitations. Therefore, the aforementioned related issues must be further studied in future.

DATA AVAILABILITY STATEMENT

The datasets presented in this study can be found in online repositories. The names of the repository/repositories and accession number(s) can be found below: https://github.com/yanyu-holo/Augmented-Reality-Based-Holographic-stereogram.

REFERENCES

1. Brotherton-Ratcliffe D. *Ultra-realistic Imaging: Advanced Techniques in Analogue and Digital Colour Holography,Hans Bjelkhagen and David Brotherton-Ratcliffe*. Boca Raton, FL: Ultra-Realistic Imaging - Advanced Techniques in Analogue and Digital Colour Holography (2013).
2. Su J, Yan X, Huang Y, Jiang X, Chen Y, and Zhang T. Progress in the Synthetic Holographic Stereogram Printing Technique. *Appl ences* (2018) 8(6):851. doi:10.3390/app8060851
3. Yamaguchi M. Light-Field and Holographic Three-Dimensional Displays [Invited]. *J Opt Soc Am A* (2016) 33(12):2348. doi:10.1364/josaa.33.002348
4. Gabor D. A New Microscopic Principle. *Nature* (1948) 161:777. doi:10.1038/161777a0
5. Qian N. Binocular Disparity and the Perception of Depth. *Neuron* (1997) 18(3):359–68. doi:10.1016/s0896-6273(00)81238-6
6. Wang Z, Lv G, Feng Q, Wang A, and Ming H. Enhanced Resolution of Holographic Stereograms by Moving or Diffusing a Virtual Pinhole Array. *Opt Express* (2020) 28(15):22755–66. doi:10.1364/OE.396639
7. Wang Z, Lv GQ, Feng QB, Wang AT, and Ming H. Resolution Priority Holographic Stereogram Based on Integral Imaging With Enhanced Depth Range. *Opt Express* (2019) 27(3):2689–702. doi:10.1364/OE.27.002689
8. Li Q, He W, Deng H, Zhong F-Y, and Chen Y. High-Performance Reflection-Type Augmented Reality 3D Display Using a Reflective Polarizer. *Opt Express* (2021) 29(6):9446. doi:10.1364/oe.421879
9. Shi L, Li B, Kim C, Kellnhofer P, and Matusik W. Towards Real-Time Photorealistic 3D Holography With Deep Neural Networks. *Nature* (2021) 591(7849):234–9. doi:10.1038/s41586-020-03152-0
10. Maimone A, Georgiou A, and Kollin JS. Holographic Near-Eye Displays for Virtual and Augmented Reality. *ACM Trans Graph* (2017) 36(4):1–16. doi:10.1145/3072959.3073624
11. Yang X, Zhang H, and Wang Q-H. A Fast Computer-Generated Holographic Method for VR and AR Near-Eye 3D Display. *Appl Sci* (2019) 9(19):4164. doi:10.3390/app9194164
12. Starner T. Project Glass: An Extension of the Self. *IEEE Pervasive Comput* (2013) 12(2):14–6. doi:10.1109/mprv.2013.35

13. Gottmer ML. *Merging Reality and Virtuality with Microsoft HoloLens*. MS thesis (2015).
14. Breen D, Whitaker RT, Rose E, and Tuceryan M. Interactive Occlusion and Automatic Object Placement for Augmented Reality. *Computer Graphics Forum* (1996) 15:11. doi:10.1111/1467-8659.1530011
15. Ong KC, Teh HC, and Tan TS. Resolving Occlusion in Image Sequence Made Easy. *Vis Computer* (1998) 14(4):153–65. doi:10.1007/s003710050131
16. Newcombe RA, Izadi S, Hilliges O, Molyneaux D, and Fitzgibbon AW. KinectFusion: Real-Time Dense Surface Mapping and Tracking. In: *IEEE International Symposium on Mixed & Augmented Reality* (2012).
17. Wloka MM. Resolving Occlusion in Agumented Reality. In: *Proceedings of the 1995 symposium on Interactive 3D graphics* (1995) 5–12.
18. Fischer J, Huhle B, and Schilling A. Using Time-Of-Flight Range Data for Occlusion Handling in Augmented Reality. In: Proceedings of the 13th Eurographics conference on Virtual Environments (2007). p. 109–16.
19. Berger MO. Resolving Occlusion in Augmented Reality: a Contour Based Approach without 3D Reconstruction. *Proc IEEE Computer Soc Conf Computer Vis Pattern Recognition* (2002) 91–96. doi:10.1109/CVPR.1997.609304
20. Wang HL, Sengupta K, Kumar P, and Sharma R. Occlusion Handling in Augmented Reality Using Background-ForeGround Segmentation and Projective Geometry. *Presence: Teleoperators & Virtual Environments* (2005) 14(3):264–77. doi:10.1162/105474605323384636
21. Wang HL, Sengupta K, and Sharma R. Augmented Reality with Occlusion Rendering Using Background-ForeGround Segmentation and Trifocal Tensors. In: International Conference on Multimedia & Expo (2003).
22. Setohara H, Kato H, Kawamoto K, and Tachibana K. A Simple Solution of Occlusion Problem in Augmented Reality and its Application for Interaction. *Trans Virtual Reality Soc Jpn* (2004) 9:387–95. doi:10.18974/tvrsj.9.4_387
23. Roxas M, Hori T, Fukiage T, Okamoto Y, and Oishi T. Occlusion Handling Using Semantic Segmentation and Visibility-Based Rendering for Mixed Reality. In: Proceedings of the 24th ACM Symposium on Virtual Reality Software and Technology (2018).
24. He K, Gkioxari G, Dollár P, and Girshick R. Mask R-CNN. *IEEE* (2017) 2980–2988. doi:10.1109/ICCV.2017.322

AUTHOR CONTRIBUTIONS

Conceptualization, YL, ML and XY; methodology, YL, SC and XY; software, XW, ML and TJ; validation, PL, XJ and XW; formal analysis, YL and TJ; resources, XY and SC; data curation, XL; writing—original draft preparation, YL, XL and ML; writing—review and editing, YL and ML; visualization, SC; supervision, XY; project administration, XY; funding acquisition, XY All authors have read and agreed to the published version of the manuscript.

FUNDING

ACKNOWLEDGMENTS

25. Jian S, Quan Y, Huang Y, Jiang X, and Yan X. Method of Single-step Full Parallax Synthetic Holographic Stereogram Printing Based on Effective Perspective Images' Segmentation and Mosaicking. *Opt Express* (2017) 25(19):23523–44. doi:10.1364/OE.25.023523

26. Su J, Yan X, Jiang X, Huang Y, Chen Y, and Zhang T. Characteristic and Optimization of the Effective Perspective Images' Segmentation and Mosaicking (EPISM) Based Holographic Stereogram: an Optical Transfer Function Approach. *Sci Rep* (2018) 8(1):4488. doi:10.1038/s41598-018-22762-3

27. Roy A, and Todorovic S. Monocular Depth Estimation Using Neural Regression Forest. In: 2016 IEEE Conference on Computer Vision and Pattern Recognition. (Seattle, WA: CVPR) (2016).

28. Fu H, Gong M, Wang C, and Tao D. A Compromise Principle in Deep Monocular Depth Estimation. arXiv preprint arXiv:170808267. (2017).

29. Yan H, Zhang S, Zhang Y, and Zhang L. Monocular Depth Estimation with Guidance of Surface normal Map. *Neurocomputing* (2017) 280(MAR.6):86–100. doi:10.1016/j.neucom.2017.08.074

30. Isard M, and Blake A. CONDENSATION—Conditional Density Propagation for Visual Tracking. *Int J Computer Vis* (1998) 29(1):5–28. doi:10.1023/a:1008078328650

31. Sekine Y. Effects of Country-Of-Origin Information on Product Evaluation: An Information Processing Perspective. *Neurosci Biobehavioral Rev* (2017) 72(6):232. doi:10.1016/j.neubiorev.2016.12.003

32. Chang JR, and Chen YS. Pyramid Stereo Matching Network. In: 2018 IEEE/CVF Conference on Computer Vision and Pattern Recognition. (Salt Lake City, UT: CVPR) (2018).

33. Liu F, Shen C, Lin G, and Reid I. Learning Depth from Single Monocular Images Using Deep Convolutional Neural Fields. *IEEE Trans Pattern Anal Mach Intell* (2015) 38(10):2024–39. doi:10.1109/TPAMI.2015.2505283

34. Schwarz M, Schulz H, and Behnke S. RGB-D Object Recognition and Pose Estimation Based on Pre-Trained Convolutional Neural Network Features. In: IEEE International Conference on Robotics & Automation (2015).

35. Zhan H, Garg R, Weerasekera CS, Li K, Agarwal H, and Reid I. *Unsupervised Learning of Monocular Depth Estimation and Visual Odometry with Deep Feature Reconstruction.* Salt Lake City, UT: IEEE (2018).

36. Hc A, Xq A, Ly A, Qd A, Jq B, and Pah A. DCAN: Deep Contour-Aware Networks for Object Instance Segmentation from Histology Images - ScienceDirect. *Med Image Anal* (2017) 36:135–46. doi:10.1016/j.media.2016.11.004

37. Xu Y, Li Y, Liu M, Wang Y, Lai M, and Chang IC. Gland Instance Segmentation by Deep Multichannel Side Supervision. *IEEE Trans Biomed Eng* (2016) 99:1. doi:10.1007/978-3-319-46723-8_57

38. Girshick R. Fast R-CNN. *Computer Sci* (2015):1440–1448. doi:10.1109/iccv.2015.169

Recognition of Multiscale Dense Gel Filament-Droplet Field in Digital Holography With Mo-U-Net

Zhentao Pang[1], Hang Zhang[1], Yu Wang[1], Letian Zhang[2], Yingchun Wu[2]* and Xuecheng Wu[2]

[1]College of Energy Engineering, Zhejiang University, Hangzhou, China, [2]State Key Laboratory of Clean Energy Utilization, Zhejiang University, Hangzhou, China

Accurate particle detection is a common challenge in particle field characterization with digital holography, especially for gel secondary breakup with dense complex particles and filaments of multi-scale and strong background noises. This study proposes a deep learning method called Mo-U-net which is adapted from the combination of U-net and Mobilenetv2, and demostrates its application to segment the dense filament-droplet field of gel drop. Specially, a pruning method is applied on the Mo-U-net, which cuts off about two-thirds of its deep layers to save its training time while remaining a high segmentation accuracy. The performances of the segmentation are quantitatively evaluated by three indices, the positive intersection over union (PIOU), the average square symmetric boundary distance (ASBD) and the diameter-based prediction statistics (DBPS). The experimental results show that the area prediction accuracy (PIOU) of Mo-U-net reaches 83.3%, which is about 5% higher than that of adaptive-threshold method (ATM). The boundary prediction error (ASBD) of Mo-U-net is only about one pixel-wise length, which is one third of that of ATM. And Mo-U-net also shares a coherent size distribution (DBPS) prediction of droplet diameters with the reality. These results demonstrate the high accuracy of Mo-U-net in dense filament-droplet field recognition and its capability of providing accurate statistical data in a variety of holographic particle diagnostics. Public model address: https://github.com/Wu-Tong-Hearted/Recognition-of-multiscale-dense-gel-filament-droplet-field-in-digital-holography-with-Mo-U-net.

Keywords: gel droplet, secondary breakup, digital holography, deep learning, image segmentation

1 INTRODUCTION

Gel propellant, with the merits of high specific, strong density impulse [1, 2], smooth ignition [3], stable combustion [4] and good storage condition [5, 6], shows great potential in the field of rocket propellant for its unique properties. Recent years, studies on gel propellant involve formation [7], atomization [8, 9], flow characterization [10, 11] and combustion [12–14]. In practice, gel propellant is atomized in crossing flow and then combusts, and particularly, secondary atomization in downstream can dramatically influence the mixing and combustion efficiency [15]. Thus, the spatial-temporal evolution of the breakup of gel droplet, including morphology, droplet and fragment size and velocity, is of essential significance. The breakup process of a Newtonian droplet varies with the Weber number (We = $\rho v^2 \iota / \sigma$, where ρ is the fluid density, v is the characteristic velocity, ι is the characteristic length, σ is the surface tension coefficient of the fluid) and Ohnesorge number (Oh), and can be divided into five modes (vibrational, bag, multi-

mode, sheet thinning and catastrophic breakup), with distinctive transition on the shape and size of broken droplet fragments [16]. As a typical non-Newtonian fluid, the secondary breakup of a gel droplet differs from that of a Newtonian one. Moreover, the extreme breakup condition of a gel propellant droplet under a high internal flow of a rocket, with We even over one thousand, makes the breakup complicated and subsequently its characterization more challenging.

To quantify the droplet breakup process, several advanced optical particle instruments have been applied to measure the droplet, e.g., phase Doppler analyzer (PDA) [17, 18] and Malvern particle size analyzer (MPSA). PDA can only deal with spherical particles and MPSA can only measure the one-dimensional particle descriptor, that is, equivalent size. However, the breakup of a gel droplet generates a large amount of irregular fragments, filaments and nonspherical droplets, and their morphological characterization, especially in 3D, are vitally important to have an insight into the mechanism of gel droplet breakup process. Digital in-line holography (DIH), as a real 3D imaging technique, can measure geometric parameters of particles, including 3D position, diameter and morphology, and 3D velocity when combined with particle imaging/tracking velocimetry (PIV/PTV) strategy, and thus suits to droplet dynamics characterization. Based on DIH, Radhakrishna, et al. [19] obtained the size and velocity of droplets with different We ranging from 30 to 120, explored the breakup pattern and thus gave the percent of required minimum reflux velocity, Prasad, et al. [20] explored the impact of density on cloud dynamics and examined two particle clouds with similar granularity and morphology and thus provided a measurement of velocity and concentration before ignition, Liebel, et al. [21] combined transient microscope and successfully demonstrated the time-resolved spectroscopy of gold nanoparticles to lay a foundation for single shot three-dimensional microscopic imaging on any timescale. One of the common challenges in filament-droplet field characterization during secondary breakup is accurately detecting and segmenting the object from background. Nowadays, threshold algorithms [22] especially adaptive-threshold methods (ATM) [23–25] are widely employed. The threshold value is calculated based on models originally derived from image by direct photography, while the reconstructed slice image in DIH has intrinsic twin-image noises. Besides, the liquid filaments with various morphology and multi-scale droplets pose additional challenge to their segmentations. These factors deteriorate the performance of threshold-based algorithms.

In nature, the segmentation of the reconstructed holographic image is equivalent to semantic segmentation in the field of deep learning. Fully convolutional neural network (FCN) [26] opened the door of deep learning to the field of semantic segmentation, and several models, e.g., Deeplab [27], Segnet [28], E-net [29], U-net [30] etc., were proposed. Among them, U-net is a classic network for semantic segmentation, and it is also embedded in various popular large models as a classic network backbone. Especially, U-net was widely used in the semantic segmentation of medical images owing to the mixture of low level features and high level features [30]. Tuning the loss function and data augmentation through cropping and

rotating the initial image, can increase the accuracy and the robustness of the deep neural network prediction. The application scenario of this method is extended to DIH and become a feasible approach to segment the reconstructed holographic images. Altman, et al. [31] completed the characterization and track of hologram to recognize and locate the colloidal particles and thus eliminated the proprieties of it with deep convolutional network. Midtvedt, et al. [32] developed a weighted average convolutional network to analyze the hologram of single suspended nanoparticle and quantified the size and refractive index of a single subwavelength particle. But until now, these works mainly focus on relatively large [33, 34], spherical object [35, 36], sparse small particle field [37–39] or other objects (e.g., fiber internal structure [40], cell identification [41]), yet few focused on dense particle field consisted of liquid droplets and filaments with various morphological shapes like gel atomization field. And the combination of digital holography and deep learning methods were also extended to other particle-like objects, Belashov, et al. [42] utilized holographic microscopy combined with cell segmentation algorithm using machine learning to characterize the dynamic process of apoptosis and the accuracy achieved 95.5% and Wang, et al. [43] segmented some terahertz images of gear wheel and used average structural similarity to get the relatively best results which were proved to be better than some traditional segmentation algorithms in their paper.

This study combines semantic segmentation model based on deep neural network with the holographic images of gel secondary atomization field and proposes Mo-U-net to deal with this segmentation task. Experimental results show that Mo-U-net has a superior performance in overall, local boundary, internal structure prediction and particle retrieval of different scales than ATM in different conditions. Therefore, using the Mo-U-net can lay a solid foundation for the later mechanism analysis in droplet breakup, which also provides a feasible approach to segmenting other kinds of holograms.

2 EXPERIMENTAL SETUP

The experimental setup for gel droplet breakup in a crossing flow measured with DIH is shown in **Figure 1**. A gel droplet with a size ranging from 1.74 to 2.58 mm was produced by a needle generator, and then fell into a high-speed crossing flow, with a velocity ranging from 63.7 m/s to 118.2 m/s. All gel samples were distributed on the same day, with a density of 1,356.8 kg/m^3 and a surface tension of 24.56 mN/m. The droplet was then accelerated and was broken up into filaments and small droplets, with the We spanning from 514 to 1768 and Reynolds number (Re) from 1.078×10^4 to 2.033×10^4. The experiments were carried out under five conditions as shown in **Table 1**. In this table, d means the droplet diameter, v_c is the central velocity in the flow field, Re is the Reynolds number (Re = $\rho VL/\mu$, where ρ, μ are the density and dynamic viscosity coefficient of the fluid respectively, and V and L are the characteristic velocity and length of the flow field). The breakup processes of the gel droplets were visualized by a 25 kHz high-speed DIH system.

FIGURE 1 | Schematic of the high-speed DIH system for measuring crossing flow atomization of gel droplet.
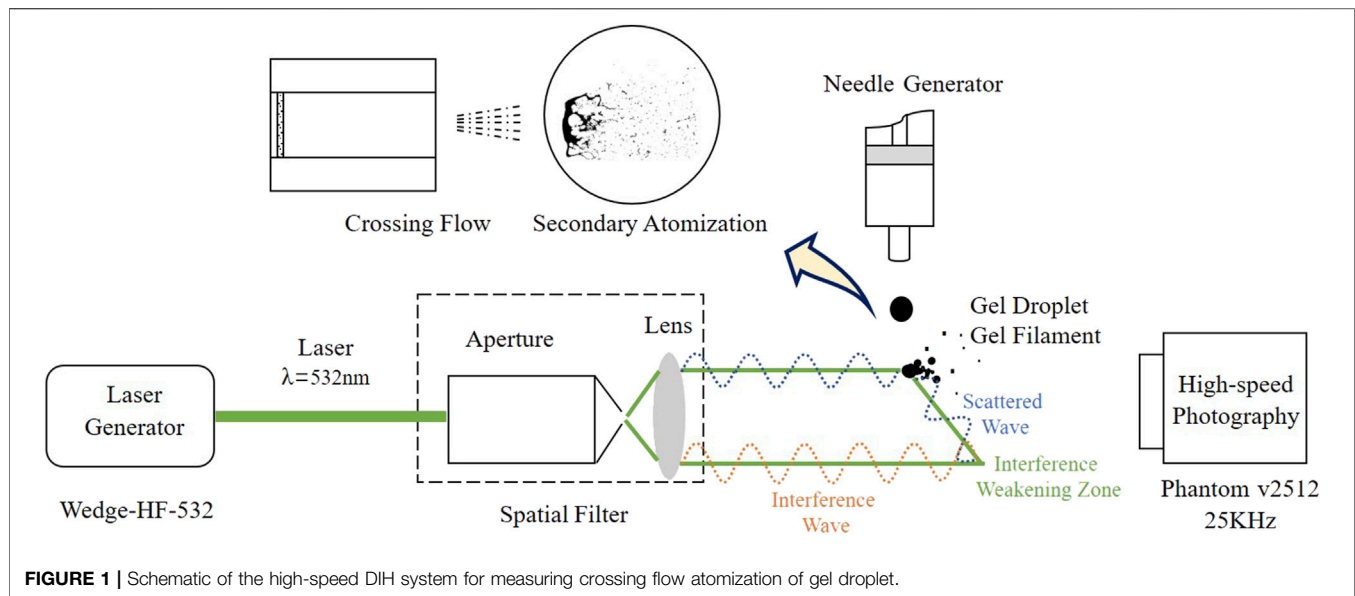
TABLE 1 | Parameters of five experimental conditions.

case	d (mm)	v_c (m/s)	We	Re
1	2.58 ± 0.01	63.7	514	1.096×10^4
2	2.58 ± 0.01	92.9	1,092	1.598×10^4
3	2.58 ± 0.01	118.2	1768	2.033×10^4
4	2.13 ± 0.03	92.9	902	1.319×10^4
5	1.74 ± 0.02	92.9	737	1.078×10^4

A laser beam of λ = 532 nm wavelength was first generated by a pico-second pulsed laser, passed through a spatial filter, and then collimated into a plane wave. The plane wave traveled through the test region and illuminated the filament-droplet field. Part of the beam was scattered as the object wave and interfered with the reference wave without being scattered to generate the hologram with size of M ×N = 1,280 × 800, and equivalent horizontal and vertical pixel size Δx and Δy of 28 μm

in this study. The holograms obtained in this study are shown in **Figure 2A**.

The recorded hologram noted as $I_h(m, n)$ was then reconstructed by angular spectrum method [44] as follows

$$E_r(k, l, z_r) = \mathcal{F}^{-1}\left\{ \mathcal{F}[R \cdot I_h(m, n)] \times \exp\left[-i\frac{2\pi z_r}{\lambda}\sqrt{1 - \left(\frac{\lambda m}{M\Delta x}\right)^2 - \left(\frac{\lambda n}{N\Delta y}\right)^2}\right]\right\},$$

where $E_r(k, l, z_r)$ denotes the complex amplitude of the reconstructed image, z_r and (k, l) denotes the reconstruction distance from the recording plane and the pixel coordinates of the reconstructed image respectively. And $R = 1$, denotes the reference light for reconstruction of DIH. $h(m, n)$ is the hologram, and (m, n) is the pixel coordinate in the hologram.

In this study, 301 sections between 210 and 240 mm in the Z axis were reconstructed with 0.1 mm spacing in order to obtain a full 3D droplet field information while keep a relatively high reconstruction speed. Because the depth of field (DoF) of the

FIGURE 2 | Experimental data for crossing-flow atomization of gel particles. Images with black boundary are the primitive images. Images with red boundary on the left upper side are enlarged ones of what the red dotted box frames. The subgraph **(A)** is the raw hologram obtained by the high speed camera. The subgraph **(B)** is one of the slices from a reconstructed hologram. The subgraph **(C)** is the EFI generated from all reconstructed slices.

FIGURE 3 | The structure of Mo-U-net. The blocks and arrows marked as gray areas denote the parts that are pruned in actual use.

holographic imaging system is calculated to be about 290 μm [45], as long as the section spacing is shorter than the DoF, then all particles in experimental space can be focused on certain section and if the spacing is too small, the time of reconstruction maybe extremely long. Due to the limited depth of field of reconstructed image, each reconstructed slice only had a few droplets in-focus, as shown in **Figure 2B**. So it is necessary to reconstruct multiple sections of particle field. To facilitate the subsequent droplet recognition and locating as well as speed up this process, the whole reconstructed 3D particle field was fused into one image called extended focus image (EFI) as shown in **Figure 2C**, using a region-based image depth-of-field extension algorithm [46]. The gel filament-droplet field in the EFIs has the following characteristics. 1) Due to the characteristics of digital in-line holography, the foreground twin-image is generated in the background of EFI accompanied with the bright and dark background stripes. They interfere with the gray distribution of the local foreground and produce some noises in the final recognition result. 2) In complex dense filament-droplet field, the twin-images generated by the foreground of EFI interfere with each other and form complex, changeable and irregular noises, which cripple the segmentation effect of classical threshold

method based on gray statistics. 3) The shapes of gel filaments in EFIs are variable, and the scale span of gel filaments is very large (hundreds of microns to a few centimeters). These two factors make the general processing method based on geometry and morphology unfeasible, and increase the difficulty of threshold segmentation methods.

Thus, in this study, the EFIs will be processed with a deep neural network called Mo-U-net to overcome the difficulties mentioned above.

3 METHODS

3.1 Model Setup
U-net consists a shrinking path named encoder and an expanding path named decoder. The shrinking path is used to extract the context information of the image while the expanding path is used to reconstruct the foreground and the background of the image precisely according to the information. The symmetrical two paths form a structure like "U" for which this network is called "U-net" [30]. Because of the complex segmentation scene and fine segmentation requirements, U-net adopts layer skipping

FIGURE 4 | Rough ground truth produced by the ATM.
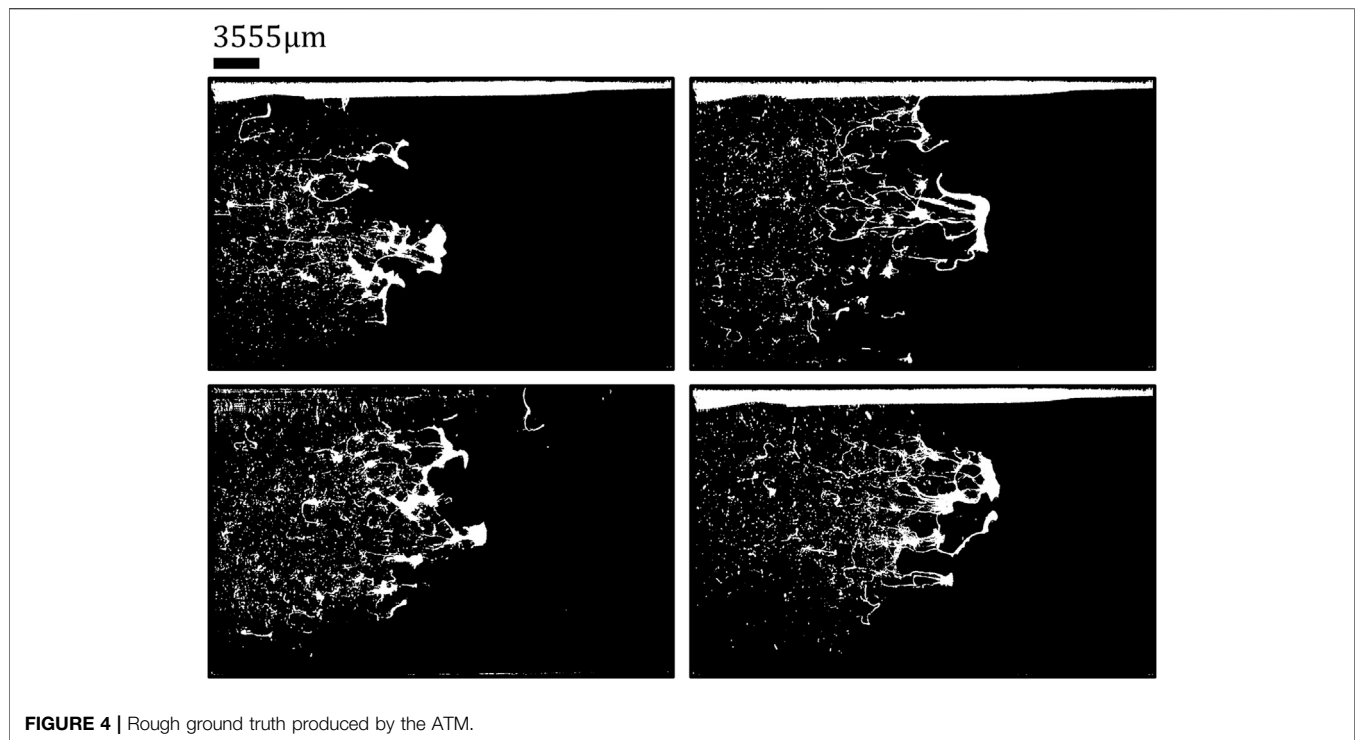
link, which fuses the bottom information extracted by the encoder with the corresponding high-level feature map from the decoder layer by layer to make up for the lost features in encoding.

As is shown in **Figure 3**, the Mo-U-net used in this study, is based on the structure of U-net, and is improved in two aspects. 1) The original four down sampling blocks is replaced with a network named Mobilenetv2 [47] as our new encoder. Mobilenetv2 completely discards the pooling layer to retain more low-level features in down sampling and replaces normal convolution with depth-wise separable convolution and point-wise convolution, which enables a more precise and faster segmentation. And it is also consistent with the segmentation characteristics of the gel filament-droplet field in EFIs. 2) Block7 to 14 from Mobilenetv2 are removed to simplify the encoder and only two up-sampling and feature fusing process are kept to simplify the decoder for the timeliness of image processing and finite computing resources. Since the features of gel droplets and filaments are primitive in this study, a network with relative small capacity and few skipping connection will be qualified enough to extract adequate semantic information for fine segmentation while saving quantities of training time due to its fewer parameters.

3.2 Dataset Establishment and Data Augmentation

The dataset for neural network training generally includes input images and true values which are also called ground truth in image segmentation field. In this study, the dataset is established in two steps. In the first step, the ATM [48] is used to preprocess a batch of EFIs to obtain relatively rough ground truth. Then, the obviously defective truth value labels are ruled out while the rest is regarded as the ground truth for training and testing. The reasons for this are as follows. 1) The current image processing method cannot make pixel-wise ground truth, and manual calibration costs a lot of time, which is unfeasible for subsequent experiments and industrial applications. 2) Different from the traditional threshold and regression algorithm, owing to the gradient back propagation and batch processing mechanism, deep neural network shows great robustness in noisy learning (the process of learning from a dataset containing partial error samples is usually called noisy learning), and has been verified in many experiments [49]. A total of 2,167 images were collected in the experiment. After filtered by ATM, a total of 2021 images with rough ground truth were obtained as shown in **Figure 4**.

The second step is data augmentation. The EFIs obtained in experiment have some defects, which can be mainly divided into three aspects. 1) Uneven spatial distribution. As the red box shown in **Figure 5B**, the spatial distribution of the droplet particle field is of great unevenness. Under the experimental conditions, most of the gel droplet particle field is concentrated in the upper and the right parts which may cause a positional bias to network when training, thus affecting the generalization ability. 2) Black long-strip noise. The blue box in **Figure 5B** shows that, due to the limitation of lens range, black noise with long strip shape appears on the edge of the image. Although it is not a droplet, the ATM will mistake it as a foreground, which is harmful for the feature learning. 3) Dot-like black noise. From the yellow box in **Figure 5B**, the static dot-like black noise appears because some particles are attached to the cavity wall after being blown away during experiment. Although such noises donot

FIGURE 5 | Defective dataset. The subgraphs in column **(A)** are the images chosen randomly from the dataset with the same defects. The subfigure **(B)** is the specific defects. The red frame denotes where the uneven spatial distribution of droplets are, the blue frame denotes the black noises with long black strip shape and the yellow frame refers to the black noise with a dot-like shape.

belong to the dynamic particle field, its characteristics are the same as real particles in the EFIs. So it will not affect the learning of the characteristics of the EFIs of gel filaments and particles, and there is no need for extra calibration.

To deal with the first two main defects, the original dataset is augmented in two corresponding ways. 1) The image size is cropped from $1,280 \times 800$ to 672×672 to remove the unqualified boundary. 2) The images are rotated by 90°, 180° and 270° respectively and then added to the dataset. So the spatial distribution of the dataset can be normalized. Finally, a dataset contains 8,084 images with 672×672 resolution is obtained, as shown in **Figure 6**. Although the image is cropped in the experiment, the model after training does not strictly limit the input image size. If only the size meets the integer times of 224 and with the same height and width, the model can adjust to it after a fine tune with a very small cost.

3.3 Train Setting

In order to achieve good segmentation performance, the train strategy is set as follows. A pre-training weights is firstly used to accelerate the model convergence and improve the segmentation accuracy. The weights obtained from the famous image dataset "ImageNet" [50] is used as pre-training weights of the Mobilenetv2 in the experiment. Then we use transfer learning strategy to fine tune. In detail, the initial learning rate of the model is set to 0.001 during training and the encoder layer with pre-training weights is frozen to improve the model performance and speed up the training process. Besides, cross entropy loss (CEL) function and Adam optimizer [51] are selected to accelerate the model convergence. An early stop strategy (stop training when the

loss value is no longer decreased) and a linear decreasing learning rate strategy (when the loss is no longer decreased, the learning rate will be changed, in the experiment, the patient is set to three epochs, and the change ratio is 0.1) are employed to ensure that the model can be closer to the optimal solution, and avoid over-fitting in the later training. Finally, the network is trained for 100 epochs to ensure an adequate train.

4 RESULTS AND DISCUSSIONS

4.1 Training and Validation

The dataset mentioned in **Section 3.2** is divided into train set and validation set by 8:2 ratio to train model and validate its performance respectively. Based on the environment of tensorflow2.4.0, the Mo-U-net is trained with 2 T P100-PCIE-16 GPUs. And a Mo-U-net without pruning is also trained in the same case to evaluate the effect of the improvements mentioned in **Section 3.1**. As a result, Mo-U-net with pruning cost 8.5 min per epoch to train on average while Mo-U-net without pruning cost 14.6 min per epoch to train on average, which means a nearly 41% saving of training time by using pruning. Besides, the following test result shown in **Section 4.3** also proves that pruning will not affect the performance of the model in this study. And to show the improvements by using Mobilenetv2, an original U-net is also trained in the same condition. The result in **Section 4.3** shows that the original U-net also achieved excellent performance of 82.66% PIOU and 1.1721 ASSD, exceeding the performance of ATM in five working conditions. This shows that deep learning method has considerable advantages for the segmentation of complex dense droplet-filament-mixed field in
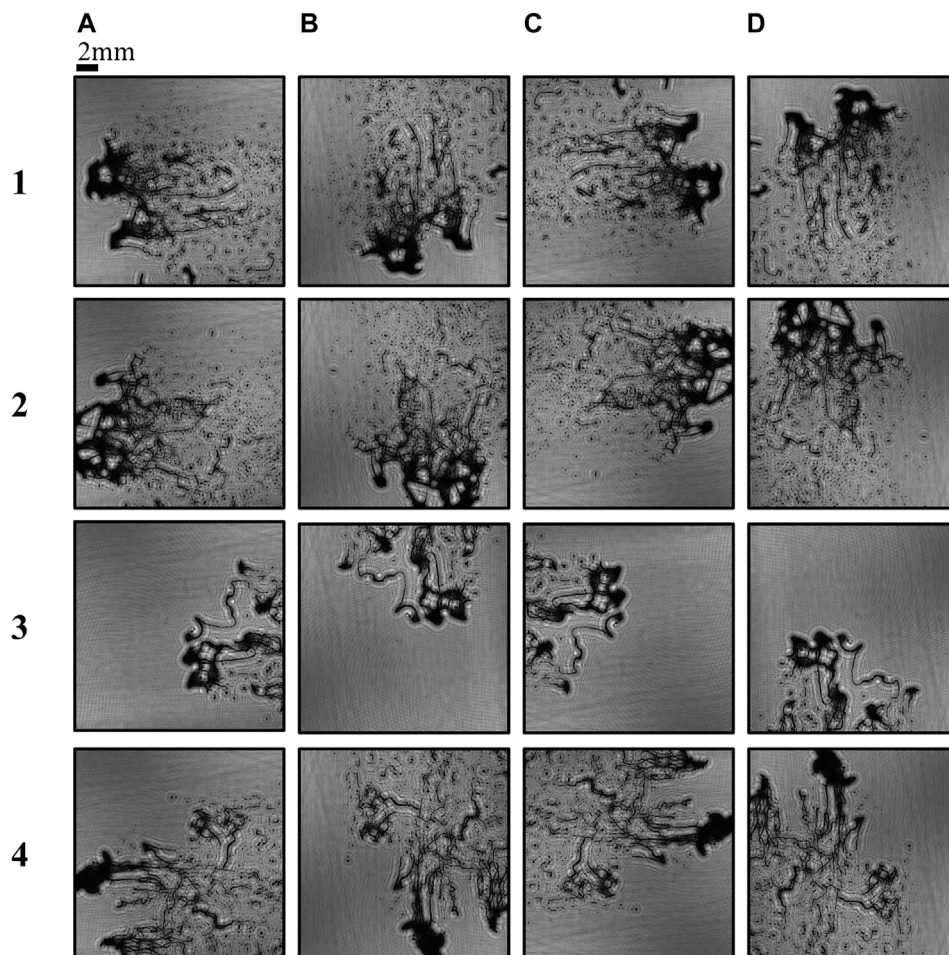
FIGURE 6 | Dataset with data augmentation. The subgraphs **(1)** to **(4)** in column **(A)** are the original images chosen randomly from the dataset which has been cropped into 672×672. The column **(B)** to D refer to the augmented images generated by rotating the original images by 90°,180°and 270°respectively.

EFIs. However, it can still be modified. On this basis, Mo-U-net proposed in this study has achieved better performance in PIOU (area segmentation accuracy) and ASSD (boundary segmentation error) than the original U-net, especially in the extreme complex disaster crushing of gel droplet (working conditions 4 and 5). This is precisely because we use the Mobilenetv2 to replace the four basic convolutional encoding blocks of the original U-net. After improvement, the Mo-U-net obtains a deeper coding path to form a stronger capacity of representation, so it can extract higher-level semantic information. Therefore, it will have better generalization ability and robustness in the face of complex scene in segmentation.

4.2 Morphological Analysis

As shown in **Figure 7**, Mo-U-net has the ability to segment the foreground and background of the EFIs after training. To have a more lucid assessment between the performances of the Mo-U-net and the ATM, a comparison is conducted by the validation set. The experimental results show that the Mo-U-net outperforms the ATM in area, boundary and multi-scale droplet recognition.

1) As for the prediction of inner structure, Mo-U-net outdoes ATM. As the orange circles shown in **Figure 8**, in the experimental conditions, Mo-U-net can precisely recognize a big lump of gel droplets and the internal structure while ATM couldnot, e.g., ATM lost internal structures of eight areas from just five small blocks in **Figure 8**. This shortcoming is caused by its segmenting mechanism. ATM mainly segments the image according to the gray values in its selected region. However, in the EFIs of gel atomization field, the dense diffraction fringes of twin-images would decrease the gray values of the droplets and filaments with hollow parts inside, which leads to an incorrect threshold. Besides, from **Figures 8B–E**, there exist many inner structures of various scales. Even though it is possible to get the nearly identical inner structure through adjusting the size of processing block, extending the precise results to the whole image is far more difficult. But such a complex problem is actually an easy task for Mo-U-net. In **Figure 8**, inner structures of the gel droplet were well predicted whatever the scale.
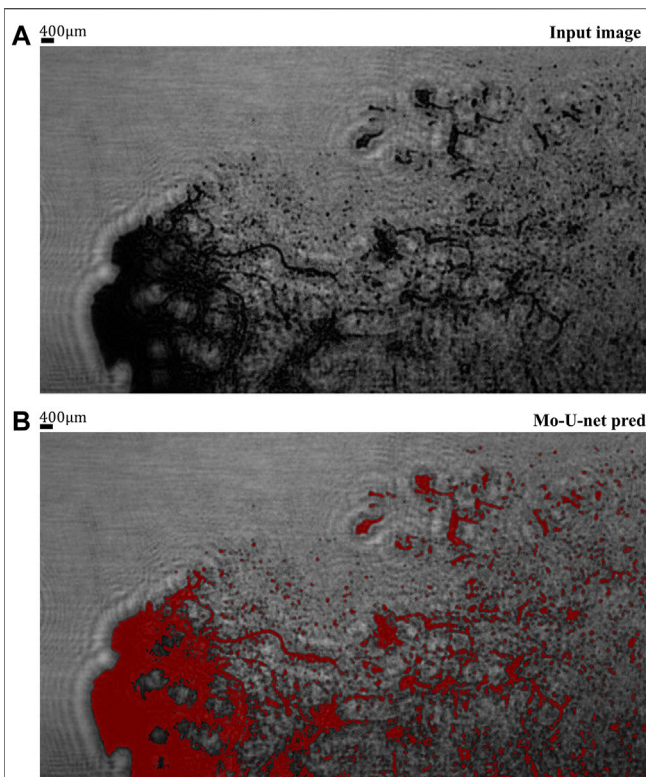
FIGURE 7 | The overview of Mo-U-net predicting performance. Subgraph **(A)** shows the input image of filament-droplet field in case 5. Subgraph **(B)** is the superposition of the Mo-U-net prediction and input image, in which the predicted pixels are painted red.

Fundamentally, the way Mo-U-net forms its criteria to segment the image determines its superior performance. The criteria comes from the context information from the whole image scale, which is wider and deeper than the statistics information depending on gray values of ATM. Thus, Mo-U-net can utilize not only the features of gray values in only one region or one image but also the overall distribution features to judge whether the pixel is foreground or not.

2) In terms of complex liquid filament morphology predicting, Mo-U-net shows an outstanding performance. As the green circles shown in **Figure 8**, ATM is quite sensitive to the brightness change when segmenting consecutive and slender liquid filaments. In details, only if there is some bright spots, ATM will "cut off" the filament in this position (e.g., **Figure 8E**). What is more, the noises in the vicinity will harm the ATM segmentation and bring about a contractile boundary (e.g., **Figures 8A,C,D** total loss of filament (e.g., **Figure 8B**). These weaknesses can also be overcome by Mo-U-net. Assisted by the global information mentioned in **Section 4.2**(1), it can locate most of the liquid filaments, get rid of the interference from noises and omit the tiny brightness change of liquid filaments. The last two strengths account for the consecutive and complete liquid filament prediction.

3) Mo-U-net displays its distinguishing properties when predicting small droplets. ATM usually performs poorly to segment the droplets only with several pixels. Especially, in the EFIs of dense droplet and filament field, the tiny droplet itself has lower gray contrast and is interfered by the noises. For both of these two reasons, ATM can easily omit tiny droplets in the selected regions. As the blue circles shown in **Figure 8**, ATM lost a large number of small droplets in the dense field while Mo-U-net does well and is able to make up for this shortcoming by using the information including gray changing and particle distribution learned from other EFIs in the same train set.

4) Besides, Mo-U-net shares a same excellent performance on the prediction in sparse region with that in dense field. As the purple box shown in **Figure 8**, ATM will mistake the background to foreground in a high probability. In sparse region, gray values of background will be the main factor to choose the threshold. If there is no droplet and the gray values of background is lower in the chosen region, ATM will be more likely to mistake some areas in the background with low gray values to foreground. However, Mo-U-net has a superior performance in distinguishing the particles from both bright and dark background, because the criterion for judgement comes from the global information learned by the Mo-U-net when training, which provides hundreds of samples containing different kinds of background situations. So the Mo-U-net can make full use of these information and give a more accurate prediction result.

The comparison of Mo-U-net and ATM demonstrates that Mo-U-net is qualified enough to the segmentation of dense filament-droplet field in the EFIs. And predictions of Mo-U-net are closer to the reality in large droplet, filament morphology and multi-scale particles, which are relatively unfeasible for ATM.

4.3 Quantitative Analysis
4.3.1 Test Dataset
In order to evaluate the performance of the Mo-U-net and ATM objectively and precisely, a batch of data is selected from five working conditions mentioned in **Section 2** that have never participated in the model training process as a test set. Meanwhile, to guarantee the reliability of the evaluation metrics and the validity of subsequent analysis, the previous ground truths produced ATM are examined and corrected artificially. The test set consists 25 images with 672×672 resolution.

4.3.2 Evaluating Metrics
In this study, the quantitative evaluation of the model segmentation performance can be divided into three parts 1) the Positive Intersection over Union (PIOU), 2) the Average Square Symmetric Boundary Distance (ASBD), 3) the Diameter-Based Prediction Statistics (DBPS). These three metrics judge the performance from the perspective of global, local and multi-scale so as to comprehensively demonstrate the advantages and disadvantages of Mo-U-net segmentation results.
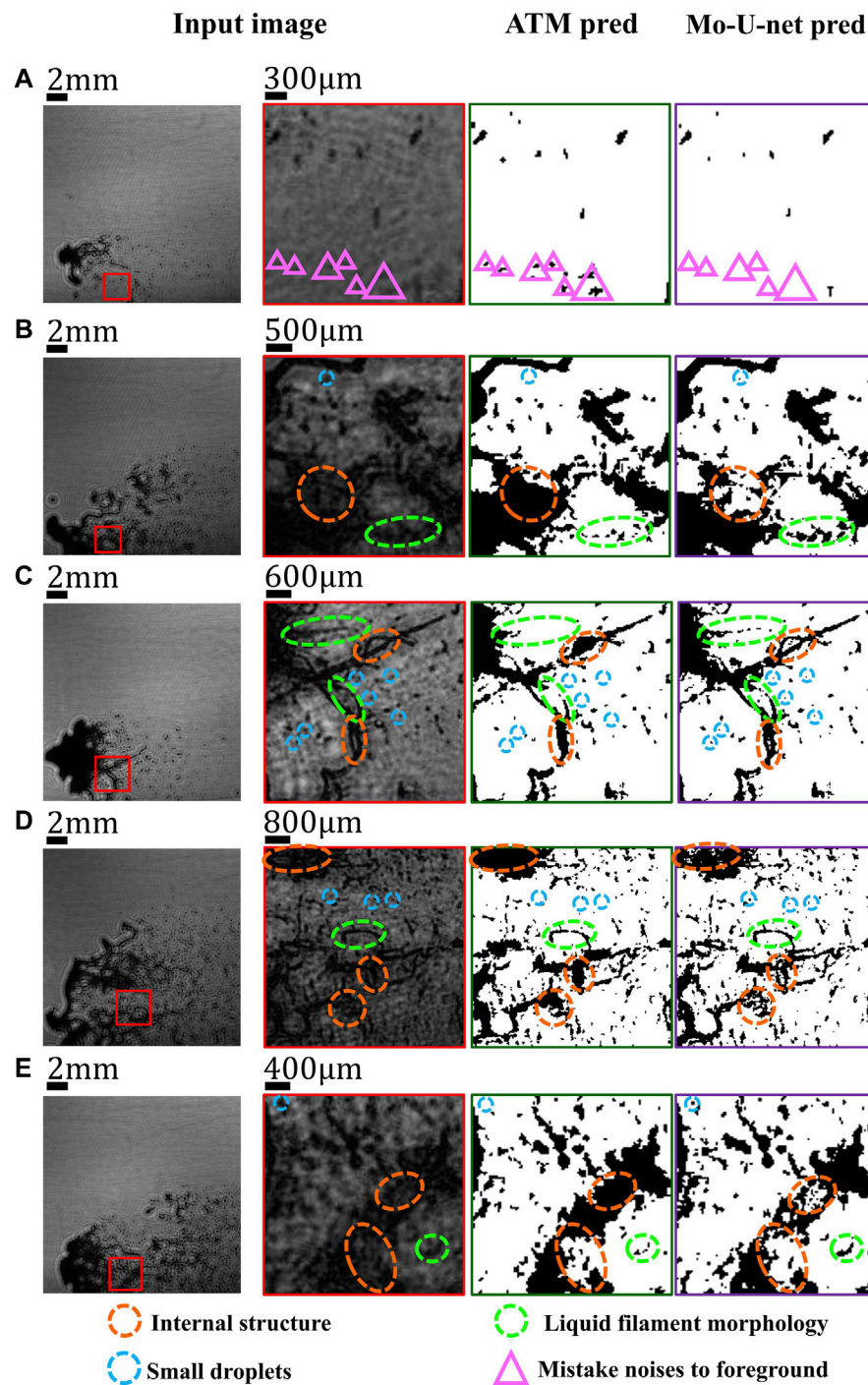
FIGURE 8 | Morphological comparison. The prediction of adaptive-threshold method is called ATM pred, the prediction of Mo-U-net is called Mo-U-net pred. The subgraphs **(A)** to E belong to case 1 to case 5 respectively. The subgraphs with red boundary are the enlarged ones of what the red boxes frame, meanwhile the blackish green refers to ATM pred and the purple denotes Mo-U-net-pred.
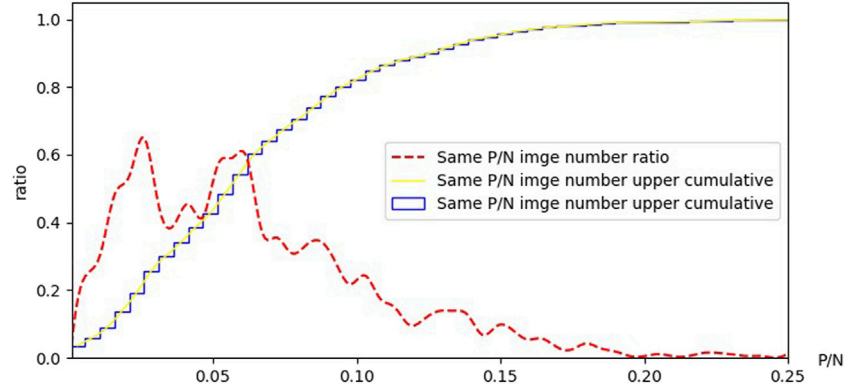
FIGURE 9 | Statistical histogram of positive and negative samples of dataset. In this study, a pixel from a droplet is called a positive sample, and a pixel from the background is called a negative sample. Same P/N means images have the same ratio of positive to negative samples.

1) The prototype of PIOU used in this study is MIOU, a metric proposed to measure the similarity between two sets. MIOU is defined as follows

$$MIOU = \frac{1}{k_c} \sum_i \frac{p_{ii}}{T_i + \sum_j p_{ji} - p_{ii}},$$

In this formula, k_c denotes the number of category, in this situation k_c is two, p_{ii} means the number of pixels which are marked as the category i in both label and predicted output, p_{ij} is the number of pixels which are marked as the category i in label while marked as other category j in predicted output, i and T_i denote the number of all pixels and the number of pixels of category i in labels respectively.

In fact, the EFIs in this experiment have an extreme sample imbalance, which means the number of samples in certain category is far more than that in other categories. In this study, samples denotes pixels. As shown in **Figure 9**, the average ratio of positive to negative samples is 0.065. In some specific circumstances, the ratio even reaches an exaggerated point of 0.01 (100 times). Thus, in such a condition, the normal MIOU will have a poor performance because it takes both the foreground (droplet) and background into consideration. Consequently, whether segmentation of the foreground which we really concern about is right or not makes nearly no contribution to the results. Therefore, we proposed PIOU to deal with the problem. PIOU is a special form of MIOU, which only considers the intersection and union ratio of the required classes through calculating the area of positive samples in predicted results and in ground truth. In this study, PIOU can be defined as follows

$$PIOU = \frac{p_{ii}}{T_i + p_i - p_{ii}}.$$

2) Average Symmetric Boundary Distance (ASBD) can serve as a powerful evaluation metric to measure the consistency of the boundary between the prediction and the ground truth. In this study, we use the ASBD to assess the performance of our model in boundary segmentation to show its ability to obtain the micro

characteristics. The smaller the value is, the more accurate the predicted boundary is. The ASBD is defined as follows

$$ASBD = \frac{\sum d(S_A - S(A)) + \sum d(S_B - S(B))}{S(A) + S(B)},$$

where A and B denote foreground and background respectively, S_A and S_B mean certain predicted marginal pixels in the foreground and the background respectively, $S(A)$ and $S(B)$ denotes all true marginal pixels in foreground and background, the function $d(\cdot)$ is used to calculate the shortest distance between an input pixel and the corresponding true set of that pixel. In this study, a pixel-width distance in the EFIs denotes a 28 μm distance in reality.

3) In this study, a Diameter-Based Prediction Statistics (DBPS) is used to measure the segmentation performance of the model for gel filaments and particles in different scales. When testing, the number of droplets is first calculated based on their diameter in Mo-U-net prediction and artificial ground truth. Then two histograms based on the diameter and number of droplets are drawn to show the distribution of Mo-U-net predictions and the artificial ground truths. The closer the fitting curves of the two histograms are, the better the model prediction is.

4.3.3 Metrics Analysis

According to the three evaluating metrics in **Section 4.3.2**, a comprehensive comparison can be obtained between our model and ATM in terms of the performance from three perspectives of global, local and multi-scale when segmenting the gel atomization field in the EFIs. The test set is utilized to assess Mo-U-net and ATM respectively and get the statistical results. The results of PIOU and ASBD are shown in **Table 2** while the result of DBPS is shown in **Figure 9**.
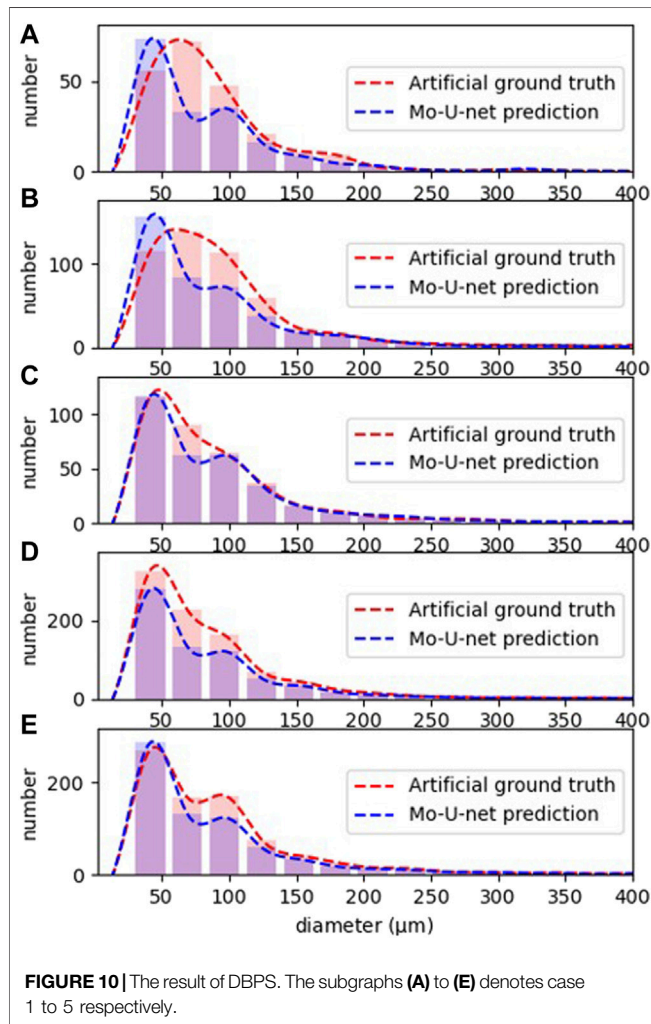
From **Table 2**, it is clearly illustrated that Mo-U-net has superior performance in both PIOU and ASBD whatever the working condition is.

Considering the overall segmentation effect (PIOU), these two methods both achieve around 80% but Mo-U-net surpasses ATM

TABLE 2 | The test results of PIOU and ASBD.

Metric	PIOU				ASBD			
Methods	ATM	U-net	Mo-U-net (NP)	Mo-U-net (P)	ATM	U-net	Mo-U-net (NP)	Mo-U-net (P)
Case 1	0.7502	0.8182	0.8031	0.8018	6.8226	0.9751	0.9831	1.1110
Case 2	0.7625	0.7929	0.8108	0.8005	2.3286	1.2872	1.0718	1.2337
Case 3	0.8712	0.9076	0.9061	0.9035	2.6958	1.1000	1.0197	1.1034
Case 4	0.8076	0.8147	0.8441	0.8369	1.4781	1.2135	0.9857	1.0975
Case 5	0.7399	0.7996	0.8349	0.8259	3.0487	1.2850	0.9954	1.1241
AVE	0.7863	0.8266	0.8398	0.8337	3.2748	1.1721	1.0111	1.1339

In this table, the U-net denotes the original model without our improvement, the Mo-U-net (NP) denotes the Mo-U-net without pruning, the Mo-U-net (P) denotes the Mo-U-net with pruning, AVE means an average result of all cases.

FIGURE 10 | The result of DBPS. The subgraphs **(A)** to **(E)** denotes case 1 to 5 respectively.

small droplet in the EFI always contains four or more pixels) distance to a pixel-width distance in the EFIs. This metric shows the ability of these two methods to segment fine structure e.g., the inner structure and the boundary of filaments in **Section 4.2**. The specific reason can be divided into two aspects as follows. On the one hand, whether ATM recognizes the pixel as foreground or background completely depends on whether its gray values surpasses the threshold or not, which accounts for the rough edge with some serrated areas, skin needing and boundary defects. On the other hand, Mo-U-net will not only consider the pixel gray values but also the adjacent edges and the regional shape so that it can segment the boundary more smoothly and get a more precise prediction of the inner structure than ATM.

As shown in **Figure 10**, under five different conditions, Mo-U-net has a very similar size distribution of multi-scale droplets to the artificial ground truth. Specifically, in most experimental conditions, they share a homologous peak area around 50 μm, and the nearly same decreasing tendency from 100 μm. However, in the range of 50–100 μm in diameter, there is a discrepancy in particle number between Mo-U-net prediction and the artificial ground truth. As shown in **Figure 10**, the number of the droplets 75 μm diameter predicted by Mo-U-net is lower than the artificial ground truth (more than a dozen droplets got lost) in general. Particularly, as shown in **Figure 10**, in case 1 and case 2, the number of the droplets around 50 μm diameter predicted by Mo-U-net surpasses the artificial ground truth in the same time. These phenomena may be related with low image resolution. In fact, in the EFIs, 50 μm denotes only two pixel-width and 75 μm denotes only three pixel-width respectively. That is to say, Mo-U-net only mistakes one pixel when predicting a three pixel-wise droplet and the mistaken three pixel-width droplets are then reduced to two pixel-width droplets. It is why the number of droplets around 75 μm diameter is relatively lower compared with the artificial ground truth while that of droplets around 50 μm diameter is relatively higher in case 1 and case 2. The reasons are also consistent with the result of ASBD in **Table 2**, which shows the disparity of the boundary between Mo-U-net prediction and artificial ground truth is around one pixel-width. Besides, as mentioned in the morphological analysis in **Section 4.2** and metrics analysis in above, as a "teacher", ATM suffers a low accuracy and will cause unexpected defeats in micro-droplets segmentation. Therefore, trained with the ground truth produced by ATM, Mo-U-net can hardly gain the capability to conduct a perfect segmentation in micro-droplets. Generally

nearly 5%, which is coherent with 1) (3) 4) in **Section 4.2**. And when judging some pixels with obscure meanings, ATM can only make use of the extracted gray values in its processing block while Mo-U-net can utilize the features learned from the whole train set. With the adequate understanding of fundamental distribution, Mo-U-net performs better than ATM.

As **Table 2** shown, the ASBD of Mo-U-net is over 60% lower than ATM. That means when using Mo-U-net, the boundary loss of segmentation can be decreased from nearly a droplet-width (a

speaking, the prediction provided by Mo-U-net is basically consistent with the real size distribution of gel dense filament-droplet field in the EFIs, which can offer a relatively accurate statistical information of size distribution for subsequent research and analysis in droplets.

In all the three metrics, Mo-U-net shows a better performance in area prediction and boundary segmentation than ATM, and shares a coherent size distribution of multi-scale droplets to the artificial ground truth. These results are consistent with what morphological analysis claims in **Section 4.2**, which proves that Mo-U-net can automatically learn the characteristics provided by a large number of positive samples, and ignore small amount of noises in the real ground truth. In the final test, the model shows better performance than the ground truth produced by ATM, and gives an eloquent proof that neural network can be "better than its teacher".

5 CONCLUSION

This work has investigated a deep neural network called Mo-U-net and its application to the segmentation of dense gel filament-droplet field in digital holography, with progresses as follows.

- A Mo-U-net model is proposed to segment dense filament-droplet field. The model is mainly based on the U-net and modified by two steps as follows. Firstly, the original four down sampling blocks of U-net are replaced with Mobilenetv2 to retain more low-level features when encoding. Secondly, the model is pruned by cutting off all the down sampling blocks below the sixth block and only reserve two corresponding up sampling blocks to reduce the parameters of the model. As a result, Mo-U-net achieves a high accuracy in segmentation while saves 41% of training time compared with the Mo-U-net without pruning.
- A morphological comparison is conducted by the validation set to assess the segmentation performance between the Mo-U-net and the ATM. The experimental results show that, the Mo-U-net achieves a finer boundary segmentation in large droplet, a more precise internal structure prediction in filament with complex morphology and a stronger ability in recognizing multi-scale particles than the ATM.
- Three metrics contain PIOU, ASBD and DBPS are proposed for a quantitative evaluation between the Mo-U-net and the ATM. The test results show that the area prediction accuracy (PIOU) of Mo-U-net reaches 83.3%, which is about 5% higher than that of adaptive-threshold method (ATM). The boundary prediction error (ASBD) of Mo-U-net is only about one pixel-wise length, which is about one third of that of ATM. And Mo-U-net also shares a coherent size distribution (DBPS) prediction of droplet diameters with the reality.

In EFIs, complex background noises, changeable shape of filaments and large span geometric size distribution are the main obstacles for the classical algorithm to deal with the particle detection task. However, the proposed model can adjust to it well. 1) Mo-U-net, as a specific neural network is a data-driven model which can avoid the difficulty to judge whether the pixel belongs to the foreground from the mechanism. It learns the distribution law under the data itself so that can deal with the problems that not be handled by morphology alone. 2) Mo-U-net extracts various information in the EFI by convolution, including multi-dimensional global information, shape and spatial position which enriches its segmentation basis, suppresses the influence of background noises and finally overcomes the limitations of traditional gray-statistics-based threshold methods. 3) Mo-U-net gains the predicted foreground and background segmentation image by deconvolution, step skipping and fusion methods. The combination of multi-level semantic information enables it to get a satisfied internal structure prediction. And there are many other similar scenarios. For example, in swirl atomization [52], there are vertical stripe noises caused by the spatial modulation of reference light and transmitted laser; interference between reference light and droplet diffraction light and irregular spots produced by the superposition of a large number of droplets and the surrounding interference fringes. The model is foreseeable to have a great performance in these tasks. At the same time, the Mo-U-net's extensive information source also makes it not confined to the segmentation and recognition of holographic image of particle liquid filaments. It can also be expanded to medical imaging, biological cells, material defects and other fields of small dense objects. As long as a relatively good dataset can be obtained, a robust performance can be expected after a fine tune.

DATA AVAILABILITY STATEMENT

The datasets presented in this study can be found in online repositories. The names of the repository/repositories and accession number(s) can be found below:https://github.com/Wu-Tong-Hearted/Recognition-of-multiscale-dense-gel-filament-droplet-field-in-digital-holography-with-Mo-U-net.

AUTHOR CONTRIBUTIONS

ZP conceived the idea, conducted the experiments. HZ participated in the experiments. YW participated in the experiments. LZ did experiments raw data and provided gel materials. XW and YW supervised the project. All the authors contributed to the discussion on the results for this manuscript.

FUNDING

REFERENCES

1. Haddad A, Natan B, and Arieli R. The Performance of a boron-loaded Gel-Fuel Ramjet. *Prog propulsion Phys* (2011) 2:499–518. doi:10.1051/eucass/201102499

2. Natan B, and Rahimi S. The Status of Gel Propellants in Year 2000. *Combustion Energetic Mater* (2002) 5(1-6):172–94. doi:10.1615/intjenergeticmaterialschemprop.v5.i1-6.200

3. Cabeal J. *System Analysis of Gelled Space Storable Propellants*. 6th Propulsion Joint Specialist Conference (1970). 609.

4. Ciezki HK, and Naumann KW. Some Aspects on Safety and Environmental Impact of the German green Gel Propulsion Technology. *Propellants, Explosives, Pyrotechnics* (2016) 41:539–47. doi:10.1002/prep.201600039

5. Varma M, Pein R, and Propulsion C. Optimisation of Processing Conditions for Gel Propellant Production. *Int J Energetic Mater Chem Prop* (2009) 8:501–13. doi:10.1615/intjenergeticmaterialschemprop.v8.i6.30

6. Pinto PC, Hopfe N, Ramsel J, Naumann W, Thumann A, and Kurth G. *Scalability of Gelled Propellant Rocket Motors*. Milan, Italy: 7th European conference for aeronautics and space sciences (EUCASS) (2017).

7. Padwal MB, and Mishra DP. Synthesis of Jet A1 Gel Fuel and its Characterization for Propulsion Applications. *Fuel Process Tech* (2013) 106:359–65. doi:10.1016/j.fuproc.2012.08.023

8. Padwal MB, and Mishra DP. Characteristics of Gelled Jet A1 Sprays Formed by Internal Impingement of Micro Air Jets. *Fuel* (2016) 185:599–611. doi:10.1016/j.fuel.2016.08.012

9. Ma Y-c., Bai F-q., Chang Q, Yi J-m., Jiao K, and Du Q. An Experimental Study on the Atomization Characteristics of Impinging Jets of Power Law Fluid. *J Non-Newtonian Fluid Mech* (2015) 217:49–57. doi:10.1016/j.jnnfm.2015.01.001

10. Baek G, and Kim C. Rheological Properties of Carbopol Containing Nanoparticles. *J Rheology* (2011) 55:313–30. doi:10.1122/1.3538092

11. Fernández-Barbero JE, Galindo-Moreno P, Avila-Ortiz G, Caba O, Sánchez-Fernández E, and Wang HL. Flow Cytometric and Morphological Characterization of Platelet-Rich Plasma Gel. *Clin Oral Implants Res* (2010) 17:687–93. doi:10.1111/j.1600-0501.2006.01179.x

12. Mishra DP, Patyal A, and Padhwal M. Effects of Gellant Concentration on the Burning and Flame Structure of Organic Gel Propellant Droplets. *Fuel* (2011) 90:1805–10. doi:10.1016/j.fuel.2010.12.021

13. Jyoti BVS, Naseem MS, and Baek SW. Hypergolicity and Ignition Delay Study of Pure and Energized Ethanol Gel Fuel with Hydrogen Peroxide. *Combustion and Flame* (2017) 183:101–112. doi:10.1016/j.combustflame.2016.11.018

14. Botchu V, Siva J, Muhammad S, Seung WB, Hyung JL, Sung-june C, et al. *Hypergolicity and Ignition Delay Study of Gelled Ethanolamine Fuel* (2017).

15. Brandenburg JE, Fox MD, and Garcia RH, Ethanol Based Gel Fuel for a Hybrid Rocket Engine. *US Patent* (2012) 8:101–032. doi:10.2514/6.2007-5361

16. Pilch M, and Erdman CA. Use of Breakup Time Data and Velocity History Data to Predict the Maximum Size of Stable Fragments for Acceleration-Induced Breakup of a Liquid Drop. *Int J Multiphase Flow* (1987) 13:741–57. doi:10.1016/0301-9322(87)90063-2

17. Snyder SE. *Spatially Resolved Characteristics and Analytical Modeling of Elastic Non-newtonian Secondary Breakup, Heidelberg, Germany*. Thesis (2015).

18. Rivera CL. *Secondary Breakup of Inelastic Non-newtonian Liquid Drops* (2010).

19. Radhakrishna V, Shang W, Yao L, Chen J, and Sojka PE. Experimental Characterization of Secondary Atomization at High Ohnesorge Numbers. *Int J Multiphase Flow* (2021) 138:103591, 2021 . ARTN 103591. doi:10.1016/j.ijmultiphaseflow.2021.103591

20. Prasad S, Schweizer C, Bagaria P, Saini A, Kulatilaka WD, and Mashuga CV. Investigation of Particle Density on Dust Cloud Dynamics in a Minimum Ignition Energy Apparatus Using Digital In-Line Holography. *Powder Tech* (2021) 384:297–303. doi:10.1016/j.powtec.2021.02.026

21. Liebel M, Camargo FVA, Cerullo G, and van Hulst NF. Ultrafast Transient Holographic Microscopy. *Nano Lett* (2021) 21:1666–71. doi:10.1021/acs.nanolett.0c04416

22. Guildenbecher DR, Gao J, Reu PL, and Chen J. Digital Holography Simulations and Experiments to Quantify the Accuracy of 3d Particle Location and 2d Sizing Using a Proposed Hybrid Method. *Appl Opt* (2013) 52:3790–801. doi:10.1364/Ao.52.003790

23. Singh DK, and Panigrahi PK. Automatic Threshold Technique for Holographic Particle Field Characterization. *Appl Opt* (2012) 51:3874–87. doi:10.1364/Ao.51.003874

24. Yao L, Wu X, Wu Y, Yang J, Gao X, Chen L, et al. Characterization of Atomization and Breakup of Acoustically Levitated Drops with Digital Holography. *Appl Opt* 54 (2015) A23–A31. doi:10.1364/Ao.54.000a23

25. Luo ZX, Ze-Ren LI, Zuo-You LI, and Yan YEJAPS. *An Automatic Segmenting Method for the Reconstructed Image of High Speed Particle Field* (2007).

26. Long J, Shelhamer E, and Darrell T. Fully Convolutional Networks for Semantic Segmentation. In: Ieee Conference on Computer Vision and Pattern Recognition. (Boston, MA: Cvpr) (2015). 3431–40. doi:10.1109/cvpr.2015.7298965

27. Chen LC, Papandreou G, Kokkinos I, Murphy K, and Yuille AL. Deeplab: Semantic Image Segmentation with Deep Convolutional Nets, Atrous Convolution, and Fully Connected Crfs. *Ieee Trans Pattern Anal Machine Intelligence* (2018) 40:834–48. doi:10.1109/Tpami.2017.2699184

28. Badrinarayanan V, Kendall A, and Cipolla R. Segnet: A Deep Convolutional Encoder-Decoder Architecture for Image Segmentation. *Ieee Trans Pattern Anal Machine Intelligence* (2017) 39:2481–95. doi:10.1109/Tpami.2016.2644615

29. Paszke A, Chaurasia A, Kim S, and Culurciello E. *Enet: A Deep Neural Network Architecture for Real-Time Semantic Segmentation* (2016).

30. Ronneberger O, Fischer P, and Brox T. U-net: Convolutional Networks for Biomedical Image Segmentation. *Medical Image Computing And Computer-Assisted Intervention. Pt Iii* (2015) 9351:234–41. doi:10.1007/978-3-319-24574-4_28

31. Altman LE, and Grier DG. Catch: Characterizing and Tracking Colloids Holographically Using Deep Neural Networks. *J Phys Chem B* (2020) 124:1602–10. doi:10.1021/acs.jpcb.9b10463

32. Midtvedt B, Olsen E, Eklund F, Hook F, Adiels CB, Volpe G, et al. Fast and Accurate Nanoparticle Characterization Using Deep-Learning-Enhanced off-axis Holography. *Acs Nano* (2021) 15:2240–50. doi:10.1021/acsnano.0c06902

33. Ye H, Han H, Zhu L, and Duan QJJPCS. *Vegetable Pest Image Recognition Method Based on Improved Vgg Convolution Neural Network* 1237 (2019). 032018. doi:10.1088/1742-6596/1237/3/032018

34. Wang J, Li YN, Feng HL, Ren LJ, Du XC, and Wu J. Common Pests Image Recognition Based on Deep Convolutional Neural Network. *Comput Elect Agric* (2020) 179. , 2020 ARTN 105834. doi:10.1016/j.compag.2020.105834

35. Yi FL, Moon I, and Javidi B. Automated Red Blood Cells Extraction from Holographic Images Using Fully Convolutional Neural Networks. *Biomed Opt Express* (2017) 8:4466–79. doi:10.1364/Boe.8.004466

36. Nguyen T, Bui V, Lam V, Raub CB, Chang LC, and Nehmetallah G. Automatic Phase Aberration Compensation for Digital Holographic Microscopy Based on Deep Learning Background Detection. *Opt Express* (2017) 25:15043–57. doi:10.1364/Oe.25.015043

37. Li DY, Wang Z, and Zhang HL. Coal Dust Image Recognition Based on Improved Vgg Convolution Network. *Int Symp Artif Intelligence Robotics* (2020) 11574:, 2020 2020. Artn 115740o. doi:10.1117/12.2576974

38. Wu X, Li X, Yao L, Wu Y, Lin X, Chen L, et al. Accurate Detection of Small Particles in Digital Holography Using Fully Convolutional Networks. *Appl Opt* (2019) 58:G332–G344. doi:10.1364/AO.58.00G332

39. Zhu Y, Yeung CH, and Lam EYJAO. Digital Holographic Imaging and Classification of Microplastics Using Deep Transfer Learning. *Appl Opt* (2021) 60:A38–A47. doi:10.1364/AO.403366

40. Di J, Han W, Liu S, Wang K, Tang J, and Zhao JJAO. Sparse-view Imaging of a Fiber Internal Structure in Holographic Diffraction Tomography via a Convolutional Neural Network *Applied Optics* (2021) 60:A234–A242.doi:10.1364/ao.404276

41. O'Connor T, Anand A, Andemariam B, and Javidi BJBOE. Deep Learning-Based Cell Identification and Disease Diagnosis Using Spatio-Temporal Cellular Dynamics in Compact. *digital holographic Microsc* (2020) 11:4491–508. doi:10.1364/BOE.399020

42. Belashov A, Zhikhoreva A, Belyaeva T, Kornilova E, Salova A, Semenova I, et al. *In Vitro* monitoring of Photoinduced Necrosis in Hela Cells Using Digital Holographic Microscopy and Machine Learning. *J Opt Soc Am A Opt Image Sci Vis* (2020) 37:346–52. doi:10.1364/JOSAA.382135

43. Wang Y, Li Q, and Wang Y. Research on Bp Neural Network for Terahertz Image Segmentation. In: Eleventh International Conference on Information Optics and Photonics, Xi'an, China. CIOP (2019). doi:10.1117/12.2547541

44. Kreis T. *Handbook Of Holographic Interferometry (Handbook of Holographic Interferometry: Optical and Digital Methods)* (2005).

45. Meinhart CD, Wereley ST, and Gray Mjms T. Volume Illumination for Two-Dimensional Particle Image Velocimetry. *Meas Sci Tech* (2000) 11:809–14. doi:10.1088/0957-0233/11/6/326

46. Wu YC, Wu XC, Yang J, Wang ZH, Gao X, Zhou BW, et al. Wavelet-based Depth-Of-Field Extension, Accurate Autofocusing, and Particle Pairing for Digital Inline Particle Holography. *Appl Opt* (2014) 53:556–64. doi:10.1364/Ao.53.000556

47. Howard A, Zhmoginov A, Chen LC, Sandler M, and Zhu M. *Inverted Residuals and Linear Bottlenecks: Mobile Networks for Classification, Detection and Segmentation* (2018).

48. Bradley D, and Roth GJJ. Adaptive Thresholding Using the Integral. *image* (2007) 12:13–21. doi:10.1080/2151237x.2007.10129236

49. Algan G, and Ulusoy IJKBS. Image Classification with Deep Learning in the Presence of Noisy Labels. *A Surv* (2021) 215:106771. doi:10.1016/j.knosys.2021.106771

50. Jia D, Wei D, Socher R, Li LJ, Kai L, Li F, et al. *Imagenet: A Large-Scale Hierarchical Image Database* (2009). 248–55.

51. Kingma DP, and Ba J. L. *Adam: A Method for Stochastic Optimization* (2014).

52. Yw A, Lei WA, Wl A, Ge SB, Yong HA, Xw A, et al. Picosecond Pulsed Digital off-axis Holography for Near-Nozzle Droplet Size and 3d Distribution Measurement of a Swirl Kerosene spray. *Fuel* (2021) 283. doi:10.1016/j.fuel.2020.119124

Conflict of Interest: The authors declare that the research was conducted in the absence of any commercial or financial relationships that could be construed as a potential conflict of interest.

Publisher's Note: All claims expressed in this article are solely those of the authors and do not necessarily represent those of their affiliated organizations, or those of the publisher, the editors, and the reviewers. Any product that may be evaluated in this article, or claim that may be made by its manufacturer, is not guaranteed or endorsed by the publisher.

Partially Coherent Illumination Based Point-Diffraction Digital Holographic Microscopy Study Dynamics of Live Cells

Kequn Zhuo[1†], Yu Wang[1†], Yang Wang[1], Kai Wen[1], Min Liu[1,2], Ying Ma[1,2], Juanjuan Zheng[1,2,3]* and Peng Gao[1]

[1]School of Physics and Optoelectronic Engineering, Xidian University, Xi'an, China, [2]Academy of Advanced Interdisciplinary Research, Xidian University, Xi'an, China, [3]State Key Laboratory of Transient Optics and Photonics, Xi'an Institute of Optics and Precision Mechanics, Chinese Academy of Sciences, Xi'an, China

This paper presents a partially coherent point-diffraction digital holographic microscopy (PC-pDHM) prototype and demonstrates its application in label-free imaging of the dynamic processes of live cells. In PC-pDHM, the light scattered by a rotating diffuser is coupled into a multi-mode fiber, and the output light is used as the partially coherent illumination (PCI), which reduces the speckle noise significantly in PC-pDHM. A polarization-grating is used to remold the object and the reference waves, and the fringe contrast of the generated hologram can be adjusted by changing the polarization of the illumination wave. Using the PC-pDHM prototype, transparent samples and notably the dynamic processes of live cells were imaged with high contrast and in a label-free manner, discovering the pathological mechanisms of biology in the cellular and sub-cellular levels.

Keywords: quantitative phase microscopy (QPM), digital holographic microscopy (DHM), point-diffraction, partially coherent illumination, live-cell imaging

INTRODUCTION

Despite fluorescence microscope allows visualization of live samples with specificity and even with a resolution beyond the diffraction limit [1], sometimes it is also desirable to observe live samples in their natural state [2, 3]. Yet, biological samples are often transparent under visible light, and hence their images have low contrast under conventional light microscopy. Digital holographic microscopy (DHM), being a fast, minimally-invasive imaging technique with intrinsic contrast by exploring the phase of the imaging field, is a label-free, high-contrast image for transparent samples [4, 5]. DHM features a nanometer-ranged axial resolution [6, 7] and autofocusing capability. Nowadays, the reconstruction of DHM can be finished by deep learning frameworks [8], which enhance the performances of DHM in general. So far, DHM has been widely applied to many fields, including industrial inspection [9, 10], biomedical study [11–15], and so on.

Among different types of DHM techniques, point-diffraction digital holographic microscopy (PD-DHM) features high stability against environmental disturbance due to its common-path configuration [16–18]. In PD-DHM, a diffraction grating was used to divide the object wave into two parts, one was still used as the object wave, and the other was converted into a reference wave after being pinhole-filtered on the Fourier plane. Initially, PD-DHM employs an off-axis configuration, which can real-time image samples with a price of reduced spatial-band width product (SBP). In

2010, our group [19] proposed a phase-shifting in-line DPM based on a pair of gratings and later incorporated it with a parallel phase-shifting module for real-time phase imaging [20]. These configurations can maximize the SBP of the camera and provide a higher spatial resolution in the reconstruction. Recently, we proposed a polarization-grating based point-diffraction DHM (PG-DPM), with which the fringe contrast can be adjusted by using a polarization diffraction grating [21]. PG-DPM relies on coherent illumination, and hence its reconstruction suffers from speckle noise, which, in turn, restrict the measurement accuracy for the detection of optical path length changes [22]. Partially coherent light (PCI) sources allow for noise reduction in DHM [23], and offer an increased phase resolution. A wide variety of approaches to generate PCIs were proposed, including the induction of vibrations to a multi-mode optical fiber, the usage of a rotating ground glass-diffuser [23–28], or light emitting diodes (LEDs) [29, 30]. Popescu proposed white-light point-diffraction DHM, which has an enhanced signal-to-noise ratio (SNR) [31]. However, for PD-DHM, a broadly-extended light source (such as LEDs) will broaden the undiffracted component (the dc term) of the object wave, and hence it is difficult to generate a uniform and intense reference wave by pinhole-filtering.

In this paper, we propose a partially coherent point-diffraction DHM (PC-pDHM) prototype, which utilizes a multi-mode fiber for PCI generation and a polarization grating for beam splitting. This device retains the advantages of conventional point-diffraction DHM, i.e., real-time measurement, high stability, and high phase-measurement accuracy. Meanwhile, this prototype has two additional merits. First, the coherent noise is significantly reduced by the PCI generated by a multi-mode fiber that couples the light instantly scattered by a rotating diffuser. Second, the fringe contrast can be adjusted or optimized with the combination of a quarter-wave plate (QW) and a polarization diffraction grating (PG). Moreover, we demonstrate the proposed PC-pDHM by phase imaging of glue interlinkage, ascaris egg, and the dynamic process of live cells.

METHODS

Experimental Setup of PC-pDHM

The schematic diagram of the PC-pDHM system is shown in **Figure 1A**. A 532-nm solid-state crystal laser (1875-532L, Laserland, Wuhan, China) is used as the illumination source. The diameter of the laser output is 4 mm. A microscope objective MO_1 (20X/0.4, Nanjing Yingxing Optical Instrument Co., Ltd., Nanjing, China) focuses the light on a rotating glass diffuser (diffusing angle is 15°), and the scattered light is collimated by a lens L_1 (f = 75 mm). The diffuser is fixed on a motor (KN335714, Huatong Electronics, Co., Ltd., China), and is rotated at a speed of around 2000 revolutions per second (RPS). Then, the collimated light is refocused by a lens L_2 (f = 75 mm) into a 50 μm-diameter multi-mode fiber (DH-FMM050-FC-1A, Daheng Optics, China). At the other end of the fiber, the output light is

collimated by a CCTV lens (f = 12 mm, HM1214MP5, China), yielding a versatile partially coherent illumination (PCI) for the PC-pDHM. The regime of PCI generation lies in the fact that the focused light beam (λ, k_1) is transiently scattered by a specific point (with the intex n) on the diffuser, yielding an illumination vector k_1-k_n on the sample plane. It means that any point on the sample plane experiences time-varying illumination with different propagation vectors (λ_1, k_1-k_n). k_n has a spatial dependence of the rotating diffusor, which changes with time. Eventually, being averaged with time, the speckle noise at a point on the sample varied can be suppressed by the superimposing and averaging the time-varying illumination, as is shown in **Figure 1C**. The spatial coherence of the PCI can be adjusted by translating the diffuser along the optical axis. The spatial coherence is maximized when the rotating diffuser is placed at the focal plane of the telescope system MO_1-L_1. In our experiment, we set the distance between the diffuser and the focal plane of MO_1 to ~0.3 mm, compromising the spatial coherence of the illumination and the coupling coefficient of the MMF.

At the other end of the fiber, the output light is converted by a polarizer P_1 into linear polarized light with its polarization along the horizontal direction. And then, the illumination beam, being reflected by the mirror M_1, passes through a quarter-wave plate (QW), which turns the illumination light into an elliptically polarized beam. Under such partially coherent illumination (PCI), a sample is imaged by a telescope system consisting of a microscopic objective MO_2 (10X/0.45, CFI Plan Apochromat, Nikon, Japan) and a tube lens L_3 (f = 150 mm). Consequently, the intermediate image of the sample appears at the back focal plane of the tube lens L_3. At this plane, a polarization grating G (#12-677, 159 grooves/mm, Edmund Optics, New Jersey, America) is located and it splits the object wave into different copies along the diffraction orders. Among these, the ±1st diffraction orders have more than 42.5% total energy for each. Of note, the polarization grating has a unique polarization-dependent diffraction characteristic. For instance, the majority of the diffracted intensity will go to the +1st (−1st) order upon the incidence of a left (right) circularly polarized beam. Similar to conventional point-diffraction DHM, in the PC-pDHM system, the +1st order passes through a large hole on the filter mask with its spectrum not being affected, while the −1st order is filtered by a pinhole PH (diameter-50 μm, GCO-P50A, Daheng Optics, Beijing, China) and used as the reference wave, as shown in the inset of **Figure 1A**. It should be noted that, in PC-pDHM, the pinhole PH has a diameter d_{PH} close to 1 airy unit (AU) and meanwhile $d_{MMF} = d_{PH}/M$, with M = 1 being the magnification of the imaging system shown in **Figure 1B**. In this case, the reference wave of PC-pDHM has sufficient intensity, and at the same time, it is uniform in the whole field of view (FOV) of the camera. By contrast, such an ideal reference wave can not be generated by using LEDs for illumination. It is because the emitter of an LED often has a larger diameter, which will, in turn, expand the dc term of the object wave. The generated reference wave either has higher intensity (using a large PH) or
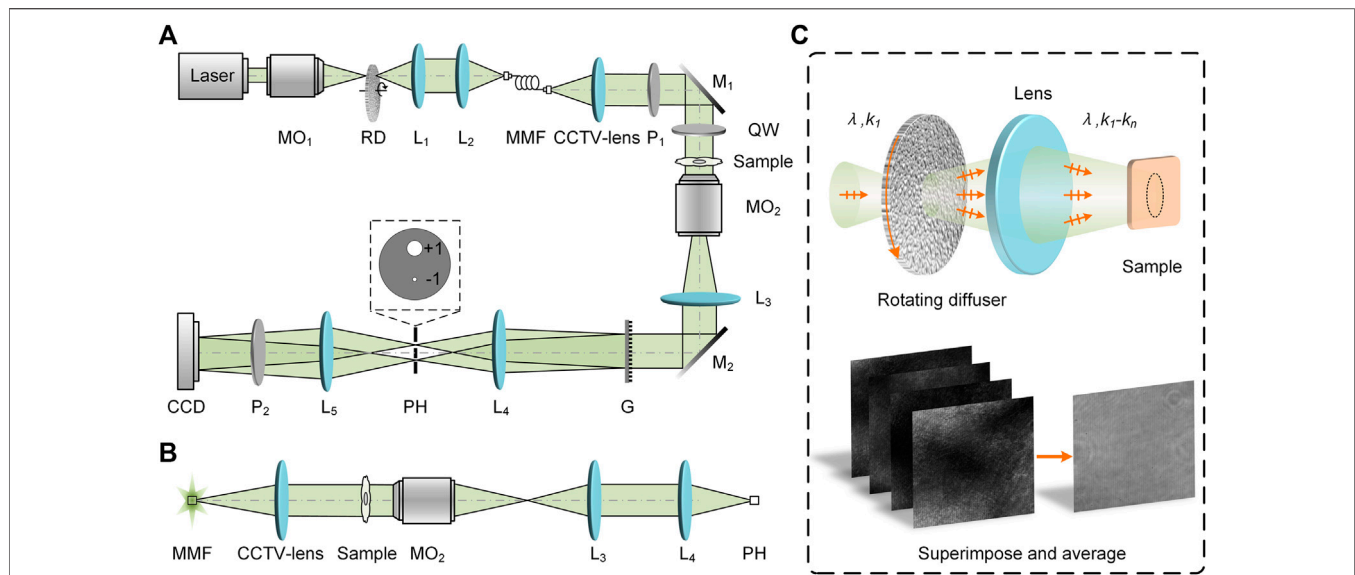
FIGURE 1 | Schematic diagram of PC-pDHM. **(A)** Experimental setup; **(B)** Relation between the diameters of MMF and PH. **(C)** The generation of partially coherent illumination (PCI) by using a rotating optical diffuser. CCD, charge-coupled device; G, polarization grating; L_1-L_5, achromatic lens; M_1 and M_2, Mirrors; MMF, multi-mode fiber; MO_1 and MO_2, microscopic objectives; P_1-P_2, polarizers; PH, pinhole; QW, quarter-wave plate; RD, rotating diffuser.

uniform intensity distribution (using a small PH), but not the two at the same time.

Before the CCD camera, a linear polarizer P_2 with a 45° polarization azimuth is located on the beam path of the object and reference waves to convert the two into the same polarization. The object and reference waves interfere with each other on the plane of a CCD camera (4,000 × 3,000, pixels size 1.85 μm, DMK 33UX226, The Imaging Source Asia Co., Ltd., China). The period of the off-axis hologram generated is 9.6 μm sampled by 5.2 pixels at the CCD plane. The total magnification of the PC-pDHM system is 23× and the theoretical spatial resolution is $\delta = 0.61\lambda/NA = 0.72$ μm. The exposure time of the camera in these experiments is 30 ms, which can average out all the varying scattering along with the rotating diffuser at 2,000 revolutions per second.

In conventional point-diffraction DHM, the reference wave intensity varies with specific samples, and therefore, the fringe contrast is difficult to maximize. In PC-pDHM, the polarization grating G converts the ±1st orders (the object and reference waves) into elliptically polarized beams with orthogonal principal axes. Consequently, the intensities of the object and reference waves change with the azimuth θ of the QW, i.e., in the form of $\cos^2\theta$ and $\sin^2\theta$ [21]. Therefore, the intensity of the object and reference waves can be balanced by rotating the QW. And eventually, the fringe contrast of the generated hologram can be maximized, which will, in turn, yield a high signal-to-noise ratio (SNR) in the reconstruction.

Numerical Reconstruction of PC-pDHM

Assuming that the principal axis azimuth of the QW is θ with respect to the horizontal direction, and the polarization orientation of P_2 has an angle of 45° with respect to the

horizontal direction, the complex amplitude of the object and reference waves on the camera plane can be expressed as

$$\tilde{O} = \gamma_1 \cdot \cos\theta \cdot \begin{bmatrix} 1 \\ 1 \end{bmatrix}, \tilde{R} = \gamma_2 \sin\theta \cdot \begin{bmatrix} 1 \\ 1 \end{bmatrix}. \qquad (1)$$

Here γ_1 and γ_2 are the constant coefficients, which depend on the diffraction efficiency of the ±1st orders of the polarization grating G and the diameter of the pinhole. It can be inferred from **Eq. 1** that the relative intensities of the object and reference waves can be adjusted by rotating the QW. On the CCD plane, the interference of the object and reference waves gives rise to the intensity distribution:

$$I(\vec{r}) = |\tilde{O}|^2 + |\tilde{R}|^2 + 2|\tilde{O}||\tilde{R}| \cdot \cos\left\{\varphi(\vec{r}) + \vec{K} \cdot \vec{r}\right\}, \qquad (2)$$

where, $\vec{K}$ and $\vec{r} = (x, y)$ denote the carrier-frequency vector of the interference fringes and the two-dimensional coordinates on the camera plane, respectively. The off-axis hologram depicted with **Eq. 2** can be seen in **Figures 3B, F**. There are many parallel stripes due to the angle between the object and reference waves. $\varphi(\vec{r})$ denotes the phase distribution of the sample. The complex amplitude of the object wave on the image plane with a defocus distance d_0 away from the camera plane can be reconstructed with

$$O_r(\vec{r}, d_0) = IFT\left\{FT\left[I(\vec{r}) \cdot R_D\right] \cdot \tilde{W}(\xi, \eta) \right.$$
$$\left. \cdot \exp\left[ikd_0\sqrt{1 - (\lambda\xi)^2 - (\lambda\eta)^2}\right]\right\}, \qquad (3)$$

where, $FT\{\cdot\}$ and $IFT\{\cdot\}$ represent the Fourier transform and inverse Fourier transform, respectively. A digital reference wave $R_D = \exp(-i\vec{K} \cdot \vec{r})$ is used to compensate for the spectral shift caused by the angle between the object wave and the reference wave. In the experiment, $R_D(x,y)$ can be determined by measuring
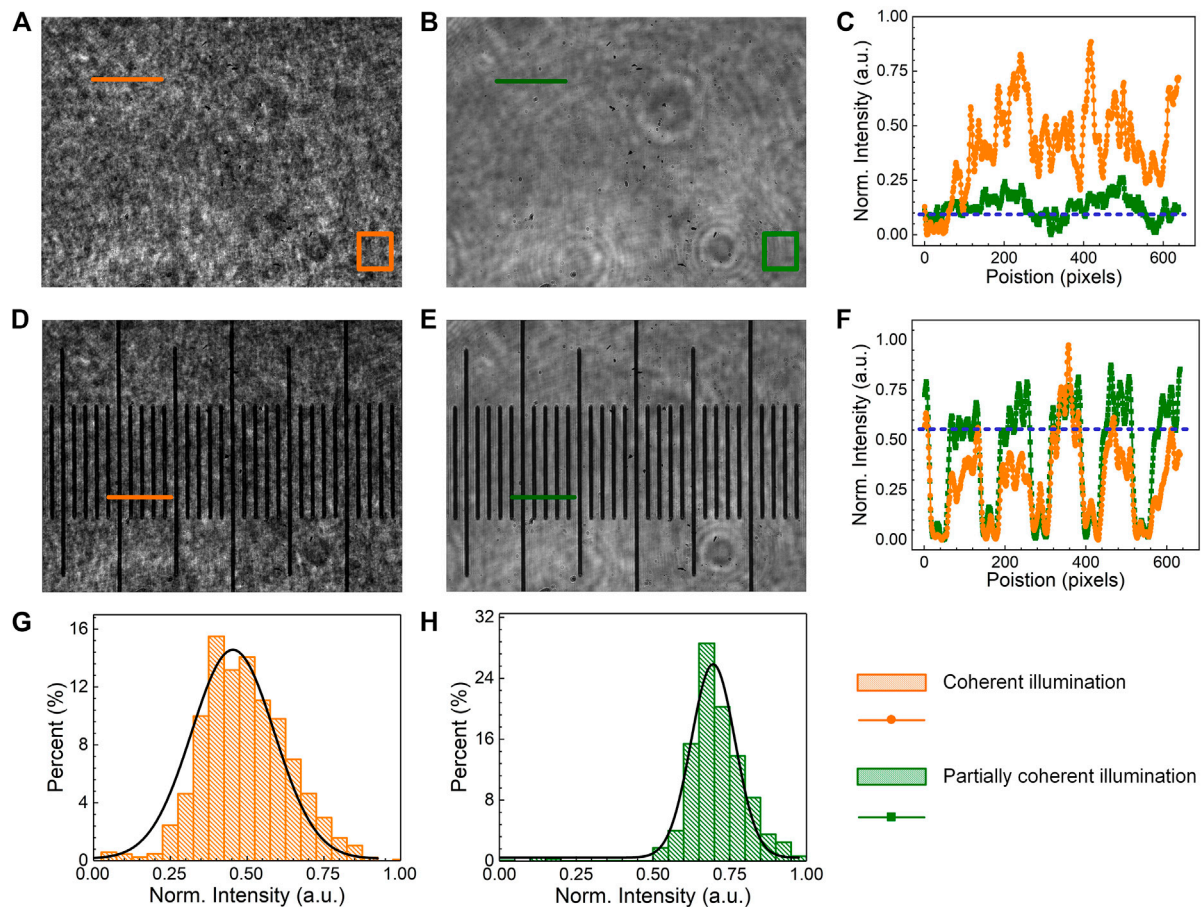
FIGURE 2 | The comparison of speckle-noise in CI and PCI. **(A,B)**, the intensity of CI and PCI without samples, respectively. **(C)** the intensity profiles along the orange/green lines in **(A,B)**. **(D,E)**, the images of a micro-ruler under CI and PCI. **(F)** intensity profiles along the origin/green solid lines in **(D,E)**. **(G,H)** are the histograms of the intensity within the orange and green boxes in **(A,B)**.

the carrier frequency vector $\vec{K}$ of the interference stripe. An exemplary frequency spectrum of $I(\vec{r}) \cdot R_D$ is shown in **Figure 4B**. There are three components in the spectrum, the dc term $(|O|^2+|R|^2) \cdot R_D$, real image spectrum $(OR^\star \cdot R_D)$, and twin image spectrum $(O^\star R \cdot R_D)$. Once the spectrum of $OR^\star \cdot R_D$ in the middle of the spectrum is selected by $\tilde{W}(\xi, \eta)$ (indicated with the dash-white circle in **Figure 4B**), the complex amplitude of the object wave can be obtained after an inverse Fourier transform. Eventually, with **Eq. 3** the amplitude and phase distribution of the sample can be retrieved from the complex amplitude accordingly. Further, the three-dimensional morphology $h(\vec{r})$ and the refractive index distribution $n(\vec{r})$ of the measured sample can be accurately calculated using the relation $\varphi = 2\pi/\lambda \cdot nh$.

EXPERIMENTAL RESULTS

Speckle Noise of the Illumination in PC-pDHM

In the first experiment, we demonstrate that the PCI generated by using a rotating diffuser and a multi-mode fiber allows for speckle

noise reduction in DHM. A comparison of the uniformity and the speckle noise level between CI and PCI was conducted. In this experiment, the reference wave was blocked, and images were taken for the following two cases: first, using coherent illumination (CI) from a laser coupled and delivered with a single-mode fiber (SMF), and second, using partially coherent illumination (PCI) in virtue of the rotating diffuser and the multi-mode fiber (MMF). **Figures 2A,B** show the CI and PCI images taken in the absence of any samples in the PC-pDHM system, and **Figures 2D,E** are the images obtained when using a micro-ruler as the sample. Further, **Figures 2C,F** show the normalized intensity distributions along the orange/green lines in **Figures 2A, B, D, E**, respectively. The comparison confirms that the PCI image is more uniform and has a much lower speckle noise. To further quantify the level of speckle noise, the standard deviation (STD) of the intensities within the orange/green boxes (with 150×150 pixels) in **Figures 2A,B** were calculated. The results turn out that the STD is 0.09 ± 0.048 (mean ± s.d.) for CI and 0.04 ± 0.02 for PCI. It is meant that PCI reduces the speckle noise by two folds. Moreover, the intensity histograms of the illumination in **Figures 2A,B** were calculated and fitted with a
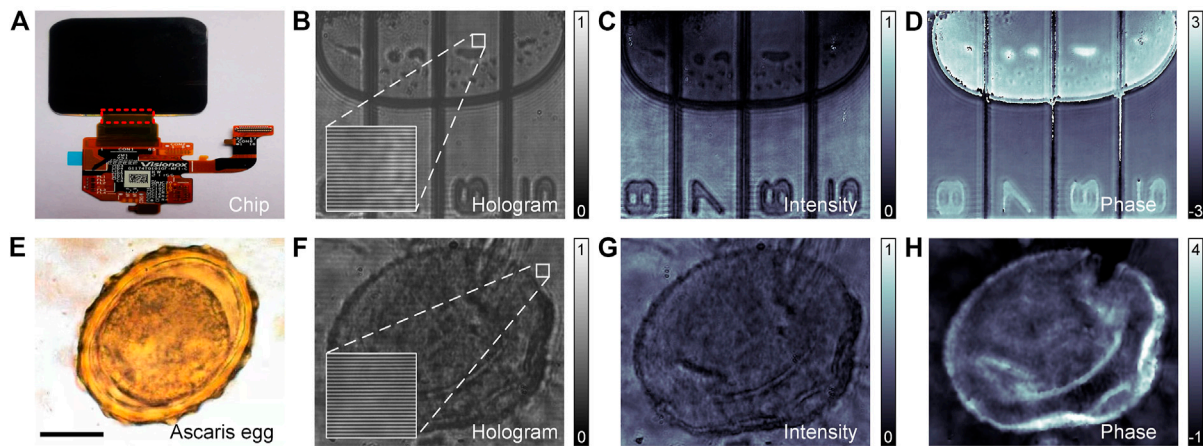
FIGURE 3 | Imaging of glue-interlinkage and ascaris egg slice with PC-pDHM. **(A–D)** The real image, the hologram, the reconstructed amplitude (a.u.), and phase (rad) images of the glue-interlinkage. **(E–H)** The real image, the hologram, the reconstructed amplitude (a.u.), and phase images (rad) of the ascaris egg slice, respectively. The scale bar in **(E)**, 20 μm.
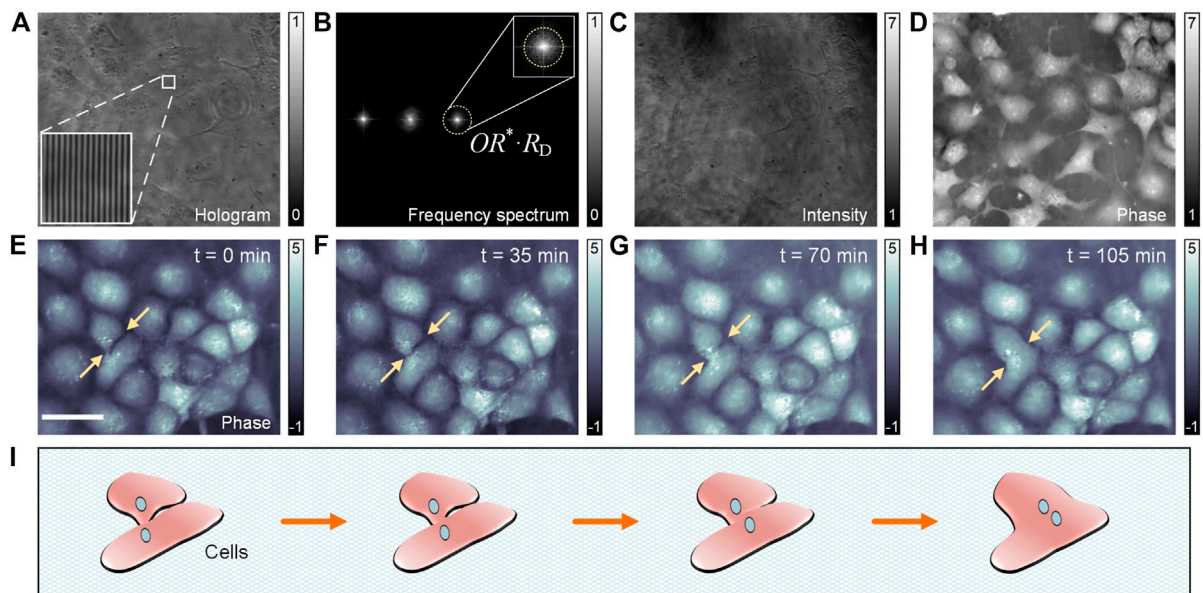
FIGURE 4 | Tracking of the fusion process of live cells with PC-pDHM. **(A)** A PC-pDHM hologram. **(B)** The spectrum of $I(\vec{r}) \cdot R_D$. **(C, D)**, the reconstructed amplitude (a.u.) and phase (rad) images of the cos-7 cells, respectively. **(E–H)** are the image series of the live cos-7 cells at a time interval of 35 min, of which the fusion process of two neighboring cells can be visualized. **(I)** Schematic drawing of cell fusion. The scale bar in **(E)**, 40 μm.

Gaussian function in **Figures 2G, H**. The fits tell the full width at the half maximum (FWHM) is 0.32 ± 0.02 for the CI and 0.17 ± 0.01 for the PCI, implying that the PCI is more uniform than the CI due to the time-averaging of the scattered illumination light.

Imaging of Static Samples Using PC-pDHM

PC-pDHM has been applied for phase imaging of two static and transparent samples, namely, glue interlinkage of IC devices and ascaris egg slice. As the first sample, glue interlinkage is commonly used in industry, for instance, to connect different

integrated circuit (IC) devices. Air bubbles, being one of the mainstream artifacts, often occurs in the glue interlinkage, degrading the interlinkage and hence the performance of IC devices as a whole. Due to the transparency of the glue interlinkage, there is a lack of commercially available instruments to inspect the air bubbles. Here, we demonstrate that PC-pDHM can be a versatile tool to inspect the air bubbles in glue interlinkages. **Figure 3A** shows an exemplary picture of the glue interlinkage that connects the chip and IC board. **Figure 3B** shows an off-axis hologram of the glue interlinkage, from which

the amplitude and phase images were reconstructed and shown in **Figures 3C,D**, respectively. The comparison between the amplitude and phase images tells the phase imaging capability of PC-pDHM can visualize air bubbles with higher contrast and in a quantitative manner if the refractive index of the glue is prior-known.

Second, PC-pDHM was used to image an ascaris egg slice (LIOO Optics, Beijing Jinghao Yongcheng Trading Co., Beijing, China), which was sandwiched between two cover-slips. **Figure 3E** shows the wide-field image of the ascaris egg under mercury lamp illumination. With PC-pDHM, the amplitude and phase images of the ascaris egg slice were reconstructed from the hologram (**Figure 3F**), and shown in **Figures 3G,H**, respectively. The thickness information of the ascaris egg slice missing in the amplitude image due to its transparency. By contrast, quantitative phase distribution ($2\pi/\lambda \Delta n Ll$, in term of optical path difference, OPD) of the ascaris egg slice can be visualized in the phase image. The comparison implies that PC-pDHM is capable of extracting fine structures of transparent samples.

Tracking the Fusion Dynamics of Live Cos-7 Cells Using PC-pDHM

In the third experiment, PC-pDHM was used to track one of the vital processes, namely, the fusion of cells without fluorescent labeling. Cell fusion is an important cellular process in which several uninucleate cells (cells with a single nucleus) combine to form a multinucleate cell, known as a syncytium, as is shown in **Figure 4I**. Cell fusion often occurs during the differentiation of myoblasts, osteoblasts, and trophoblasts, during embryogenesis, and morphogenesis. In this experiment, Cos-7 cells (Q239X mutant in African green monkey kidney cells) were seeded on petri dishes and cultured in high glucose DMEM supplemented with 10% FBS (HyClone) and 1% penicillin-streptomycin (HyClone). Then, the cells were moved to PC-pDHM setup and were imaged continuously for 6 hours. **Figure 4A** shows one of the recorded off-axis holograms. The frequency spectrum of $I(\vec{r}) \cdot R_D$ was obtained by Fourier transform on $I(\vec{r}) \cdot R_D$ and is shown in **Figure 4B**. The complex amplitude of the object wave was obtained by choosing the real image spectrum ($OR^* \cdot R_D$) and taking inverse Fourier transform. Then, the reconstructed amplitude and phase images were obtained from the complex amplitude and shown in **Figures 4C,D**, respectively. The live cos-7 cells are not observable in the amplitude image (**Figure 4C**) due to their transparency, but they can be clearly seen in the phase images **Figure 4D**.

To track the fusion process of the live cos-7 cells, the cells were imaged with PC-pDHM continuously for 6 h at a time interval of 20 s. Four phase images at $t = 0$, 35, 70, and 105 min are shown in **Figures 4E–H**. In the image series here, the fusion process of two neighboring cells (indicated with two arrows) can be observed with high contrast and in a quantitative manner (for morphology assessment). The whole fusion process from the beginning to the end lasted 105 min. It is worthy to point out that, PC-pDHM can be used to track other vital life processes of cells, such as cell division, apoptosis, attachment, and detachment from surfaces.

DISCUSSION

In this paper, we proposed a partialy coherent point-diffraction digital holographic microscopy (PC-pDHM) prototype and applied it to imaging transparent samples and dynamic processes of live cells. A partially coherent illumination (PCI) was generated by the combination of a rotating diffuser a multi-mode fiber. A polarization grating is used to diffract the object wave into several copies, and the $+1^{st}$ diffraction orders are used as the object wave and the -1st order as the reference wave after being pinhole-filtered. The relative intensity of the object and reference waves can be freely adjusted by rotating a quarter-wave plate, and therefore, the stripe contrast of the recorded holograms can be maximized. PC-pDHM has the advantages of high stability, high accuracy, low speckle noise, and instant amplitude/phase imaging. Using the proposed PC-pDHM system, we can image transparent samples with high contrast and in a label-free manner. Due to its instant measurement capability, PC-pDHM could be used to track the dynamic process of live cells.

It is also worthy to note that when the PC-pDHM is used to image samples with intrinsic birefringence, the fringe contrast and the measured phase will be influenced by the birefringence. While, on the other side, the birefringence of the sample can be characterized once the phase of the sample is measured with different polarizations of the illumination wave. Another limitation of PC-pDHM is the lack of specificity, and the combination of PC-pDHM with a fluorescence channel will be conducted in the near future.

DATA AVAILABILITY STATEMENT

The original contributions presented in the study are included in the article/Supplementary Material, further inquiries can be directed to the corresponding author.

AUTHOR CONTRIBUTIONS

JZ and PG conceived and supervised the project. KZ, YuW and YaW performed experiments. All the authors contributed to data analysis.

FUNDING

REFERENCES

1. Hell SW, Wichmann J. Breaking the Diffraction Resolution Limit by Stimulated Emission: Stimulated-Emission-Depletion Fluorescence Microscopy. *Opt Lett* (1994) 19:780–2. doi:10.1364/ol.19.000780

2. Li J, Matlock A, Li Y, Chen Q, Zuo C, Tian L. High-speed *In Vitro* Intensity Diffraction Tomography. *Adv Photon* (2019) 1:066004. doi:10.1117/1.AP.1.6.066004

3. Zheng C, Jin D, He Y, Lin H, Hu J, Yaqoob Z, et al.High Spatial and Temporal Resolution Synthetic Aperture Phase Microscopy. *Adv Photon* (2020) 2:065002. doi:10.1117/1.AP.2.6.065002

4. Osten W, Faridian A, Gao P, Körner K, Naik D, Pedrini G, et al.Recent Advances in Digital Holography [Invited]. *Appl Opt* (2014) 53:G44–G63. doi:10.1364/ao.53.000g44

5. Gao P, Pedrini G, Osten W. Structured Illumination for Resolution Enhancement and Autofocusing in Digital Holographic Microscopy. *Opt Lett* (2013) 38:1328–30. doi:10.1364/ol.38.001328

6. Kim MK. Principles and Techniques of Digital Holographic Microscopy. *J Photon Energ* (2010) 1:018005. doi:10.1117/6.0000006

7. Mann CJ, Yu L, Lo C-M, Kim MK. High-resolution Quantitative Phase-Contrast Microscopy by Digital Holography. *Opt Express* (2005) 13:8693–8. doi:10.1364/opex.13.008693

8. Ren Z, Xu Z, Lam EY. End-to-end Deep Learning Framework for Digital Holographic Reconstruction. *Adv Photon* (2019) 1:016004. doi:10.1117/1.AP.1.1.016004

9. Emery Y, Cuche E, Marquet F, Aspert N, Marquet P, Kuhn J, et al.Digital Holography Microscopy (DHM): Fast and Robust Systems for Industrial Inspection with Interferometer Resolution. In: *Optical Measurement Systems for Industrial Inspection IV*. Munich, Germany: International Society for Optics and Photonics (2005).

10. Kebbel V, Hartmann H-J, Jüptner WP. Application of Digital Holographic Microscopy for Inspection of Micro-optical Components. In: *Optical Measurement Systems for Industrial Inspection II: Application in Industrial Design*. Munich, Germany: International Society for Optics and Photonics (2001).

11. Yamaguchi I, Kato J-i., Ohta S, Mizuno J. Image Formation in Phase-Shifting Digital Holography and Applications to Microscopy. *Appl Opt* (2001) 40:6177–86. doi:10.1364/ao.40.006177

12. Emery Y, Cuche E, Colomb T, Depeursinge C, Rappaz B, Marquet P DHM (Digital Holography Microscope) for Imaging Cells, et al. DHM (Digital Holography Microscope) for Imaging Cells. *J Phys Conf Ser* (2007).61, 1317–1321. doi:10.1088/1742-6596/61/1/260

13. Marquet P, Rappaz B, Magistretti PJ, Cuche E, Emery Y, Colomb T, et al.Digital Holographic Microscopy: a Noninvasive Contrast Imaging Technique Allowing Quantitative Visualization of Living Cells with Subwavelength Axial Accuracy. *Opt Lett* (2005) 30:468–70. doi:10.1364/ol.30.000468

14. Carl D, Kemper B, Wernicke G, von Bally G. Parameter-optimized Digital Holographic Microscope for High-Resolution Living-Cell Analysis. *Appl Opt* (2004) 43:6536–44. doi:10.1364/ao.43.006536

15. Dubois F, Yourassowsky C, Monnom O, Legros J-C, Debeir O, Van Ham P, et al.Digital Holographic Microscopy for the Three-Dimensional Dynamic Analysis of *In Vitro* Cancer Cell Migration. *J Biomed Opt* (2006) 11:054032. doi:10.1117/1.2357174

16. Medecki H, Tejnil E, Goldberg KA, Bokor J. Phase-shifting point Diffraction Interferometer. *Opt Lett* (1996) 21:1526–8. doi:10.1364/ol.21.001526

17. Naulleau PP, Goldberg KA, Lee SH, Chang C, Attwood D, Bokor J. Extreme-ultraviolet Phase-Shifting point-diffraction Interferometer: a Wave-Front Metrology Tool with Subangstrom Reference-Wave Accuracy. *Appl Opt* (1999) 38:7252–63. doi:10.1364/ao.38.007252

18. Popescu G, Ikeda T, Dasari RR, Feld MS. Diffraction Phase Microscopy for Quantifying Cell Structure and Dynamics. *Opt Lett* (2006) 31:775–7. doi:10.1364/ol.31.000775

19. Gao P, Harder I, Nercissian V, Mantel K, Yao B. Phase-shifting point-diffraction Interferometry with Common-Path and In-Line Configuration for Microscopy. *Opt Lett* (2010) 35:712–4. doi:10.1364/ol.35.000712

20. Gao P, Yao B, Min J, Guo R, Zheng J, Ye T, et al.Parallel Two-step Phase-Shifting point-diffraction Interferometry for Microscopy Based on a Pair of Cube Beamsplitters. *Opt Express* (2011) 19:1930–5. doi:10.1364/oe.19.001930

21. Zhang M, Ma Y, Wang Y, Wen K, Zheng J, Liu L, et al.Polarization Grating Based on Diffraction Phase Microscopy for Quantitative Phase Imaging of Paramecia. *Opt Express* (2020) 28:29775–87. doi:10.1364/oe.404289

22. Chavel P. Optical Noise and Temporal Coherence. *J Opt Soc Am* (1980) 70:935–43. doi:10.1364/josa.70.000935

23. Dubois F, Novella Requena M-L, Minetti C, Monnom O, Istasse E. Partial Spatial Coherence Effects in Digital Holographic Microscopy with a Laser Source. *Appl Opt* (2004) 43:1131–9. doi:10.1364/ao.43.001131

24. Dubois F, Yourassowsky C, Minetti C, Queeckers P. Benefits of the Spatial Partial Coherence for the Applications in Digital Holography Microscopy. In: *Digital Holography and Three-Dimensional Imaging*. Washington: Optical Society of America (2010).

25. Dubois F, Callens N, Yourassowsky C, Hoyos M, Kurowski P, Monnom O. Digital Holographic Microscopy with Reduced Spatial Coherence for Three-Dimensional Particle Flow Analysis. *Appl Opt* (2006) 45:864–71. doi:10.1364/ao.45.000864

26. Stangner T, Zhang H, Dahlberg T, Wiklund K, Andersson M. Step-by-step Guide to Reduce Spatial Coherence of Laser Light Using a Rotating Ground Glass Diffuser. *Appl Opt* (2017) 56:5427–35. doi:10.1364/ao.56.005427

27. Kumar A, Banerji J, Singh RP. Intensity Correlation Properties of High-Order Optical Vortices Passing through a Rotating Ground-Glass Plate. *Opt Lett* (2010) 35:3841–3. doi:10.1364/ol.35.003841

28. Wen K, Gao Z, Fang X, Liu M, Zheng J, Ma Y, et al.Structured Illumination Microscopy with Partially Coherent Illumination for Phase and Fluorescent Imaging. *Opt Express* (2021) 29:33679–93. doi:10.1364/oe.435783

29. Kemper B, Stürwald S, Remmersmann C, Langehanenberg P, von Bally G. Characterisation of Light Emitting Diodes (LEDs) for Application in Digital Holographic Microscopy for Inspection of Micro and Nanostructured Surfaces. *Opt Lasers Eng* (2008) 46:499–507. doi:10.1016/j.optlaseng.2008.03.007

30. Stürwald S, Kemper B, Remmersmann C, Langehanenberg P, von Bally G. Application of Light Emitting Diodes in Digital Holographic Microscopy. *Proc SPIE - Int Soc Opt Eng* (2008) 6995:699507. doi:10.1117/12.781186

31. Shan M, Kandel ME, Majeed H, Nastasa V, Popescu G. White-light Diffraction Phase Microscopy at Doubled Space-Bandwidth Product. *Opt Express* (2016) 24:29033–9. doi:10.1364/oe.24.029033

Direct Observation of Axial Dynamics of Particle Manipulation With Weber Self-Accelerating Beams

Sha An [1,2], Tong Peng [1,2,3], Shaohui Yan [1], Baoli Yao [1,2]* and Peng Zhang [1]*

[1]*State Key Laboratory of Transient Optics and Photonics, Xi'an Institute of Optics and Precision Mechanics, Chinese Academy of Sciences, Xi'an, China,* [2]*University of Chinese Academy of Sciences, Beijing, China,* [3]*School of Science, Xi'an Jiaotong University, Xi'an, China*

Optical manipulation of micro-particles with nondiffracting and self-accelerating beams has been successfully applied in many research fields such as chemicophysics, material sciences and biomedicine. Such operation mainly focuses on the particle transport and control in the beam propagation direction. However, the conventional optical microscopy is specifically designed for obtaining the sample information located in the lateral plane, which is perpendicular to the optical axis of the detecting objective lens, making the real-time observation of particle dynamics in axial plane a challenge. In this work, we propose and demonstrate a technique which integrates a special beam optical tweezer with a direct axial plane imaging system. Here, particles are transported in aqueous solution along a parabolic trajectory by a designed nonparaxial Weber self-accelerating beam, and the particle motion dynamics both in lateral and axial plane are monitored in real-time by the axial plane imaging technique.

Keywords: axial plane optical microscopy, nonparaxial beams, self-accelerating beams, optical tweezer, particle transport

1 INTRODUCTION

Self-accelerating beams have attracted great interest since the first demonstration in 2007 [1, 2]. As exact solutions of the paraxial wave equation, Airy beams propagate along parabolic trajectories and remain invariant intensity profiles. By virtue of the remarkable features of non-diffracting, self-accelerating, and self-healing [3, 4], applications of Airy beams have been developed in many research fields, such as particle manipulation [5–8], optical microscopy [9–11], plasmons [12–14] and material processing [15, 16]. However, Airy beams are destructive when bending to large angles due to the paraxial limit. Against this drawback, nonparaxial self-accelerating beams, such as Mathieu beams and Weber beams, have been proposed and demonstrated theoretically and experimentally [17–22]. Such novel beams are found as exact solutions of the Helmholtz equation in different coordinate systems without the paraxial approximation. Therefore, compared to Airy beams, they can bend to larger angles and maintain the non-diffracting and self-healing capabilities as well.

With the development of optical field modulation technique, introducing novel beams into optical tweezers is convenient to achieve. For example, Baumgartl J *et al.* used Airy beam to guide particles vertically along a parabolic trajectory [5]. Zhang Z *et al.* experimentally demonstrated stable trapping of multiple particles using an array of optical bottle beams by employing multiple Airy beams [23]. Schley R *et al.* steered particles to much steeper angles in absorbing media with loss-proof accelerating beams [24]. However, there are challenges in observing the axial dynamics of
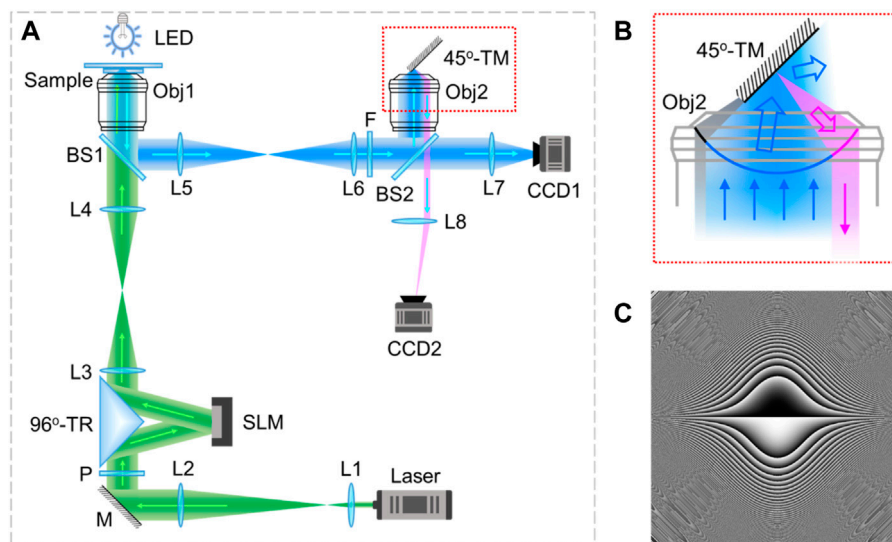
FIGURE 1 | Schematic diagram of the Weber beam optical tweezer system equipped with APOM. **(A)** Optical setup; **(B)** enlarged view of the area marked with red dotted rectangle in **(A)**; **(C)** phase mask loaded on the SLM. L: lens, M: mirror, P: polarizer, 96°-TR: 96°-triangle reflector, BS: beam splitter, Obj: objective, LED: light emitting diode, F: filter, CCD: Charge coupled device, 45°-TM: 45°-tilted mirror.

trapping behavior in the light propagation direction. Most the conventional optical microscopes equipped for optical tweezers can only observe the particle motion occurred in the lateral plane (perpendicular to the optical axis) [25, 26]. The acquisition of axial plane (parallel to the optical axis) information usually relies on setting another objective orthogonally [24] or axial scanning [27, 28]. The former restricts the sample mounting strategy and the numerical aperture (NA) of objectives. The latter needs to extract a certain axial plane from the three-dimensional (3D) bulk reconstructed by stacking a series of lateral frames, limiting the image speed and resulting in data redundancy. It's worth mentioning that a novel technique termed axial plane optical microscopy (APOM) has been developed to directly image the axial cross-section of samples without scanning [29]. This technique employed a 45°-tilted mirror to convert the axial plane information into a lateral plane and then re-image onto a camera. This innovative approach has been successfully applied in single-molecule super-resolution microscopy [30, 31].

In this work, we introduce the nonparaxial Weber beam into the optical tweezer system for particle manipulation. To observe the trapping dynamics, the APOM technique is assembled in the special beam optical tweezer system, directly observing both the particle motion along the parabolic trajectory in axial plane and the "focus/defocus" status in lateral plane. The proposed system integrates the special beam generation module based on spatial light modulator (SLM) and the APOM technique together. It allows real-time observation of trapping behavior in lateral and axial planes simultaneously. Due to the large field of view and real-time capability in nature, this technique is suitable for investigating special beams with axial particularities such as non-diffracting and self-accelerating, and has potential applications in biomedicine and biophysics.

2 METHODS

2.1 Optical Setup

The optical setup of the Weber beam optical tweezer system equipped with APOM was shown in **Figure 1A**. In the optical tweezer part, a laser beam with the wavelength of 532 nm (MW-GL-532A/3000 mW-16020122, Changchun Laser Optoelectronics Technology Co., Ltd., China) was expanded and collimated by a pair of achromatic lenses L1 (f = 50 mm) and L2 (f = 100 mm). After matching the polarization by a polarizer P, the horizontal polarized light beam was guided by a 96°-triangle reflector (96°-TR) onto a SLM (PLUTO-VIS-016, HoloEye Inc., Germany, 1920 pixels × 1080 pixels, pixel size: 8.0 μm, frame rate: 60 Hz) and then back to the original optical path. Instead of normal incidence, the 96°-TR allowed the small angle (= 6°) incidence modality of SLM to be used for enhancing the light efficiency while maintaining the compact experimental configuration. Here, the SLM was located in the focal plane of L3 (f = 200 mm). The pre-designed masks (**Figure 1C**) were loaded on the SLM for beam modulation. After focusing by L3, the SLM-modulated special beam was generated in the focal region of L3. Then, a tube lens (L4, f = 200 mm) and an objective (Obj1, 100×, NA = 1.4, oil immersion, Nikon Corp., Japan) were used to shrink the special beam in the focal region of Obj1 for particle trapping and transporting.

In the optical microscopy part, a light emitting diode (LED) with a central wavelength of 488 nm was used for wide-field illumination. The signal with sample information was collected by Obj1 and reflected by a beam splitter (BS1, 50:50), then relayed to another beam splitter (BS2, 50:50) by a 4f-system consisting of L5 (f = 200 mm) and L6 (f = 200 mm). Before BS2, a short-pass optical filter F with a cut-off wavelength of 500 nm was used to

distinguish the trapping laser and imaging light. With BS2, the signal was split into two parts of transmission and reflection. The transmitted part directly formed a lateral plane image on a charge-coupled device (CCD1, DMK23G445, The Imaging Source Inc., Germany, 1280 pixels × 960 pixels, pixel size: 3.75 μm, frame rate: 30 fps) through a condenser (L7, f = 75 mm). The reflected part went through an identical objective lens Obj2 and then formed an intermediate image of the sample in the focal region of Obj2. A custom-made 45°-tilted mirror (45°-TM) was placed in front of Obj2 for converting the axial plane image into the lateral plane, and then a part of the signal light was re-collected by Obj2. After transmitting through BS2, the returned light finally formed an axial plane image of the sample on another CCD camera (CCD2, DMK23U445, The Imaging Source Inc., Germany, 1280 pixels × 960 pixels, pixel size: 3.75 μm, frame rate: 30 fps) through a condenser (L8, f = 75 mm).

The 45°-TM was made by coating a thin layer of silver on the surface of a right-angle prism with a straight and sharp edge. According to the principle of reflection, a ray can be rotated 90° when it comes to a mirror at an incident angle of 45°. Likewise, the 45°-TM can rotate an axial plane image to lateral plane. The reflection details of the 45°-TM were shown in **Figure 1B**. After reflecting, the light rays were divided into three parts, marked with different colors of gray, blue and magenta respectively. The gray part represented rays blocked by the 45°-TM. The blue part was reflected by the 45°-TM to directions which cannot be collected by Obj2. Whereas rays indicated in magenta were reflected back by the 45°-TM and collected by Obj2 to perform axial plane imaging.

2.2 Generation of Weber Self-Accelerating Beams

Comparing with the Airy beam, Weber beam is an exact solution of the Helmholtz equation in parabolic coordinates without the paraxial approximation, so it can travel longer distance and bend to larger angle while preserving all the unique characteristics of the Airy beam. Therefore, in this paper, we designed and selected the proper Weber beam for particle transporting along parabolic trajectory in axial space.

To investigate the propagation characteristics of Weber beams, we followed the similar procedures as our previous work [32], loading the predesigned masks on an SLM. The Fourier spectrum φ_W associated with Weber beams can be expressed as:

$$\varphi_W(f_x, f_y) = \frac{\exp\left[i\gamma\left(\frac{f_x}{k} + \frac{f_y}{k}\right) + i\gamma\ln\left(\tan\left(\arccos\left(\frac{f_x}{k}\right)/2\right)\right) + i\gamma\ln\left(\tan\left(\arccos\left(\frac{f_y}{k}\right)/2\right)\right)\right]}{\sqrt{k^2 - f_x^2 - f_y^2}}$$

(1)

where, f_x and f_y are the spatial frequencies in x and y directions, respectively. λ is the wavelength in the medium. $k = 2\pi/\lambda$ is the wave number. γ is related to the separation constant. Considering the paraxial approximation, we assumed $f_x/k \ll 1$ and $f_y/k \ll 1$, so the **Eq. 1** can be derived as:

$$\varphi_A(f_x, f_y) = \exp\left(-i\gamma\frac{f_x^3}{3k^3} - i\gamma\frac{f_y^3}{3k^3}\right)/k \qquad (2)$$

which is the typical Fourier spectrum of Airy beams, indicating that Airy beams are the paraxial approximation of Weber beams.

In simulation, the Fourier spectrum was produced according to **Eq. 1**. The lateral light fields were calculated by the angular spectrum theory of diffraction [33], and the axial cross-sections of Weber beams were formed by reconstruction. In experiment, the pre-designed mask according to **Eq. 1** was loaded on the SLM. A flat mirror was placed in the sample position, and it was controlled by a one-dimensional translation stage to acquire a series of lateral plane images of the generated Weber beam on CCD1 by axial scanning. Then, the axial cross-section of the beam was extracted from the 3D light field rendered by stacking up these lateral plane images.

3 RESULTS AND ANALYSIS

3.1 Simulated and Experimental Results of Weber Self-Accelerating Beams

To investigate the propagation characteristics of Weber beams, simulations and the counterpart experiments were carried out. The corresponding results were shown in **Figure 2**. In simulation, the size of Weber beams can be adjusted flexibly by changing the value of γ in **Eq. 1**. Given $\lambda = 532$ nm, the central lateral and axial cross-sections of Weber beams were calculated by the beam propagation method based on the angular spectrum theory of diffraction [33]. The simulated results were shown in **Figures 2C,D** and **Figures 2E,F** when the value of γ was taken as 300 and 800, respectively, suggesting that a larger γ resulted in a larger main lobe size, longer propagation distance and smaller curvature.

The use of SLM also made the beam size modulation easy to implement in experiment. The phase patterns of masks loaded on SLM were shown in **Figures 2A,B** with the value of γ as 300 and 800, respectively. After sending a Gaussian beam to the SLM with these pre-designed masks, Weber beams were generated by the Fourier transformation of a convex lens L3, and then presented in the focal region of Obj1 with a strong focusing form suitable for particle trapping. When a flat mirror was set in the focal plane of Obj1, the central lateral cross-sections of Weber beams were imaged by CCD1, as shown in **Figure 2G** ($\gamma = 300$) and **Figure 2I** ($\gamma = 800$). The corresponding axial cross-sections were obtained from 300 lateral frames captured by scanning the flat mirror along axial direction. The experimental results were shown in **Figure 2H** ($\gamma = 300$) and **Figure 2J** ($\gamma = 800$), indicating the effect of γ on the characteristic of Weber beams was that the larger γ is, the larger main lobe size is, and the longer propagation distance is, but the smaller curvature of the parabolic trajectory is. It was consistent with the conclusion suggested by the simulated results.

Moreover, taking $\gamma = 300$ as an example to compare the experimental and simulated results, the side lobes in experiment (**Figure 2G**) were less than in simulation (**Figure 2C**), and the propagation distance in experiment (**Figure 2H**) was shorter than in simulation (**Figure 2D**). This was caused by the aperture limitation of experimental elements and the very low initial
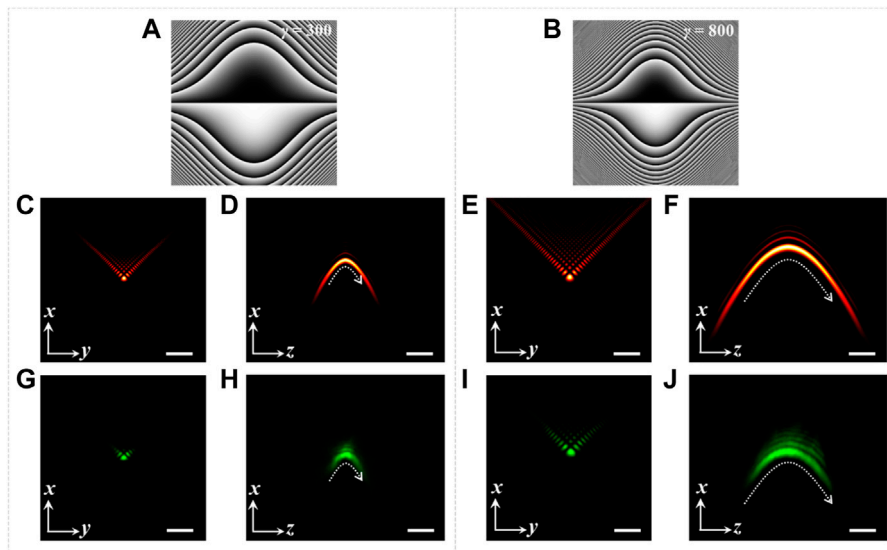
FIGURE 2 | Modulation of Weber beams. **(A,B)** Phase masks of Weber beams with γ = 300 and 800, respectively; **(C–F)** simulated results of the lateral and axial cross-sections of Weber beams, **(C)** and **(D)** correspond to γ = 300, **(E)** and **(F)** correspond to γ = 800; **(G–J)** experimental results of the lateral and axial cross-sections of Weber beams corresponding to **(C–F)**, respectively. Scale bar: 2 μm.
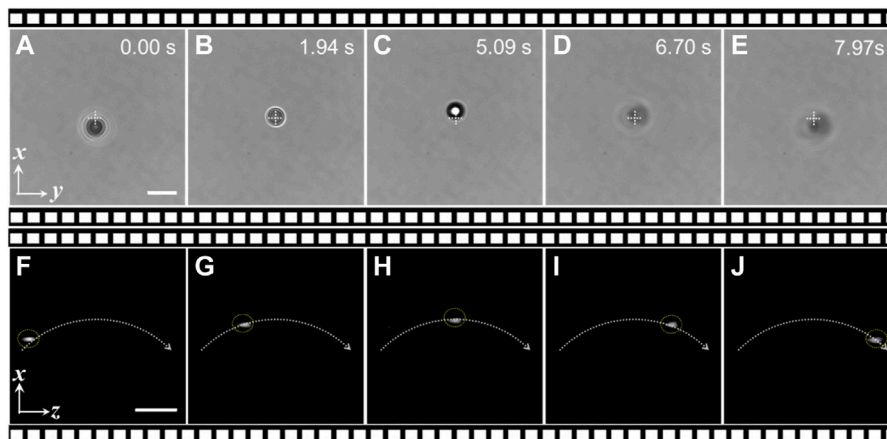
FIGURE 3 | Experimental observation results of particle transporting dynamics along the Weber beam trajectory. **(A–E)** The lateral (x-y) plane images of a trapped particle at different time; **(F–J)** the axial (x-z) plane images corresponding to **(A–E)**. Particles: polystyrene beads of 5 μm in diameter. Scale bar: 10 μm.

incident laser intensity of about 2 μW we set for beam measurement. Nevertheless, as the white dashed curves shown in **Figures 2D,H** the experimental and simulated beams still shared the same parabolic trajectory. And the case of γ = 800 gave the same phenomenon.

3.2 Experimental Results of Particle Transporting and Imaging

Based on the above investigation of Weber beams both in simulation and experiment, it is expected to transport particle in the axial space along a curved trajectory with Weber beams, and the dynamics can be monitored in real-time by the presented system shown in **Figure 1A**.

This system has intrinsic large field of view in axial plane, which is greater than 70 μm × 70 μm in this work. In order to get a long transporting distance in optical manipulation experiment, we set a large value of γ = 3600 to produce a mask pattern according to **Eq. 1** and then loaded it on the SLM. Comparing to the beam measurement mentioned above, the beam intensity for particle trapping was set to a much higher value of about 20 mW to guarantee the stability of optical trap.

The experimental observation results of transporting a polystyrene bead of 5 μm in diameter along a parabolic trajectory of the Weber beam were shown in **Figure 3**. The lateral (x-y) plane and the corresponding axial (x-z) plane information of the transporting dynamics were captured by CCD1 and CCD2 simultaneously,

FIGURE 4 | Quantification of the particle motion. **(A)** Schematic diagram of the primary forces acting on the particle. G: gravity, F: floatage, LG: lateral gradient force, AG: axial gradient force, S: scattering force; **(B)** velocities of the particle at different axial positions.

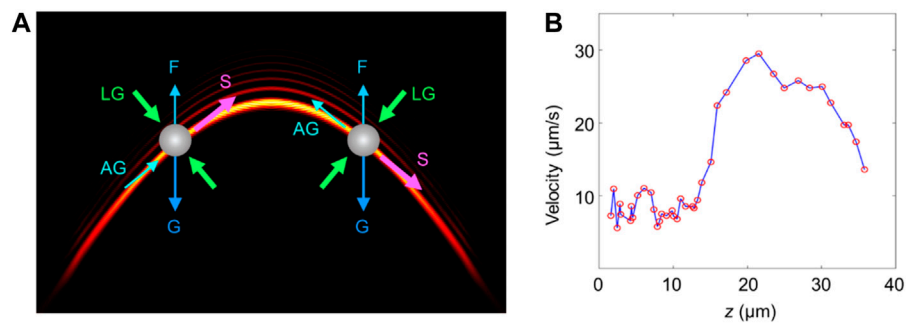displayed as screenshots at different time in **Figures 3A–E** and **Figures 3F–J**, respectively. As can be seen from **Figures 3A–E**, the trapped particle underwent a process of "defocus-focus-defocus" accompanied by the displacement up and down along x direction. Obviously, these lateral images obtained by CCD1 were not enough to give an intuitive description of the particle motion. However, as shown in **Figures 3F–J**, the axial plane images obtained by CCD2 visually displayed that the trapped particle moved along a curved trajectory in x-z plane and stayed in focus throughout the whole journey of about 35 μm.

The whole experimental system was set in horizontal alignment; the used sample was aqueous solution containing polystyrene beads; there was enough axial space for implementing the particle transportation; the target bead was stably trapped in lateral dimension and transported along parabolic trajectory of the designed Weber beam. In view of above conditions, the primary forces acting on the target bead were shown in **Figure 4A**, including the gravity, floatage, scattering force, lateral gradient force and axial gradient force. Among them, the lateral gradient force and scattering force played dominant roles in the particle manipulation. The former performed a 2D trap in lateral dimension and bounded the particle to the main lobe area of the Weber beam, and the latter pushed the particle moving along the beam propagation trajectory.

From the axial plane real-time monitoring results directly captured by CCD2, the motion of the trapped particle can be quantified conveniently. We measured the velocities of the particle at different z positions. As shown in **Figure 4B**, the results indicated that the particle moved faster in the middle region of the transporting path than on either side. It was because the maximum scattering force and quite small axial gradient force of the Weber beam occurred in this region. Moreover, the particle moved faster in the latter half of its motion path than in the first half. This difference was mainly caused by the gravity. As shown in **Figure 4A**, the gravity component along beam trajectory was in opposite direction of the scattering force in the first half, so as to impede the particle movement. The case of the latter half was on the contrary.

manipulation technique and axial plane optical microscopy together, achieving particle transporting along parabolic trajectory of the designed Weber self-accelerating beam with the real-time observation in lateral and axial planes, simultaneously. This method solves the problem that the axial capture dynamics cannot be directly observed in traditional optical tweezers. Because there is only a single objective for both beam generation and signal detection, this system has no particular geometric requirement for sample preparation, and the objectives with high NA are allowed to be used for improving the resolution. In addition, this technique can be further developed to perform particle tracking, because arbitrary plane information of samples can be acquired by translating and rotating the tilted mirror. In a word, by virtue of the flexible light modulation based on the use of SLM, the direct axial plane imaging with the intrinsic large field of view, and good compatibility with other technologies, we believe the proposed technique will become a useful tool for studying a variety of novel beams, and find applications in fields of chemicophysics and biomedicine.

DATA AVAILABILITY STATEMENT

The original contributions presented in the study are included in the article/Supplementary Material, further inquiries can be directed to the corresponding authors.

AUTHOR CONTRIBUTIONS

SA, TP, BY, and PZ conceived the project. BY and PZ supervised the study. SA and TP performed the experiments. SA and SY analyzed the data. SA wrote the draft of the manuscript. All the authors edited the manuscript.

4 CONCLUSION

In this work, we proposed an integrated system which combined the SLM-based special beam generation module, optical

FUNDING

REFERENCES

1. Siviloglou GA, Christodoulides DN. Accelerating Finite Energy Airy Beams. *Opt Lett* (2007) 32:979–81. doi:10.1364/OL.32.000979

2. Siviloglou GA, Broky J, Dogariu A, Christodoulides DN. Observation of Accelerating Airy Beams. *Phys Rev Lett* (2007) 99:213901. doi:10.1103/PHYSREVLETT.99.213901

3. Broky J, Siviloglou GA, Dogariu A, Christodoulides DN. Self-healing Properties of Optical Airy Beams. *Opt Express* (2008) 16:12880–91. doi:10.1364/OE.16.012880

4. Chu X. Evolution of an Airy Beam in Turbulence. *Opt Lett* (2011) 36:2701–3. doi:10.1364/OL.36.002701

5. Baumgartl J, Mazilu M, Dholakia K. Optically Mediated Particle Clearing Using Airy Wavepackets. *Nat Photon* (2008) 2:675–8. doi:10.1038/NPHOTON.2008.201

6. Cheng H, Zang W, Zhou W, Tian J. Analysis of Optical Trapping and Propulsion of Rayleigh Particles Using Airy Beam. *Opt Express* (2010) 18:20384–94. doi:10.1364/OE.18.020384

7. Zhang P, Prakash J, Zhang Z, Mills MS, Efremidis NK, Christodoulides DN. Trapping and Guiding Microparticles with Morphing Autofocusing Airy Beams. *Opt Lett* (2011) 36:2883–5. doi:10.1364/OL.36.002883

8. Zheng Z, Zhang B-F, Chen H, Ding J, Wang H-T. Optical Trapping with Focused Airy Beams. *Appl Opt* (2011) 50:43–9. doi:10.1364/AO.50.000043

9. Jia S, Vaughan JC, Zhuang X. Isotropic Three-Dimensional Super-resolution Imaging with a Self-Bending point Spread Function. *Nat Photon* (2014) 8:302–6. doi:10.1038/nphoton.2014.13

10. Vettenburg T, Dalgarno HIC, Nylk J, Coll-Lladó C, Ferrier DEK, Čižmár T. Light-sheet Microscopy Using an Airy Beam. *Nat Methods* (2014) 11:541–4. doi:10.1038/NMETH.2922

11. Kafian H, Lalenejad M, Moradi-Mehr S, Birgani SA, Abdollahpour D. Light-sheet Fluorescence Microscopy with Scanning Non-diffracting Beams. *Sci Rep* (2020) 10:8501. doi:10.1038/S41598-020-63847-2

12. Polynkin P, Kolesik M, Moloney JV, Siviloglou GA, Christodoulides DN. Curved Plasma Channel Generation Using Ultraintense Airy Beams. *Science* (2009) 324:229–32. doi:10.1126/science.1169544

13. Salandrino A, Christodoulides DN. Airy Plasmon: a Nondiffracting Surface Wave. *Opt Lett* (2010) 35:2082–4. doi:10.1364/OL.35.002082

14. Li L, Li T, Wang SM, Zhang C, Zhu SN. Plasmonic Airy Beam Generated by In-Plane Diffraction. *Phys Rev Lett* (2011) 107:126804. doi:10.1103/PHYSREVLETT.107.126804

15. Mathis A, Courvoisier F, Froehly L, Furfaro L, Jacquot M, Lacourt PA. Micromachining along a Curve: Femtosecond Laser Micromachining of Curved Profiles in diamond and Silicon Using Accelerating Beams. *Appl Phys Lett* (2012) 101:071110. doi:10.1063/1.4745925

16. Götte N, Winkler T, Meinl T, Kusserow T, Zielinski B, Sarpe C. Temporal Airy Pulses for Controlled High Aspect Ratio Nanomachining of Dielectrics. *Optica* (2016) 3:389–95. doi:10.1364/OPTICA.3.000389

17. Novitsky AV, Novitsky DV. Nonparaxial Airy Beams: Role of Evanescent Waves. *Opt Lett* (2009) 34:3430–2. doi:10.1364/OL.34.003430

18. Kaminer I, Bekenstein R, Nemirovsky J, Segev M. Nondiffracting Accelerating Wave Packets of Maxwell's Equations. *Phys Rev Lett* (2012) 108:163901. doi:10.1103/PHYSREVLETT.108.163901

19. Courvoisier F, Mathis A, Froehly L, Giust R, Furfaro L, Lacourt PA. Sending Femtosecond Pulses in Circles: Highly Nonparaxial Accelerating Beams. *Opt Lett* (2012) 37:1736–8. doi:10.1364/OL.37.001736

20. Zhang P, Hu Y, Cannan D, Salandrino A, Li T, Morandotti R. Generation of Linear and Nonlinear Nonparaxial Accelerating Beams. *Opt Lett* (2012) 37:2820–2. doi:10.1364/OL.37.002820

21. Zhang P, Hu Y, Li T, Cannan D, Yin X, Morandotti R. Nonparaxial Mathieu and Weber Accelerating Beams. *Phys Rev Lett* (2012) 109:193901. doi:10.1103/PHYSREVLETT.109.193901

22. Bandres MA, Rodríguez-Lara BM. Nondiffracting Accelerating Waves: Weber Waves and Parabolic Momentum. *New J Phys* (2013) 15:013054. doi:10.1088/1367-2630/15/1/013054

23. Zhang Z, Zhang P, Mills M, Chen Z, Christodoulides DN, Liu J. Trapping Aerosols with Optical Bottle Arrays Generated through a Superposition of Multiple Airy Beams. *Chin Opt Lett* (2013) 11:033502. doi:10.3788/col201311.033502

24. Schley R, Kaminer I, Greenfield E, Bekenstein R, Lumer Y, Segev M. Loss-proof Self-Accelerating Beams and Their Use in Non-paraxial Manipulation of Particles' Trajectories. *Nat Commun* (2014) 5:5189. doi:10.1038/NCOMMS6189

25. Maragò OM, Jones PH, Gucciardi PG, Volpe G, Ferrari AC. Optical Trapping and Manipulation of Nanostructures. *Nat Nanotech* (2013) 8:807–19. doi:10.1038/nnano.2013.208

26. Xin H, Xu R, Li B. Optical Trapping, Driving and Arrangement of Particles Using a Tapered Fibre Probe. *Sci Rep* (2012) 2:818. doi:10.1038/srep00818

27. Vossen DLJ, van der Horst A, Dogterom M, van Blaaderen A. Optical Tweezers and Confocal Microscopy for Simultaneous Three-Dimensional Manipulation and Imaging in Concentrated Colloidal Dispersions. *Rev Scientific Instr* (2004) 75:2960–70. doi:10.1063/1.1784559

28. Curran A, Tuohy S, Aarts DGAL, Booth MJ, Wilson T, Dullens RPA. Decoupled and Simultaneous Three-Dimensional Imaging and Optical Manipulation through a Single Objective. *Optica* (2014) 1:223–6. doi:10.1364/OPTICA.1.000223

29. Li T, Ota S, Kim J, Wong ZJ, Wang Y, Yin X. Axial Plane Optical Microscopy. *Sci Rep* (2015) 4:7253. doi:10.1038/SREP07253

30. Kim J, Wojcik M, Wang Y, Moon S, Zin EA, Marnani N. Oblique-plane Single-Molecule Localization Microscopy for Tissues and Small Intact Animals. *Nat Methods* (2019) 16:853–7. doi:10.1038/S41592-019-0510-Z

31. An S, Ziegler KF, Zhang P, Wang Y, Kwok T, Xu F. Axial Plane Single-Molecule Super-resolution Microscopy of Whole Cells. *Biomed Opt Express* (2020) 11:461–79. doi:10.1364/BOE.377890

32. An S, Peng T, Yan S, Zhang P, Li M, Yao B. Direct Axial Plane Imaging of Particle Manipulation with Nondiffracting Bessel Beams. *Appl Opt* (2021) 60:2974–80. doi:10.1364/AO.417854

33. Poon T-C, Banerjee PP. Single and Double Lens Image Processing Systems. In: *Contemporary Optical Image Processing with MATLAB*. Oxford, United Kingdom: Elsevier (2001). p. 133–67. doi:10.1016/b978-008043788-0/50005-6

3D Reconstruction of Non-Lambertian Surfaces by Perspective Shape-From-Shading With Fast Viscosity Solution

Guohui Wang * and Hao Zheng*

School of Optoelectronic Engineering, Xi'an Technological University, Xi'an, China

Shape-from-shading (SFS) is an important method to reconstruct three-dimensional (3D) shape of a surface in photometry and computer vision. Lambertian surface reflectance and orthographic camera projection are two fundamental assumptions which generally result in undesirable reconstructed results since inaccurate imaging model is adopted. In this paper, we propose a new fast 3D shape reconstruction approach *via* the SFS method relaxing the two assumptions. To this end, the Oren-Nayar reflectance and perspective projection models are used to establish an image irradiance equation which depicts the relationship between the 3D shape of non-Lambertian surfaces and its corresponding two-dimensional (2D) shading image. Considering the light attenuation of the near point source, the image irradiance equation is transformed into a static Hamilton-Jacobi partial differential equation (PDE) by solving a quadratic equation. The viscosity solution of the resultant Hamilton-Jacobi PDE is approximated by using optimal control theory and iterative fast marching method starting from a viscosity supersolution. The performance of the proposed approach is evaluated on both synthetic and real-world images and the experimental results demonstrate that the proposed approach is accurate and fast.

Keywords: 3D reconstruction, shape-from-shading, non-Lambertian surfaces, perspective projection, viscosity solution, iterative fast marching

INTRODUCTION

Shape-from-shading (SFS) is an important method to reconstruct three-dimensional (3D) surfaces in the field of photometry and computer vision. The work has been initiated by Horn [1, 2] who established an image irradiance equation depicting the relationship between the 3D shape of a surface and its corresponding two-dimensional (2D) shading image. Inspired by his work, a lot of different SFS methods are extensively studied (for surveys, see [3, 4]). In these methods, Lambertian surface reflectance and orthographic camera projection are two fundamental assumptions. Even for the diffuse surfaces, however, the Lambertian model has been proved to be inaccurate expression of the reflectance property [5–7]. Furthermore, the image can be seen as formed through a so-called pin-hole camera which should be modeled by perspective projection. Since these methods do not adopt accurate physical and/or optical imaging model, the reconstructed results lack accuracy.

Recently, Tankus et al. [8] changed the classical orthographic projection assumption to a perspective one and formulated the image irradiance equation. They suggested the orthographic fast marching method of Kimmel and Sethian [9] as the initial solution and then approximated the perspective image irradiance equation using an iterative fast marching method. Another perspective

SFS was addressed by Courteille et al. [10] who considered the "pseudo-Eikonal equation" and solved it with a prior knowledge. Yuen et al. [11] proposed an alternative perspective SFS which is also based on the fast marching method of Kimmel and Sethian [9]. Their method, however, does not require the iterative process. It is well worth mentioning that Prados and his colleagues [12, 13] had made a great contribution to the SFS field. They presented a more realistic imaging model for SFS problem, where the orthographic camera projection is substituted by the perspective projection and the light source is assumed to be placed at the optical center of the camera. Moreover, a light attenuation term $1/d^2$ (d defines the distance between the 3D surface point and the position of the light source) has been considered. They generalized the SFS problem and related the derived image irradiance equation with a Hamiltonian and approximated its viscosity solution using optimal control strategy. With their work, Ahmed and Farag [6, 7] replaced Lambertian reflectance by a more advanced Oren-Nayar reflectance and proposed a non-Lambertian SFS method. In addition, they used the Lax-Friedrichs sweeping scheme [14] to solve the explicit partial differential irradiance equation and got a promising reconstructed result. Although [6, 7] worked well on the non- Lambertian surfaces, they still need the exact values on the boundary. Moreover, it is difficult to find a good estimate for the artificial viscosity term and it would take too much time to reach the stopping criterion. To avoid these problems, Vogel and Cristiani [15] used the Upwind scheme to get a more efficient solution with less convergence time. Ju et al. [16] extended the work of Galliani et al. [17]. They used spherical surface parameterization to Oren-Nayar reflectance model and thus could deal with an arbitrary position of the light source. Compared with the method of [6, 7, 15], this work can obtain a very compact and elegant image irradiance equation. Unfortunately, the solving process need transform the fast marching method described in Cartesian coordinates [18] into spherical coordinates. Tozza and Falcone [19, 20] presented another non-Lambertian SFS method using a semi-Lagrangian approximation scheme and proved a convergence result. However, their work still assumes an orthographic camera projection and a distant light source. More recently, some SFS approaches have been proposed by deep learning techniques [21–23]. Yang and Deng [21] addressed the SFS problem by training deep networks with only synthetic images which can not be rendered by any external shape dataset. Henderson and Ferrari [22] presented a unified framework for both reconstruction and generation of 3D shapes, which was trained to model 3D meshes using only 2D supervision. Tokieda et al. [23] proposed a high-frequency shape recovery from shading method using CNN which the U-Net structure was employed. The approaches [21–23] can achieve state-of-the-art performance. However, they need sufficient amount of data for training.

In the current study, based on our previous work [24–27], we propose a new fast perspective SFS approach for non-Lambertian surface reconstruction. The Oren-Nayar reflectance model is also adopted to approximate the surface reflectance property. Then, with a point light source close to the projection center of the camera which performs perspective projection, we formulate the image irradiance equation that can be transformed into a quadratic equation. The main contribution of our work is that we establish a static Hamilton-Jacobi partial differential equation (PDE) by solving the quadratic image irradiance equation that contains the 3D shape, after which we attempt to get the viscosity solution of the resultant PDE by using optimal control theory and iterative fast marching method. It is worth mentioning that the light attenuation term $1/d^2$ has also been employed to remove the ambiguity which leads SFS to be an ill-posed problem. Compared with other existing SFS approach, the proposed approach is more accurate and faster.

The remainder of the paper is structured as follows. In **section 2**, we give the SFS imaging model of non-Lambertian surfaces to derive the image irradiance equation that serves as the basis for our approach. **Section 3** presents a new method to approximate the viscosity solution of the image irradiance equation using optimal control theory and iterative fast marching method. Experimental results on both synthetic and real-world images are performed and discussed in **section 4**. Finally, we conclude our approach in **section 5**.

IMAGE IRRADIANCE EQUATION

SFS Imaging Model of Non-Lambertian Surfaces

To derive the image irradiance equation of non-Lambertian SFS, we firstly make a brief review of the imaging process for the SFS problem which describes the relationship between the 3D shape of a surface and its corresponding 2D shading image. It is well-known that the following relationship between the image irradiance and the surface reflected radiance [1, 25] is modeled as:

$$E_i = L_s \frac{\pi}{4} \left(\frac{D}{F}\right)^2 \cos^4 \chi, \qquad (1)$$

where E_i is image irradiance, which is usually considered to be proportional to the image brightness I. L_s defines the surface reflected radiance along the direction of the camera. The camera lens focuses light from the surface on the imaging sensor (i.e., the image plane) and D, F are its diameter and focal length, respectively. χ is the angle between optical axis and the line of sight to a 3D surface point of a corresponding 2D image point. The term $\cos^4 \chi$ implies non-uniform image irradiance even for uniform radiance, but the actual optical system of the camera is generally designed to correct it. Consequently, we may consider the image irradiance E_i to be proportional to the surface reflected radiance L_s, i.e., $E_i = \eta L_s$.

For an ideal diffuse surface and a distant point light source, the surface has a Lambertian reflectance and the reflected radiance can be expressed as [1]:

$$L_s(\theta_i) = \frac{\rho}{\pi} I_0 \cos \theta_i, \qquad (2)$$

where ρ is the diffuse albedo and I_0 is the intensity of the point light source. The term $\cos \theta_i$ is the scalar product between the surface normal vector $\mathbf{n}$ and the light source vector $\mathbf{L}$.
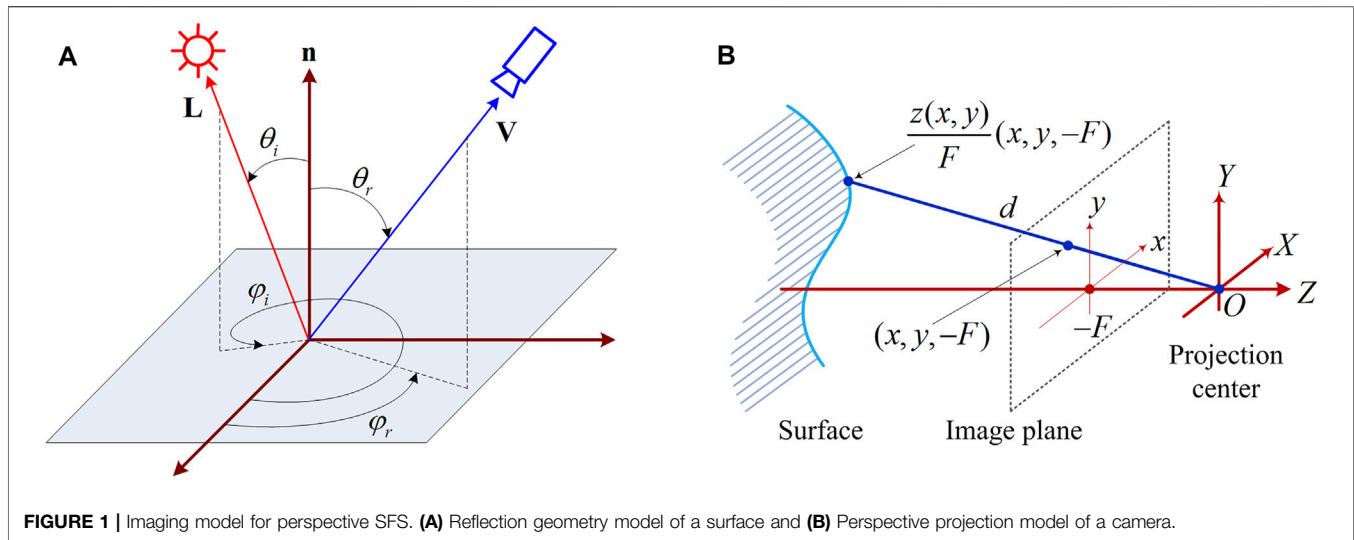
FIGURE 1 | Imaging model for perspective SFS. **(A)** Reflection geometry model of a surface and **(B)** Perspective projection model of a camera.

However, the Lambertian model has been proved to be inaccurate expression of the reflectance property for the real-world diffuse surfaces [5–7]. In order to eliminate the inaccuracy resulting from the assumption of the Lambertian surface reflectance, Oren and Nayar [5] developed an advanced reflectance model for rough diffuse surfaces. Assuming that the surface is composed of extended symmetric V-shaped cavities and each V-cavity has two planar facets following the Lambert's law, they applied the roughness model that the surface roughness is specified using a probability function for the facet orientations to obtain the expression for the surface reflected radiance. For a Gaussian distribution, with reflection geometry shown in **Figure 1A**, L_s is formulated as:

$$L_s\left(\theta_i, \varphi_i; \theta_r, \varphi_r; \sigma\right) = \frac{\rho}{\pi} I_0 \cos\theta_i \left(A + B\max\left[0, \cos\left(\varphi_r - \varphi_i\right)\right]\right)$$
$$\sin\alpha\tan\beta), \qquad (3)$$

where θ_i, φ_i and θ_r, φ_r are the slant, tilt angles of **L** and the camera vector **V**, respectively,

$$A = 1 - 0.5\frac{\sigma^2}{\sigma^2 + 0.33}, \quad B = 0.45\frac{\sigma^2}{\sigma^2 + 0.09}, \qquad (4)$$

$\alpha = \max[\theta_i, \theta_r]$ and $\beta = \min[\theta_i, \theta_r]$. The parameter σ denotes the standard deviation of the Gaussian distribution and is employed as a measure of the surface roughness.

Taking **Eq. 3** into **Eq. 1**, the image irradiance equation of non-Lambertian SFS is now:

$$E_i\left(\theta_i, \varphi_i; \theta_r, \varphi_r\right) = \eta\frac{\rho}{\pi} I_0 \cos\theta_i \left(A + B\max\left[0, \cos\left(\varphi_r - \varphi_i\right)\right]\right)$$
$$\sin\alpha\tan\beta). \qquad (5)$$

Since the image irradiance is usually considered to be proportional to the image brightness, we denote $I = \pi E_i/\eta\rho I_0$ and the image irradiance **Eq. 5** is rewritten as:

$$I\left(\theta_i, \varphi_i; \theta_r, \varphi_r\right) = \cos\theta_i \left(A + B\max\left[0, \cos\left(\varphi_r - \varphi_i\right)\right]\sin\alpha\tan\beta\right). \qquad (6)$$

Image Irradiance Equation of Perspective SFS

As shown in **Figure 1B**, for a perspective camera projection whose center is O, $S(X, Y, Z)$ represents the 3D shape of interested surface for a certain image domain Ω, and can be parameterized by

$$S(X, Y, Z) = \frac{z(x, y)}{F}(x, y, -F), \quad (x, y) \in \Omega, \qquad (7)$$

where $F > 0$ and $z(x, y) > 0$ is the distance between the surface point (X, Y, Z) and $O - XY$ plane. To get a surface normal vector, we calculate the tangent vectors in both x and y directions, respectively and compute their cross product. Then the normal vector $\mathbf{n}(x, y)$ at the point (X, Y, Z) is formulated as:

$$\mathbf{n}(x, y) = \left(F\frac{\partial z}{\partial x}, F\frac{\partial z}{\partial y}, z + x\frac{\partial z}{\partial x} + y\frac{\partial z}{\partial y}\right). \qquad (8)$$

With the point light source whose attenuation term $1/d^2$ has been considered to remove the ambiguity which leads SFS to be an ill-posed problem is located near the projection center O, the light source vector $\mathbf{L}(x, y)$ at the point (X, Y, Z) is given by

$$\mathbf{L}(x, y) = (-x, -y, F) \qquad (9)$$

and the parameters in Oren-Nayar reflectance model satisfy

$$\theta_i = \theta_r = \alpha = \beta, \quad \varphi_i = \varphi_r. \qquad (10)$$

Therefore, the image irradiance **Eq. 6** is simplified to

$$I(\theta_i) = \frac{1}{d^2}\left(A\cos\theta_i + B\sin^2\theta_i\right). \qquad (11)$$

Since the term $\cos\theta_i$ is the scalar product between $\mathbf{n}(x, y)$ and $\mathbf{L}(x, y)$, substituting **Eqs 8**, **9** into **Eq. 11**, we can obtain the image irradiance equation of perspective SFS:

$$I(x, y) = \frac{1}{d^2}\left(A\frac{Q(x,y)}{V(x,y,\nabla u)} + B\frac{V(x,y,\nabla u)^2 - Q(x,y)^2}{V(x,y,\nabla u)^2}\right),$$

$$(12)$$

where $u = \ln z(x,y)$, $V(x,y,\nabla u) = \sqrt{(F\partial u/\partial x)^2 + (F\partial u/\partial y)^2 + (x\partial u/\partial x + y\partial u/\partial y + 1)^2}$, $Q(x,y) = F/(x^2 + y^2 + F^2)^{1/2}$, $d = z(x,y)/Q(x,y) = e^u/Q(x,y)$.

METHOD OF SOLVING THE IMAGE IRRADIANCE EQUATION

Obviously, the image irradiance **Eq. 12** can be described by a quadratic equation with respect to the variable $V(x,y,\nabla u)$. Then the equation is transformed into

$$\left(I(x,y)e^{2u}Q(x,y)^{-2} - B\right)V(x,y,\nabla u)^2 - AQ(x,y)V(x,y,\nabla u)$$
$$+ BQ(x,y)^2 = 0.$$
$$(13)$$

Solving the quadratic **Eq. 13** and satisfying $V(x,y,\nabla u) > 0$, we have

$$V(x,y,\nabla u) = \frac{A + \sqrt{A^2 - 4\left(I(x,y)e^{2u}Q(x,y)^{-2} - B\right)B}}{2\left(I(x,y)e^{2u}Q(x,y)^{-2} - B\right)}Q(x,y).$$
$$(14)$$

Now, we can obtain a novel image irradiance equation

$$-\frac{1}{A - \sqrt{A^2 - 4\left(I(x,y)e^{2u}Q(x,y)^{-2} - B\right)B}}$$
$$+ \frac{1}{2BQ(x,y)}\sqrt{\left(F\frac{\partial u}{\partial x}\right)^2 + \left(F\frac{\partial u}{\partial y}\right)^2 + \left(x\frac{\partial u}{\partial x} + y\frac{\partial u}{\partial y} + 1\right)^2} = 0.$$
$$(15)$$

It is easy to see that **Eq. 15** does not have classical solutions since it is a first-order non-linear PDE. Thus one can appeal to the notion of viscosity solution [28, 29] that is a solution in the weak sense. For the PDE **(15)**, to ensure the uniqueness of the viscosity solution, Dirichlet boundary conditions usually need to be imposed, and therefore a static Hamilton-Jacobi PDE could be got

$$\begin{cases} H(x,y,u,\mathbf{g}) = 0, \forall(x,y) \in \Omega, \\ u(x,y) = \chi(x,y), \forall(x,y) \in \partial\Omega, \end{cases}$$
$$(16)$$

where $\chi(x,y)$ is a real function which is defined on $\partial\Omega$ and

$$H(x,y,u,\mathbf{g}) = -\left(A - \sqrt{A^2 - 4\left(I(x,y)e^{2u}Q(x,y)^{-2} - B\right)B}\right)^{-1}$$
$$+ W(x,y)\sqrt{F^2\|\mathbf{g}\|^2 + ((x,y)\cdot\mathbf{g} + 1)^2}$$
$$(17)$$

is the associated Hamiltonian, where $W(x,y) = (2BQ(x,y))^{-1}$ and $\mathbf{g} = (\partial u/\partial x, \partial u/\partial y)$. According to [12, 29] and our previous work [24], using viscosity solution and optimal control theories, the Hamiltonian **(17)** can be addressed as a control-type formulation

$$H(x,y,u,\mathbf{g}) = -\left(A - \sqrt{A^2 - 4\left(I(x,y)e^{2u}Q(x,y)^{-2} - B\right)B}\right)^{-1}$$
$$+ \sup_{\mathbf{a}\in B_2(0,1)}\{-l_c(x,y,\mathbf{a}) - \mathbf{f}_c(x,y,\mathbf{a})\cdot\mathbf{g}\},$$
$$(18)$$

where $B_2(0,1)$ is the unit ball of center 0 in $\mathbb{R}^2$, $\mathbf{f}_c(x,y,\mathbf{a}) = -W(x,y)\mathbf{R}^T(x,y)\mathbf{D}(x,y)\mathbf{R}(x,y)\mathbf{a}$ and $l_c(x,y,\mathbf{a}) = -\sqrt{1 - \|\mathbf{a}\|^2}/2B - W(x,y)\mathbf{R}^T(x,y)\mathbf{v}(x,y)\cdot\mathbf{a}$ with

$$\mathbf{R}(x,y) = \begin{cases} \begin{pmatrix} x(x^2+y^2)^{-1/2} & y(x^2+y^2)^{-1/2} \\ -y(x^2+y^2)^{-1/2} & x(x^2+y^2)^{-1/2} \end{pmatrix}, & x^2+y^2 \neq 0, \\ \begin{pmatrix} 1 & 0 \\ 0 & 1 \end{pmatrix}, & x^2+y^2 = 0, \end{cases}$$
$$(19)$$

$$\mathbf{D}(x,y) = \begin{pmatrix} \sqrt{x^2+y^2+F^2} & 0 \\ 0 & F \end{pmatrix},$$
$$\mathbf{v}(x,y) = \begin{pmatrix} \sqrt{(x^2+y^2)(x^2+y^2+F^2)^{-1}} \\ 0 \end{pmatrix}.$$
$$(20)$$

We approximate $H(x,y,u,\mathbf{g})$ by

$$H(x,y,\mathbf{g}) \approx -\left(A - \sqrt{A^2 - 4\left(I(x,y)e^{2u}Q(x,y)^{-2} - B\right)B}\right)^{-1}$$
$$+ \sup_{\mathbf{a}\in B_2(0,1)}\{-l_c(x,y,\mathbf{a}) + \min[-f_1(x,y,\mathbf{a}),0]g_1^+ + \max$$
$$[-f_1(x,y,\mathbf{a}),0]g_1^- + \min[-f_2(x,y,\mathbf{a}),0]g_2^+ + \max$$
$$[-f_2(x,y,\mathbf{a}),0]g_2^-\},$$
$$(21)$$

where $f_k(x,y,\mathbf{a})$ is the kth component of $\mathbf{f}_c(x,y,\mathbf{a})$ and g_k^+, g_k^- stand for the corresponding forward and backward difference approximations of the kth component of $\mathbf{g}$ respectively. Obviously, for the approximation method **(21)**, it is necessary to solve the optimum problem and we can use optimal control theory and our proposed approach in [24] to get it.

The explicit time marching scheme for the Hamilton-Jacobi PDE **(16)** applying the forward Euler as the time discretization could be described in the form:

$$u^{n+1} = u^n - \Delta t H(x,y,\mathbf{g}),$$
$$(22)$$

where Δt is a time step. In order to accelerate the convergence speed of scheme **(22)**, our proposed iterative fast marching strategy in [24] is adopted.

The method to approximate the viscosity solution of the resultant Hamilton-Jacobi PDE **(16)** is organized as follows:
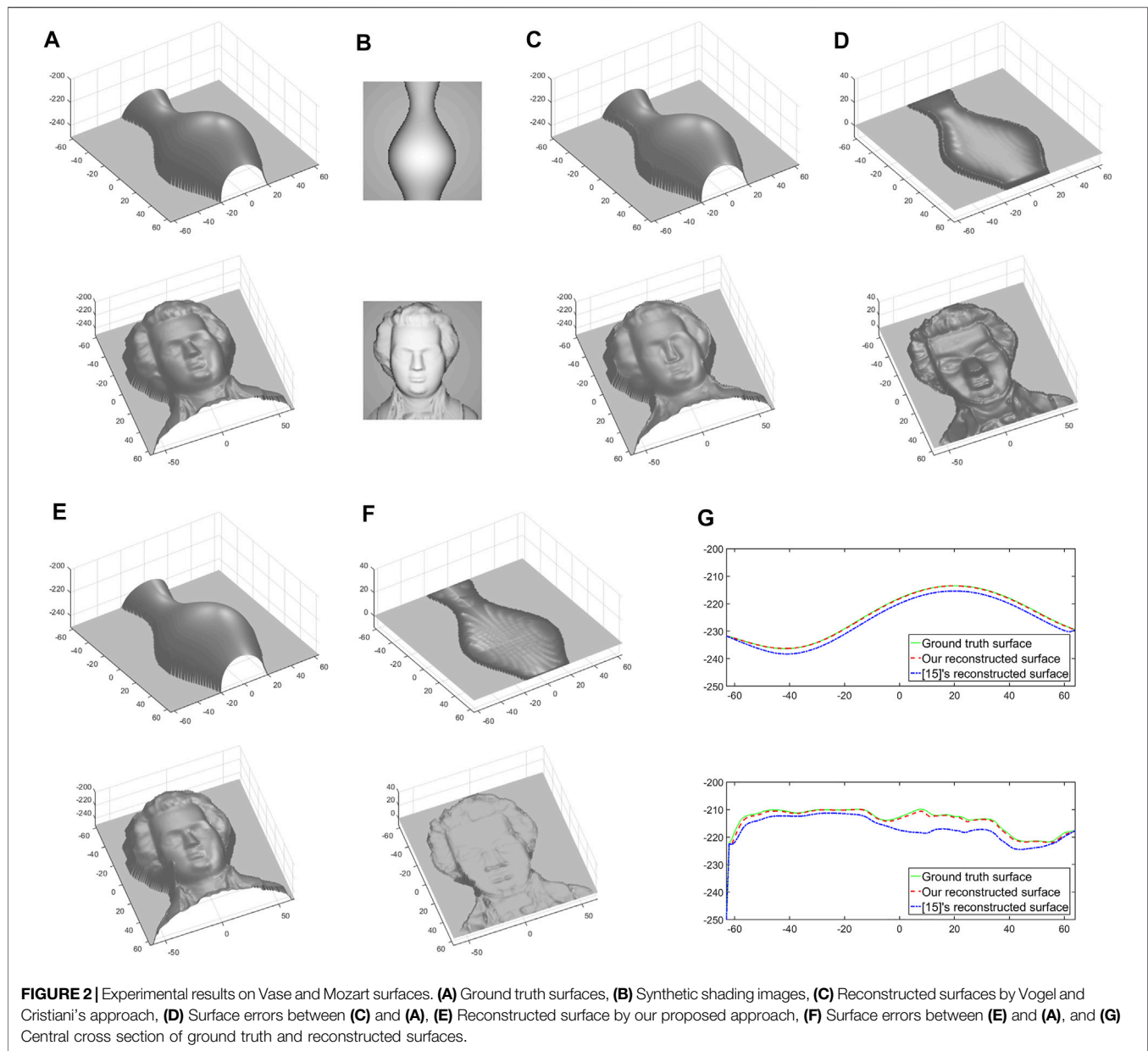
FIGURE 2 | Experimental results on Vase and Mozart surfaces. **(A)** Ground truth surfaces, **(B)** Synthetic shading images, **(C)** Reconstructed surfaces by Vogel and Cristiani's approach, **(D)** Surface errors between **(C)** and **(A)**, **(E)** Reconstructed surface by our proposed approach, **(F)** Surface errors between **(E)** and **(A)**, and **(G)** Central cross section of ground truth and reconstructed surfaces.

1) Initialization (iteration $n = 0$). Set $u^0 = u_0(x_i, y_j)$, where (x_i, y_j) is the discretization of (x, y) at grid point (i, j) and u_0 is a viscosity supersolution. In this paper, $u_0(x_i, y_j) = 0.5 \ln(A) - 0.5 \ln(I(x_i, y_j)Q(x_i, y_j)^{-2})$.

2) Iterative Marching (iteration $n + 1$).

(1) Definitions. Each grid point (i, j) is assigned to one of three sets, *known*, *front*, *unknown*, in the following:

- *Known* is the set of the initial grid points corresponding to the extremums of u. *Known* points are the seeded points whose values will not be recalculated.
- *Front* is the set of the neighbours of *known* points, not in *known*. In our method, *front* points are the four nearest neighbours of *known* points and their values will be recalculated later.

- *Unknown* is the rest of the grid points, where there is not yet a calculation for u.

(2) Marching.

- Let $(i_{\min}, j_{\min})$ be the point among all *front* points that has the smallest u value.
- Remove the point $(i_{\min}, j_{\min})$ from *front* and add it to *known*.
- Label as neighbours any points $(i_{\min}, j_{\min} + 1)$, $(i_{\min} + 1, j_{\min})$, $(i_{\min}, j_{\min} - 1)$, $(i_{\min} - 1, j_{\min})$ which are either in *front* or *unknown*. If the neighbour belongs to *unknown*, add it to *front* and remove it from *unknown*.
- Recalculate the value of u at the four nearest neighbours of $(i_{\min}, j_{\min})$ that are in *front* by applying the scheme **(22)**.
- If all grid points are *known* then exit, otherwise return to top of *marching*.

TABLE 1 | Comparisons of approaches for Vase and Mozart surfaces.

Surface	Method	MA (pixel)	RMS (pixel)	CPU time (s)
Vase	Vogel and Cristiani's approach	0.7916	1.3365	0.19
Vase	Our proposed approach	0.1419	0.2950	0.04
Mozart	Vogel and Cristiani's approach	1.4706	2.2806	0.26
Mozart	Our proposed approach	0.3204	0.8784	0.05
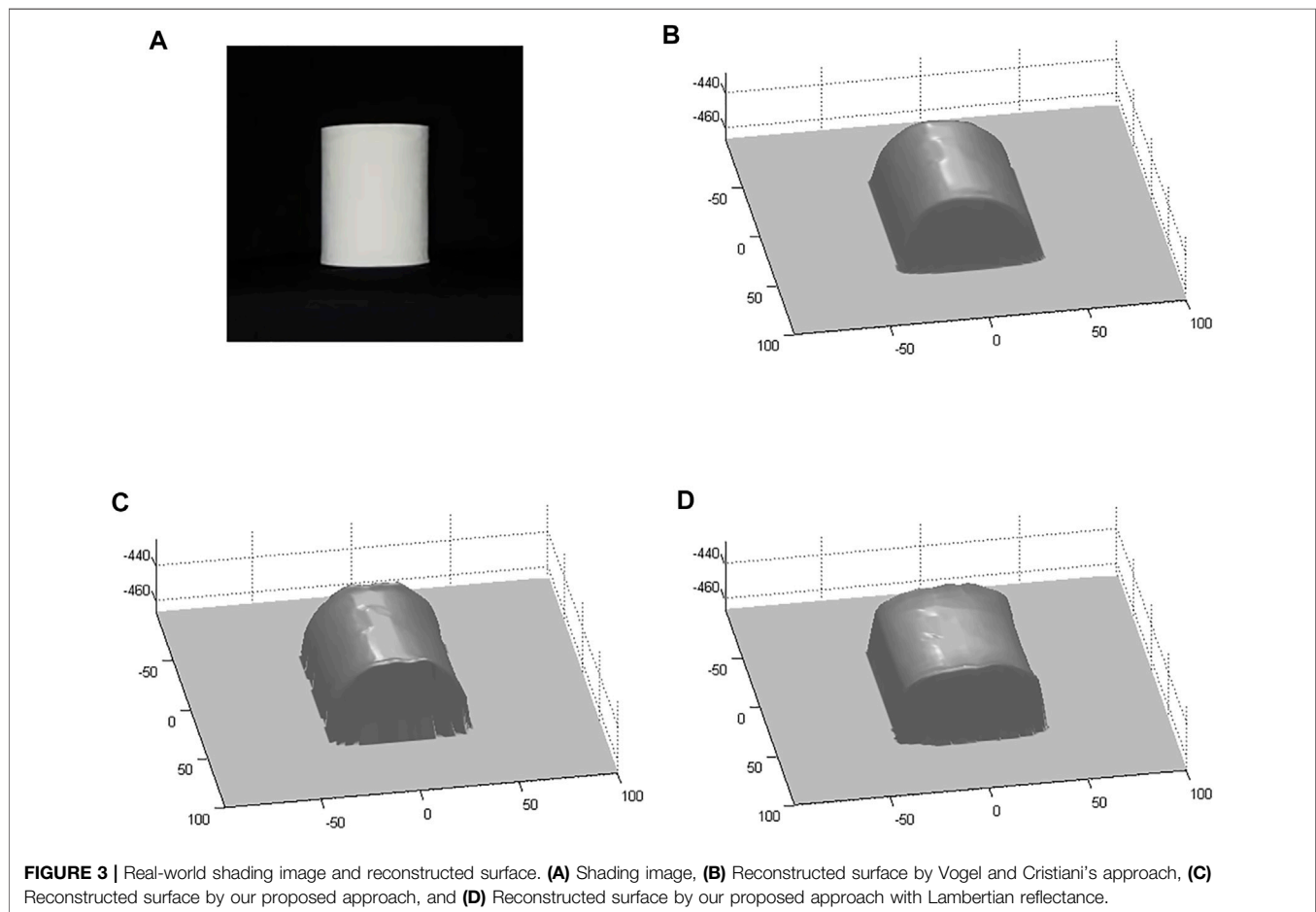
FIGURE 3 | Real-world shading image and reconstructed surface. **(A)** Shading image, **(B)** Reconstructed surface by Vogel and Cristiani's approach, **(C)** Reconstructed surface by our proposed approach, and **(D)** Reconstructed surface by our proposed approach with Lambertian reflectance.

(3) Convergence test. If $\|u^{n+1} - u^n\|_{L^1} \leq \delta$, where δ is a given stopping strategy, the method converges and stops; otherwise returns to 2). In this paper, $\delta = 10^{-5}$.

EXPERIMENTAL RESULTS AND DISCUSSION

Several experiments on two synthetic Vase and Mozart and one real-world shading images have been carried out in order to evaluate the performance of the proposed approach. We compare our proposed approach with Vogel and Cristiani's approach [15]

because it has a better performance than Ahmed and Farag's approach [6, 7]. We implement the two approaches in Matlab, using C mex functions. All the experiments are conducted on a computer with a Xeon E5-1650 processor and 16 GB of DDR3 memory. The unit in the experiments is pixel.

Experimental Results on Synthetic Images

Figure 2 illustrates the experimental results on Vase and Mozart surfaces. **Figure 2A** shows the ground truth surfaces which are benchmark Dataset given by Zhang et al. [3]. **Figure 2B** illustrates the synthetic shading images of Vase and Mozart surfaces with the surface roughness $\sigma = 0.2$ and image domain $\Omega = 128 \times 128$.

Figures 2C,D show the reconstructed surfaces and errors by Vogel and Cristiani's approach respectively. **Figures 2E,F** show the reconstructed surfaces and errors by our proposed approach respectively. **Figure 2G** illustrates the central cross section of ground truth and reconstructed surfaces of Vase and Mozart surfaces.

It is seen from **Figures 2C–G** that both Vogel and Cristiani's and our approaches can give satisfactory surface reconstruction. Furthermore, we can see that our proposed approach produces reconstruction results with smaller errors and exhibits better than Vogel and Cristiani's approach. The performance of Vogel and Cristiani's approach and our proposed approach is further quantitatively described by the mean absolute (MA) error, root mean square (RMS) error and running time. The MA and RMS errors defines as:

$$MA = \frac{1}{m \times n} \sum_{i=1}^{m} \sum_{j=1}^{n} |z_{ij} - \tilde{z}_{ij}|, \tag{23}$$

$$RMS = \sqrt{\frac{1}{m \times n} \sum_{i=1}^{m} \sum_{j=1}^{n} |z_{ij} - \tilde{z}_{ij}|^2}, \tag{24}$$

where $m \times n$ denotes the size of the image domain Ω and $z_{ij}, \tilde{z}_{ij}$ denote the reconstructed surface and the ground truth surface respectively.

Table 1 demonstrates the quantitative comparisons of approaches for Vase and Mozart surfaces. It can be observed obviously that our proposed approach has much more superiority both in the MA and RMS errors. The MA and RMS errors of our proposed approach are about one-fifth and one-fourth of Vogel and Cristiani's approach for the Vase, and about one-fifth and one-third for the Mozart, respectively because our image irradiance equation is approximated by using control-type Hamiltonian and iterative fast marching method while Vogel and Cristiani's is approximated by Upwind scheme. In addition, it is also seen that our approach is much faster than Vogel and Cristiani's approach as the same reason above.

Experimental Results on Real-World Image

Figure 3 illustrates the experiments on the real-world shading of a paper cylinder which is shown in **Figure 3A**. **Figures 3B,C** demonstrate the reconstructed surfaces by Vogel and Cristiani's approach and our proposed approach respectively. **Figure 3D** shows the special case of our proposed approach with Lambertian reflectance, that is, the surface roughness $\sigma = 0$. From the experimental results illustrated in **Figures 3B,C**, it is also seen that both Vogel and Cristiani's and our approaches can give satisfactory surface reconstruction for the real-world shading. Furthermore, our approach also exhibits a slightly better performance that is more vivid than Vogel and Cristiani's approach. It is well worth noting that **Figure 3D** shows a

worse performance since it uses the Lambertian model which is inaccurate expression of the reflection property.

CONCLUSION

We have proposed a fast 3D shape reconstruction approach for non-Lambertian surfaces *via* perspective SFS and viscosity solution. We first formulated the image irradiance equation as a quadratic equation with respect to the variable that contains the 3D shape of the surface and thus a static Hamilton-Jacobi PDE was derived by solving the quadratic equation. We employed an optimal control scheme and an iterative fast marching strategy to compute the viscosity solution of the resultant PDE. Finally, the experimental results verified that our proposed approach can provide satisfactory surface reconstruction with a higher accuracy in less running time. Further study of non-Lambertian SFS includes faster approximated methods and the more accurate imaging models.

DATA AVAILABILITY STATEMENT

The raw data supporting the conclusions of this article will be made available by the authors, without undue reservation.

AUTHOR CONTRIBUTIONS

Both authors contributed to the research work. GW proposed the approach; GW and HZ performed the experiments and analyzed the data; GW wrote the manuscript.

FUNDING

ACKNOWLEDGMENTS

REFERENCES

1. Horn BKP. *Shape from Shading: A Method for Obtaining the Shape of a Smooth Opaque Object from One View*. PhD dissertation. Cambridge (MA): Massachusetts Institute of Technology (1970).

2. Horn BKP, Brooks MJ. The Variational Approach to Shape from Shading. *Computer Vis Graphics, Image Process* (1986) 33:174–208. doi:10.1016/0734-189X(86)90114-3

3. Zhang R, Tsai PS, Cryer JE, Shah M. Shape-From-Shading: A Survey. *IEEE Trans Pattern Anal Machine Intell* (1999) 21:690–706. doi:10.1109/34.784284

4. Durou JD, Falcone M, Sagona M. Numerical Methods for Shape-From-Shading: A New Survey with Benchmarks. *Computer Vis Image Understanding* (2008) 109:22–43. doi:10.1016/j.cviu.2007.09.003

5. Oren M, Nayar SK. Generalization of the Lambertian Model and Implications for Machine Vision. *Int J Comput Vis* (1995) 14:227–51. doi:10.1007/bf01679684

6. Ahmed AH, Farag AA. A New Formulation for Shape from Shading for Non-lambertian Surfaces. In: Proceedings of the IEEE Conference on Computer Vision and Pattern Recognition (2006) 1817–24. doi:10.1109/cvpr.2006.35

7. Ahmed AH. *Shape from Shading Under Various Imaging Conditions*. PhD dissertation. Louisville (KY): University of Louisville (2008).

8. Tankus A, Sochen N, Yeshurun Y. Shape-From-Shading Under Perspective Projection. *Int J Comput Vis* (2005) 63:21–43. doi:10.1007/s11263-005-4945-6

9. Kimmel R, Sethian JA. Optimal Algorithm for Shape From Shading and Path Planning. *J Math Imaging Vis* (2001) 14:237–44. doi:10.1023/A:1011234012449

10. Courteille F, Crouzil A, Durou JD, Gurdjos P. Shape from Shading for the Digitization of Curved Documents. *Machine Vis Appl* (2007) 18:301–16. doi:10.1007/s00138-006-0062-y

11. Yuen SY, Tsui YY, Chow CK. A Fast Marching Formulation of Perspective Shape From Shading Under Frontal Illumination. *Pattern Recognition Lett* (2007) 28:806–24. doi:10.1016/j.patrec.2006.11.008

12. Prados E. *Application of the Theory of the Viscosity Solutions to the Shape from Shading Problem*. PhD dissertation. Nice (France): University of Nice-Sophia Antipolis (2004).

13. Prados E, Camilli F, Faugeras O. A Unifying and Rigorous Shape from Shading Method Adapted to Realistic Data and Applications. *J Math Imaging Vis* (2006) 25:307–28. doi:10.1007/s10851-006-6899-x

14. Kao CY, Osher S, Qian J. Lax-Friedrichs Sweeping Scheme for Static Hamilton-Jacobi Equations. *J Comput Phys* (2004) 196:367–91. doi:10.1016/j.jcp.2003.11.007

15. Vogel O, Cristiani E. Numerical Schemes for Advanced Reflectance Models for Shape from Shading. In: Proceedings of the 18th IEEE International Conference on Image Processing (2011) 5–8. doi:10.1109/ICIP.2011.6116621

16. Ju YC, Tozza S, Breuss M, Bruhn A, Kleefeld A. Generalised Perspective Shape from Shading with Oren-Nayar Reflectance. In: Proceedings of the 24th British Machine Vision Conference (2013). doi:10.5244/C.27.42

17. Galliani S, Ju YC, Breuß M, Bruhn A. Generalised Perspective Shape from Shading in Spherical Coordinates. In: Proceedings of the International Conference on Scale Space and Variational Methods in Computer Vision (2013) 222–33. doi:10.1007/978-3-642-38267-3_19

18. Sethian JA. Fast Marching Methods. *SIAM Rev* (1999) 41:199–235. doi:10.1137/S0036144598347059

19. Tozza S, Falcone M. Analysis and Approximation of Some Shape-From-Shading Models for Non-lambertian Surfaces. *J Math Imaging Vis* (2016) 55:153–78. doi:10.1007/s10851-016-0636-x

20. Tozza S, Falcone M. A Comparison of Non-lambertian Models for the Shape-From-Shading Problem. In: M Breuß, A Bruckstein, P Maragos, S Wuhrer, editors. *Perspectives in Shape Analysis*. Cham, Switzerland: Springer International Publishing AG (2016) 15–42. doi:10.1007/978-3-319-24726-7_2

21. Yang D, Deng J. Shape from Shading through Shape Evolution. In: Proceedings of the IEEE/CVF Conference on Computer Vision and Pattern Recognition (2018) 3781–90. doi:10.1109/CVPR.2018.00398

22. Henderson P, Ferrari V. Learning Single-Image 3D Reconstruction by Generative Modelling of Shape, Pose and Shading. *Int J Comput Vis* (2020) 128:835–54. doi:10.1007/s11263-019-01219-8

23. Tokieda K, Iwaguchi T, Kawasaki H. High-frequency Shape Recovery from Shading by CNN and Domain Adaptation. In: Proceedings of the IEEE International Conference on Image Processing (2021) 3672–6. doi:10.1109/ICIP42928.2021.9506450

24. Wang G, Han J, Zhang X. Three-dimensional Reconstruction of Endoscope Images by a Fast Shape from Shading Method. *Meas Sci Technol* (2009) 20:125801. doi:10.1088/0957-0233/20/12/125801

25. Wang G, Cheng J. Three-Dimensional Reconstruction of Hybrid Surfaces Using Perspective Shape from Shading. *Optik* (2016) 127:7740–51. doi:10.1016/j.ijleo.2016.05.120

26. Wang G, Zhang X, Cheng J. A Unified Shape-From-Shading Approach for 3D Surface Reconstruction Using Fast Eikonal Solvers. *Int J Opt* (2020) 2020:6156058. doi:10.1155/2020/6156058

27. Wang G, Zhang X. Fast Shape-From-Shading Algorithm for 3D Reconstruction of Hybrid Surfaces Under Perspective Projection. *Acta Optica Sinica* (2021) 41:1215003. doi:10.3788/AOS202141.1215003

28. Crandall MG, Lions PL. Viscosity Solutions of Hamilton-Jacobi Equations. *Trans Amer Math Soc* (1983) 277:1–42. doi:10.1090/S0002-9947-1983-0690039-8

29. Bardi M, Capuzzo-Dolcetta I. *Optimal Control and Viscosity Solutions of Hamilton-Jacobi-Bellman Equations*. Boston, MA: Birkhäuser Press (1997).

Characterization Method for Particle Extraction From Raw-Reconstructed Images Using U-Net

Zhitao Hao[1†], Wei-Na Li[2†], Bowen Hou[1], Ping Su[1]* and Jianshe Ma[1]

[1]*Tsinghua Shenzhen International Graduate School, Tsinghua University, Shenzhen, China,* [2]*College of Science, Shantou University, Shantou, China*

Digital holographic imaging can capture a volume of a particle field and reconstruct three-dimensional (3D) information of the volume from a two-dimensional (2D) hologram. However, it experiences a DC term, twin-images, defocus images of other particles and noise induced by the optical system. We propose the use of a U-net model to extract in-focus particles and encode the in-focus particles as squares at ground truth z. Meanwhile, zero-order images, twin-images, defocused images of other particle and noise induced by the optical system are filtered out. The central coordinate of the square represents the lateral position of the particle, and the side length of the square represents the particle diameter. The 2D raw-reconstructed images generated from the pre-processed hologram by utilizing backward Fresnel propagation serve as the input of the network. A dense block is designed and added to the encoder and decoder of the traditional U-net model. Each layer takes the inputs from all previous layers and passes the feature maps to all subsequent layers, thereby facilitating full characterization of the particles. The results show that the proposed U-net model can extract overlapping particles along the z-axis well, allowing the detection of dense particles. The use of that squares characterize particles makes it more convenient to obtain particle parameters.

Keywords: digital holography, particle imaging, 3D imaging, U-net, image reconstruction

INTRODUCTION

The particle fields comprise small objects, such as bubbles, biological cells, droplets. In recent years, 3D imaging has been widely used in particle detection (including shape, location, and motion) across many scientific domains, such as materials [1], chemical engineering [2–4], biology [5–7], medical sciences [8–10], and environmental science [11–13]. Digital holography (DH) encodes the 3D information of objects into a 2D hologram using the interference of the reference wave and object wave. Owning to only a single hologram can be reconstructed to restore the 3D information of the objects, DH has emerged as a powerful tool for 3D imaging in recent years. A spherical wave was first used as reference wave to observe particles distributed in water [14], the lateral position and size of each particle were gained. Thereafter, a plane wave was used as a reference wave to observe the bubbles in the air [15]. Conventional reconstruction methods have also been proposed. For example, the minimum intensity was applied to detect the edges of the bubbles from raw-reconstructed images. However, the minimum intensity method depends on the threshold setting to distinguish the particles from the background. Background noise and overlapped particles have serious effects [16]. Various criteria (such as edge sharpness and intensity distribution) [15, 17, 18] were applied to characterize the focus level of particles. However, these criteria are sensitive to the detailed

characteristics and noise level in the holograms, limiting their application in low-concentration particle fields with low background and cross-interference noise. The deconvolution method [19, 20] models the observed blur in 3D reconstruction as the convolution of an object and a point spread function (PSF). However, the PSF must be based on the known diffraction formula or obtained through a hologram of a point-like object in the experiment. The compressive holography method [21–23] is an effective reconstruction method to eliminate noise because of the sparsity of the signal, but it is time-consuming and requires complicated fine-tuning parameters to obtain optimal results.

Recently, machine learning using deep neural networks (DNNs) [24] has been applied to image analysis. First, the application of deep learning in DH appeared in medical examination [25–28, 34] as well as in the classification of particles in holograms [29, 30]. DNNs were also applied to acquire the depth information of particles [31, 32], and autofocus is accomplished. Further studies have reported impressive results using DNNs for phase recovery [25, 33], phase aberration compensation [34, 35], hologram pixel super-resolution [36, 37] and digital holographic reconstruction [38–40]. Shimobaba et al. [41] first used a U-net model [42] to realize the holographic reconstruction of multiple particles. Shao et al. [43] proposed a U-net model to reconstruct hologram with higher-concentration particles. However, the sizes of the particles were not obtained. Li et al. [44] proposed using a short U-net with average pooling to extract in-focus particles at ground truth z and remove zero-order images, twin-images, and the defocused images of other particles from raw-reconstructed images; lateral position and the size of particles were obtained. However, it is complicated to obtain parameters of particles that are assumed to be circles [45]. Wu et al. [46] proposed the Dense-U-net and obtained particle information directly from the hologram and encoded them into a series of rectangles because it is convenient to identify and calculate the length and width of the rectangles. However, it is difficult to find completely overlapped particles along the z-axis from one single hologram. Inspired by the previous study, we found that encoding in-focus particles into squares is more conducive to the extraction of particle parameters. Simultaneously, to distinguish the particles completely overlapping along the z-axis, it will be better to train the neural network by feeding raw-reconstructed images that are generated from a hologram.

In this study, we propose the use of a U-net network to extract in-focus particles from raw-reconstructed images and encode them into a series of squares. The center coordinate of the square represents the lateral position of the particle, and the side length of the square represents the diameter of the particle. The rest of the paper is organized as follows: hologram preparation, U-net model, and characterization method are introduced in *Principles*. In *Simulation Results* the simulation results are presented. Experiment results are introduced in *Experimental Results*. The discussion is presented in *Evaluation and Discussions*. Finally, the conclusions are summarized in *Conclusion*.

PRINCIPLES

Holography and Fresnel Diffraction Algorithm

Suppose there are n particles in the particle field in **Figure 1A**, each particle p_i has a different size and different distance z_i away from the camera. When a plane wave $R(x, y)$ illuminates the particle field, the Fresnel diffraction [47] of each particle on the sensor plane is depicted in **Eq. 1**, and the object wave $O(x, y)$, which is the coherent superposition of the diffraction fields by all the particles is shown in **Eq. 2**. The hologram is recorded on the sensor plane, which is the interference of $R(x, y)$ and $O(x, y)$. This process is depicted in **Eq. 3**.

$$O_i(x, y, z_i) = F^{-1}\{\exp(jkz_i) \times F\{p_i(\xi, \eta)\} \times \exp\left(-j\pi\lambda z_i(f_x^2 + f_y^2)\right)\} \tag{1}$$

$$O(x, y) = \sum_{i=1}^{n} O_i(x, y, z_i) \tag{2}$$

$$I(x, y) = |O(x, y)|^2 + |R(x, y)|^2 + O(x, y)R^*(x, y) + O^*(x, y)R(x, y) \tag{3}$$

$$= |O(x, y)|^2 + 1 + O(x, y) + O^*(x, y)$$

$$I_{final}(x, y) = |O(x, y)|^2 + O(x, y) + O^*(x, y) = O(x, y) + nse \tag{4}$$

$$O'(x', y', z_i) = \left|F^{-1}\{\exp(-jkz_i)F\{I_{final}(x, y)\} \times \exp(j\pi\lambda z_i(f_x^2 + f_y^2))\}\right| \tag{5}$$

Here (ξ, η), (x, y), (x', y'), and (f_x, f_y) represent the particle (lateral) plane, sensor plane, reconstructed plane, and spatial frequency domain, respectively. $F\{\cdot\}$ and $F^{-1}\{\cdot\}$ denote Fourier transform and inverse Fourier transform, respectively. $I(x, y)$ denotes the recorded hologram, and $O^*(x, y)$ denotes the complex conjugate of $O(x, y)$. The plane wave is assumed to be $R(x, y) = 1$ in **Eq. 3**. Therefore, the pre-processed hologram is $I_{final}(x, y) = I(x, y) - 1$, as shown in **Figure 1B**. Moreover the pre-processed hologram is rewritten in **Eq. 4**, in which $nse = |O(x, y)|^2 + O^*(x, y)$. A raw-reconstructed image $O'(x', y', z_i)$ shown in **Figure 1C** is obtained from the pre-processed hologram using 42, depicted in **Eq. 5**, at a certain ground truth z_i. It comprises in-focus images, zero-order images, conjugate images, and defocus images of other particles [44]. Noted that the original objects are generated using the Mie scattering model [48].

Particle Characterization Method

Each particle in a particle field is characterized by (x, y, z_i, D_i), where (x, y) represents the lateral position, z_i denotes the distance to the sensor plane, and D_i is the diameter of the particle. We propose the use of squares to represent particles. The central coordinate of the square represents the central coordinate of the particle, and the side length of the square is equal to the diameter of the particle. In this study, raw-reconstructed images with in-focus particles, as shown in **Figure 1C**, serve as the input of the model. The areas encompassed by the red solid line in **Figure 1C** are in-focus

FIGURE 1 | (A) In-line digital holographic experimental setup; **(B)** pre-processed hologram; **(C)** raw-reconstructed image at 5,238 μm; **(D)** the proposed U-net model; **(E)** the predicted image of the U-net model corresponding to **(C)**.
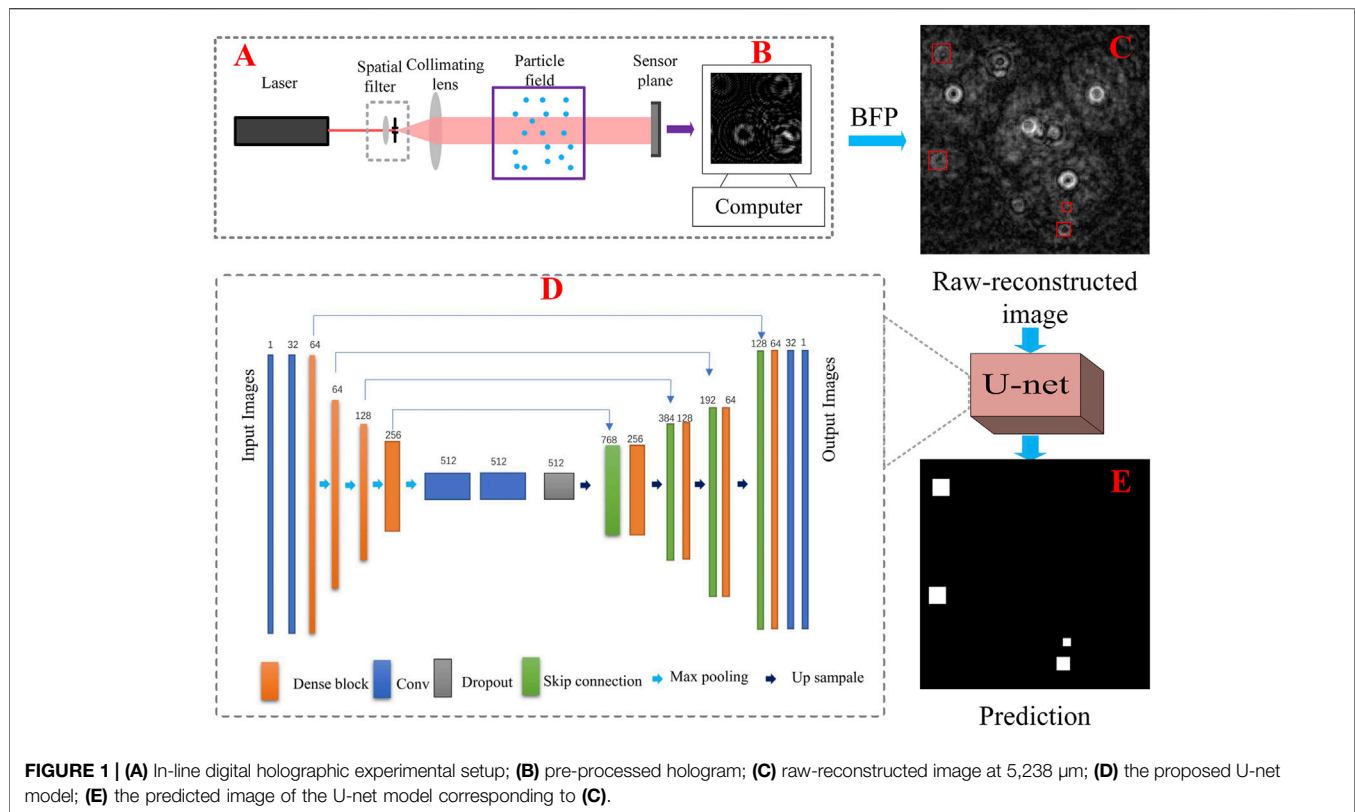
particles. Via the special characterization method, the in-focus particles in **Figure 1C** are encoded into different squares, which is shown in **Figure 1E**. The images with squares shown in **Figure 1E** serve as the output of the model. And the U-net model is described below.

U-Net Model

A U-net model can be regarded as a black box. When many images are fed into it, the model learn the features of these images and obtain the mapping function f, which is calculated automatically through multi-layer network parameters, and is expressed as **Eq. 6**.

$$Y = f(X, \theta) \tag{6}$$

Where X, Y denote the input and output of the network, respectively, and f denotes the mapping function. θ denotes the parameters of the model, and it is updated every epoch during training.

The proposed model, which is shown in **Figure 1D**, includes four down-samplings and four up-samplings. A dropout layer is applied to prevent overfitting. To simplify the training process, a residual neural network (ResNet) [49] is used to form a dense block. Each dense block consists of two Conv_Blocks which contains convolution, batch standardization, and activation layer. The output of each dense block is connected to the input of the dense block via a skip connection structure, which combines the high signal-to-noise ratio and the low signal-to-noise ratio features of the images for training in the

deeper stages of the network. In this section, the raw-reconstructed images serve as the input of the U-net model. The images shown in **Figure 1E** serve as output of the proposed model, meanwhile, mean square error is applied as the loss function of the model.

SIMULATION RESULTS

In the simulation section, we use the same Mie scattering model [48] to obtain the original particles. 51 holograms with the size of 256×256 are generated. A hologram shown in **Figure 2A** contains a volume $512 \times 512 \times 500\ \mu m^3$. Thirteen transparent particles with diameter of 20, 30, and 40 μm are randomly distributed in this volume. The hologram is backward Fresnel propagated to 5 different distances, including 5,138, 5,238, 5,338, 5,438, and 5,538 μm, respectively, to generate the raw-reconstructed images. Finally, 255 raw-reconstructed images corresponding to 51 holograms and 255 ground truth images are used as the dataset to train the U-net models. Because the particle field contains multiple transparent particles, we observe that the raw-reconstructed volume shown in **Figure 2B** is full of noise, including the zeros-order images, conjugate images, and defocused images of the other particles. The U-net model distinguishes in-focus particles from noisy images.

The hologram in **Figure 2A** is first used to test the model. The raw-reconstructed volume comprised five raw-reconstructed images is shown in **Figure 2B**. The corresponding predictions

FIGURE 2 | Simulation result; **(A)** a pre-processed hologram with multiple particles; **(B)** the reconstruction of **(A)** using BFP; **(C)** prediction of **(B)** by the U-net model; **(D)** ground truth position of the particle field, the blue circles represent ground truth particles; **(E)** 3D predicted position of the particle field by extracting the information in **(C)**; **(F)** Combination of ground truth and prediction; **(G)** a pre-processed hologram with overlapped particles; **(H)** raw-reconstructed images of **(G)**; **(I)** prediction corresponding to **(H)**.

are presented in **Figure 2C**. We observe that the in-focus particles are extracted from the noisy images and encoded into squares, and the noise is filtered out. Hence, we obtain the coordinates and side lengths of the squares. The coordinates and the diameters are acquired, and the predicted location of particles are depicted in **Figure 2E**. The ground-truth distribution of the particle field is shown in **Figure 2D**. **Figure 2F** is the combination of ground truth and prediction; the coincidence of the blue circles and red dots represents the correct prediction, and the single blue circle represents the unpredicted particle. **Figure 2G** also shows a pre-processed hologram comprised of two overlapped particles along the z-axis, in which the spacing between the two particles equals the theoretical axial resolution of DH system (10 mm). The diameter of the particles equals 40 μm. The raw-reconstructed images of **Figure 2G** are depicted in **Figure 2H**. **Figure 2I** is the corresponding prediction of **Figure 2H**. We observe that the overlapped particles are

successfully extracted at ground truth z. The theoretical axial resolution reaches 100 μm when a 10× microscope objectives (MO) is used. 75 raw-reconstructed images corresponding to 15 holograms with the same specifications but different particle distributions are generated for testing. The extraction rate of the particle field is 95.8%, and the lateral positioning error was less than 2 μm. The error of diameter is less than 4 μm. Simulation results show that the U-net network is successful in extracting the information of in-focus particles from the raw-reconstructed images at ground truth z and encoding them into squares. Zero-order images, twin-images, and defocused images of other particles are filtered out simultaneously. When compared with [44], squares are more conducive to extracting particle parameters than circles. Compared with [46], this study can easily distinguish particles with the same lateral position when the depth spacing is greater than 100 μm.
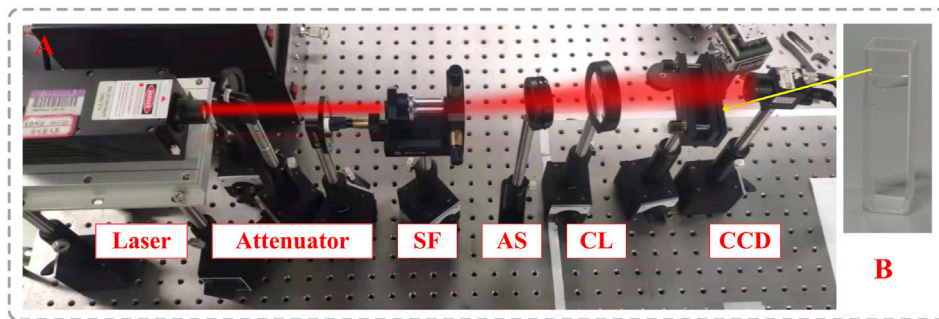
FIGURE 3 | (A) Experimental setup, laser, attenuators, spatial filter, SF; aperture stop, AS; collimating lens, CL; particle field, and CCD; **(B)** particle field in a cuvette.
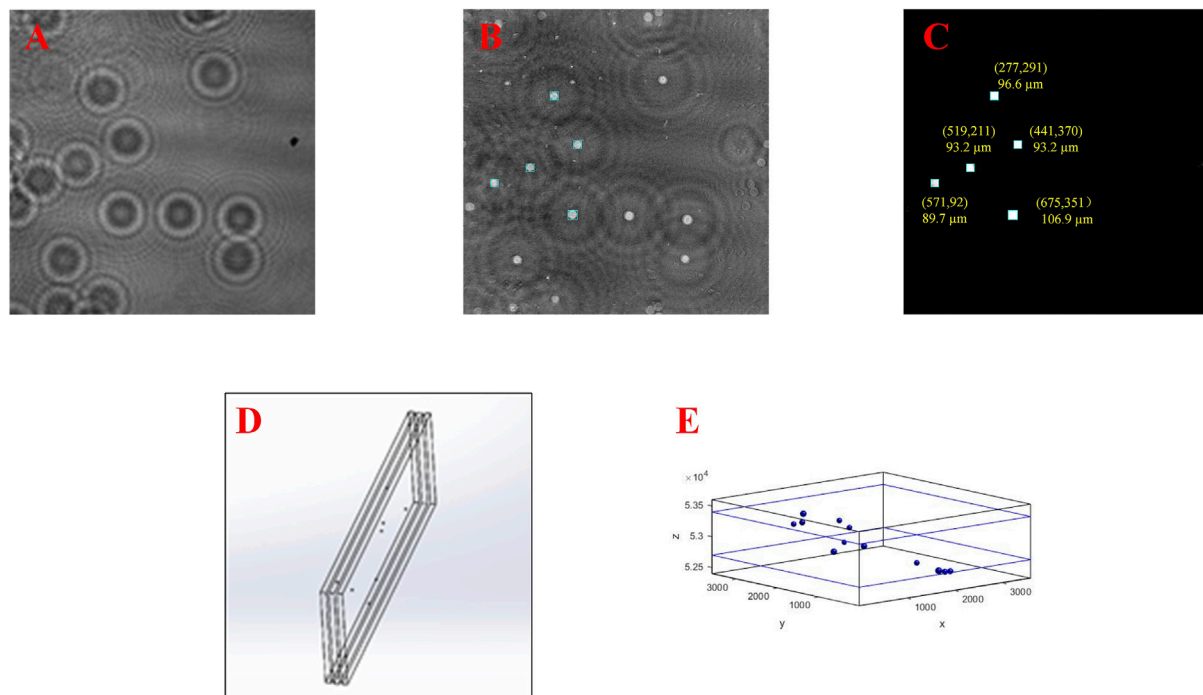
FIGURE 4 | Experimental result; **(A)** captured hologram with multiple particles; **(B)** the raw-reconstructed image at 52.7 mm; **(C)** prediction of the U-net model; **(D)** particle field of the second dataset; **(E)** 3D distribution of particle field.

EXPERIMENTAL RESULTS

Figure 3 shows the experimental setup, in which the wavelength of the laser is 632.8 nm, the size of the camera (charge-coupled device, CCD) is 2456 by 2058, and its pixel pitch is 3.45 μm. A hologram is generated by capturing a volume of 200 polystyrene particles per ml distributed in milli-Q water (diameter = 90 ~ 110 μm).

In the experiment, the holograms have different features from the holograms in simulation because they are composed of noise induced by the optical system (especially the laser). Therefore, a new model was trained using the dataset obtained in experiment. We use polystyrene spheres distributed in milli-Q water shown in **Figure 3B** to generate the first dataset (**Supplementary Material**), 60 holograms are obtained. And the second dataset containing 20 holograms is created using the method described below. The particles are deposited between every two adjacent slides in three slides, as shown in **Figure 4D**. The z-axis position of each slice is similar. Raw-reconstructed images in the dataset are generated by reversed holograms $I_{revs}(x, y) = 255 - I(x, y)$ by utilizing BFP from 42 to 65 mm away from the sensor plane, and the corresponding ground truth images, as shown in **Figures 4A,B**,

respectively, are generated by the proposed method in [50] through image segmentation, and the minimum intensity is used as a focus metric. Noted that the method is not completely stable and accurate when the noise increases in a hologram which can be caused by cross interference [43] and oblique slides. Bad data (i.e., the holograms with severe noise mentioned above) is manually eliminated in this study. We adopt 120 raw-reconstructed images (256×256) as the inputs in the dataset to train the U-net for 400 epochs, 20 raw-reconstructed images among them are from the second dataset which is generated by adhering particles between every two adjacent slides in three slides. The test result is carried out when the raw-reconstructed image in the second dataset, which is shown in **Figure 4B**, is predicted by the U-net model. The area encompassed by the turquoise solid lines is the in-focus particles. The corresponding prediction is shown in **Figure 4C**. We observe that the in-focused particles are successfully extracted and encoded into squares. Lateral position and diameter of each square are obtained. It is noted that the size of the raw-reconstructed images for testing is 1024×1024 pixels, we divide the big raw-reconstructed image into smaller ones with a size 256×256 to conveniently feed them into the U-net model. Thereafter, they are stitched together to form the large images. Eventually, the test images can be rendered as a 3D volume depicted in **Figure 4E**.

EVALUATION AND DISCUSSIONS

As shown in **Figure 4C**, the in-focus particles in **Figure 4B** are properly restored, and the shapes of all the particles are squares, we can find squares to locate the lateral position of each particle, including the center coordinate and the diameter of each particle. As depicted in **Figure 4E**, the particle field is restored successfully. The positioning error is less than 3.45 μm (1 pixel) in the x, y directions, the error of diameter is less than 6.9 μm (2 pixel). The holograms are reconstructed when the depth spacing equals 200 μm. We use polystyrene spheres distributed in the milli-Q water to obtain one dataset, and we make the second dataset through adhering particles between every two adjacent slides in three slides because 1) the particles in the second dataset we make are few and scattered, which ensures the correctness of the lateral position of particles, 2) The thickness of the slides is known, so the depth spacing is certain, which is helpful to determine the position of particles along the z-axis. However, as the number of slides increases, the captured hologram is of poor quality. This may be primarily because the slides are not completely perpendicular to the optical axis of the optical system and noise is induced by the slides, therefore, we chose the simplest way by using three slides to divide the particles into two slices. Finally, the simulation and experimental results show that the proposed method is

promising, and the time to obtain the prediction of a hologram is less than 96 s, which is much faster than the conventional iterative optimization methods. The raw-reconstructed images are trained to match the ground truth images that in-focus particles are encoded into squares to easily obtain the information of the particles.

CONCLUSION

In this study, a U-net model is used to extract in-focus particles from the raw-reconstructed images at ground truth z and encode them into squares. Zero-order images, twin-images, defocused images of other particles and noise induced by the optical system are filtered out simultaneously. The center of the square represents the center of the particle, and the side length of the square represents the diameter of the particle. Finally, the information for each particle is obtained. We used squares instead of circles to represent particles because the squares are more convenient to acquire information of particles. The simulation and experimental results demonstrate that the proposed model is feasible. Eventually, a 3D particle field is restored.

DATA AVAILABILITY STATEMENT

The raw data supporting the conclusions of this article will be made available by the authors, without undue reservation.

AUTHOR CONTRIBUTIONS

FUNDING

SUPPLEMENTARY MATERIAL

The Supplementary Material for this article can be found online at: https://www.frontiersin.org/articles/10.3389/fphy.2021.816158/full#supplementary-material

REFERENCES

1. Batenburg KJ, Bals S, Sijbers J, Kübel C, Midgley PA, Hernandez JC, et al. 3D Imaging of Nanomaterials by Discrete Tomography. *Ultramicroscopy* (2009) 109(6):730–40. doi:10.1016/j.ultramic.2009.01.009

2. Yu J, Wu C, Sahu SP, Fernando LP, Szymanski C, McNeill J. Nanoscale 3D Tracking with Conjugated Polymer Nanoparticles. *J Am Chem Soc* (2009) 131(51):18410–4. doi:10.1021/ja907228q

3. Wang A, Marashdeh Q, Fan L-S. ECVT Imaging of 3D Spiral Bubble Plume Structures in Gas-Liquid Bubble Columns. *Can J Chem Eng* (2014) 92(12):2078–87. doi:10.1002/cjce.22070

4. Wu X, Li X, Yao L, Wu Y, Lin X, Chen L, et al. Accurate Detection of Small Particles in Digital Holography Using Fully Convolutional Networks. *Appl Opt* (2019) 58(34):G332–G44. doi:10.1364/AO.58.00G332

5. Prevedel R, Yoon Y-G, Hoffmann M, Pak N, Wetzstein G, Kato S, et al. Simultaneous Whole-Animal 3D Imaging of Neuronal Activity Using Light-Field Microscopy. *Nat Methods* (2014) 11(7):727–30. doi:10.1038/nmeth.2964

6. Kumar SS, Sun Y, Zou S, Hong J. 3D Holographic Observatory for Long-Term Monitoring of Complex Behaviors in Drosophila. *Sci Rep* (2016) 6:33001. doi:10.1038/srep33001

7. Adams JK, Boominathan V, Avants BW, Vercosa DG, Ye F, Baraniuk RG, et al. Single-frame 3D Fluorescence Microscopy with Ultraminiature Lensless FlatScope. *Sci Adv* (2017) 3(12):e1701548. doi:10.1126/sciadv.1701548

8. Choi Y-S, Lee S-J. Three-dimensional Volumetric Measurement of Red Blood Cell Motion Using Digital Holographic Microscopy. *Appl Opt* (2009) 48(16):2983–90. doi:10.1364/AO.48.002983

9. Su T-W, Xue L, Ozcan A. High-throughput Lensfree 3D Tracking of Human Sperms Reveals Rare Statistics of Helical Trajectories. *Proc Natl Acad Sci* (2012) 109(40):16018–22. doi:10.1073/pnas.1212506109

10. Taute KM, Gude S, Tans SJ, Shimizu TS. High-throughput 3D Tracking of Bacteria on a Standard Phase Contrast Microscope. *Nat Commun* (2015) 6(1). doi:10.1038/ncomms9776

11. Ekvall MT, Bianco G, Linse S, Linke H, Bäckman J, Hansson L-A, et al. Three-Dimensional Tracking of Small Aquatic Organisms Using Fluorescent Nanoparticles. *PLoS ONE* (2013) 8(11):e78498. doi:10.1371/journal.pone.0078498

12. Beals MJ, Fugal JP, Shaw RA, Lu J, Spuler SM, Stith JL. Holographic Measurements of Inhomogeneous Cloud Mixing at the Centimeter Scale. *Science* (2015) 350(6256):87–90. doi:10.1126/science.aab0751

13. Lindensmith CA, Rider S, Bedrossian M, Wallace JK, Serabyn E, Showalter GM, et al. A Submersible, off-Axis Holographic Microscope for Detection of Microbial Motility and Morphology in Aqueous and Icy Environments. *PLOS ONE* (2016) 11(1):e0147700. doi:10.1371/journal.pone.0147700

14. Darakis E, Khanam T, Rajendran A, Kariwala V, Naughton TJ, Asundi AK. Microparticle Characterization Using Digital Holography. *Chem Eng Sci* (2010) 65(2):1037–44. doi:10.1016/j.ces.2009.09.057

15. Tian L, Loomis N, Domínguez-Caballero JA, Barbastathis G. Quantitative Measurement of Size and Three-Dimensional Position of Fast-Moving Bubbles in Air-Water Mixture Flows Using Digital Holography. *Appl Opt* (2010) 49(9):1549–54. doi:10.1364/AO.49.001549

16. Malek M, Allano D, Coëtmellec S, Lebrun D. Digital In-Line Holography: Influence of the Shadow Density on Particle Field. *Opt Express* (2004) 12(10):2270–9. doi:10.1364/OPEX.12.002270

17. Shao S, Li C, Hong J. A Hybrid Image Processing Method for Measuring 3D Bubble Distribution Using Digital Inline Holography. *Chem Eng Sci* (2019) 207:929–41. doi:10.1016/j.ces.2019.07.009

18. Guildenbecher DR, Gao J, Reu PL, Chen J. Digital Holography Simulations and Experiments to Quantify the Accuracy of 3D Particle Location and 2D Sizing Using a Proposed Hybrid Method. *Appl Opt* (2013) 52(16):3790–801. doi:10.1364/AO.52.003790

19. Latychevskaia T, Gehri F, Fink H-W. Depth-resolved Holographic Reconstructions by Three-Dimensional Deconvolution. *Opt Express* (2010) 18(21):22527–44. doi:10.1364/OE.18.022527

20. Latychevskaia T, Fink H-W. Holographic Time-Resolved Particle Tracking by Means of Three-Dimensional Volumetric Deconvolution. *Opt Express* (2014) 22(17):20994–1003. doi:10.1364/OE.22.020994

21. Brady DJ, Choi K, Marks DL, Horisaki R, Lim S. Compressive Holography. *Opt Express* (2009) 17(15):13040–9. doi:10.1364/OE.17.013040

22. Li W-N, Zhang Z, Su P, Ma J, Wang X. Removal of Defocused Images Using Three-Dimensional Nonlinear Diffusion Based on Digital Holography. *J Opt* (2019) 22(1):015701. doi:10.1088/2040-8986/ab5bad

23. Chen W, Tian L, Rehman S, Zhang Z, Lee HP, Barbastathis G. Empirical Concentration Bounds for Compressive Holographic Bubble Imaging Based on a Mie Scattering Model. *Opt Express* (2015) 23(4):4715–25. doi:10.1364/OE.23.004715

24. Barbastathis G, Ozcan A, Situ G. On the Use of Deep Learning for Computational Imaging. *Optica* (2019) 6(8):921–43. doi:10.1364/OPTICA.6.000921

25. Wu Y, Rivenson Y, Zhang Y, Wei Z, Günaydin H, Lin X, et al. Extended Depth-Of-Field in Holographic Imaging Using Deep-Learning-Based Autofocusing and Phase Recovery. *Optica* (2018) 5(6):704–10. doi:10.1364/OPTICA.5.000704

26. Wang H, Lyu M, Situ G. eHoloNet: a Learning-Based End-To-End Approach for In-Line Digital Holographic Reconstruction. *Opt Express* (2018) 26(18):22603–14. doi:10.1364/OE.26.022603

27. Liu T, de Haan K, Rivenson Y, Wei Z, Zeng X, Zhang Y, et al. Deep Learning-Based Super-resolution in Coherent Imaging Systems. *Sci Rep* (2019) 9(1):3926. doi:10.1038/s41598-019-40554-1

28. Liu T, Wei Z, Rivenson Y, Haan K, Zhang Y, Wu Y, et al. Deep Learning-based Color Holographic Microscopy. *J Biophotonics* (2019) 12(11):e201900107. doi:10.1002/jbio.201900107

29. Göröcs Z, Tamamitsu M, Bianco V, Wolf P, Roy S, Shindo K, et al. A Deep Learning-Enabled Portable Imaging Flow Cytometer for Cost-Effective, High-Throughput, and Label-free Analysis of Natural Water Samples. *Light Sci Appl* (2018) 7(1):66. doi:10.1038/s41377-018-0067-0

30. O'Connor T, Anand A, Andemariam B, Javidi B. Deep Learning-Based Cell Identification and Disease Diagnosis Using Spatio-Temporal Cellular Dynamics in Compact Digital Holographic Microscopy. *Biomed Opt Express* (2020) 11(8):4491–508. doi:10.1364/BOE.399020

31. Ren Z, Xu Z, Lam EY. Learning-based Nonparametric Autofocusing for Digital Holography. *Optica* (2018) 5(4):337–44. doi:10.1364/OPTICA.5.000337

32. R Zhenbo, X Zhimin, YL Edmund, editors. *Autofocusing in Digital Holography Using Deep Learning*. San Francisco, CA: ProcSPIE (2018).

33. Rivenson Y, Zhang Y, Günaydin H, Teng D, Ozcan A. Phase Recovery and Holographic Image Reconstruction Using Deep Learning in Neural Networks. *Light Sci Appl* (2018) 7(2):17141. doi:10.1038/lsa.2017.141

34. Liu S, Lian Q, Xu Z. Phase Aberration Compensation for Digital Holographic Microscopy Based on Double Fitting and Background Segmentation. *Opt Lasers Eng* (2019) 115:238–42. doi:10.1016/j.optlaseng.2018.12.001

35. Nguyen T, Bui V, Lam V, Raub CB, Chang L-C, Nehmetallah G. Automatic Phase Aberration Compensation for Digital Holographic Microscopy Based on Deep Learning Background Detection. *Opt Express* (2017) 25(13):15043–57. doi:10.1364/oe.25.015043

36. Luo Z, Yurt A, Stahl R, Lambrechts A, Reumers V, Braeken D, et al. Pixel Super-resolution for Lens-free Holographic Microscopy Using Deep Learning Neural Networks. *Opt Express* (2019) 27(10):13581–95. doi:10.1364/OE.27.013581

37. de Souza JC, Freire RBR, dos Santos PAM. Compressive Holography with Resolution Improvement and Lensless Adjustable Magnification. *Opt Commun* (2019) 437:337–41. doi:10.1016/j.optcom.2018.12.081

38. Zeng T, So HK-H, Lam EY. RedCap: Residual Encoder-Decoder Capsule Network for Holographic Image Reconstruction. *Opt Express* (2020) 28(4):4876–87. doi:10.1364/OE.383350

39. Wang K, Kemao Q, Di J, Zhao J. Y4-Net: a Deep Learning Solution to One-Shot Dual-Wavelength Digital Holographic Reconstruction. *Opt Lett* (2020) 45(15):4220–3. doi:10.1364/OL.395445

40. Go T, Lee S, You D, Lee SJ. Deep Learning-Based Hologram Generation Using a white Light Source. *Sci Rep* (2020) 10(1):8977. doi:10.1038/s41598-020-65716-4

41. Shimobaba T, Takahashi T, Yamamoto Y, Endo Y, Shiraki A, Nishitsuji T, et al. Digital Holographic Particle Volume Reconstruction Using a Deep Neural Network. *Appl Opt* (2019) 58(8):1900–6. doi:10.1364/AO.58.001900

42. Ronneberger O, Fischer P, Brox T. U-net: Convolutional Networks for Biomedical Image Segmentation. In: International Conference on Medical Image Computing and Computer-Assisted Intervention (2015).

43. Shao S, Mallery K, Kumar SS, Hong J. Machine Learning Holography for 3D Particle Field Imaging. *Opt Express* (2020) 28(3):2987–99. PubMed PMID: 32121975. doi:10.1364/OE.379480

44. Li W-N, Su P, Ma J, Wang X. Short U-Net Model with Average Pooling Based on In-Line Digital Holography for Simultaneous Restoration of Multiple Particles. *Opt Lasers Eng* (2021) 139:106449. doi:10.1016/j.optlaseng.2020.106449

45. Fish J, Scrimgeour J. Fast Weighted Centroid Algorithm for Single Particle Localization Near the Information Limit. *Appl Opt* (2015) 54(20):6360–6. doi:10.1364/AO.54.006360

46. Wu Y, Wu J, Jin S, Cao L, Jin G. Dense-U-net: Dense Encoder-Decoder Network for Holographic Imaging of 3D Particle fields. *Opt Commun* (2021) 493:126970. doi:10.1016/j.optcom.2021.126970

47. Goodman JW. *Introduction to Fourier Optics*. New York (1968).

48. Bohren CF, Huffman DR. *Absorption and Scattering of Light by Small Particles*. Weinheim, Germany: Wiley-VCH Verlag GmbH (1998).

49. K He, X Zhang, S Ren, J Sun, editors. *Deep Residual Learning for Image Recognition*. In:IEEE Conference on Computer Vision and Pattern Recognition (CVPR), 27-30 June 2016 (2016).

50. T Siddharth, S James, K Joseph, T Michael, C Helen, D Percy, et al. editors. *Application of* In-Situ *Digital Holography in the Study of Particles, Organisms and Bubbles within Their Natural Environment*. Baltimore, MD: ProcSPIE (2012).

Conflict of Interest: The authors declare that the research was conducted in the absence of any commercial or financial relationships that could be construed as a potential conflict of interest.

Lensless Fourier-Transform Terahertz Digital Holography for Full-Field Reflective Imaging

Yaya Zhang[1], Jie Zhao[1,2]*, Dayong Wang[1,2], Kunlun Li[1], Lu Rong[1,2] and Yunxin Wang[1,2]

[1]College of Physics and Optoelectronics, Faculty of Science, Beijing University of Technology, Beijing, China, [2]Beijing Engineering Research Center of Precision Measurement Technology and Instruments, Beijing, China

Continuous-wave terahertz digital holography (TDH) is a full-field lensless phase imaging approach usually with the coherent THz laser. It has the potential to be applied to nondestructive testing. In order to simplify the reconstruction and utilize the THz radiation with higher efficiency, a full-field reflective lensless Fourier-transform TDH (RLF-TDH) configuration is proposed with oblique illumination mode based on 2.52 THz radiation. A spherical reference beam is generated by a reflective concave mirror in order to reduce the loss of THz radiation, which is different from other configurations of the same kind. In the reconstruction process, the complex-amplitude image can be obtained by directly applying single Fourier transform to the digital hologram; thus, it is very possible to achieve real-time imaging. A tilted plane correction method is implemented to correct the anamorphism caused by the nonparallel planes between the object and recording plane. The profile information of the object can be measured from the unwrapped, aberration-free phase image. Two reflective gold-coated samples are adopted to demonstrate the validity of the RLF-TDH imaging system.

Keywords: THz digital holography, lensless fourier-transform, phase contrast imaging, reflective imaging, profile measurement

INTRODUCTION

Terahertz (THz) spectral range lies between approximately 0.1 and 10 THz. The THz band owns the unique property and broad prospects in many fields, for example, security inspection, art protection, and studies on biological samples [1]. Reflective THz imaging technology is suitable for obtaining the surface profiles of the object, for example, nondestructive testing [2], *in vivo* imaging of burned skin [3], and measurement of explosive compounds [4]. The reflection THz pulsed imaging can provide a broadband spectral image with both amplitude and phase information [5, 6]. However, the reflective imaging receives the signal of weak reflection from the nonuniformity surface of the object. Thus, most such imaging systems suffer from the problems of relatively high optical complexity and lack of high-power sources. Continuous-wave (CW) THz reflective imaging approaches are blooming based on the laser with high output power. The amplitude distribution of an object can be obtained by using a reflective CW THz confocal microscopy with high resolution [7], but the imaging speed is limited by the mechanical scanning rate, and the pinhole in this approach leads to much loss of THz radiation. Another method that needs to scan is self-mixing, which needs quantum cascade laser as the transceivers [8]. Besides, the surface profile of object can be also measured by THz heterodyne profilometry based on an independent local oscillator reference signal [9]. The above scanning imaging approaches are limited by the time-consuming recording process and mechanical inertia.

With the maturity development of THz array detectors, such as microbolometer and pyroelectric detector, CW THz full-field phase imaging has become a promising imaging method. THz ptychography can retrieve the complex amplitude distribution of the object from a set of diffraction patterns originating of sample's partially overlapped illumination areas [10]. This method cannot realize recording in real time presently.

Reflective THz digital holography (TDH) is a full-field phase imaging method. It can obtain the amplitude and phase information of the object from the numerical reconstruction of a recorded digital hologram and acquire the surface profile and depth information of the sample. Different from the transmission TDH, it has been used for imaging of the sample hidden behind the material, which is transparent to THz wave [11, 12]. Reflection TDH can achieve high-resolution imaging by recording holograms with double parallel recording planes; the inherent "twin image" problem is eliminated by using iterative phase restoration algorithm [13], but it needs to record several holograms. Fresnel off-axis reflection TDH imaging can yield the complex amplitude of the object by recording single-frame hologram, whereas the reconstruction algorithm includes Fresnel or angular spectrum propagation, which requires accurate reconstruction distance and multiple Fourier transform [14, 15]. In lensless Fourier-transform digital holographic imaging configuration, the spherical reference beam is brought to focus on the object plane. Usually, a pinhole or lens is introduced to lead to a spherical reference beam in other spectral regions. This imaging layout is simple and compact; meanwhile, the numerical reconstruction only needs one Fourier transform of the digital hologram, which is conducive to real-time imaging [16]. This method has been carried out in a lot of imaging researches in visible light, X-ray, and ultraviolet bands [17–21]. However, when the method is expanded to THz band, because the categories of the available elements are relatively few, and the loss of the energy is high, the configuration is better to avoid applying the transmission elements or use less elements and is better to be compact and has high utilization rate of the energy.

In this article, we investigate a full-field reflective lensless Fourier-transform THz digital holographic (RLF-TDH) imaging method with oblique illumination. In the proposed geometry, a concave mirror is used to form a spherical reference beam. The experimental setup is built based on a 2.52-THz laser and a pyroelectric array detector. A single Fourier transform is performed to yield the complex amplitude of the object wavefront at the image plane in almost real time. A tilted plane correction method is implemented to correct the deformation caused by the nonparallel between the object and detector planes. Two gold-coated objects with Chinese character are used to demonstrate the ability for the surface profiling.

METHODOLOGY

Lensless Fourier-Transform Digital Holographic Interferometry

The schematic of the RLF-TDH setup is shown in **Figure 1**, where x_0-y_0 and x-y are the coordinate systems as the object plane and
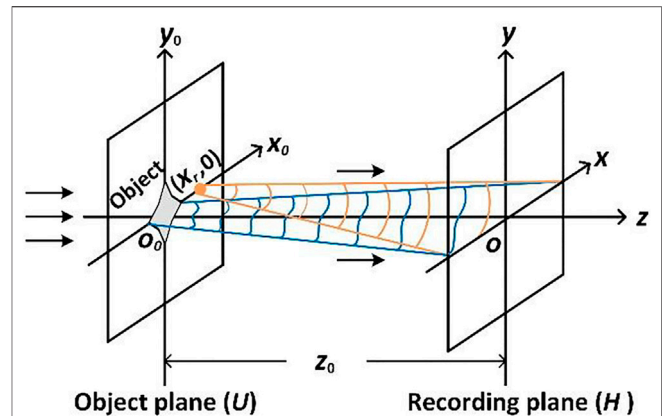

FIGURE 1 | Schematic of the coordinate system of object plane and recording plane of lensless Fourier-transform hologram.

hologram recording plane, respectively. The object is illuminated by a plane wave in the positive z direction. In the RLF-TDH configuration, the object and the point source of the reference beam must be kept in the same plane.

Assuming that the object is illuminated by a normally incident plane wave with unit amplitude, the complex distribution of the object beam in the object plane is denoted by $O_0(x_0, y_0)$. Then the diffraction propagation of object beam arriving at the recording plane is described by the Fresnel–Kirchhoff integral as [22]

$$O(x, y) \propto \exp\left[\frac{jk}{2z_0}(x^2 + y^2)\right] \times \iint_\infty O_0(x_0, y_0) \exp\left\{\frac{jk}{2z_0}\left[(x - x_0)^2\right.\right.$$

$$\left.\left. + (y - y_0)^2\right]\right\} dx_0 dy_0 \propto \exp\left[\frac{jk}{2z_0}(x^2 + y^2)\right] \iint_\infty O_0(x_0, y_0) \exp\left[\frac{jk}{2z_0}(x_0^2 + y_0^2)\right]$$

$$\times \exp\left[-\frac{jk}{z_0}(xx_0 + yy_0)\right] dx_0 dy_0 \propto \exp\left[\frac{jk}{2z_0}(x^2 + y^2)\right] FT\{O_0'(x_0, y_0)\}\big|, \quad (1a)$$

$$O'_0(x_0, y_0) = O_0(x_0, y_0) \exp\left[\frac{jk}{2z_0}(x_0^2 + y_0^2)\right], \quad (1b)$$

where $FT\{\cdot\}$ denotes the two-dimensional Fourier transformation, λ is the wavelength, z_0 is the distance between the object and detector, and the wave number $k = 2\pi/\lambda$. In the geometry of lensless Fourier-transform hologram, the effect of the spherical phase factor associated with the Fresnel diffraction pattern of the object is eliminated by use of a spherical reference beam $R(x, y)$ with the same average curvature as

$$R(x, y) \propto \exp\left[\frac{jk}{2z_0}(x^2 + y^2)\right] \exp\left[\frac{jk}{z_0}(xx_r)\right], \quad (2)$$

in which $(x_r, 0)$ is the coordinate of the point source of the spherical reference beam. The object beam and the reference beam interfere at the recording plane to produce a hologram. The intensity of hologram can be expressed as

$$I(x, y) = |O + R|^2 = |O|^2 + |R|^2 + O^*R + OR^*, \quad (3)$$

where * indicates a complex conjugation. The first two terms contain the DC components associated with the zero-order term, and the third and fourth terms correspond to the interference terms containing the complex-value information of object. To suppress the DC term and twin image effect, Fourier spectrum analysis approach is utilized to separate the term supporting the object. The fourth term in **Eq. 3** can be extracted as

$$O(x, y)R^*(x, y) \propto \exp\left[-\frac{jk}{z_0}(xx_r) \right] FT\{O_0'(x_0, y_0)\}. \quad (4)$$

The reconstructed object wave field $O(x', y')$ can be finally reconstructed as

$$O_{+1}(x', y') = FT^{-1}\{O(x, y)R^*(x, y)\}$$
$$\propto O_0(x' - x_r, y') \exp\left[\frac{jk}{2z_0}\left((x' - x_r)^2 + y'^2 \right) \right], \quad (5)$$

where x'-y' is the coordinate of the reconstructed image plane, and $FT^{-1}\{\}$ denotes the inverse Fourier transformation. The relationships between the recording plane and the reconstructed image plane are $\Delta x' = \frac{\lambda z_0}{(M \Delta x)}$ and $\Delta y' = \frac{\lambda z_0}{(N \Delta y)}$. Δx and Δy, and $\Delta x'$ and $\Delta y'$ are the pixel size of the two planes; M and N are the pixel numbers on the recording plane, respectively.

The reconstructed phase distribution of the object $O(x', y')$ can be calculated by

$$\varphi(x', y') = \arctan\left\{ \frac{\text{Re}\left[O(x', y')\right]}{\text{Im}\left[O(x', y')\right]} \right\}, \quad (6)$$

where the operators Re and Im denote the real and imaginary parts of a complex function, respectively. The calculated phase distribution from **Eq. 6** is wrapped within the range $[-\pi, \pi)$, which is coincident with the output range of the arctangent function. Then, a least-square phase unwrapping algorithm [23] is used to obtain the unwrapped phase. The method of least-square surface fitting is finally applied to eliminate the aberrations and to access the practical phase distribution of the object [24]. The above reconstructed algorithm, involving only a single Fourier transform, is fast enough compared with other existing methods such as the Fresnel method [11, 12, 14, 15] and phase shifting method [18], and so on, which involve several Fourier transforms or complex multiplications and slow down the reconstruction process. For reflective object (in air $n = 1$), the surface topography $h(x', y')$ can be retrieved as:

$$h(x', y') = \frac{\varphi(x', y')\lambda}{4\pi \cos\theta}, \quad (7)$$

where θ is half of the angle between the illumination and the observation directions in the case of inclined illumination, which is coincident with our proposed configuration.

The Correction of Tilted Illumination RLF-TDH

The model of the RLF-TDH *via* tilted illumination is established and shown in **Figure 2**. The incident wave plane is not parallel to

FIGURE 2 | Schematic of the correction to the tilted reconstructed image under tilted illumination.
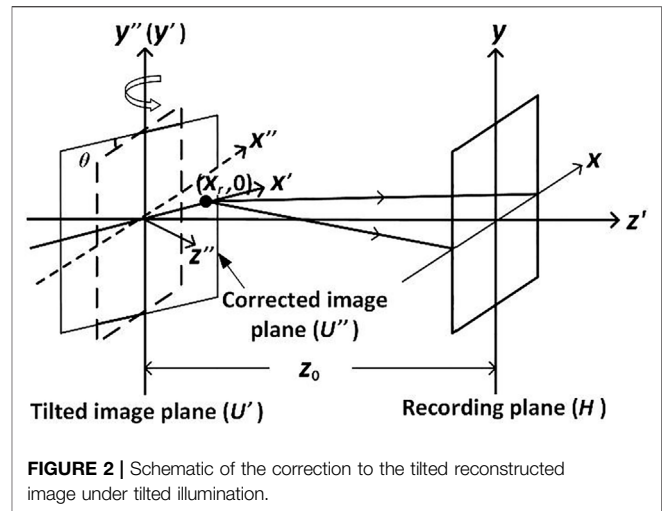
the object plane, and the object plane is not parallel to the recording plane. In this case, the reconstruction results are incorrect based on the traditional diffraction propagation theory between parallel planes. The correction of tilted illumination needs to be adopted.

It can be seen from the reconstruction principle in the previous section that the complex optical field can be obtained by a single inverse Fourier transform of the recorded hologram $I(x, y)$ on the tilted reconstructed image plane $U'(x', y')$, which is parallel to the detector plane at a distance z_0. In tilted illumination scheme, first, the Fourier spectrum of $U'(x', y')$ is calculated as $\hat{U}'(f_{x'}, f_{y'})$. Then, $\hat{U}'(f_{x'}, f_{y'})$ is transformed into the frequency spectrum to obtain the corrected plane by using the coordinate transformation by rotating the θ along the y-axis. At last, by using the inverse Fourier transformed to the rotated spectrum to calculate the corrected wave field $U''(x'', y'')$. Here, it is assumed the two coordinates of $U'(x', y')$ and $U''(x'', y'')$ share the origin, so that only the formulation of the coordinate rotation needs to be processed.

The Fourier spectral distribution of the reconstructed image $U'(x', y')$ is given by

$$\hat{U}'(f_{x'}, f_{y'}) = \Im\{U'(x', y')\}, \quad (8)$$

where $(f_{x'}, f_{y'})$ denotes the coordinate in frequency domains of the titled plane. It should be noted that the Fourier transform of the reconstructed image is not the hologram, but only the spectral distribution on the image plane. The transformation matrix used to rotate coordinates on the y-axis with the angle of θ is given by [15, 25].

$$\begin{pmatrix} f_{x''} \\ f_{y''} \\ f_{z''} \end{pmatrix} = \begin{pmatrix} \cos\theta & 0 & \sin\theta \\ 0 & 1 & 0 \\ -\sin\theta & 0 & \cos\theta \end{pmatrix} \begin{pmatrix} f_{x'} \\ f_{y'} \\ f_{z'} \end{pmatrix}, \quad (9)$$

where $f_{x''}$ and $f_{y''}$ are the spatial frequency coordinates of the corrected plane. If the **Eq. (9)** is expanded, the following formulas can be obtained:
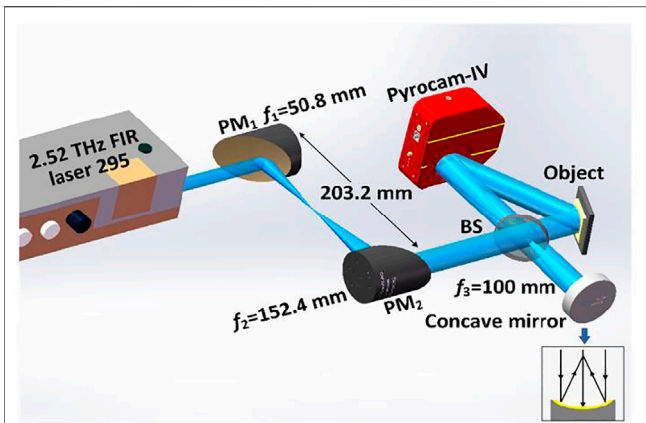
FIGURE 3 | Experimental setup of RLF-TDH. BS, beam splitter; PM$_i$, off-axis parabolic mirror.

$$\begin{cases} f_{x''} = \xi\left(f_{x'}, f_{y'}\right) = f_{x'}\cos\theta + f_{z'}\sin\theta, \\ f_{y''} = \eta\left(f_{x'}, f_{y'}\right) = f_{y'} \end{cases} \quad (10)$$

where $f_{z'} = \sqrt{\frac{1 - (f_{x'})^2 - (f_{y'})^2}{\lambda}}$. After coordinate transformation in the frequency domain, if the inverse Fourier transform is applied to express the optical field, the integral area must satisfy the mathematical relationship $df_{x''}df_{y''} = |J(f_{x'}, f_{y'})|df_{x'}df_{y'}$, where the Jacobian $J(f_{x'}, f_{y'})$ is defined as [26]

$$\left|J\left(f_{x'}, f_{y'}\right)\right| = \begin{bmatrix} \dfrac{\partial \xi}{\partial f_{x'}} & \dfrac{\partial \xi}{\partial f_{y'}} \\ \dfrac{\partial \eta}{\partial f_{x'}} & \dfrac{\partial \eta}{\partial f_{y'}} \end{bmatrix} = \cos\theta + \sin\theta\dfrac{f_{x'}}{f_{z'}}. \quad (11)$$

Thus, the corrected complex amplitude of the field is written as

$$U''(x'', y'') = \iint \hat{U}'\left(\xi\left(f_{x'}, f_{y'}\right), \eta\left(f_{x'}, f_{y'}\right)\right) \times \\ \exp\left[j2\pi\left(f_{x'}x', + f_{y'}y'\right)\right]\left|J\left(f_{x'}, f_{y'}\right)\right|df_{x'}df_{y'}. \quad (12)$$

When the calculation for fast Fourier transform is processed, the sampling points need to be on an equidistant grid. Thus, the complex value of the spectrum $U'(f_{x'}, f_{y'})$ can be obtained by even sampling to $\hat{U}'(f_{x'}, f_{y'})$. As the complex value of the spectrum must be sampled on an equidistant grid, the bi-cubic interpolation operation needs to be applied here. The sampling interval of the rotated plane needs to satisfy the inequation of $\Delta x'' > \lambda/(2\cos\theta)$ [27], where $\Delta x''$ is the pixel pitch in the corrected image plane and is equal to $\Delta x'$. Coordinate rotation with uniform sampling and interpolation will eventually give a correct wave field at the rotated plane.

Experimental Setup

The schematic of the experimental setup of the RLF-TDH is depicted in **Figure 3**. In the configuration, an optically pumped far-infrared gas laser (295 FIR, Edinburgh Instruments, 2.52 THz) was used as a coherent light source. The laser emitted a CW THz beam at a wavelength of 118.83 μm with

the maximum output power of 500 mW. The beam size was expanded to 22 mm by a pair of gold-coated off-axis parabolic mirrors (PM$_1$ and PM$_2$). The collimated beam was divided into two parts using a HRFZ-Si beam splitter, whose splitting ratio at 2.52 THz was 54% for transmission and 46% for reflection. The reflected beam was reflected by a gold-coated concave mirror with a focal length of 100 mm for constituting a diverging spherical reference beam. The gold-coated concave mirror used here could offer more than 99% reflection of the THz wave; thus, the loss of the THz radiation can be significantly minimized compared by using a pinhole or lens. The transmitted beam was reflected by the surface of the object with an incidence angle of approximate 45° measured by a protractor. The sample was mounted on a precision rotary stage in order to capture the direct reflected intensity by using the camera. The reference point source and the object were located at the same plane. The tilted object beam interfered with the spherical reference beam at the recording plane to form a lensless Fourier-transform hologram, which was recorded by a pyroelectric array detector (Pyrocam-IV, Ophir Spiricon), whose pixel pitch was 80×80 μm and featuring 320×320 pixels. The off-axis angle between the object beam and the spherical reference beam was approximately 38°, which enabled the zero-order term and the twin image to be separated in

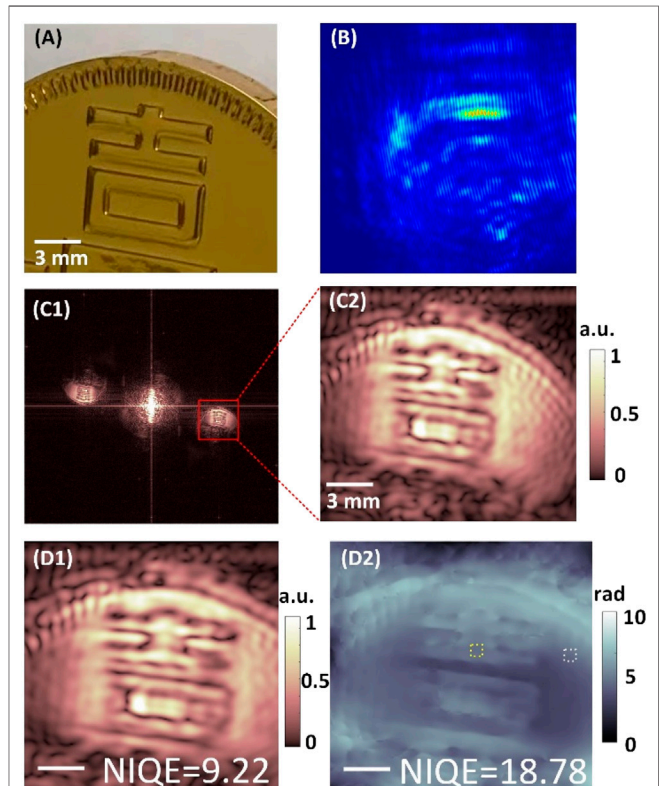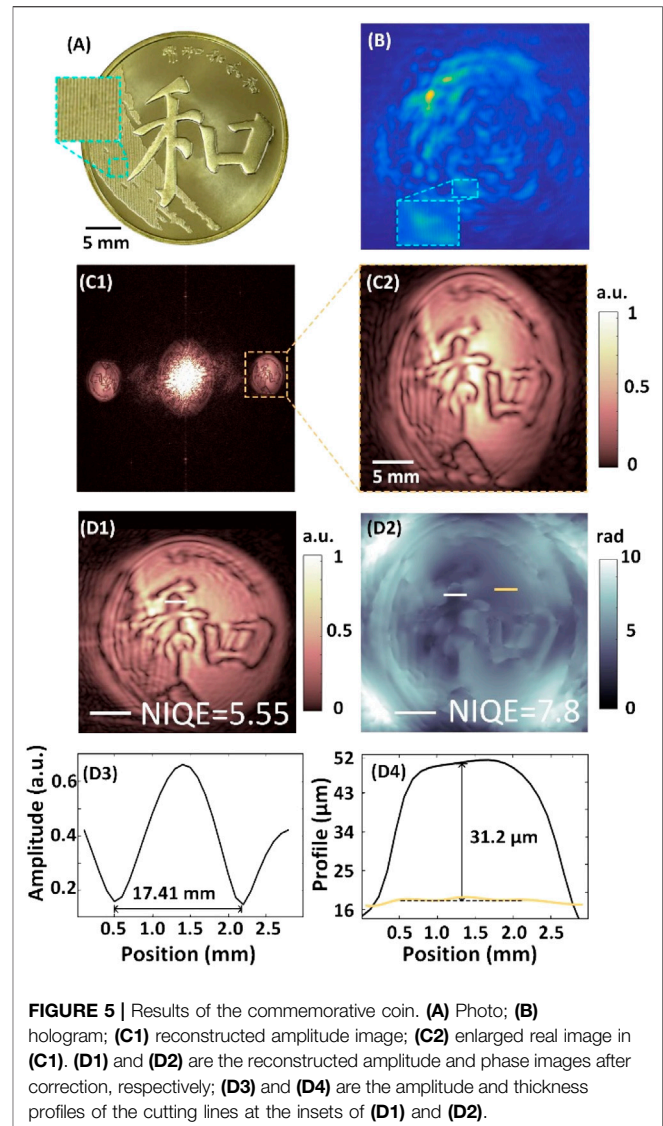**FIGURE 4 |** Reconstruction results of the gold-coated tinfoil sample. **(A)** Picture of the illuminated area of the object; **(B)** and **(C1)** are the digital hologram and reconstructed amplitude image; **(C2)** is the zoomed area of the +1 order in **(C1)**; **(D1)** is the reconstructed amplitude map after tilted plane correction; **(D2)** is the reconstructed unwrapped, aberration-free and corrected phase image.

the Fourier spectrum domain. In this case, the spatial frequency of fringe pattern was satisfied the Nyquist criterion and avoided the risk of undersampling. The chopping frequency of the detector was 50 Hz. To enhance the signal to noise ratio of the diffraction patterns, 500 frames were recorded at each position and accumulated via Gaussian fitting [28].

Experimental Results and Discussion

Two different samples were measured in order to test the performance and resolution of the proposed RLF-TDH setup. The first adopted object is a gold-coated tinfoil; a Chinese character "Ji" was impressed in a convex manner on its surface as shown in **Figure 4A**. The etching depth of the Chinese character is approximately 200 μm as measured by a vernier caliper. It was placed at a distance of 92.0 mm upstream from the detector. The theoretical lateral resolution of the imaging system is $\Delta x'' = 427.04$ μm. It is worth noting that the object plane and the recording plane are not parallel, as shown in **Figure 3**. The sample is obliquely positioned to ensure the reflected laser beam being recorded by the detector. The hologram with high-contrast interference fringes is shown in **Figure 4B**. The reconstructed amplitude distribution is shown in **Figure 4C1**. **Figure 4C2** is the zoomed area of the +1 order in **Figure 4C1**, and the Chinese character can be visually distinguished. It is noted that significant noise is introduced by the inclined plane, which is the object plane is not parallel to the recorded plane. Then, the tilted plane correction is applied, and the corrected amplitude distribution of the object is shown in **Figure 4D1**. Because the tinfoil sample cannot be supported well, its surface is not so plain. Thus, the effect of the tilted plane correction approach does not work very well for this sample. **Figure 4D2** shows the regular distribution of patterns on the specimen's surface under the unwrapping, eliminating aberration and correction, in which phase values correspond to different height distributions. Two regions are chosen to represent the object phase and the background phase, which are denoted by yellow and white dashed frame in **Figure 4D2**, respectively. Based on the average phase values of 30.84 and 13.44 rad of two corresponding regions, the relative etching depth of Chinese character can be accessed as 215 μm by **Eq. (7)**. Because the edge's surface of the handicraft is etched with texture, the reconstruction quality is decreased compared with the other areas. In order to quantitatively evaluate the quality of the reconstructed results, the Natural Image Quality Evaluator (NIQE) parameter [29] is adopted. It is a blind image quality assessment model that only makes use of measurable deviations from statistical regularities observed in natural images, without training on human-rated distorted images and indeed without any exposure to distorted images. The lower NIQE values represent better reconstruction quality. The NIQE values of our reconstructed results are similar to those of the off-axis Fresnel THz reflective digital holography system in Ref. 12 and better than that of the THz reflective ptychography system in Ref. 10. Besides, the computational time for the complete reconstruction of recording hologram, on a desktop PC with 3.4 GHz i5-7,500, 8 GB RAM, and R2016B MATLAB, is approximately 0.187 s, which is nearly real time.

FIGURE 5 | Results of the commemorative coin. **(A)** Photo; **(B)** hologram; **(C1)** reconstructed amplitude image; **(C2)** enlarged real image in **(C1)**. **(D1)** and **(D2)** are the reconstructed amplitude and phase images after correction, respectively; **(D3)** and **(D4)** are the amplitude and thickness profiles of the cutting lines at the insets of **(D1)** and **(D2)**.

Another investigated sample is a commemorative coin made of yellow copper alloy with a diameter of 30 mm, as depicted in **Figure 5A**. On the surface of the coin, the main pattern is a Chinese character "He" with a regular script style, and there are many grooves, as shown in the square dashed-line regions. The depth of the Chinese character was measured by a vernier caliper as 30 μm. **Figure 5B** shows the digital hologram of the coin, and the period of the resulting interference fringe is approximately 5.31 lp/mm in the zoomed region. The reconstructed amplitude distribution and enlarged image of the coin are shown in **Figure 5C1** and **Figure 5C2**, respectively. The shape aberration with the elliptic outline along the horizontal direction is caused by only a small portion of the illuminated area at the object plane and is in focus. Thus, the tilted plane correction is needed. In order to determine the angle θ accurately, the aspect ratio parameter is introduced to quantitatively evaluate the shape of sample, and the original value of the Chinese character "口" is 1.31. After tilted plane correction introduced

above, the reconstructed amplitude distribution and the unwrapped, aberration-free phase distribution are shown in **Figure 5D1** and **Figure 5D2**. It is clearly seen that the reconstructed results are stretched along the x-axis and closer to the real distributions at the object plane. At this time, the length–width ratios of the Chinese character "口" are 1.02 and 1.33 before and after the tilted plane correction, respectively, and the rotation angle and the sampling interval are calculated as 40° and 77.6 μm. In this case, $\Delta x''$ (427.04 μm) is larger than $\lambda/(2\cos\theta)$ (77.6 μm). It verifies the feasibility of the correction of the tilted illumination approach. However, there are still some residual aberration and out-of-focus in the reconstructed results. That is because the correction of tilted illumination could work well when the tilted angle is small and the field of view is also small. Besides, the etching depth of some areas of the engraved metal samples we use is relatively large, which makes part of the illumination beam unable to be reflected to the recording plane. It results in the dark area of the reconstructed images, especially near the border of the Chinese character. **Figure 5D3** and **Figure 5D4** show the amplitude and phase distribution curves taken along the white dotted lines shown in **Figure 5D1** and **Figure 5D2**. In order to verify the measurement effective of the proposed method, the white and yellow lines are drawn in **Figure 5D2**, representing the "He" stroke and background, whose phase values are 3.32 and 5.17 rad, respectively. Thus, the calculated etching depth of the selected part of the Chinese character is 31.5 μm.

CONCLUSION

In this article, we have implemented a reflective lensless Fourier-transform TDH (RLF-TDH) imaging configuration based on tilted illumination. The proposed method has compact configuration and high utilization rate of the energy, which is suitable for the reflective samples. Compared with other TDHs in reflection imaging methods, the spherical reference beam, generated by a concave mirror, guarantees the almost similar intensity with the object beam. It avoids the occasion that the intensity of THz radiation is weakened by a pinhole or the lens with high absorptivity, for example, polyethylene lens. At the same time, the numerical reconstruction of RLF-TDH requires only a single inverse Fourier transform. Thus, the speed of reconstruction is obviously accelerated; thus, it is very possible to achieve real-time imaging. Because of its oblique illumination geometry, a frequency spectrum coordinate transformation method is used for correcting the complex amplitude of the object wavefront at the tilted image plane. The proposed method is verified by two reflective samples. The first detected sample has a relatively rough surface than the second sample; thus, the restructured results are not as good as that of the coin. The proposed imaging configuration has great potential to open new opportunities toward applications in material characterization and dynamic nondestructive testing. Besides, this useful and emerging imaging technology can be applied to coherent diffraction imaging field in other wave bands.

DATA AVAILABILITY STATEMENT

The raw data supporting the conclusion of this article will be made available by the authors, without undue reservation.

AUTHOR CONTRIBUTIONS

JZ and DW supervised the project and funding acquisition. YZ designed and built the setup, performed experiments and wrote the draft of the manuscript. JZ, KL, LR, and YW contributed to data analysis. JZ and DW reviewed and edited of the manuscript; All authors have read and agreed to the published version of the manuscript.

FUNDING

REFERENCES

1. Zhang Y, Wang C, Huai B, Wang S, Zhang Y, Wang D, et al.Continuous-Wave THz Imaging for Biomedical Samples. *Appl Sci* (2021) 11:71. doi:10.3390/app11010071

2. Lee ES, Kim M, Moon K, Lee IM, Park DW, Shin JH, et al.High-Speed and Cost-Effective Reflective Terahertz Imaging System Using a Novel 2D Beam Scanner. *J Lightwave Technol* (2020) 38:4237–43. doi:10.1109/JLT.2020.2988890

3. Taylor ZD, Singh RS, Culjat MO, Suen JY, Grundfest WS, Lee H, et al.Reflective Terahertz Imaging of Porcine Skin burns. *Opt Lett* (2008) 33:1258–60. doi:10.1364/ol.33.001258

4. Zhong H, Redo-Sanchez A, Zhang XC. Identification and Classification of Chemicals Using Terahertz Reflective Spectroscopic Focal-Plane Imaging System. *Opt Express* (2006) 14:9130–41. doi:10.1364/oe.14.009130

5. Lee Y. *Principles of Terahertz Science and Technology*. New York, US: Springer (2009). p. 1–56.

6. Jiang Z, Xu XG, Zhang XC. Improvement of Terahertz Imaging with a Dynamic Subtraction Technique. *Appl Opt* (2000) 39:2982–7. doi:10.1364/ao.39.002982

7. Li Q, Zhou Y, Yang YF, Chen GH. 252 Terahertz Dual-axis Reflection Confocal Scanning Microscope. *J Opt Soc Am A* (2016) 33:637–41. doi:10.1364/josaa.33.000637

8. Wienold M, Hagelschuer T, Rothbart N, Schrottke L, Biermann K, Grahn HT, et al.Real-time Terahertz Imaging through Self-Mixing in a Quantum-cascade Laser. *Appl Phys Lett* (2016) 109:11102–5. doi:10.1063/1.4955405

9. Löffler T, May T, am Weg C, Alcin A, Hils B, Roskos HG. Continuous-wave Terahertz Imaging with a Hybrid System. *Appl Phys Lett* (2007) 90:91111–3. doi:10.1063/1.2711183

10. Rong L, Tang C, Zhao Y, Tan F, Wang Y, Zhao J, et al.Continuous-wave Terahertz Reflective Ptychography by Oblique Illumination. *Opt Lett* (2020) 45:4412–5. doi:10.1364/ol.400506

11. Valzania L, Zolliker P, Hack E. Topography of Hidden Objects Using THz Digital Holography with Multi-Beam Interferences. *Opt Express* (2017) 25:11038–47. doi:10.1364/oe.25.011038

12. Wang D, Zhao Y, Rong L, Wan M, Shi X, Wang Y, et al.Expanding the Field-Of-View and Profile Measurement of Covered Objects in Continuous-Wave Terahertz Reflective Digital Holography. *Opt Eng* (2019) 58:1–023115. doi:10.1117/1.OE.58.2.023111

13. Petrov NV, Perraud JB, Chopard A, Guillet JP, Smolyanskaya OA, Mounaix P. Terahertz Phase Retrieval Imaging in Reflection. *Opt Lett* (2020) 45:4168–71. doi:10.1364/ol.397935

14. Locatelli M, Ravaro M, Bartalini S, Consolino L, Vitiello MS, Cicchi R, et al.Real-time Terahertz Digital Holography with a Quantum cascade Laser. *Sci Rep* (2015) 5:13566. doi:10.1038/srep13566

15. Zolliker P, Hack E. THz Holography in Reflection Using a High Resolution Microbolometer Array. *Opt Express* (2015) 23:10957–67. doi:10.1364/oe.23.010957

16. Wagner C, Seebacher S, Osten W, Jüptner W. Digital Recording and Numerical Reconstruction of Lensless Fourier Holograms in Optical Metrology. *Appl Opt* (1999) 38:4812–20. doi:10.1364/ao.38.004812

17. Dong J, Jia S, Jiang C. Surface Shape Measurement by Multi-Illumination Lensless Fourier Transform Digital Holographic Interferometry. *Opt Commun* (2017) 402:91–6. doi:10.1016/j.optcom.2017.05.051

18. Yamagiwa M, Minamikawa T, Minamiji F, Mizuno T, Tokizane Y, Oe R, et al.Visualization of Internal Structure and Internal Stress in Visibly Opaque Objects Using Full-Field Phase-Shifting Terahertz Digital Holography. *Opt Express* (2019) 27:33854–3368. doi:10.1364/oe.27.033854

19. Kumar M, Shakher C. Experimental Characterization of the Hygroscopic Properties of wood during Convective Drying Using Digital Holographic Interferometry. *Appl Opt* (2016) 55:960–8. doi:10.1364/ao.55.000960

20. Tadesse GK, Eschen W, Klas R, Hilbert V, Schelle D, Nathanael A, et al.High Resolution XUV Fourier Transform Holography on a Table Top. *Sci Rep* (2018) 8:8677. doi:10.1038/s41598-018-27030-y

21. Guehrs E, Günther CM, Könnecke R, Pfau B, Eisebitt S. Holographic Soft X-ray Omni-Microscopy of Biological Specimens. *Opt Express* (2009) 17:6710–20. doi:10.1364/oe.17.006710

22. Goodman JW. *Introduction to Fourier Optics*. Colorado: Roberts and company publishers (2005). p. 491.

23. Pritt MD, Shipman JS. Least-squares Two-Dimensional Phase Unwrapping Using FFT's. *IEEE Trans Geosci Remote Sensing* (1994) 32:706–8. doi:10.1109/36.297989

24. Di J, Zhao J, Sun W, Jiang H, Yan X. Phase Aberration Compensation of Digital Holographic Microscopy Based on Least Squares Surface Fitting. *Opt Commun* (2009) 282:3873–7. doi:10.1016/j.optcom.2009.06.049

25. Matsushima K. Formulation of the Rotational Transformation of Wave fields and Their Application to Digital Holography. *Appl Opt* (2008) 47:D110–D116. doi:10.1364/ao.47.00d110

26. Matsushima K, Schimmel H, Wyrowski F. Fast Calculation Method for Optical Diffraction on Tilted Planes by Use of the Angular Spectrum of Plane Waves. *J Opt Soc Am A* (2003) 20:1755–62. doi:10.1364/JOSAA.20.001755

27. Kim Y-H, Kim GH, Ryu H, Chu H-Y, Hwang C-S. Exact Light Propagation between Rotated Planes Using Non-uniform Sampling and Angular Spectrum Method. *Opt Commun* (2015) 344:1–6. doi:10.1016/j.optcom.2015.01.029

28. Rong L, Latychevskaia T, Wang D, Zhou X, Huang H, Li Z, et al.Terahertz In-Line Digital Holography of Dragonfly Hindwing: Amplitude and Phase Reconstruction at Enhanced Resolution by Extrapolation. *Opt Express* (2014) 22:17236–45. doi:10.1364/oe.22.017236

29. Mittal A, Soundararajan R, Bovik AC. Making a "Completely Blind" Image Quality Analyzer. *IEEE Signal Process Lett* (2013) 20:209–12. doi:10.1109/LSP.2012.2227726

Conflict of Interest: The authors declare that the research was conducted in the absence of any commercial or financial relationships that could be construed as a potential conflict of interest.

Publisher's Note: All claims expressed in this article are solely those of the authors and do not necessarily represent those of their affiliated organizations, or those of the publisher, the editors and the reviewers. Any product that may be evaluated in this article, or claim that may be made by its manufacturer, is not guaranteed or endorsed by the publisher.

Digital In-Line Holography of Condensed-Phase Particles in Solid Rocket Motor Plume

Bingning Jin*, Hongbo Xu, Siying Yang, Xiaoyu Lei, Yaxin Ding and Peijin Liu*

Science and Technology on Combustion, Internal Flow and Thermo-Structure Laboratory, Northwestern Polytechnical University, Xi'an, China

Condensed phase particles (CCPs) of plume flows in solid rocket motors (SRMs) are one of the major causes of smog and other signal characteristics, which leads to attenuation of weapons guidance system signals. In order to study the dynamic combustion characteristics of the exhaust plume in a high pressure solid rocket motor with highly-aluminized propellanta digital in-line holographic (DIH) measurement system was used for identification and analysis of CCPs of exhaust plume flows in a SRM under 10 MPa pressure. During the SRM firing, the plume particles characteristic in the field of 9–11.5 cm away from the non-expanding nozzle outlet plane was measured and analyzed. Further, in order to improve the efficiency and accuracy of particle identification, a target recognition method suitable for autonomous recognition of plume particles in a complex background from digital holographic images was established. About 12,400 individual particles from two thousand holographic images were recognized, and the 3D spatial information (number and volume probability density function) and mean diameters were obtained and analyzed. The results showed that digital in-line holography measurement technology with target recognition method established in this paper can be applied well to real-time measurement of the 3D dynamic characteristics of the plume particle field anywhere outside of the nozzle outlet of an SRM with highly aluminized propellants. By identifying each reconstructed particle, the 3D spatial distribution, CCPs size distribution and velocity in the measurement area can be obtained.

Keywords: digital in-line holography, solid rocket motor, plume, condensed phase particles, deep learning

INTRODUCTION

Aluminum powder has been widely used as a metal additive in solid propellants for solid rocket motors (SRMs). The addition of aluminum powder can improve the specific impulse and damping high-frequency combustion instability [1, 2]. However, the aluminum powder leads to adverse effects because of the condensed phase particles of exhaust plumes flowing in a solid rocket motor, which are primary constituents of smoke and other infrared characteristic signals [3–5]. The size and concentration of smoke particles affect the penetrating ability of various optical signals and the diffusion speed of smoke, which leads to attenuation of the signal of the weapons guidance system. Therefore, in order to suppress the plume characteristic signal of the SRM, it is necessary to investigate the characteristics of the condensed combustion products (CCPs) of the plume flow in an SRM with used a highly aluminized propellant, and so as to deeply understand the mid-infrared radiation characteristics of the plume.
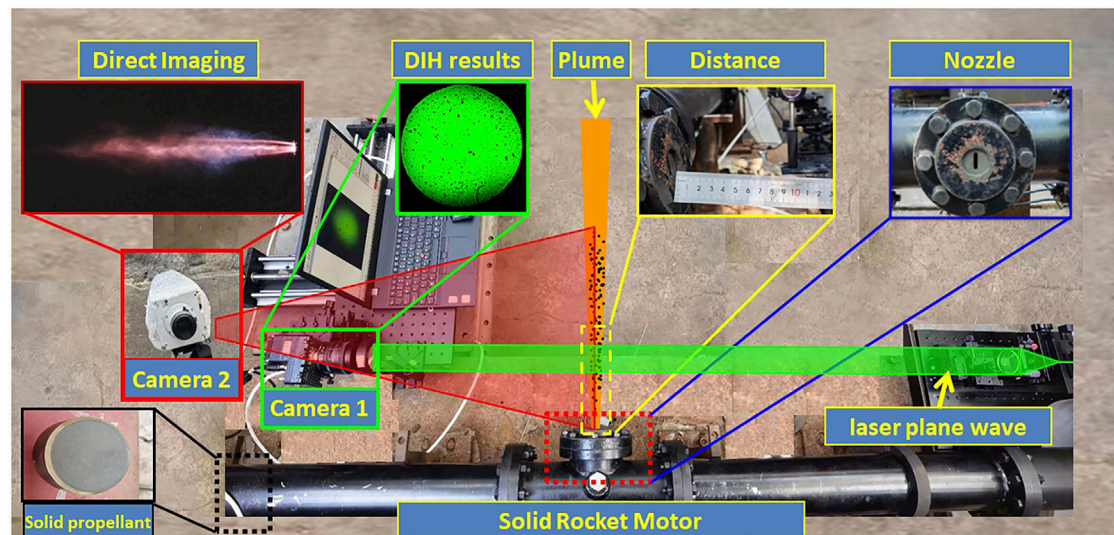
FIGURE 1 | Experimental system for DIH measurement of solid rocket plume flow field.

A lot of experimental research has been conducted on the characteristics of CCPs in plumes, such as the mechanical collection and optical measurement method [6–11]. The traditional particle collection method can reveal the particle size distribution of the condensed phase particles; however it modifies the flow field structure and particle state, resulting in a different actual plume state. Moreover, it does not provide information about the particle size, 3D spatial distribution, and dynamic process of the particles in the plume. In contrast to the collection method, imaging techniques are useful to obtain the CCP dynamic characteristics. However, the small focal depth, high pressure, high temperature, high velocity, and strong emission intensity of the traditional optical techniques limits dynamic CCP measurement. Only a few effective plume particles can be obtained in the focal plane, preventing accurate distribution sizes of the particle in the plume unless lots of experiments are performed.

To overcome these shortcomings, the digital in-line holography technique was used for imaging CCPs in the SRM plume in this study [12–15]. In this paper, holographic in-line technology was used to measure the plume particle characteristics in the field of the non-expanding 2D nozzle outlet plane and reconstruct the holographic image, and a target recognition method suitable for autonomous recognition of plume particles in a complex background from digital holographic images was established. About tens of thousands of individual particles from two thousand holographic images were recognized, and the 3D spatial information (number and volume probability density function) and mean diameters were obtained and analyzed. These results are expected to expand the knowledge on plume particle distribution characteristics in the SRM and also could provide a diagnostic technique for studying the plume dynamic characteristics at different nozzle sections during the SRM firing.

METHODS

Digital In-Line Holography System

The experimental system for the digital in-line holographic (DIH) measurement of a solid rocket plume flow field constitutes four components: an SRM, microscopic imaging system, pressure recording device, and DIH system (**Figure 1**). An AP/RDX/HTPB composite propellant sample containing 18% aluminum was placed at both ends of the SRM chamber and ignited by heating a wire. The nozzle without the divergent section placed at the center of the chamber. In order to ensure that the particle concentration of the plume field is not too high, the thickness of the plume field perpendicular to the laser path direction needs to be thin. Therefore, under the 10 MPa pressure condition in the SRM, the thickness of 2D nozzle throat is 2 mm, as shown in **Figure 1**. When the SRM fires, the product gas exhaust flow from both ends of the motor converges at the middle, passed through the convergence section, escapes from the nozzle throat, and forms a plume flowfield outside the nozzle. A pressure measuring device was used to collect the pressure data.

To obtain information pertaining to the plume flow field particles, two high-speed cameras were used: Camera 1 (Micro C110) for DIH system and Camera 2 for microscopic imaging. Due to the radiation light, influence of the plume field was weak near 532 nm, the wavelength of the incoming laser light. A narrow optical bandpass 532 ± 10 nm notch filter was used to reduce the broadband emission from aluminum particles while approximately capturing the entire laser light. The typically size of particles in plumes ranges between 10^0–10^2 microns, requiring long-distance microscopic lenses to obtain the particle image. However, the high-temperature radiation from the plume field (approximately 2500 K) affects the imaging system. The position of the camera should be sufficiently far from the measurement area at approximately 1 M distance. Thus, a 0.5× (approximate)
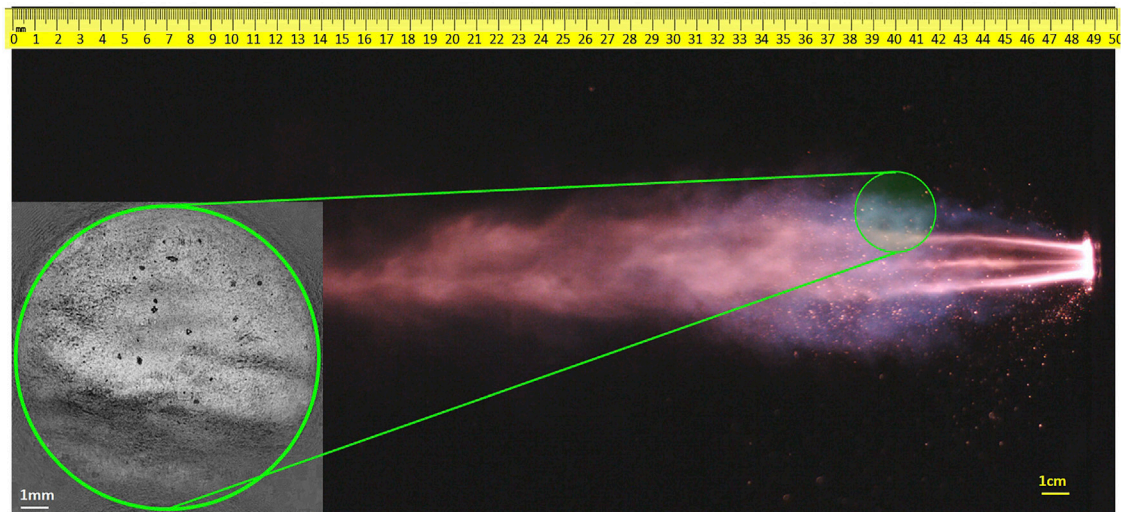
FIGURE 2 | Typical image results of SRM plume field.

magnification system was used together with Camera 1, resulting in an actual pixel size of approximately 30 × 30 μm, which covered a large fraction of plume particles. The holographic measurement area was approximately 26 × 26 mm^2, and its center was approximately 10 cm away from the nozzle outlet plane. The camera was operated at 1,000 fps, with an exposure time of 5 μs Camera 2 (EVO 640) was used to image the entire plume flow field and obtain its dynamic characteristics. Camera 2 was operated at 2000 fps at an exposure time of 1 μs When the plume particles directly escaped from the throat, without accelerated through the expansion section, the particles could slowly down. According to the measured results, the observed plume particles velocity is rang of 200–700 m/s, and there no obvious motion blurring phenomenon in the results of two cameras. The plume image results are show in **Figure 2**. The holographic field is higher than the central area, the upper part of the holographic field was less disturbed by the exhaust gas flow, and a large amount of diffraction information of plume particles can be obtained. However, the lower part of the holographic field of view is strongly affected by high density exhaust gas flow and the laser could not pass through it, so clear holographic information of particles could not be obtained.

Numerical Reconstruction and Target Recognition Method

The DIH measurement process consists of two steps: hologram recording and reconstruction. In this study, a planar light wave travelling across the plume flow field was recorded using a CCD, which obtained the original holographic image of the plume field particle. After denoising the original holographic image, and the final holographic image was reconstructed through the angle spectrum method. When the reconstructed and imaging distances are equal, the complex light field amplitude of the object can be obtained. Based on the spatial distribution range

and particle size distribution range of the plume flowfield, a sufficient z-axis depth (Δz) was set to approximately 25 μm. To obtain a locally-focused hologram at different Z-axis positions and 4,000 slices were reconstructed across a distance of approximately 0 ≤ z ≤ 100 mm from the focal plane. By using the depth-of-field extension method, all the particles in a series of plane images were focalized in a single synthesis image that is in a single-frame hologram.

To obtain all plume information during motor operation, all hologram images should be processed. The effective working time of the SRM was about 2 s, and 2000 original DIH images were obtained in the test. The depth of field range of holographic measurement method is much larger than that of the microscopic imaging method, so the number of reconstructed holographic particles is much larger, corresponding to tens of thousands of particles, and hundreds of particles respectively. Therefore, the traditional target detection method of manual identification and positioning is very time-consuming and inefficient to extract all particle information from all holograms in the whole experiment process, which greatly restricts the rapid and accurate application of holographic technology. Therefore, to improve the post-processing efficiency and accuracy of this process, this study established a target recognition method suitable for autonomous recognition of solid propellant aluminum combustion particles in a complex background from digital holographic images [16].

First, 500 effectively reconstructed holographic images were selected for plume particle labeling, and a total of 20,000 independent sample particles with particle size distribution ranging from 65 to 900 microns were labeled, forming a relatively rich plume particle information data set.

Second, the data set is divided into training, verification and test sets in a 6:2:2 ratios. Considering that the object of target recognition is a plume holographic particle, which has the characteristics of large flow, fast speed, loud noise and complex background, this paper selects the YOLO V3 model,
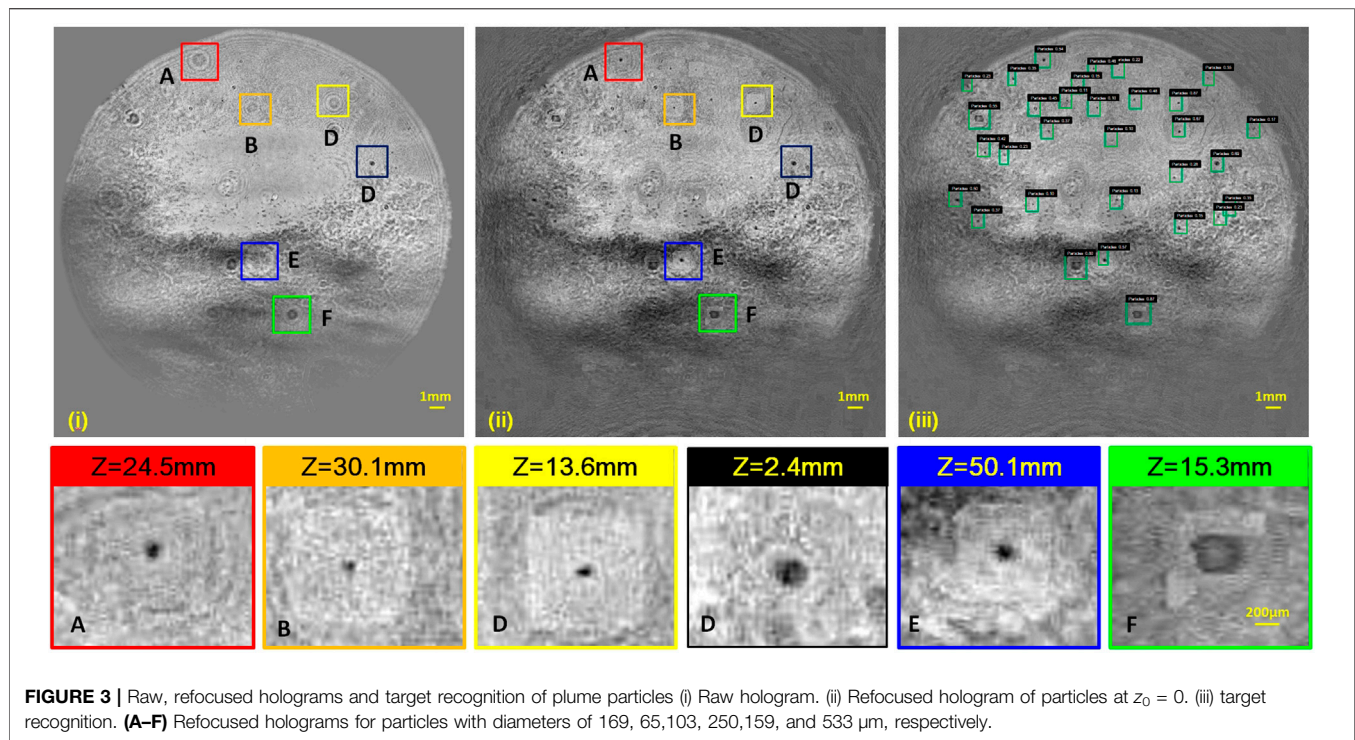
FIGURE 3 | Raw, refocused holograms and target recognition of plume particles (i) Raw hologram. (ii) Refocused hologram of particles at $z_0 = 0$. (iii) target recognition. **(A–F)** Refocused holograms for particles with diameters of 169, 65,103, 250,159, and 533 μm, respectively.

which has good detection accuracy and detection speed in small target recognition, and as the main frame. The YOLO V3 target recognition model is trained with the data of the training set, and a training model which can effectively recognize digital holographic image particles is obtained.

Third, train the model with the training sets, and verify the trained model with verification sets. The confidence threshold was set to 0.6, and for single holographic images the prediction process was about 65 ms. In **Figure 3iii** the discrete single particle image shows good identification of particles (marked by the green bounding box), with an average accuracy of about 0.85. The result shows that the model training meets the needs of target detection of holographic plume particles.

Finally, the model was used to detect the other unlabeled holographic images, and about 12,000 effective particles were identified. The granularity and coordinate information of all identified particles were obtained by the watershed segmentation algorithm, allowing information of all holographic plume particles in the whole experiment measurement to be obtained.

RESULTS

Typical Digital In-Line Holographic Results

Figure 3i shows typical holograms recorded in the SRM plume flowfield. Because the shape of holographic field of view is limited by the laser source, the central circular region is the holographic diffraction region. The hologram was reconstructed and refocused in the Z-direction to obtain the information about the shape and granularity of the particles in the 3D plume flow

field. Approximately 25–30 particles in the entire 3D space were projected onto the image at the z = 0 plane, as shown in **Figure 3ii**. A large fraction of the particles were observed to be spherical, whereas a small fraction showed irregular shapes. None of the particles showed a visible flame configuration. Therefore, it is believed that all the particles are condensed combustion products (CCPs).

Figure 3iii shows a typical result of the target recognition of the plume particles in the green bounding box from **Figure 2**. For particles with small background interference and large particle size, the recognition accuracy is higher with a mAP value above 0.9. In contrast, the accuracy of model recognition is lower for particles with smaller particle size and larger background influence, with a mAP value around 0.4. Of course, the model also exhibits phenomena such as missing recognition and wrong recognition. Therefore, in order to ensure the accuracy of analysis results, particles with a confidence rate above 0.6 were counted as effective particles.

Figure 3ii shows several typical fine particles in the plume field. **Figure 3ii,A** shows a particle with a diameter D = 169 μm (approximately), and z = 24.5 mm. The particles are spherical, large, and long distance from the focal plane. Therefore, the diffraction aperture in the hologram image is clearly visible. There is no flame edge surrounding the particle, indicating that the particles are condensed combustion products (CCPs) and have complete burning out.

Limited by the imaging magnification and pixel size of Camera 1, **Figure 3ii,B** shows the smallest viewable particle of diameter D = 65 μm (approximately) and z = 30.1 mm, which also is the smallest particle obtained by visual real-time dynamic measurement in the plume particle field. The particle sizes in
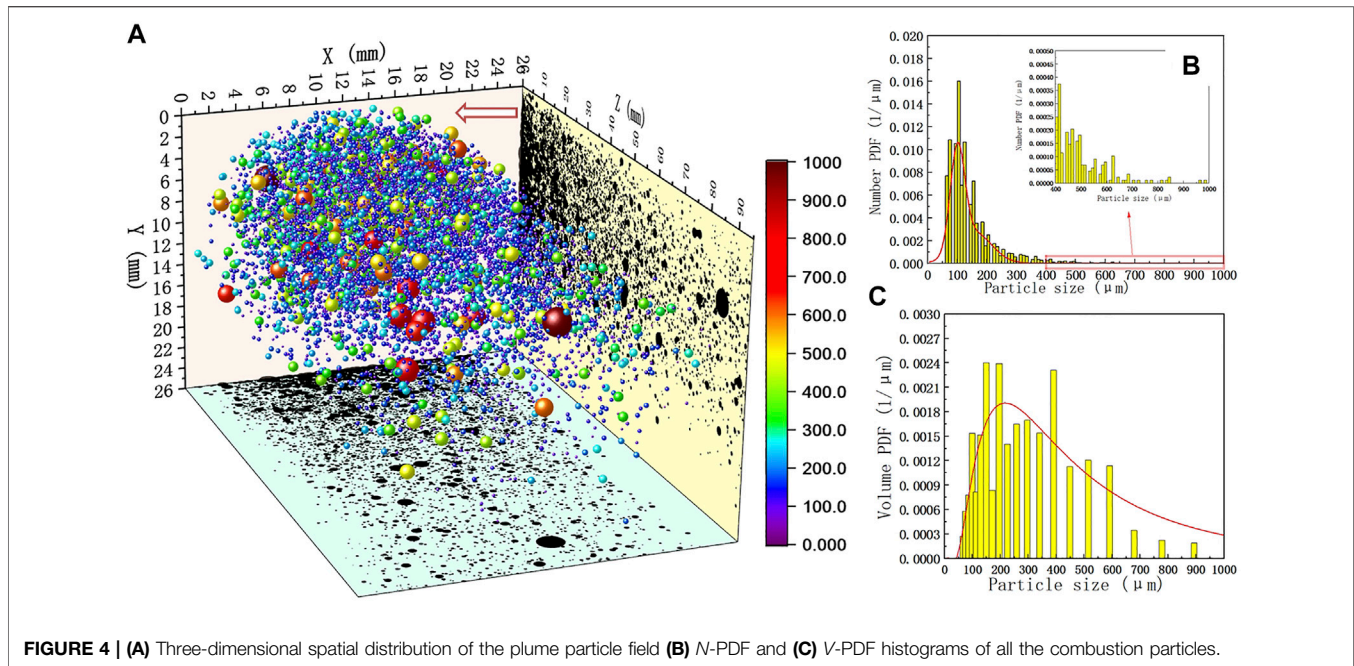
FIGURE 4 | (A) Three-dimensional spatial distribution of the plume particle field **(B)** N-PDF and **(C)** V-PDF histograms of all the combustion particles.

Figure 3ii,C are larger (about 103 um) than those in **Figure 3ii,B**, based on obvious diffraction stripes, and the reconstructed particle is approximately 13.6 mm away from the focal plane. Many particles of this size were observed from the reconstructed image.

Figure 3ii,D shows a large particle of diameter D = 250 μm (approximately). This size accounts for a large proportion of the condensed combustion products and is common in condensate product collection reports. During combustion in the SRM, as the propellant combustion surface regresses, the embedded virgin aluminum particles (diameter = 30 μm) melt, accumulate, and merge in the vicinity of the burning surface, finally forming agglomerated particles of the order of 10^2 μm. These particles ignite and burn rapidly in the vicinity of the combustion surface, move to the nozzle along the flow field, and finally escape from the nozzle to form plume particles. Compared with the original holographic image, the diffraction information of the particle is weak and the particle edge is clear, so it can be considered that the particles are near the focal plane. The reconstructed distance Z value = 2.4 mm confirms this result.

The particle size in **Figure 3iii,E** is approximately equal to that in **Figure 3A** (169 μm). However, the spatial location was different, resulting in different sizes of the original holographic diffraction fringes. The diffraction fringe is large because the distance between the specific focal plane and the particle was large (50 mm approximately).

The particle size in **Figure 3iii,F** is large, approximately 533 μm. Although the particle size is larger, it is close to the defocus plane (z = 15 mm), so the diffraction aperture in the original hologram is smaller. It can be seen from the field of view that the number of particles at this scale is relatively low, which is consistent with the actual particle size distribution of CCPs in SRMs.

Particles Distribution

The number and volume probability density function (N-PDF and V-PDF, respectively) methods (based on the particle diameter information) were used to analyze the particle size distribution. The N-PDF and V-PDF can respectively be expressed as follows [17, 18].

$$N_0 = \frac{N}{\sum N \times \Delta d} \tag{1}$$

$$V = \frac{N \times d^3}{\sum (N \times d^3) \times \Delta d} \tag{2}$$

The normal Gaussian distributions were fitted for the N-PDFs, and lognormal Gaussian distributions were fitted for the V-PDFs, as provided in **Eqs 1**, **2**, respectively:

$$f(D)_{Number} = \sum_{i=1}^{n} \frac{w_i}{\sigma_i \sqrt{\pi/2}} e^{-\frac{(D-\mu_i)^2}{\sigma_i^2}} \tag{3}$$

$$f(D)_{Volume} = \sum_{i=1}^{n} \frac{w_i}{D\sigma_i \sqrt{2\pi}} e^{-\frac{(lnD-\mu_i)^2}{2\sigma_i^2}} \tag{4}$$

where w is the relative weight, σ is the standard deviation on the natural log scale, μ is the mean on the natural log scale, and i denotes different aluminum particles.

Two thousand holograms were reconstructed, refused, and identified through this analysis method. Almost 12,400 particles in the holographic images were observed to be unique and non-repeating, and the X, Y, Z, and D, of each particle were obtained. **Figure 4A** shows the three-dimensional spatial distribution of the plume particle field at 10 cm distance from the throat outlet plane of the SRM. The plane projection on the Y-Z plane in **Figure 4A** shows a large fraction of large particle (200–800 μm) concentration in the 0–3 mm region, which is the center of

the plume field. The small particles were distributed throughout the 0–10 mm region. The particle density along the Z-direction decreases gradually with increasing distance, accompanied by a small number of large particles.

The *N*-pdf and *V*-PDF analyses were performed on all particles (**Figure 4B,C**). The particle size distribution showed a single peak, and the fraction of particles between the size of 60–150 μm was large (70%). The fraction of particles with a diameter larger than 400 μm was small. Based on the particle diameter, the mean diameters of all the particles in the 3D plume fields were obtained. The D32 = 188.4 μm, and D43 = 280.4 μm (approximately). The mean diameter D50 = 241.1 μm.

Limited by the imaging magnification (×0.1) and pixel size (~10 um) of Camera 2, the minimum discernible particle size in plume photography results is about 200 um. Based on the X,Y information of each particle their 2D velocity can be obtained. The statistical results show that the particle size distribution for 200–900 um particles with velocity of 200–700 m/s. This also explains why the three-dimensional velocity results of particles cannot be obtained from the hologram in this study under the limited sampling rate.

In the future, this method will be used to obtain the plume characteristic under different pressure in the SRM, and more research on the plume particles near the throat.

DISCUSSION

In this study, a digital holographic measurement system for the identification of condensed-phase particles of an exhaust plume flow in a solid rocket motor (SRM) was developed, which used an aluminized AP/HTPB composite propellant. During the SRM combustion at 10 MPa pressure, the plume particle characteristics in the field of 9–11.5 cm away from the non-expanding 2D nozzle outlet plane was measured and analyzed. In order to improve the efficiency and accuracy of particle identification, a target recognition method suitable for the autonomous recognition of plume particles in a complex background from digital holographic images were established for identification particle

size and spatial location of all particles in the plume field. The 3D spatial information (*N*-PDF, and *V*-PDF) and mean diameters were obtained and analyzed. The obtained results were as follows.

1. The target recognition method established in this paper can effectively distinguish particles in the plume flow with diameter in the range 50–1,000 μm, with measurement error <5%.
2. About 12,400 individual particles from two thousand holographic images were recognized. Particles size distribution from 65 um to 900 um, 3D spatial information (*N*-PDF, and *V*-PDF), and mean diameters were obtained and analyzed.
3. The DIH measurement technology with target recognition method established in this paper can be applied well to real-time online measurement of the 3D dynamic characteristics of the plume particle field anywhere outside of the nozzle outlet of an SRM with highly aluminized propellants.

DATA AVAILABILITY STATEMENT

The original contributions presented in the study are included in the article/Supplementary Material, further inquiries can be directed to the corresponding authors.

AUTHOR CONTRIBUTIONS

Conceptualization, BJ; methodology, BJ; software, BJ, HX, and SY; validation, SY, YD, and XL; analysis, BJ and PL; data curation, BJ; writing—BJ; All authors have read and agreed to the published version of the manuscript.

FUNDING

REFERENCES

1. Blomshield FS. Lessons Learned in Solid Rocket Combustion Instability. AIAA Paper 2007-5803. In: 43rd AIAA/ASME/SAE/ASEE Joint Propulsion Conference & Exhibit; 8-11 July 2007; Cincinnati, OH (2007).
2. Ji S, Wang B, Zhao D. Numerical Analysis on Combustion Instabilities in End-Burning-Grain Solid Rocket Motors Utilizing Pressure-Coupled Response Functions. *Aerospace Sci Tech* (2020) 98:105701. doi:10.1016/j.ast.2020.105701
3. Ebrahimi HB, Levine J, Kawasaki A. Numerical Investigation of Twin-Nozzle Rocket Plume Phenomenology. *J Propulsion Power* (2000) 16(2):178–186. doi:10.2514/2.5572
4. Delong YAO, Song C. Study on TDLAS Measurement Method for Plume Velocity of Solid Rocket Motor. *J Appl Opt* (2020) 41(2):342–347. doi:10.5768/jao202041.0203001
5. Laredo D, McCrorie JI, Vaughn JK, Netzer DW. Motor and Plume Particle Size Measurements in Solid Propellant Micromotors. *J Propulsion Power* (1994) 10(3):410–418. doi:10.2514/3.23750
6. Liu H, Ao W, Liu P, Hu S, Lv X, Gou D, et al. Experimental Investigation on the Condensed Combustion Products of Aluminized GAP-based Propellants. *Aerospace Sci Tech* (2020) 97:105595. doi:10.1016/j.ast.2019.105595

7. Liu X, Wen A, Liu H, Liu P. Aluminum Agglomeration on Burning Surface of NEPE Propellants at 3–5 MPa. *Propellants, Explosives, Pyrotechnics* (2017) 42(3):260–268. doi:10.1002/prep.201600131
8. Glotov OG, Yagodnikov DA, Vorob'ev VS, Zarko VE, Simonenko VN. Ignition, Combustion, and Agglomeration of Encapsulated Aluminum Particles in a Composite Solid Propellant. II. Experimental Studies of Agglomeration. *Combust Explos Shock Waves* (2007) 43(3):320–333. doi:10.1007/s10573-007-0045-y
9. Glotov OG. Condensed Combustion Products of Aluminized Propellants. II. Evolution of Particles with Distance from the Burning Surface. *Combust Explos Shock Waves* (2000) 36(4):476–487. doi:10.1007/bf02699478
10. Cauty F, Erades C, Desse JM. Light Deviation Based Optical Techniques Applied to Solid Propellant Combustion. *Prog Propulsion Phys* (2011) 2:121–134. doi:10.1051/eucass/201102121
11. Devillers R, Nugue M, Tong ACH, Le Besnerais G, Pichillou J. *Experimental Analysis of Aluminum-Droplet Combustion in Solid-Propellant Conditions Using Deep Learning*. Madrid, Spain: EUCASS 2019 (2019).
12. Jin B-n., Wang Z-x., Xu G, Ao W, Liu P-j. Three-dimensional Spatial Distributions of Agglomerated Particles on and Near the Burning Surface of Aluminized Solid Propellant Using Morphological Digital In-Line

Holography. *Aerospace Sci Tech* (2020) 106:106066. doi:10.1016/j.ast.2020. 106066

13. Guildenbecher DR, Cooper MA, Sojka PE. High-Speed (20 kHz) Digital In-Line Holography for Transient Particle Tracking and Sizing in Multiphase Flows. *Appl Opt* (2016) 55(11):2892–903. doi:10.1364/AO.55.002892

14. Wu YC, Wu XC, Yang J, Zhihua W, Xiang G, Binwu Z, et al. Wavelet-based Depth-Of-Field Extension, Accurate Autofocusing, and Particle Pairing for Digital Inline Particle Holography. *Appl Opt* (2014) 53(4):556–564. doi:10. 1364/ao.53.000556

15. Wu Y, Wu X, Saengkaew S, Meunier-Guttin-Cluzel S, Chen L, Qiu K, et al. Digital Gabor and off-axis Particle Holography by Shaped Beams: A Numerical Investigation with GLMT. *Opt Commun* (2013) 305:247–254. doi:10.1016/j. optcom.2013.05.009

16. Huang R, Pedoeem J, Chen C. YOLO-LITE: a Real-Time Object Detection Algorithm Optimized for Non-GPU Computers. In: 2018 IEEE International Conference on Big Data (Big Data); Dec 10-13, 2018; Seattle, WA, USA. Piscataway, New Jersey, United States: IEEE (2018). p. 2503–2510.

17. Chen Y, Guildenbecher DR, Hoffmeister KNG, Cooper MA, Stauffacher HL, Oliver MS, et al. Study of Aluminum Particle Combustion in Solid Propellant Plumes Using Digital In-Line Holography and Imaging Pyrometry. *Combustion and Flame* (2017) 182:225–237. doi:10.1016/j.combustflame.2017.04.016

18. Powell MS, Gunduz IW, Shang W, Chen J, Son SF, Chen Y, et al. Agglomerate Sizing in Aluminized Propellants Using Digital Inline Holography and Traditional Diagnostics. *JOURNAL PROPULSION POWER* (2018) 34(4): 1002–1014. doi:10.2514/1.b36859

Single-Shot Common-Path Off-Axis Dual-Wavelength Digital Holographic Microscopy Based on Two-Dimensional Grating Diffraction

Jieyu Wang[1], Xue Wang[1,2]*, Zhao Dong[1,2]*, Huaying Wang[1,2]*, Qiaofen Zhu[1,2], Gaofu Men[1,2], Yafei Gao[3] and Wenjian Wang[1]

[1]School of Mathematics and Physics, Hebei University of Engineering, Handan, China, [2]Hebei Province Computational Optical Imaging and Photoelectric Detection Technology Innovation Center, Handan, China, [3]School of Management Engineering and Business, Hebei University of Engineering, Handan, China

We present a single-shot dual-wavelength common-path off-axis digital holographic microscopic (CO-DHM) imaging method based on two-dimensional grating diffraction. This method improves the utilization rate of the interference field under the limited photosensitive size of the camera, and further expands the original camera's field of view (FOV). In addition, the mode of orthogonal carrier frequencies close to the diagonal direction can optimize the utilization of the camera's spatial bandwidth. Compared with the traditional dual-wavelength CO-DHM using one-dimensional grating or prism beam splitting, this method effectively avoids the aliasing of high-frequency components of the +1-order spectrum of different wavelengths in the frequency domain. We provide quantitative phase imaging experiments for the full FOV of USAF resolution chart, onion epidermal cells and standard polystyrene beads. The results prove that the system can enlarge the interferometric FOV by nearly 74.0% without changing the imaging parameters, such as magnification and resolution, and can achieve high-precision quantitative phase imaging with only a single hologram.

Keywords: digital holographic microscopy, dual-wavelength, twodimensional grating, common-path, off-axis

INTRODUCTION

Digital holographic microscopy (DHM) combines traditional optical microscopy imaging technology and holographic imaging technology to quantitatively obtain the amplitude and phase distribution of the original object light in the field of microscopic imaging [1–6]. Digital holographic microscopy has the characteristics of no contact, no chemical damage, and three-dimensional dynamic imaging during the entire sample observation process. It has been widely used in life, medicine, environment, materials, manufacturing, microelectronics, and other fields [7–12]. Common-path off-axis digital holographic microscopy (CO-DHM) system based on grating diffraction, as a typical and simple DHM, can realize high-stability non-contact real-time dynamic monitoring of samples [13, 14]. The system uses a classic optical microscope and is equipped with an additional diffraction module [15–18]. The object-reference light interference pattern is obtained on the camera plane by using grating beam splitting and the diffraction field spectrum filter technology, and then the complex amplitude distribution of the object light field is reconstructed by a computer [19]. In this way, three-dimensional quantitative information of the sample is obtained [20].

Recently, CO-DHM has been adapted to many types of light sources. Researchers have improved the resolution and spatial phase sensitivity of the CO-DHM system by using broadband light sources and structured light sources [21, 22]. In 2014, Moham Reza Jafarfard et al proposed a dual-wavelength diffraction phase microscopy system to accurately measure the thickness and refractive index of samples [23]. In 2015, N.A. Talaikova et al. measured the refractive index of red blood cells using the dual-wavelength transmitted light and reflected light simultaneous irradiation mode [24]. In 2020, Manoj Kumar et al developed a dual-wavelength co-channel off-axis system based on prism splitting to measure the phase and refractive index of samples at one time [25]. However, the Fourier orders of different wavelengths in the spectrogram of the above schemes are in the same direction, and strict system parameter optimization is required to avoid aliasing of the high frequency components of the +1-order spectrum. If the selected area is too small during frequency domain filtering, High frequency components will be lost. To solve this problem, MIT Poorya Hosseini and others developed a dual-wavelength interference microscope in 2018, which provides single-lens off-axis interferometry by encoding two spectral images at orthogonal spatial frequencies, but the optical path uses two 4f systems [26]. The structure of the system is more complicated [27]. Behnam Tayebi et al developed a dual-pinhole dual-wavelength CO-DHM in 2018, which maximized the optimization of two arbitrary wavelengths and crosstalk-free two-dimensional sampling schemes [28]. Compared with the previous CO-DHM, the field of view was expanded, but the system adopted two Gratings and two pinholes, it brings higher requirements to the stability of the system.

The size of the CO-DHM system's field of view (FOV) is limited by two key factors: the size of the object reference light interference spot size and the camera's photosensitive size. In recent years, several methods have been proposed in the field of digital holography to increase the recording FOV without changing the size of the camera sensor or loss of imaging resolution. One of them is the spatial phase scanning digital holographic imaging technology, which scans the sample on a reference light field, periodically obtains multiple frames of sample phase images, and finally uses algorithms to combine them into a large field of view holographic image. However, this type of method sacrifices the time resolution or the range of the dynamic area allowed in the recorded image [29]. The other is the off-axis interferometric field of view multiplexing technology, which optically multiplexes two off-axis interferometric fields of view collected from different areas on the sample to a single camera sensor, which can realize wide-area dynamic imaging without loss of spatial resolution. However, the currently reported digital holographic microscopy optical paths using this technology require complex device design and use more optical devices [30].

To solve the above problems, we propose a dual-wavelength CO-DHM based on a two-dimensional diffraction grating. This system can multiplex two FOVs into a single off-axis interferogram without using special optical elements. And it also can obtain wider FOV imaging without losing time resolution. The two FOVs share the dynamic measurement

range of the camera and will not affect imaging parameters such as magnification and resolution. The interference area between the object light of two wavelengths and the reference beam is determined by the adjustable shearing distance that can be adjusted by controlling the axial position of the grating [31], and this distance determines the enlarged area of the field of view. Furthermore, the spatial bandwidth of the camera can be maximized by simply rotating the two-dimensional grating to form orthogonal carrier frequencies close to the diagonal direction. Quantitative phase imaging of samples can be achieved by placing the module as an additional unit on the exit port of the inverted microscope. To prove the high precision of the system, the large field of view quantitative phase imaging capability, the imaging results of the resolution plate, standard polystyrene beads and onion epidermal cell are provided.

EXPERIMENTS AND METHODS

System and Principle

Figure 1 shows the proposed experimental scheme of dual-wavelength CO-DHM based on two-dimensional gratings. The experiment uses a single longitudinal mode He-Ne laser ($\lambda_R = 632.8$ nm) and a semiconductor laser ($\lambda_G = 532$ nm) as the illumination source. The two beams of light are combined by the beam splitting prism (BS) and irradiate the sample (S) at the same time. Among them, the spatial filter (SF) plays a role in filtering out the high frequency noise of the laser and collimating and expanding the beam. The two-dimensional grating (G) is placed behind the image plane (IP) to generate different diffraction orders that carry sample information. The light beam is collimated by the tube lens (TL) into parallel light and incident on the grating. On this basis, a 4f imaging module is added to image the sample image to the camera plane. Then, for each wavelength component in the Fourier plane of the 4f system, the 0th order and +1 order diffracted lights are extracted in two mutually orthogonal directions using filters. The design of the filter (after rotating 45°) is shown in **Figure 1**. The strongest 0-order diffracted light passes through the pinhole on the spatial filter and becomes an ideal uniform spherical wave as the reference beam in interference. The weaker +1-order diffracted light passes through a larger spatial filter hole separately. The outgoing beam is used as the object light. To ensure better fringe contrast, an attenuator with a transmittance of 50% is placed behind the 0-level filter hole on the spectrum plane. Finally, the +1-order object beam with the complete information of the sample will interfere with the plane reference light on the imaging surface of the CCD sensor to generate two holograms which are captured and recorded by the CCD sensor at one time.

Since the beams of two wavelengths have the same propagation mode in this module and are independent of each other, after the beam is filtered by the Fourier plane spectrum (as shown in **Figure 2**), only the 0-order and +1-order light in a single direction can pass. For simplicity, we consider the light field distribution of a single wavelength in a one-dimensional plane. The transmittance function of a single
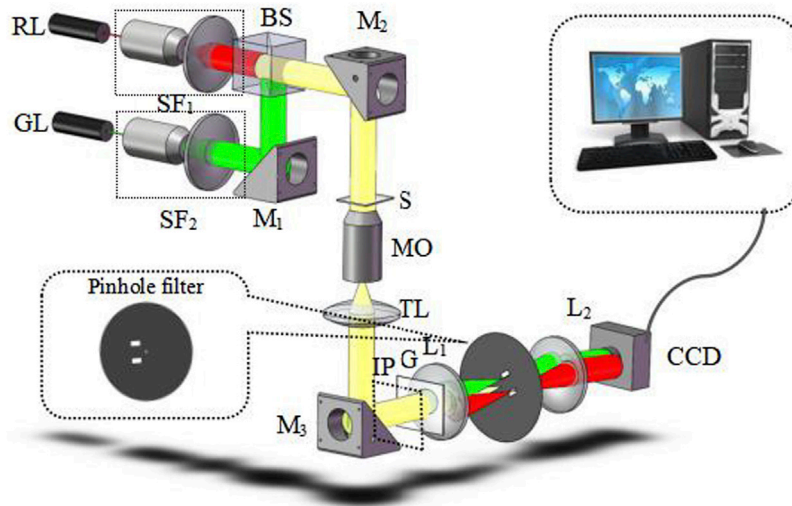
FIGURE 1 | Schematic setup of dual-wavelength CO-DHM. S, sample; SF, spatial filters. RL, red laser; GL, green laser; M, mirrors; MO, microscopy objective; TL, tube lens; G, two-dimensional grating; L, lens.
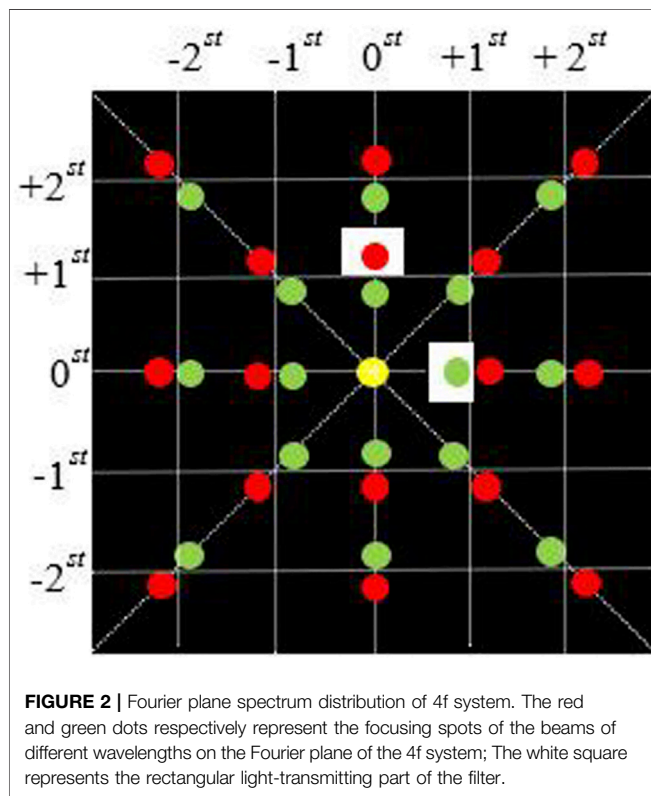

FIGURE 2 | Fourier plane spectrum distribution of 4f system. The red and green dots respectively represent the focusing spots of the beams of different wavelengths on the Fourier plane of the 4f system; The white square represents the rectangular light-transmitting part of the filter.

wavelength through a two-dimensional diffraction grating can be simplified as

$$t(y_G) = c_0 + c_1 \exp(j\beta y_G) \tag{1}$$

Here, $\beta = 2\pi/\Lambda$; Λ is the grating period; c_0, c_1 are Fourier series. **Figure 3** shows a schematic diagram of the 4f

system module and coordinate system. The sample (S) is imaged on the image plane (IP) after being magnified by the microscope objective. In this module, (x_O, y_O) are the coordinates of the IP plane; (x_G, y_G) are the coordinates of the grating plane; (x_L, y_L) are the coordinates of the first lens plane, (x_F, y_F) are the Fourier of the 4f system Plane coordinates; (x_I, y_I) are the coordinates of the camera plane. Here, we have derived **Eqs 2–8** based on **Figure 3** through the Fresnel diffraction integral formula. First, the complex amplitude of the object light field at the grating plane can be expressed as

$$U(x_G, y_G) = \frac{\exp(jkd)}{j\lambda d} \exp\left[j\frac{k}{2d}(x_G^2 + y_G^2)\right]$$

$$* \int_{-\infty}^{+\infty} A(x_o, y_0) \exp\left[j\frac{k}{2d}(x_o^2 + y_o^2)\right] \exp\left[-j\frac{k}{2d}(x_o y_G + y_o y_G)\right] dx_o dy_0 \tag{2}$$

Among them, d is the distance between the grating and the image plane. A (x_O, y_O) is the complex amplitude of the sample image of the IP plane. After the diffraction grating, the complex amplitude of the light field in front of the first Fourier lens is expressed as

$$U(x_L, y_L) = \frac{\exp(jkd_o)}{j\lambda d_0} \exp\left[j\frac{k}{2d_o}(x_L^2 + y_L^2)\right]$$

$$* \int_{-\infty}^{+\infty} U(x_G, y_G) t(y_G) \exp\left[j\frac{k}{2d_o}(x_G^2 + y_G^2)\right] \exp\left[-j\frac{k}{2d_o}(x_G x_L + y_G y_L)\right] dx_G dy_G \tag{3}$$
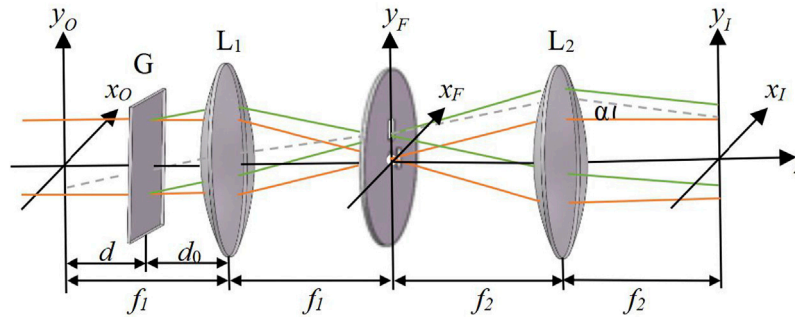
FIGURE 3 | Schematic diagram of 4f system module. f_1, f_2, focal length of lens L_1, L_2; α, off-axis interference angle; d, distance between grating and image plane; d_0, distance between lens and grating.

Substituting formula (1) and (2) into formula (3), it can be simplified to

$$U(x_L, y_L) = \frac{\exp(jkf_1)}{j\lambda f_1} \exp\left[j\frac{k}{2d_o}(x_L^2 + y_L^2)\right]$$

$$* \left\{ c_0 \int_{-\infty}^{+\infty} A(x_o, y_o) \exp\left[j\frac{k}{2f_1}(x_o^2 + y_o^2)\right] \exp\left(-j\frac{k}{f_1}(x_o x_L\right.\right.$$

$$+ y_o y_L)\bigg) dx_o dy_o + c_1 \exp\left(j\beta\frac{d}{f_1}y_L\right)$$

$$\times \int_{-\infty}^{+\infty} A(x_o, y_o) \exp\left[j\frac{k}{2f_1}(x_o^2, y_o^2)\right] \exp\left[j\frac{k}{f_1}(x_0 x_L + y_o y_L)\right]$$

$$\times \left] \exp\left(j\beta\frac{d_o}{f_1}y_o\right)\right] dx_o dy_o \right\}$$

$$(4)$$

Taking into account the Fourier transform properties of the lens, after the light field passes through the first lens of the 4f system, the distribution of the complex light field in front of the Fourier plane is

$$U(x_F, y_F) = \frac{1}{j\lambda f_1} \exp\left[j\frac{k}{2f_1}(x_F^2 + y_F^2)\right]$$

$$* \int_{-\infty}^{+\infty} U(x_L, y_L)t(x_L, y_L) \exp\left[j\frac{k}{2f_1}(x_L^2 + y_L^2)\right] \exp\left[-j\frac{k}{f_1}(x_F x_L\right.$$

$$+ y_F y_L)\bigg] dx_L dy_L$$

$$(5)$$

$$t(x_L, y_L) = \exp\left[-j\frac{k}{f_1}(x_L^2 + y_L^2)\right] \tag{6}$$

The transmittance function of lens L_1 is expressed by **Eq. 6**. A filter is placed on the Fourier plane of the lens L_1 to allow the +1-order light to pass through and further low-frequency filtering of the 0-order light, while other levels are blocked. Therefore, on the image plane, the +1-order object light that contains all the information of the original image

and the 0-order reference light that only carries the DC content of the original image can be obtained [31]. Omitting the constant exponential coefficient, the complex amplitude distribution of the object light field on the Fourier plane is

$$U(x_F, y_F) = \frac{1}{j\lambda f_1}\left[c_0 F\left\{A\left(\frac{x_F}{\lambda f_1}, \frac{y_F}{\lambda f}\right)\right\} * \delta(x_F, y_F)\right.$$

$$+ c_1 \exp\left(j\beta\frac{d}{f_1}y_F\right) F\left\{A\left(\frac{x_F}{\lambda f_1}, \frac{y_F}{\lambda f} - \frac{1}{\wedge}\right)\right\}\right] \quad (7)$$

Where F represents the Fourier transform of the function. Considering the properties of the Fourier transform of the lens, the distribution of the complex amplitude and light intensity (with the constant exponential coefficient omitted) of the image plane of a single wavelength are

$$U(x_I, y_I) = c_o\left[A(0,0)/M_{4f}\right] + c_1 \exp\left(j\frac{\beta}{M_{4f}}y_I\right)A\left[(-x_I, -y_I\right.$$

$$+ \alpha d)/M_{4f}\right]$$

$$(8)$$

$$I(x_I, y_I) = \left|c_o A\left[(0,0)/M_{4f}\right] + c_1 \exp\left(j\frac{\beta}{M_{4f}}y_I\right)A\left[(-x_I, -y_I\right.\right.$$

$$+ \alpha d)/M_{4f}\right]\bigg|^2$$

$$(9)$$

$$\alpha = \frac{\lambda f_2}{\wedge f_1} \tag{10}$$

where $M_{4f} = -f_2/f_1$, which defines the magnification of the 4f system. According to **Eq. 10**, for a certain system, the interference angle α is a constant and has nothing to do with the position of the grating G, but is only controlled by the grating period and the focal lengths of the lenses L_1 and L_2. From the geometric relationship, the shearing distance between the reference beam and the object beam on the camera plane is

$$l = \alpha d \tag{11}$$

As shown in **Figure 4**, the red and green circular areas respectively represent the light intensity distribution of the
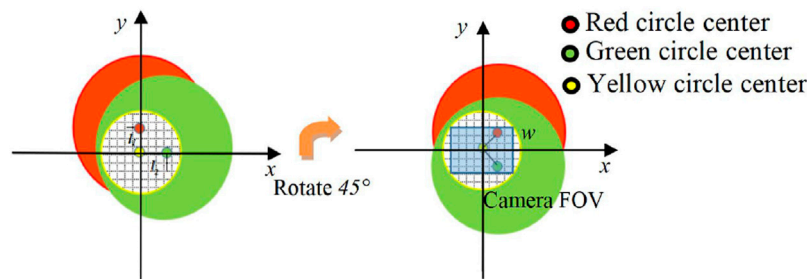
FIGURE 4 | (A) is the plane light intensity distribution diagram of the camera, l_1, l_2, the shearing distance of red and green light; **(B)** is the plane light intensity distribution of the camera after the two-dimensional grating is rotated 45°, w is the lateral width of the photosensitive surface of the camera.

object light carrying all the sample information at the corresponding frequency of the camera plane, and the area inside the yellow circle represents the object reference light interference area. The shearing distance l is the distance between the center of the object light beam and the center of the reference light, and this distance determines the position of the interference area between the object light and the reference light in the image plane. It can be seen from **Eq. 11** that the shearing distance can be adjusted by controlling the axial position of the grating. When the two-dimensional grating is located in the $x_O y_O$ plane ($d = 0$), the clipping distance l is 0. And the red and green object images are overlapped on the camera plane in **Figure 4**, and the camera captures The field of view corresponding to the two wavelength beams is the same. When the distance d increases, one of the two fields of view produces a displacement of l_1 in the x direction, and the other produces a displacement of l_2 in the y direction. This configuration produces a multiplex of two linear, orthogonal, off-axis interference holograms, corresponding to two sample fields of view. Therefore, two object light fields can be digitally extracted from a single multi-channel hologram. The beams of each wavelength of the dual-wavelength CO-DHM are split by a two-dimensional grating to generate corresponding shearing fields in mutually orthogonal directions. The expansion rate of the field of view compared to the original camera field of view area can be expressed as

$$\eta_{FOV} = \frac{\sqrt{l_1^2 + l_2^2}}{w} \tag{12}$$

Where l_1 and l_2 are the shearing distances corresponding to the light fields of different frequencies. w is the lateral width of the photosensitive surface of the camera.

$$l_1 = \frac{\lambda_1 d f_2}{\wedge f_1} \tag{13}$$

$$l_2 = \frac{\lambda_2 d f_2}{\wedge f_1} \tag{14}$$

Filter Structure Design

To design the filter diaphragm reasonably, the following three key factors must be considered: One is the distance between the pinhole and the center of the rectangular diaphragm, Through grating diffraction calculation, we can get

$$\Delta x = \frac{f_1 \lambda_G}{\wedge} \tag{15}$$

$$\Delta y = \frac{f_1 \lambda_R}{\wedge} \tag{16}$$

Where Δx and Δy are the physical distances between the 0-order and the +1-order spectrum of green and red light on the Fourier plane, and λ_G and λ_R are the wavelengths of green and red light. Second, the size of the rectangular aperture should be The design is large enough to ensure that the weaker +1-order diffracted beams pass through in the orthogonal direction individually and completely. The optimal side length dimension (L) of the rectangular diaphragm design can be expressed as:

$$L = \frac{f_1 (\lambda_R - \lambda_G)}{\wedge} \tag{17}$$

Phase Reconstruction Method

In the numerical reconstruction, the Fourier transform is performed on the image digital hologram recorded by the CCD to obtain the separable +1-order spectrum [32]. The original light field distribution can be obtained by performing frequency domain filtering on the +1-order spectra at different positions of the spectrogram, and then undergoing inverse Fourier transform. And calculate the arctangent of the complex amplitude of the object light wave to obtain the wrapped phase [33]. Here, the filtering method used in this article is the classical spectral filtering method. And the least squares unwrapping algorithm based on transverse shearing (LS-LS) is used to demodulate the wrapping phase. Among them, the phase compensation method in which the background optical complex amplitude is divided by the original light field is used to eliminate the additional phase factor and other background noise of the reference light wavefront. The distortion compensation method is detailed in Ref. [34]. It is worth pointing out that the camera only needs to collect a hologram to obtain background information of two wavelengths.

EXPERIMENTAL RESULTS

In order to verify the large field of view quantitative imaging capability of the system, a dual-wavelength CO-DHM optical
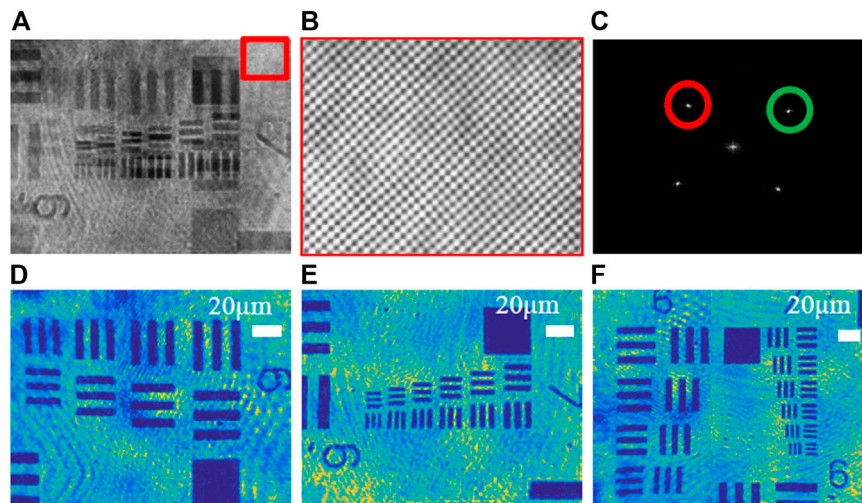
FIGURE 5 | Phase imaging of the 1951-USAF resolution chart based on dual-wavelength CO-DHM. **(A)** The multiplexed off-axis interferogram recorded during the exposure of a single CCD camera; **(B)** Enlarged image of interference fringes; **(C)** Spatial Fourier transform of the hologram; **(D)** $\lambda_1 = 632.8$ nm reconstructed intensity image. **(E)** $\lambda_2 = 532$ nm reconstruction intensity image; **(F)** The final field of view after stitching the intensity image of the resolution chart of two different fields of view.

path based on a two-dimensional diffraction grating as shown in **Figure 1** was constructed. The focal lengths of the lenses L_1 and L_2 used in the experiment are 6 cm, and all lenses are achromatic to minimize chromatic dispersion [35]. The actual horizontal magnification of the 4f module is $M_{4f} = 1$. The object beam is collimated by the tube lens into parallel light and incident on the two-dimensional Ronchi grating ($\Lambda = 8.6$ μm). The two-dimensional grating is located behind the front focal plane of the first lens (d = 3 cm) to generate diagonally orthogonal carrier frequencies. The CMOS (Basler acA 2500-14 μm, sensor for-mat: 2,592 × 1944 pixels, pixel size of 2.2 μm) is located at the back focal plane of the 4f system to record the interference hologram. The camera's dynamic range (typical value) is 60.6 dB. In our experiment, the microscope is equipped with a 40×/0.60NA objective lens. For the design of the filter, the diameter of the 0-order filter hole is 50 μm, and the two 1-order rectangular holes should be large enough to ensure that the +1-order light of this wavelength passes completely, and the +1-order light of another wavelength is filtered out.

1951-USAF Resolution Chart Imaging

Through the quantitative phase imaging of the 1951-USAF resolution chart (positive chart), the system's ability to obtain two holograms at one time and expand the field of view is verified. **Figure 5A** shows two resolution plate holograms with different fields of view recorded by a CCD camera at the same time, and **Figure 5B** shows an enlarged view of the fringes orthogonal to each other by magnifying the part of the hologram in the red rectangular frame. **Figure 5C** shows the spatial Fourier transform image of the hologram. The ±1 order spectrum of two wavelengths ($\lambda_1 = 632.8$ nm and $\lambda_2 = 532$ nm) are separated and marked with corresponding color circles. And the wrapped phase is obtained by performing frequency domain filtering on the +1 spectrum at different positions of the spectrogram. **Figure 5D** show the reconstructed intensity map after red

light frequency domain filtering. **Figure 5E** show the reconstructed intensity map of the green light. Finally, we get the final field of view size by stitching the pixels of the intensity map of two different resolution versions of the field of view, as shown in **Figure 5F**. Here, we selected the 1944 × 2,592 (camera full field of view) picture of the reconstructed resolution board illuminated by the green light source, and the (1,438 × 2,592) image size of the resolution board illuminated by the red light source. The image area (506 × 2,596) is the overlapping part of the two fields of view. From the geometric relationship, it can be calculated that the final field of view is 74.0% larger than that of the original camera.

Onion Epidermal Cell Imaging

In addition, we verified the ability of this technology to quantitatively image large scale biological cells by imaging the epidermal cells of plant onion. **Figure 6A** shows the multiplexed off-axis interference hologram recorded during the exposure of a single CCD camera; **Figure 6B** shows the spatial Fourier transform of the hologram; **Figures 6D,E** show the reconstructed intensity map, phase map and height map of $\lambda_1 = 532$ nm; **Figures 6F,G** show the reconstructed phase map and height map of $\lambda_2 = 632.8$ nm; Here, the image stitching method based on SIFT feature detection is used to reconstruct the image [36]. **Figures 6C,H6** are the intensity map and height map obtained after the two fields of view are stitched together. It is worth noting that it is unreasonable if the spliced picture is directly regarded as a complete single reconstructed image. This is manifested in two aspects: one is for the restored intensity image, because the light intensities of the two wavelengths are different. And the camera's sensitivity to different monochromatic light results in the difference in the natural intensity of the samples recorded by the CCD in the two fields of view. The solution adopted in this work is:
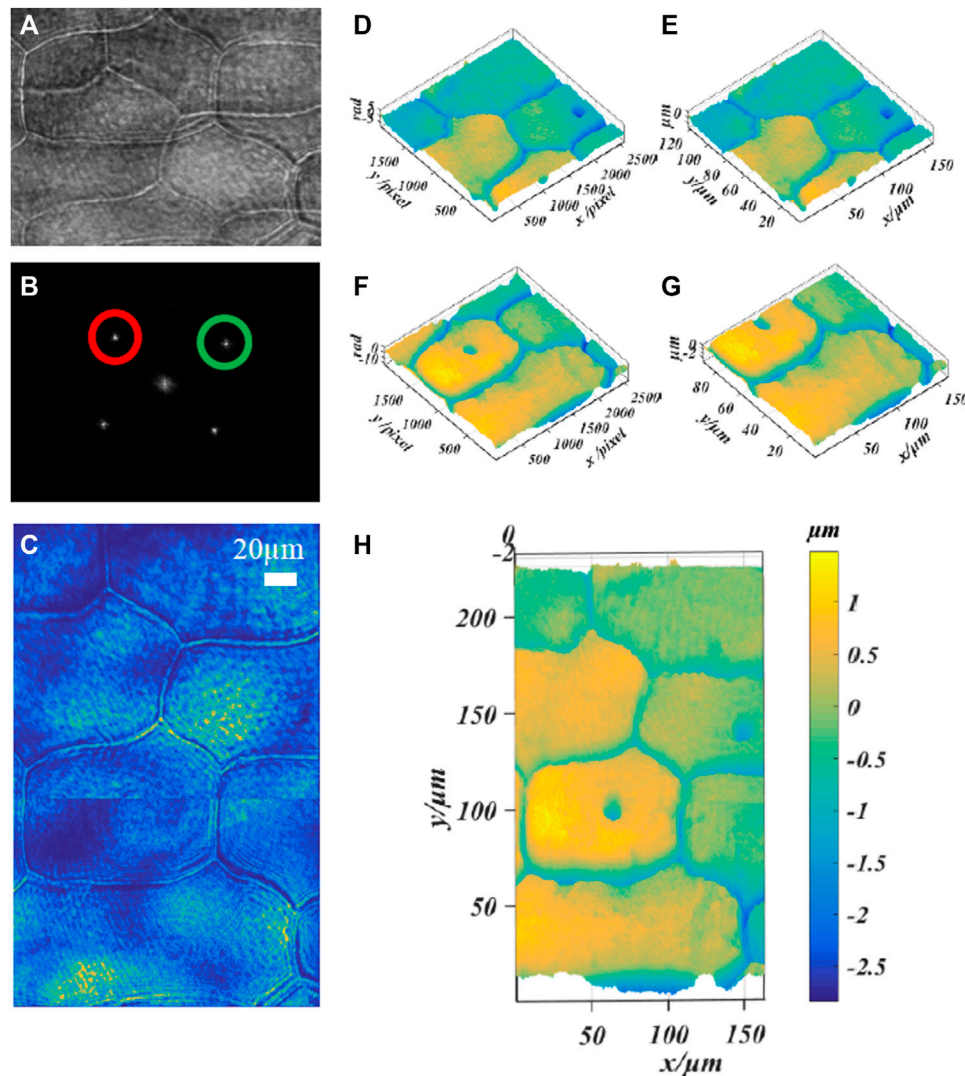
FIGURE 6 | Phase imaging of onion epidermal cells based on dual-wavelength CO-DHM based on grating diffraction. **(A)** the multiplexed off-axis interferogram recorded during the exposure of a single CCD camera; **(B)** the spatial Fourier transform of the hologram; **(D,E)**, $\lambda_1 = 532$ nm reconstruction phase map and height map; **(F,G)** $\lambda_2 = 632.8$ nm reconstruction phase map and height map. **(C,H)** Intensity map and height map obtained by splicing two fields of view.

adjust the attenuator in the optical path to approximate the same light intensity and numerical adjustment of intensity map brightness; the second is shown on the height map, this method is effective when there is no sample at the stitching boundary. But for large-size biological samples, even if the inherent height of the sample is the same (the height calculation formula can refer to Ref. [37]), it still remains at the stitched boundary with a slight difference. Because the sample has a different dispersion, refractive index and absorption for a specific wavelength of laser light. Here is only to show that the mentioned method is effective for the final expansion of the imaging field of view.

Standard Polystyrene Beads Imaging

Finally, we imaged standard polystyrene beads to verify the imaging accuracy of our system. The standard polystyrene

microspheres have a diameter of $(9.8 \pm 0.2)\mu$m and a refractive index of 1.59. Use a dropper to take a small number of microspheres and drop them on the glass slide. After the original ethanol solution has evaporated, use the refractive index matching solution to immerse the microspheres. Finally, put the standard sample into the stage and adjust the focus to make it image on the plane of the CCD camera. **Figures 7A–D** show the phase images of the microspheres with $\lambda_1 = 632.8$ nm and $\lambda_2 = 532$ nm, respectively. The red rectangular frame identifies the area as the overlapping area of different fields of view. **Figures 7E,F** respectively show the height images of the microspheres with $\lambda_1 = 632.8$ nm and $\lambda_2 = 532$ nm. The background noise of phase map and height map is caused by impurities in the medium, laser speckle and coherent parasitic fringe noise. **Figure 8** shows the one-dimensional phase and height reproduction of the same bead corresponding to the

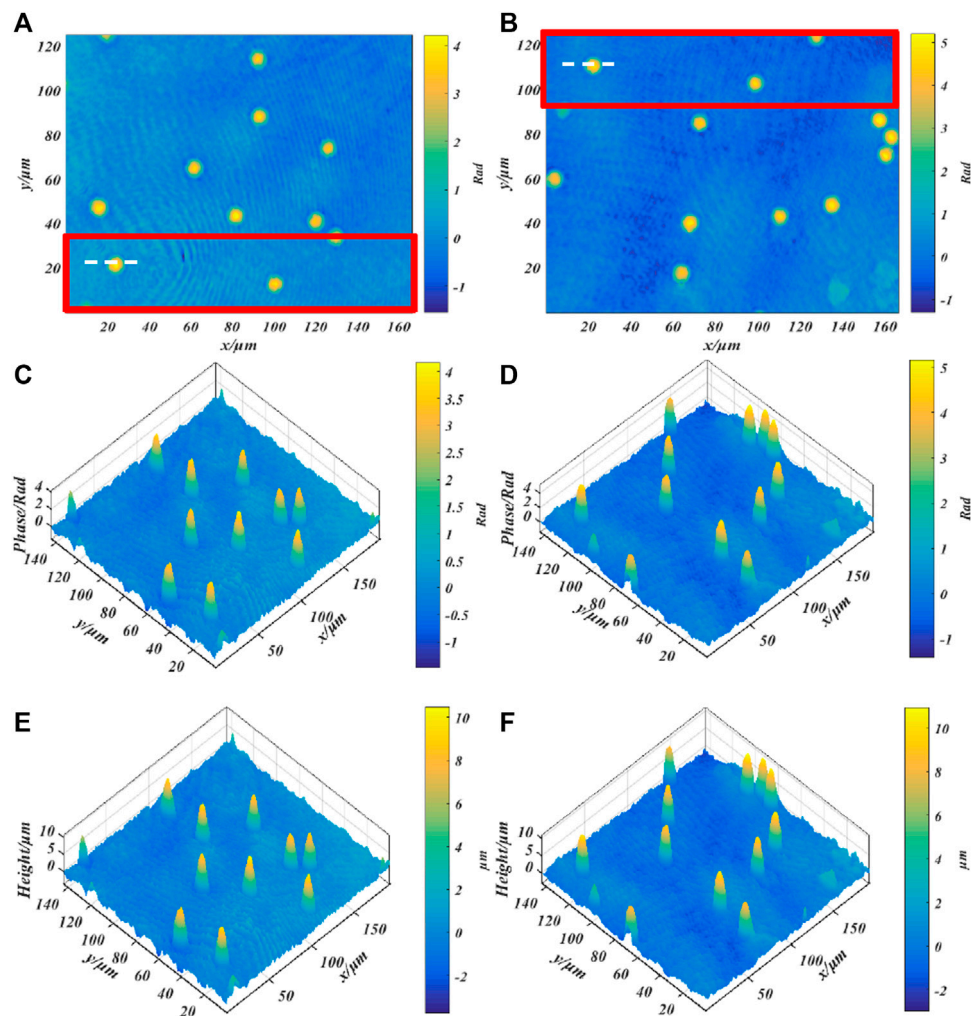**FIGURE 7 |** Quantitative phase imaging of standard polystyrene beads; **(A,C)** Phase diagram of beads with a wavelength of 632.8 nm; **(B,D)** Phase diagram of microbeads with a wavelength of 532 nm, **(E,F)** correspond to the height map.
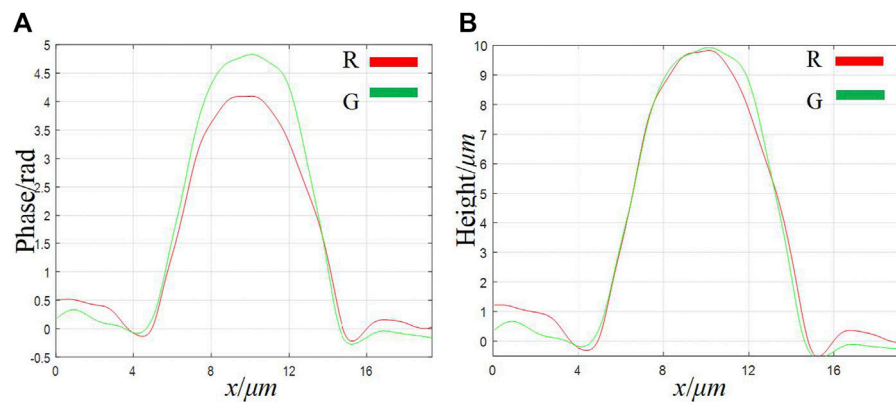

FIGURE 8 | A cross-sectional image of a single bead taken from the overlapping area of different fields of view. **(A)** phase map; **(B)** height map.

white line in the overlapping area under different fields of view. From the highest point value in **Figure 8B**, the longitudinal diameter of the microspheres illuminated by the red light source is 9.85 μm; the longitudinal diameter of the microspheres illuminated by the green light source is 10.00 μm. The main source of the errors in the measurement of the two wavelengths is due to the slight difference in refractive index of the test sample at different frequencies [23]. Here, we assume that the refractive index of the sample at different frequencies is the same; the second is the error caused by manual selection of the center position of the microbead.

CONCLUSION

In summary, we propose a two-wavelength CO-DHM system based on two-dimensional grating diffraction to improve the utilization of the interference field under the limited photosensitive size of the camera. This scheme can simultaneously perform two-wavelength and large field of view quantitative phase imaging. And compared with one-dimensional gratings and prisms as light-splitting elements, the use of two-dimensional gratings to split light to rotate 45° to form orthogonal carrier frequencies in diagonal directions can optimize the use of the spatial bandwidth product of the camera. Experimental results show that this technology can enlarge the common-path off-axis interference FOV by nearly 74.0% without changing the imaging parameters, such as magnification and resolution. It is worth pointing out that by optimizing the grating and 4f system lens parameters to the maximum, there is still room for improvement in this value to a certain extent.

At the same time, because the camera FOV and the acquisition frame rate are interchangeable, this technology can increase the camera's ability to acquire the frame rate by using fewer pixels without reducing the original reconstructed FOV [38]. By providing this module with conventional inverted microscopy, a broader FOV or faster collection rate can be provided for a given camera, thereby achieving greater and fastmoving sample imaging.

Of course, this solution also has all the advantages of single-lens multi-wavelength CO-DHM. It brings higher stability to the system by adopting the common-channel structure and multi-wavelength multiplexing method. By selecting the overlap area of the FOV of different wavelengths, the thickness, refractive index and dispersion of the sample can be measured at the same time (as mentioned in Refs. [4, 23]). This technology opens up a new way for the integration of versatility, high stability, wide field of view three-dimensional biological quantitative imaging technology.

DATA AVAILABILITY STATEMENT

The raw data supporting the conclusion of this article will be made available by the authors, without undue reservation.

AUTHOR CONTRIBUTIONS

Conceptualization, HW, and JW; methodology, GM, QZ, ZD, and JW; software, QZ, and XW; validation, XW, YG; formal analysis, JW, and HW; investigation, JW, XW; resources, HW, and WW; data curation, HW; writing—original draft preparation, JW; writing—review and editing, XW, JW, and HW; visualization, JW, and WW; supervision, HW; project administration, HW; funding acquisition, HW. All authors have read and agreed to the published version of the manuscript.

FUNDING

SUPPLEMENTARY MATERIAL

The Supplementary Material for this article can be found online at: https://www.frontiersin.org/articles/10.3389/fphy.2022.822714/full#supplementary-material

REFERENCES

1. Poon TC, Liu JP. *Introduction to Modern Digital Holography with MATLAB*. Cambridge: Cambridge University Press (2014).

2. Popescu G, Ikeda T, Dasari RR, Feld MS. Diffraction Phase Microscopy for Quantifying Cell Structure and Dynamics. *Opt Lett* (2006) 31:775–7. doi:10.1364/OL.31.000775

3. Li Y, Zhang S, Zhang J, Zhang Y, Liu D. Single-Shot Phase-Shifting Radial-Shearing Digital Holography with Fibonacci-Sieve Array Irrespective of Initial Phases. *Appl Phys Lett* (2021) 118:261101. doi:10.1063/5.0050681

4. Fu D, Choi W, Sung Y, Yaqoob Z, Dasari RR, Feld M. Quantitative Dispersion Microscopy. *Biomed Opt Express* (2010) 1:347–53. doi:10.1364/BOE.1.000347

5. Wu J, Liu K, Sui X, Cao L. High-Speed Computer-Generated Holography Using an Autoencoder-Based Deep Neural Network. *Opt Lett* (2021) 46:2908–11. doi:10.1364/OL.425485

6. Di J, Wu J, Wang K, Tang J, Li Y, Zhao J. Quantitative Phase Imaging Using Deep Learning-Based Holographic Microscope. *Front Phys* (2021) 9:113. doi:10.3389/fphy.2021.651313

7. Choi K, Yim J, Min S-W. Achromatic Phase Shifting Self-Interference Incoherent Digital Holography Using Linear Polarizer and Geometric Phase Lens. *Opt Express* (2018) 26:16212–25. doi:10.1364/OE.26.016212

8. Alemán-CastanedaLuis A, Lorenzo M, Miguel AA. Shearing Interferometry via Geometric Phase. *Optica* (2019) 6:396–9. doi:10.1364/OPTICA.6.000396

9. Cacace T, Bianco V, Mandracchia B, Pagliarulo V, Oleandro E, Paturzo M, et al.Compact off-Axis Holographic Slide Microscope: Design Guidelines. *Biomed Opt Express* (2020) 11:2511–32. doi:10.1364/BOE.11.002511

10. Patel N, Trivedi V, Mahajan S, Chhaniwal V, Fournier C, Lee S, et al.Wavefront Division Digital Holographic Microscopy. *Biomed Opt Express* (2018) 9:2779–84. doi:10.1364/boe.9.002779

11. Agour M, Falldorf C, Bergmann RB. Spatial Multiplexing and Autofocus in Holographic Contouring for Inspection of Micro-parts. *Opt Express* (2018) 26:28576–88. doi:10.1364/OE.26.028576

12. Yang Y, Cheng Z-J, Zhao H-M, Yue Q-Y, Guo C-S. Quantitative Phase Imaging System with Slightly-Off-Axis Configuration and Suitable for Objects Both Larger and Smaller Than the Size of the Image Sensor. *Opt Express* (2018) 26:17199–208. doi:10.1364/OE.26.017199

13. Wen Y, Wang H, Anand A, Qu W, Cheng H, Dong Z, et al..A Fast Autofocus Method Based on Virtual Differential Optical Path in Digital Holography: Theory and Applications. *Opt Lasers Eng* (2019) 121:133–42. doi:10.1016/j.optlaseng.2019.04.006

14. Das B, Yelleswarapu CS, Rao DVGLN. Parallel-Quadrature Phase-Shifting Digital Holographic Microscopy Using Polarization Beam Splitter. *Opt Commun* (2012) 285:4954–60. doi:10.1016/j.optcom.2012.07.101

15. Wang H, Dong Z, Wang X, Lou Y, Xi S. Phase Compensation in Digital Holographic Microscopy Using a Quantitative Evaluation Metric. *Opt Commun* (2019) 430:262–7. doi:10.1016/j.optcom.2018.08.061

16. Zheng C, Zhou R, Kuang C, Zhao G, Zhang Z, Liu X. Diffraction Phase Microscopy Realized with an Automatic Digital Pinhole. *Opt Commun* (2017) 404:5–10. doi:10.1016/j.optcom.2017.05.038

17. Shan M, Kandel ME, Majeed H, Nastasa V, Popescu G. White-Light Diffraction Phase Microscopy at Doubled Space-Bandwidth Product. *Opt Express* (2016) 24:29033–9. doi:10.1364/OE.24.029033

18. Baek Y, Lee K, Yoon J, Kim K, Park Y. White-Light Quantitative Phase Imaging Unit. *Opt Express* (2016) 24:9308–15. doi:10.1364/oe.24.009308

19. Bhaduri B, Edwards C, Pham H, Zhou R, Nguyen TH, Goddard LL, et al..Diffraction Phase Microscopy: Principles and Applications in Materials and Life Sciences. *Adv Opt Photon* (2014) 6:57–119. doi:10.1364/AOP.6.000057

20. Bhaduri B, Pham H, Mir M, Popescu G. Diffraction Phase Microscopy with white Light. *Opt Lett* (2012) 37:1094–6. doi:10.1364/OL.37.001094

21. Dubois F, Yourassowsky C. Full off-Axis Red-Green-Blue Digital Holographic Microscope with LED Illumination. *Opt Lett* (2012) 37:2190–2. doi:10.1364/OL.37.002190

22. Chowdhury S, Izatt J. Structured Illumination Diffraction Phase Microscopy for Broadband, Subdiffraction Resolution, Quantitative Phase Imaging. *Opt Lett* (2014) 39:1015–8. doi:10.1364/OL.39.001015

23. Jafarfard MR, Moon S, Tayebi B, Kim DY. Dual-Wavelength Diffraction Phase Microscopy for Simultaneous Measurement of Refractive index and Thickness. *Opt Lett* (2014) 39:2908–11. doi:10.1364/OL.39.002908

24. Talaikova NA, Kalyanov AL, Ryabukho VP. Diffraction Phase Microscopy with Transmission and Reflection Illumination for Refractive Index Measurements. *Proc SPIE* (2015) 9529:95291D–95296. doi:10.1117/12.2181946

25. Kumar M, Quan X, Awatsuji Y, Tamada Y, Matoba O. Single-Shot Common-Path off-Axis Dual-Wavelength Digital Holographic Microscopy. *Appl Opt* (2020) 59:7144–52. doi:10.1364/AO.395001

26. Hosseini P, Jin D, Yaqoob Z, So PTC. Single-Shot Dual-Wavelength Interferometric Microscopy. *Methods* (2018) 136:35–9. doi:10.1016/j.ymeth.2017.10.006

27. Min J, Yao B, Gao P, Guo R, Ma B, Zheng J, et al..Dual-Wavelength Slightly off-axis Digital Holographic Microscopy. *Appl Opt* (2012) 51:191–6. doi:10.1364/AO.51.000191

28. Tayebi B, Jeong Y, Han J-H. Dual-Wavelength Diffraction Phase Microscopy with 170 Times Larger Image Area. *IEEE J Select Top Quan Electron.* (2019) 25:1–6. doi:10.1109/JSTQE.2018.2863553

29. Kim MK. Wide Area Quantitative Phase Microscopy by Spatial Phase Scanning Digital Holography. *Opt Lett* (2020) 45(3):784–6. doi:10.1364/OL.385322

30. Frenklach I, Girshovitz P, Shaked NT. Off-Axis Interferometric Phase Microscopy with Tripled Imaging Area. *Opt Lett* (2014) 39(6):1525–8. doi:10.1364/OL.39.001525

31. Quan X, Matoba O, Awatsuji Y. Single-shot Incoherent Digital Holography Using a Dual-Focusing Lens with Diffraction Gratings. *Opt Lett* (2017) 42:383. doi:10.1364/OL.42.000383

32. Picazo-Bueno JÁ, Cojoc D, Iseppon F, Torre V, Micó V. Single-Shot, Dual-Mode, Water-Immersion Microscopy Platform for Biological Applications. *Appl Opt* (2018) 57:A242–A249. doi:10.1364/AO.57.00A242

33. Parshall D, Kim MK. Digital Holographic Microscopy with Dual-Wavelength Phase Unwrapping. *Appl Opt* (2006) 45:451–9. doi:10.1364/AO.45.000451

34. Pham HV, Edwards C, Goddard LL, Popescu G. Fast Phase Reconstruction in White Light Diffraction Phase Microscopy. *Appl Opt* (2013) 52(1):A97–101. doi:10.1364/AO.52.000A97

35. Jeon S, Cho J, Jin J-N, Park N-C, Park Y-P. Dual-Wavelength Digital Holography with a Single Low-Coherence Light Source. *Opt Express* (2016) 24:18408–16. doi:10.1364/OE.24.018408

36. Cheng DQ, Teng-Teng LI, Guo X, Bai CM, Hui XU. Improved Sift Neighborhood Voting Image Matching Algorithm. *Comput Eng Des* (2020) 41:162–168. doi:10.16208/j.issn1000-7024.2020.01.027

37. Liu B, Wang D, Zhu X, Wang H, Tian A, Liu W. Wavelength-Tuning Common-Path Digital Holographic Microscopy for Quantitative Phase Imaging of Functional Micro-Optics Components. *Appl Sci* (2020) 10:5602. doi:10.3390/app10165602

38. Girshovitz P, Shaked NT. Doubling the Field of View in off-Axis Low-Coherence Interferometric Imaging. *Light Sci Appl* (2014) 3:e151. doi:10.1038/lsa.2014.32

Conflict of Interest: The authors declare that the research was conducted in the absence of any commercial or financial relationships that could be construed as a potential conflict of interest.

Publisher's Note: All claims expressed in this article are solely those of the authors and do not necessarily represent those of their affiliated organizations, or those of the publisher, the editors and the reviewers. Any product that may be evaluated in this article, or claim that may be made by its manufacturer, is not guaranteed or endorsed by the publisher.

A Robust Checkerboard Corner Detection Method for Camera Calibration Based on Improved YOLOX

Guohui Wang[1,2]*, Hao Zheng[1] and Xuan Zhang[1]

[1]*School of Optoelectronic Engineering, Xi'an Technological University, Xi'an, China,* [2]*Shaanxi Province Key Laboratory of Photoelectricity Measurement and Instrument Technology, Xi'an Technological University, Xi'an, China*

Camera calibration plays an important role in various optical measurement and computer vision applications. Accurate calibration parameters of a camera can give a better performance. The key step to camera calibration is to robustly detect feature points (typically in the form of checkerboard corners) in the images captured by the camera. This paper proposes a robust checkerboard corner detection method for camera calibration based on improved YOLOX deep learning network and Harris algorithm. To get high checkerboard corner detection robustness against the images with poor quality (i.e., degradation, including focal blur, heavy noise, extreme poses, and large lens distortions), we first detect the corner candidate areas through the improved YOLOX network which attention mechanism is added. Then, the Harris algorithm is performed on these areas to detect sub-pixel corner points. The proposed method is not only more accurate than the existing methods, but also robust against the types of degradation. The experimental results on different datasets demonstrate its superior robustness, accuracy, and wide effectiveness.

Keywords: checkerboard corner detection, deep learning, YOLOX, Harris algorithm, camera calibration

1 INTRODUCTION

Camera calibration plays an important role in various optical measurement and computer vision applications. Accurate calibration parameters of cameras can perform better in scene reconstruction, stereo matching, and other aspects in the field of computer vision and optical measurement. The most important process in camera calibration is to find out the mapping relationship between the two-dimensional coordinates in the images captured by the camera and the three-dimensional coordinates in the real world. The relationship can be represented by feature points, such as checkerboard corners, circular array, and so on.

As a conventional feature extraction template, checkerboard corners detection is widely applied in most research. Accurate mathematical definition in corner points has not yet been proposed currently. Conventionally, the following points are usually called corner points: the junction point of two straight line edges [1], the point with sharp brightness changes in all directions of images, and the extreme point of maximum curvature of the edge curve in images [2]. Research in corner detection is mainly divided into three methods according to the definition of corners: intensity-based, contour-based, and binary-based methods [3]. Within these methods, the binary-based method is not popular in actual engineering applications.

For intensity-based methods in corner detection, the Moravec corner detection algorithm can find out the correlation between the patch combined with the neighborhood around a pixel and other surrounding patches by detecting each pixel of images [4]. This correlation was calculated by the sum of squared differences between the two patches, the smaller the value, the higher the similarity. Although the Moravec algorithm can recognize corners quickly, it is too sensitive for image edges and noise. In addition, it has limitations in direction. Activated by Moravec, Harris and Stephens [5] proposed the Harris algorithm which improved the Moravec corner detection algorithm. They calculated the autocorrelation function for each pixel in the image and defined the response function. Compared with the Moravec corner detection algorithm, the Harris algorithm possesses the rotation invariance but its threshold must be set manually. Smith and Brady [6] proposed a new method named SUSAN (Same Univalue Segment Assimilating Nucleus), which detected corners by a circular template belonging to surrounding pixels. Although the algorithm has fast speed, high location accuracy, high repeatability, and translation and rotation invariance, many detected features are located at the edges instead of real corners. In addition, it is sensitive for noise so that it performs poorly while detecting blurred images. Rosten and Drummond [7] proposed a faster corner detection algorithm which utilized machine learning to accelerate the process of corner detection.

Compared with intensity-based detection methods, contour-based detectors detect the edge contour before the corner detection, which detect corners in the contours instead of in total images, so it possesses extremely low detection error. Rachmawati et al. [8] proposed a polygon approximation technology combined with high-speed corner detection methods with the Freeman chain code. Mokhtarian and Suomela [9] proposed the corner detection method named Curvature Scale-Space (CSS). Zhong and Liao [10] proposed Direct Curvature Scale Space (DCSS). Hossain and Tushar [11] proposed Chord-to-Point Distance Accumulation (CPDA) and improved it with Chord Angle Deviation using Tangent (CADT). However, the localization of corners using the above methods may be poor if the detection is achieved on a large scale. Besides, these methods usually require complex and expensive mathematical operations.

In recent years, with great advances in deep learning for computer vision tasks, many attempts explored the possibility to use neural networks for camera calibration. The FAST (Features from Accelerated Segment Test) algorithm in the image corner detector is based on machine learning [7], and FAST-ER (FAST-Enhanced Repeatability) is its development [12, 13]. Song et al. [14] proposed a fully convolutional network (FCN)-based approach to detect building corners in aerial images. Raza et al. [15] presented a technique that uses trained convolutional neural network (CNN) to extract corners. Chen et al. [16] proposed a model based on FCN to detect corners to get a corner score on each pixel. Moreover, maximum response, non-maximum suppression (NMS), and clustering techniques are used to obtain the final pixel level corners.

In the field of object detection, deep learning performs best. There are various classical detection network structures such as R-CNN (Regions with CNN features) [17], Fast R-CNN [18], Faster R-CNN [19], SSD (Single Shot MultiBox Detector) [20], and YOLO (You Only Look Once) [21]. YOLO, as a one-stage algorithm, models object detection as a regression problem and directly predicts multiple bounding boxes from the input image. Aiming at the problem of YOLOv1 which only supports input of the same resolution image as the training image, YOLOv2 [22] improved the network in the network structure and the location prediction method, which can make the model adapt to multi-scale input. YOLOv3 [23] simply implemented independent logistic classifiers to achieve multilabel classification. However, it is not good at detecting small objects. Most recently, Bochkovskiy et al. heavily improved YOLOv3 and as a result they built YOLOv4 [24], which gives an efficient and powerful object detection model that can perfectly detect small objects. Ge et al. [25] presented some experienced improvements to the YOLO series and proposed a new high-performance detector - YOLOX. Zhang et al. [26] adopted YOLOX to obtain the detection boxes and associate them with the proposed method called BYTE. Sun et al. [27] used the YOLOX detector to perform object detection on the DanceTrack0027 video and to conduct different object association algorithms following that. Compared to the existing networks, YOLOX has been proven to be powerful for object detection.

Since all the traditional methods not only are affected by complex background, but also their threshold needs to be set manually, the above methods are difficult to detect corners on the large lens distortions checkerboard acquired from a fisheye lens or omnidirectional lens. Besides, some methods based on CNN can obtain great performance but only get pixel level corner points. In this paper, we propose a robust checkerboard corner detection method for camera calibration based on improved YOLOX deep learning network and the Harris algorithm. The improved YOLOX network is trained on a huge number of checkerboard images acquired from multiple scenarios. The corner candidate areas are first extracted by improved YOLOX and are then imported into the Harris algorithm to obtain the final sub-pixel corner points.

Our proposed method has the main advantages as follows:

(1) Recognize all checkerboard corners in such a particularly large angle between the camera's optical axis and the checkerboard plane;
(2) Recognize corners in the cases of focal blur and heavy noise when the camera is overexposed;
(3) Detect the corners in the case of severe lens distortions.

2 MATERIALS AND METHODS

2.1 Dataset and Environment Setup

Our original dataset is captured by a mobile phone (iPhone XR) and an industrial camera. The dataset consists of 141 images. Since deep learning requires sufficient data to complete the training process, the corner detection model should be robust
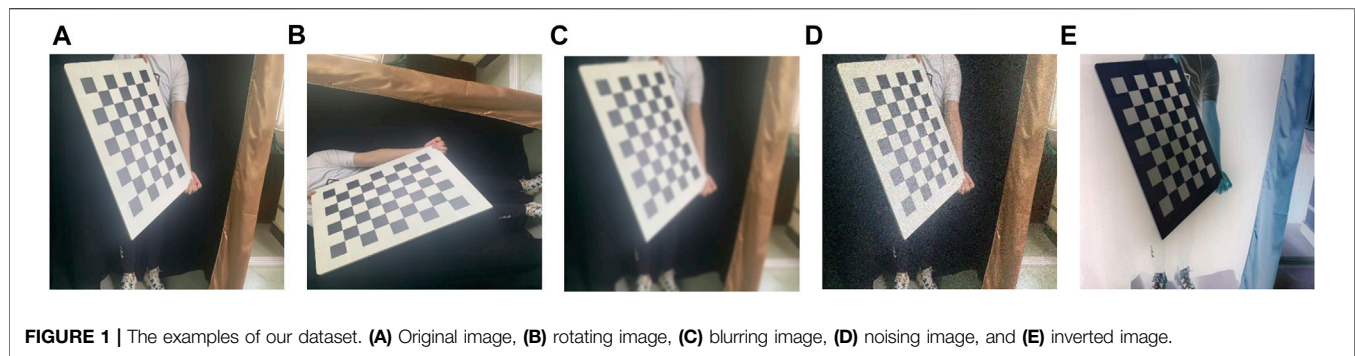
FIGURE 1 | The examples of our dataset. **(A)** Original image, **(B)** rotating image, **(C)** blurring image, **(D)** noising image, and **(E)** inverted image.
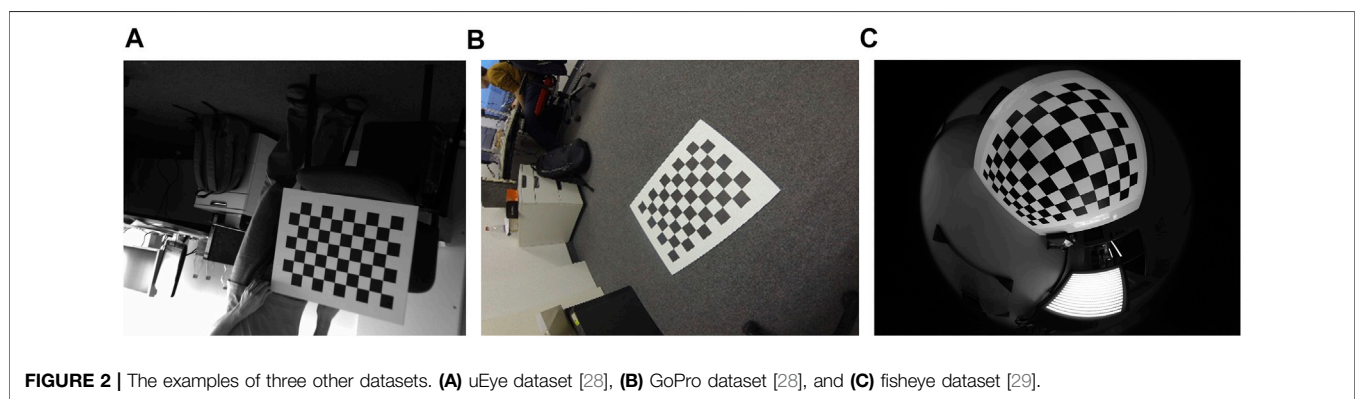

FIGURE 2 | The examples of three other datasets. **(A)** uEye dataset [28], **(B)** GoPro dataset [28], and **(C)** fisheye dataset [29].

to the types of degradation including focal blur, heavy noise, extreme poses, and large lens distortions. Therefore, the original dataset is mainly enhanced by the following four approaches: 1) rotating images (the angles include 90°, 180°, and 270°); 2) blurring images; 3) noising images; and 4) images with inverted gray value. One or more of these approaches is applied to each image. Finally, 2810 images are obtained for models training. The examples of our dataset are shown in **Figure 1**.

In addition to the dataset we created, the images for testing the generalization performance of the proposed method are from another three datasets: the uEye and GoPro datasets from ROCHADE [28], and the fisheye dataset [29]. The uEye dataset captured by IDS UI-1241LE camera has a slight distortion; the GoPro dataset is used to illustrate the robustness against large lens distortions. The fisheye dataset is captured by using a fisheye camera with 220° FOV that exhibits heavy lens distortions. Image examples of the three datasets used in our experiments are shown in **Figure 2**.

The training of the model is done using Python 3.6 with Pytorch 1.2.0 library on a Personal Computer (PC). The entire experiments are run on an Intel Core i5-9600KF CPU (3.70 GHz) and an NVIDIA RTX 2080Ti GPU with 11 G RAM.

2.2 Proposed Method

The traditional corner detection methods are difficult to avoid the influence of the image background. Once the background is complicated, the traditional methods may inevitably generate

pseudo corner points that possibly lead to further complexity. Furthermore, it is difficult to detect sub-pixel corners on the large lens distortions checkerboard acquired from the fisheye lens or the omnidirectional lens. To solve the shortcomings of traditional corner detection methods, we propose a robust corner detection method based on the improved YOLOX deep learning network and the Harris algorithm. In this method, we first detect the target and obtain the candidate areas through improved YOLOX. In the case of large lens distortions, this can accurately capture the candidate corner areas. The main work can be divided into four steps. The first step is to take the 2810 images after enhancement containing the corner areas for model training. The second step is to detect the candidate corner areas and obtain the coordinates of the areas through trained YOLOX. The third step is to extract the candidate corner areas and separate false areas by clustering algorithm. The last step is to detect the sub-pixel checkerboard corners with the Harris algorithm on these areas. The overview of the proposed method is depicted in **Figure 3**.

2.2.1 Improved YOLOX

YOLOX is an improved version of the YOLO series, which combines the advantages of each YOLO deep learning network [25]. The archor-free mechanism is implemented in this model, which significantly reduces the number of design parameters. Meanwhile, to solve the Optimal Transport (OT) problem and simplify it to get an approximate solution, SimOTA is used. YOLOX has different model structures, such as YOLOX-s, YOLOX-m, YOLOX-l, YOLOX-x, and so on. Since the features

FIGURE 3 | The overview of our proposed method.
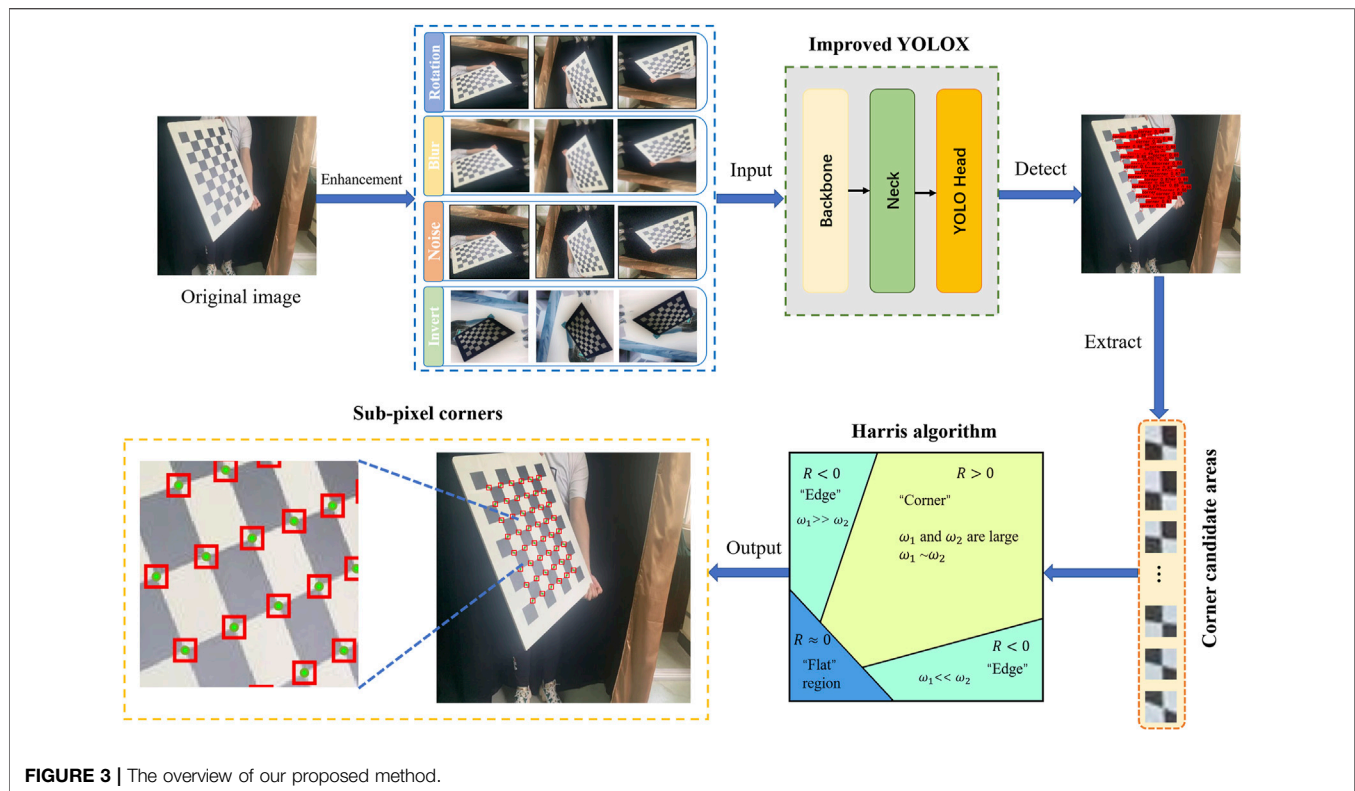
of a corner point are easier to recognize and do not require a complex detection network, the YOLOX-s model is chosen to detect the corner candidate areas in this study. The parameters and floating-point operations per second (FLOPs) of YOLOX-s are only 9 M and 26.8 G, respectively.

The overall model of YOLOX mainly consists of three key parts, which are Backbone, Neck, and YOLO Head. The Backbone is the backbone feature extraction network of the entire model. The three feature layers are obtained in the Backbone. Then three feature layers will be performed in the feature fusion in the Neck part. The YOLO Head is divided into a classifier and a regressor, which mainly makes judgements on feature points and determines whether there are objects corresponding to them. Especially, we add the squeeze-and-excitation (SE) attention mechanism [30] to capture position information after the Spatial Pyramid Pooling (SPP) module to improve the YOLOX-s model, which can also help the model to locate and recognize regions of interest more precisely. The structure of the improved YOLOX-s network is shown in **Figure 4**.

The basic components of the corner candidate areas of extraction network based on YOLOX-s are as follows:

(1) The Focus module. The input images are sliced to expand the feature dimension while retaining the complete image information in this module.
(2) The CBS (Convolution, Batch Normalization, and SiLU) module. The three subcomponents of the module are the convolution layer, batch normalization layer, and SiLU activation function.

(3) The CSP (Center and Scale Prediction) module. There are two CSP network structures used in YOLOX-s. CSP1_n is consisted of the CBS module, n residual units, and a concat function. CSP2_n is formed by the CBS module and a concat function. The functions of the two structures are to enhance the learning ability and feature integration ability of the network, respectively.
(4) The SPP module. To fuse multiscale features, the maximum pooling approach is used in this module.

The prediction process of the YOLOX network is similar to the YOLO series [31]. It also first resizes the input images so that all images have the same fixed size (640 × 640). Next, the input images are divided into grids with the size S × S. Each grid will use B bounding boxes to detect an object. Thus, for an input image, S × S × B bounding boxes will be generated. If the center of an object falls in a certain grid, the bounding boxes in this grid will predict the object. In the prediction process, confidence threshold is proposed to reduce the redundancy of bounding boxes. If the confidence score of the bounding box is higher than the confidence threshold, the bounding box will be kept; else the bounding box will be deleted. The confidence score of the bounding box can be obtained in the following:

$$C_i^j = P_{i,j} * IOU_{pred}^{truth} \qquad (1)$$

where C_i^j is the confidence score of the j th bounding box in the i th grid. $P_{i,j}$ is merely a function of the object. If the object is in the j th box of the i grid, the value of $P_{i,j}$ will be 1; otherwise $P_{i,j} = 0$.
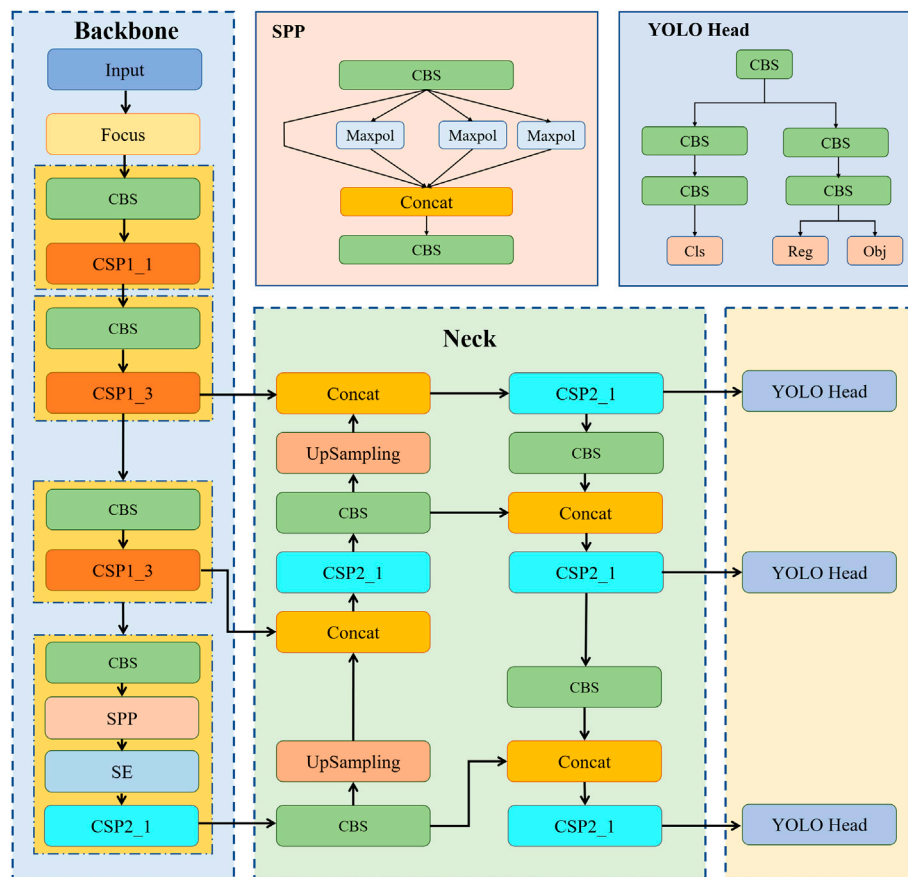
FIGURE 4 | The structure of improved YOLOX-s.

The IOU_{pred}^{truth} represents the intersection over union between the predicted box and the ground truth box. The larger the abjectness score, the closer the predicted box is to the ground truth box. The loss function of YOLOX is composed of three parts. It can be expressed as follows:

$$Loss = loss_{Reg} + loss_{Obj} + loss_{Cls} \qquad (2)$$

where $loss_{Reg}$, $loss_{Obj}$, and $loss_{Cls}$ are bounding box regression loss function, confidence loss function, and classification loss function, respectively [31].

2.2.2 Harris Algorithm

The Harris algorithm was proposed in the 1990s, and was used to image registration [5]. The algorithm analyzes the correlation between the pixel points in an image and the surrounding pixel points to detect the edge domains and corners of the image. The detection of a corner is usually judged by the gray level changing on the image in all directions. Therefore, assume that there is a small window on the image that can be moved in all directions. If the area of the small windows passed does not have gray level changed, then there is no corner in the area. If the windows move in a certain direction, the gray level changes greatly; but there is no gray level change in the other direction, which may be a straight line in this area. When the gray level of the pixel in the area shows a large change in all directions, the pixel at that location is defined as a corner. The schematic diagram is shown in **Figure 5**.

The autocorrelation function for the area near the corner is as follows:

$$Z(u,v) = \sum_{x,y} w(x,y)\left[I(x+u, y+v) - I(x,y) \right]^2 \qquad (3)$$

where u, v is the offset in the x, y direction; $I(x + u, y + v)$ is the gray level value of the offset pixel; $I(x, y)$ is the gray level value before offset; $w(x, y)$ is a window function, which can be either a constant or a Gaussian-shaped function.

Taylor's formula of the autocorrelation function $Z(u, v)$ is

$$T(u,v) \approx [u,v] * \sum_{xy} w(x,y) \begin{bmatrix} I_x^2 & I_x I_y \\ I_x I_y & I_y^2 \end{bmatrix} \begin{bmatrix} u \\ v \end{bmatrix} \qquad (4)$$

where I_x, I_y are gradients of pixels in the x, y directions, respectively. The eigenvalues of the matrix $\sum_{x,y} w(x,y) \begin{bmatrix} I_x^2 & I_x I_y \\ I_x I_y & I_y^2 \end{bmatrix}$ are ω_1, ω_2, which represents the image characteristics of the pixels. Based on the above principles, we will get the response function:

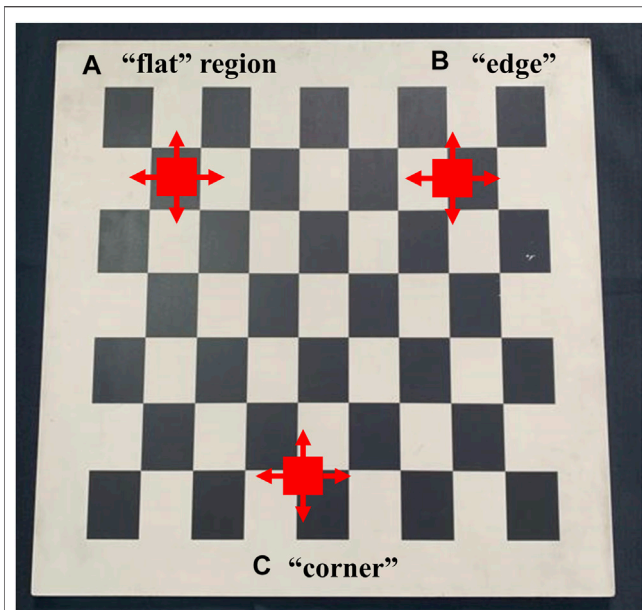**FIGURE 5 |** The schematic diagram of the Harris algorithm. **(A)** "Flat" region. **(B)** "Edge." **(C)** "Corner."
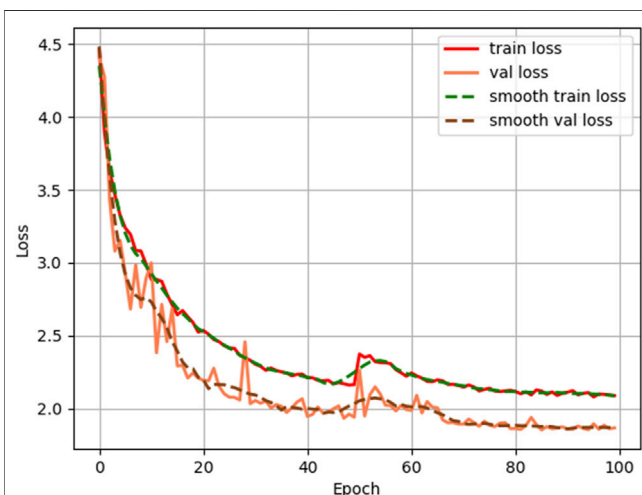

FIGURE 6 | Loss curves during training.

$$R = \omega_1\omega_2 - k(\omega_1 + \omega_2)^2 \qquad (5)$$

where k is an empirical constant. If $R \approx 0$, which represents the two eigenvalues are all small, there is a flat region; if $R < 0$, the window area is an edge; if $R > 0$ and greater than a certain threshold, there is a corner in the area.

3 EXPERIMENTS AND DISCUSSION

3.1 Model Training

The adaptive moment estimation (Adam) method is used as the optimizer. During the network training, the Mosaic data augmentation is used to learn how to identify objects that are smaller than normal, and it also encourages the model to locate different types of images in various parts of the network framework. The process of training is divided into two parts, which are freezing epoch with a batch size of 8 and unfreezing epoch with a batch size of 4, respectively. **Figure 6** shows the relationship between loss and epochs. The model training process proceeds for 100 epochs with 50 epochs for freezing and 50 epochs for unfreezing on the problem of detecting the corner candidate areas. The loss function converges rapidly at the beginning of training, and then decreases gradually in the subsequent training. After 50 epochs, the backbone of the model starts the training and gradually smoothes out as the epoch increases.

3.2 Evaluation Criteria

The evaluation criteria used in this paper are accuracy, the missed corner rate, the double detection rate, and the number of false positives on the test datasets. If the average distance between the detected corners and the ground truth corners of all images is less than five pixels, this is counted as a true positive. The missed corner rate denotes how many ground truths are detected as non-corners. The double detection rate shows how many ground truths have several detections. False positives show how many non-corner locations are detected as the corners on the whole dataset.

3.3 Experimental Results
3.3.1 Experimental Results on Our Dataset

The first experiment is focused on the robustness of our proposed method for the images (blur, noise, and extreme poses). The test results for an example image with extreme poses under blur and noise are shown in **Figures 7A,B**, respectively. The proposed method successfully detects checkerboard corners of extreme poses and maintains effective performance in the presence of blur and noise interference. From **Figure 7C**, the proposed method is almost not affected by the selected range of image noise and slightly influenced by the selected range of image blur. The accuracy defined by the average distance between the detected corners and the ground truth corners of all images is only 0.1639 at the strongest 3-pixel blur level, which is about four times as much as original images (0-pixel blur level). Therefore, our proposed method has a great accuracy and robustness of checkerboard corner detection.

In the experiments, the proposed method can effectively avoid double detections due to NMS structure of YOLOX. Besides, there are no false positives in our test images because of using the cluster algorithm. It can be demonstrated that the trained YOLOX model can accurately detect the corner candidate areas and the Harris algorithm can detect the sub-pixel corner points in the areas in different types of degradation.

3.3.2 Experimental Results on uEye and GoPro Datasets

To evaluate the performance of the proposed method, we conduct comparative experiments on the uEye dataset and GoPro dataset, which vary widely in resolution and lens distortions, from 1280 × 1024 images in uEye to 4000 × 3000 images with strong lens
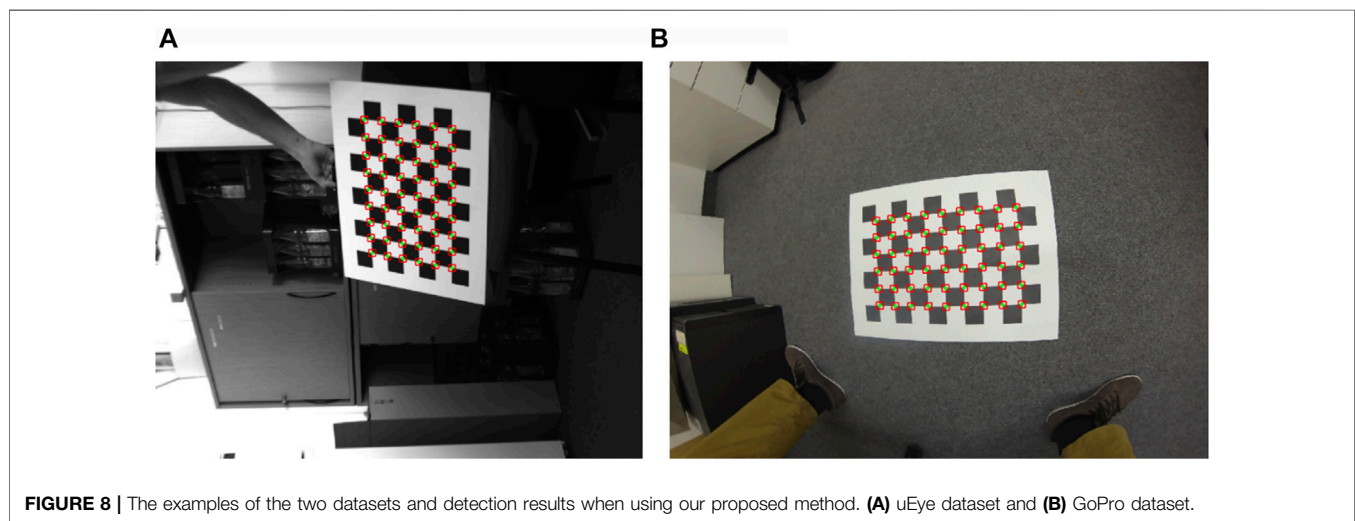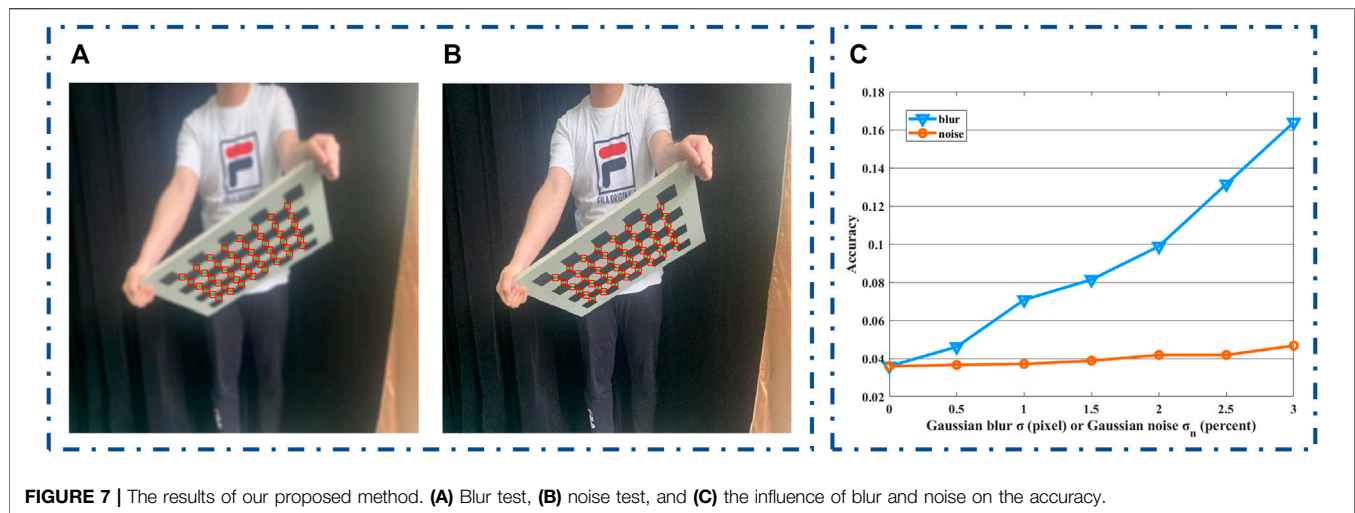
FIGURE 7 | The results of our proposed method. **(A)** Blur test, **(B)** noise test, and **(C)** the influence of blur and noise on the accuracy.

FIGURE 8 | The examples of the two datasets and detection results when using our proposed method. **(A)** uEye dataset and **(B)** GoPro dataset.

TABLE 1 | Results on the uEye dataset.

Method	Accuracy (pixel)	Missed corners (%)	Double detections (%)	False positives
CCDN	0.812	1.169	0.000	93
MATE	1.009	3.065	0.809	492
ChESS	0.946	3.398	0.000	11
ROCHADE	1.510	2.895	0.000	1
OCamCalib	0.319	0.000	0.000	0
Ours	0.086	0.000	0.000	0

distortions in the GoPro. We borrow the published results using the methods CCDN, MATE, ChESS, ROCHADE, and OCamCalib in [16]. The examples of these two datasets detection results using the proposed method are illustrated in **Figure 8**.

The results summarized in **Tables 1** and **2** show that the proposed method outperforms other methods on the two

datasets. Different than CCDN, the proposed method can achieve sub-pixel level corner detection, which also performs best in terms of accuracy. It can be found that OCamCalib does not have any false positives and double detections because it requires the number of squares in a checkerboard pattern in advance. Evaluations on the different datasets show the superior robustness and accuracy of our proposed method.

3.3.3 Experimental Results on Fisheye Dataset
In the third group of experiments, we perform several quantitative comparisons on the fisheye lens dataset (large lens distortions) using the corner detection methods of ours, CCDN, and MATLAB. As for the fisheye dataset containing images with resolution of 1600×1200, we calculate the rate of missed corners, double detections, and false positives for the three methods. The corners representative of one of the test images by the three methods are shown in **Figure 9**. From **Figure 9A**, CCDN finds 44 of the 88 corners. As illustrated in **Figure 9B**, MATLAB only detects 24 corners, in addition to 2 false positives which are shown in a red box. With the proposed method,

TABLE 2 | Results on the GoPro dataset.

Method	Accuracy (pixel)	Missed corners (%)	Double detections (%)	False positives
CCDN	0.576	0.907	0.000	0
MATE	0.835	4.566	4.556	389
ChESS	1.389	5.481	0.222	56
ROCHADE	1.807	5.593	0.000	3
OCamCalib	0.458	0.537	0.000	0
Ours	0.167	0.000	0.000	0
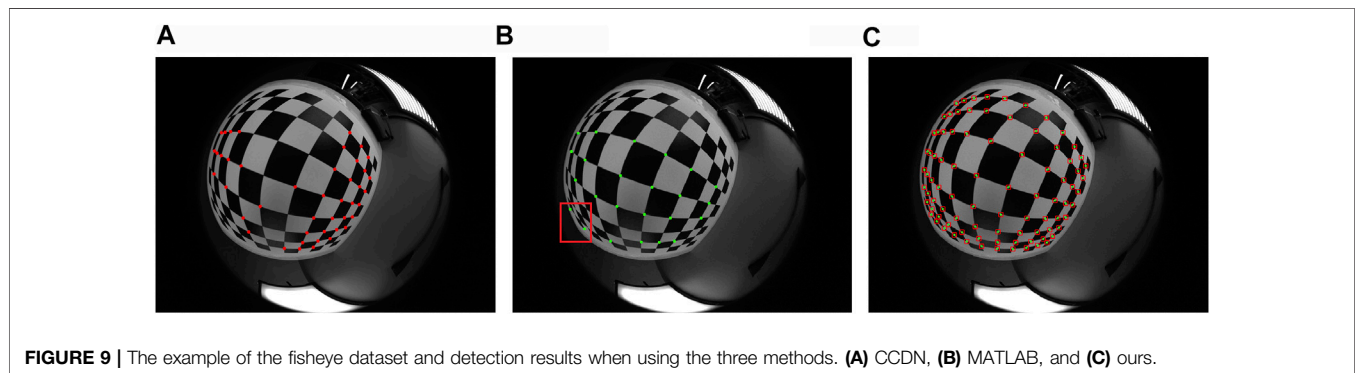
FIGURE 9 | The example of the fisheye dataset and detection results when using the three methods. **(A)** CCDN, **(B)** MATLAB, and **(C)** ours.

TABLE 3 | Results on the fisheye dataset.

Method	Missed corners (%)	False positives	Time (s)
CCDN	36.825	34	0.0688
MATLAB	62.558	4516	0.3290
Ours	3.582	0	0.0474

all corners of the checkerboard are detected accurately and can be used for calibration, which is illustrated in **Figure 9C**.

The results listed in **Table 3** show that the proposed method outperforms other methods on large lens distortion images. The trained YOLOX model can effectively extract the corner candidate areas so that false positives can be avoided. Meanwhile, the rate of missed corners using our method is only 3.582%. CCDN detects only 34 false positives, but the rate of missed corners is relatively high (up to 36.825%). MATLAB detects many false positives and has a high missed corner rate, which are 4516 and 62.558%, respectively. Besides, in terms of detect speed per image, our method requires less computation time of 0.0474 s. The detect time of MATLAB is 8 times longer than that of the proposed method, which reaches 0.329 s per image. The time required for CCDN to detect an image is 0.0688 s. It can be proven that MATLAB has inferior performance on the images of large lens distortions. The above results show that the proposed method is quite robust and fast for large lens distortions.

4 CONCLUSION

In our work, a new checkerboard corner detection method based on the improved YOLOX and the Harris algorithm is presented.

We use the improved YOLOX to detect the corner candidate areas and input them into the Harris algorithm to obtain the final sub-pixel corners. Theoretical analysis and experimental results show that the proposed method can be robust against the types of degradation (focal blur, heavy noise, extreme poses, and large lens distortions). Compared to traditional corner detection methods, the proposed method can detect not only corners against complex background, but also sub-pixel level corners. Thus, it can be seen as a specific checkerboard detector that is accurate, robust, and suitable for automatic detection and camera calibration. Our current work only discusses simple checkerboard corner detection. However, the related work of other types of calibration patterns such as deltille grids (regular triangular tiling) still needs further analysis and research. In future work, we will focus on the feature points detection model that is applicable to more types of calibration patterns.

DATA AVAILABILITY STATEMENT

The raw data supporting the conclusion of this article will be made available by the authors, without undue reservation.

AUTHOR CONTRIBUTIONS

All authors contributed to the research work. GW and HZ proposed the approach and designed the experiments; HZ and XZ performed the experiments; GW, HZ, and XZ analyzed the data and wrote the manuscript.

FUNDING

ACKNOWLEDGMENTS

REFERENCES

1. Mehrotra R, Nishan S, Ranganathan N. Corner Detection. *Pattern Recognition* (1990) 23:1223–33. doi:10.1016/0031-3203(90)90118-5

2. Dutta A, Kar A, Chatterji BN. Coner Detection Algorithms for Digital Images in Last Three Decades. *IETE Tech Rev* (2008) 25:123–33. doi:10.4103/02564602.2008.10876651

3. Wang J, Zhang W. A Survey of Corner Detection Methods. In: Proceedings of the 2018 2nd International Conference on Electrical Engineering and Automation; March 25-26, 2018; Chengdu (2018). 214–9. doi:10.2991/iceea-18.2018.47

4. Moravec HP. Techniques towards Automatic Visual Obstacle Avoidance. In: Proceedings of the 5th International Joint Conference on Artificial Intelligence (1977). 584.

5. Harris C, Stephens M. A Combined Corner and Edge Detector. In: Proceedings of the British Machine Vision Conference (1988). 147–52. doi:10.5244/C.2.23

6. Smith SM, Brady JM. SUSAN—A New Approach to Low Level Image Processing. *Int J Comput Vis* (1997) 23:45–78. doi:10.1023/A:1007963824710

7. Rosten E, Drummond T. Machine Learning for High-Speed Corner Detection. In: Proceedings of the 9th European Conference on Computer Vision (2006). 430–43. doi:10.1007/11744023_34

8. Rachmawati E, Supriana I, Khodra ML. FAST Corner Detection in Polygonal Approximation of Shape. In: Proceedings of the 3rd International Conference on Science in Information Technology (2017). 166–70. doi:10.1109/ICSITech.2017.8257104

9. Mokhtarian F, Suomela R. Robust Image Corner Detection through Curvature Scale Space. *IEEE Trans Pattern Anal Machine Intell* (1998) 20:1376–81. doi:10.1109/34.735812

10. Zhong B, Liao W. Direct Curvature Scale Space in Corner Detection. In: Proceedings of the Joint IAPR International Workshops on Statistical Techniques in Pattern Recognition and Structural and Syntactic Pattern Recognition (2006). 235–42. doi:10.1007/11815921_25

11. Hossain MA, Tushar AK. Chord Angle Deviation Using tangent (CADT), an Efficient and Robust Contour-Based Corner Detector. In: Proceedings of the 2017 IEEE International Conference on Imaging Vision Pattern Recognition (2017). 1–6. doi:10.1109/ICIVPR.2017.7890857

12. Rosten E, Porter R, Drummond T. Faster and Better: A Machine Learning Approach to Corner Detection. *IEEE Trans Pattern Anal Machine Intell* (2010) 32:105–19. doi:10.1109/TPAMI.2008.275

13. Donné S, De Vylder J, Goossens B, Philips W. MATE: Machine Learning for Adaptive Calibration Template Detection. *Sensors* (2016) 16:1858. doi:10.3390/s16111858

14. Song W, Zhong B, Sun X. Building Corner Detection in Aerial Images with Fully Convolutional Networks. *Sensors* (2019) 19:1915. doi:10.3390/s19081915

15. Raza SN, Raza ur Rehman H, Lee SG, Sang Choi G. Artificial Intelligence Based Camera Calibration. In: Proceedings of the 15th International Wireless Communications Mobile Computing Conference (2019). 1564–9. doi:10.1109/IWCMC.2019.8766666

16. Chen B, Xiong C, Zhang Q. CCDN: Checkerboard Corner Detection Network for Robust Camera Calibration. In: Proceedings of the International Conference on Intelligent Robotics and Applications (2018). 324–34. doi:10.1007/978-3-319-97589-4_27

17. Girshick R, Donahue J, Darrell T, Malik J. Rich Feature Hierarchies for Accurate Object Detection and Semantic Segmentation. In: Proceeding of the 2014 IEEE Conference on Computer Vision and Pattern Recognition (2014). 580–7. doi:10.1109/CVPR.2014.81

18. Girshick R. Fast R-CNN. In: Proceedings of the 2015 IEEE International Conference on Computer Vision (2015). 1440–8. doi:10.1109/ICCV.2015.169

19. Ren S, He K, Girshick R, Sun J. Faster R-CNN: Towards Real-Time Object Detection with Region Proposal Networks. *IEEE Trans Pattern Anal Mach Intell* (2017) 39:1137–49. doi:10.1109/tpami.2016.2577031

20. Liu W, Anguelov D, Erhan D, Szegedy C, Reed S, Fu C-Y, et al. SSD: Single Shot Multibox Detector. In: Proceedings of the European Conference on Computer Vision (2016). 21–37. doi:10.1007/978-3-319-46448-0_2

21. Redmon J, Divvala S, Girshick R, Farhadi A. You Only Look once: Unified, Real-Time Object Detection. In: Proceedings of the IEEE Conference on Computer Vision and Pattern Recognition (2016). 779–88. doi:10.1109/CVPR.2016.91

22. Redmon J, Farhadi A. YOLO9000: Better, Faster, Stronger. In: Proceedings of the 2017 IEEE Conference on Computer Vision and Pattern Recognition (2017). 6517–25. doi:10.1109/CVPR.2017.690

23. Redmon J, Farhadi A. YOLOv3: An Incremental Improvement. arXiv [Preprint] (2018). Available at: https://arxiv.org/abs/1804.02767.

24. Bochkovskiy A, Wang CY, Liao HYM. YOLOv4: Optimal Speed and Accuracy of Object Detection. arXiv [Preprint] (2020). Available at: https://arxiv.org/abs/2004.10934.

25. Ge Z, Liu S, Wang F, Li Z, Sun J. YOLOX: Exceeding YOLO Series in 2021. arXiv [Preprint] (2021). Available at: https://arxiv.org/abs/2107.08430.

26. Zhang Y, Sun P, Jiang Y, Yu D, Yuan Z, Luo P, et al. ByteTrack: Multi-Object Tracking by Associating Every Detection Box. arXiv [Preprint] (2021). Available at: https://arxiv.org/abs/2110.06864.

27. Sun P, Cao J, Jiang Y, Yuan Z, Bai S, Kitani K, et al. DanceTrack: Multi-Object Tracking in Uniform Appearance and Diverse Motion. arXiv [Preprint] (2021). Available at: https://arxiv.org/abs/2111.14690.

28. Placht S, Fürsattel P, Mengue EA, Hofmann H, Schaller C, Balda M, et al. ROCHADE: Robust Checkerboard Advanced Detection for Camera Calibration. In: Proceedings of the European Conference on Computer Vision (2014). 766–79. doi:10.1007/978-3-319-10593-2_50

29. Ha H, Perdoch M, Alismail H, Kweon IS, Sheikh Y. Deltille Grids for Geometric Camera Calibration. In: Proceedings of the 2017 IEEE International Conference on Computer Vision (2017). 5344–52. doi:10.1109/ICCV.2017.571

30. Hu J, Shen L, Sun G. Squeeze-and-excitation Networks. In: Proceedings of the 2018 IEEE Conference on Computer Vision and Pattern Recognition (2018). 7132–41. doi:10.1109/CVPR.2018.00745

31. Jiang Z, Zhao L, Li S, Jia Y. Real-time Object Detection Based on Improved YOLOv4-Tiny. arXiv [Preprint] (2020). Available at: https://arxiv.org/abs/2011.04244.

Determining the Phase Gradient Parameter of Three-Dimensional Polymorphic Beams

Xue Yun [1,2], Yansheng Liang [1,2]*, Minru He [1,2], Linquan Guo [1,2], Zhaojun Wang [1,2], Tianyu Zhao [1,2], Shaowei Wang [1,2] and Ming Lei [1,2]*

[1]*MOE Key Laboratory for Nonequilibrium Synthesis and Modulation of Condensed Matter, School of Physics, Xi'an Jiaotong University, Xi'an, China,* [2]*Shaanxi Province Key Laboratory of Quantum Information and Quantum Optoelectronic Devices, School of Physics, Xi'an Jiaotong University, Xi'an, China*

Three-dimensional polymorphic beams (3D PBs) with arbitrary 3D curves have drawn increasing attention. In this paper, we introduce the concept of phase gradient parameter (PGP) to describe the accumulation of phase along the curvilinear trajectory of a PB. To determine the magnitude and sign of the integral and fractional PGP of 3D PBs, we present an effective method called slightly defocused interference (SDI). The idea is based on the coaxial interference of two polymorphic beams of the same shape but various PGP. One of the interfered beams is slightly defocused, enabling the identification of the sign of the PGP. The efficiency of the reported method has been demonstrated with numerical simulations and experimental measurements by applying it to determining the PGP of various types of polymorphic beams. The results show high quality, indicating great potential in the applications of beam shaping.

Keywords: phase gradient, vortex beams, topological charge (TC), polymorphic beams, orbital angular momentum (OAM)

INTRODUCTION

Vortex beams (VBs), with spiral wavefront and well-defined orbital angular momentum distribution, have been serving as powerful tools in many fields [1–3]. Recently, three-dimensional polymorphic beams (3D PBs) have been proposed, advancing the symmetric vortex beam to freestyle 3D beams with arbitrary intensity trajectory [4, 5]. Due to the high-intensity gradient and programmable phase gradient, 3D PBs have inspired widespread applications, especially in the study of multi-particle dynamics in optical traps [6, 7]. In this case, the phase gradient of 3D PBs plays a critical role in the beams' focusing properties, further the optical force to drive the particle moving along the trajectory. To describe the phase gradient of 3D PBs, we introduce the concept of the phase gradient parameter (PGP). For the PBs with closed curve trajectories, such as ring-shaped beams, the phase accumulation is 2π times the PGP. In this case, the PGP is the well-known topological charge (TC) [7]. It is of significance to precisely determine the PGP of 3D PBs. Methods based on interference or diffraction have been reported for determining the TC of VBs [8–10]. The diffraction methods often use diffractive elements, such as triangular apertures [11], cylindrical lens [12, 13], and parabolic-line linear grating [14–16], to measure circular symmetric VBs. While the interference methods are mainly divided into two categories: self-interference and reference beam interference. The typical self-interference method is using Mach-Zehnder interferometer [17, 18]. By investigating the interference pattern of the vortex beam and its conjugate beam, the sign and the magnitude of the TC can be resolved. Utilizing a plane or spherical reference beam to interfere with a vortex beam is also a very popular method [19–21]. However, these methods are limited to VBs with two-

dimensional (2D) simple intensity patterns. It is an ongoing task to simultaneously determine the magnitude and sign of integral and fractional PGP of 3D PBs. As far as we know, no method to this issue has been reported. In this Letter, we present an enhanced holographic approach termed slightly defocused interference (SDI) to simultaneously determine the PGP of 3D PBs with high precision.

SLIGHTLY DEFOCUSED INTERFERENCE METHOD

We employed the holographic beam shaping technique reported by Rodrigo JA et al. [4, 5] to generate 3D PBs with specially prescribed intensity distribution and well-defined orbital angular momentum distribution. The complex amplitude of a PB satisfies

$$H(\mathbf{r}) = \frac{1}{L} \int_0^T \phi(\mathbf{r}, t) \varphi(\mathbf{r}, t) |c_3'(t)| \mathrm{d}t. \qquad (1)$$

In **Eq. 1**, $\mathbf{r} = (x, y)$ is the spatial coordinates at the input plane. $\mathbf{c}_3(t) = (x_0(t), y_0(t), z_0(t))$ denotes a 3D curve with (x_0, y_0, z_0) being the Cartesian coordinates. $L = \int_0^T |\mathbf{c}_3'(t)| \mathrm{d}t$ represents the length of the curve with $|c_3'(t)| = \sqrt{[x_0'(t)^2] + [y_0'(t)^2] + [z_0'(t)^2]}$, where $x'_0(t) = \mathrm{d}x_0(t)/\mathrm{d}t$, $y'_0(t) = \mathrm{d}y_0(t)/\mathrm{d}t$, $z'_0(t) = \mathrm{d}z_0(t)/\mathrm{d}t$. The terms $\phi(\mathbf{r}, t)$ and $\varphi(\mathbf{r}, t)$ satisfy the following relations

$$\phi(\mathbf{r}, t) = \exp\left(\frac{i}{\rho^2}\left[yx_0(t) - xy_0(t)\right]\right)\exp\left(\frac{i2\pi m}{S(T)}S(t)\right), \qquad (2)$$

and

$$\varphi(\mathbf{r}, t) = \exp\left(i\pi \frac{[x - x_0(t)]^2 + [y - y_0(t)]^2}{\lambda f^2} z_0(t)\right), \qquad (3)$$

where $t \in [0, T]$, $S(t) = \int_0^t [x_0(\tau)y_0'(\tau) - y_0(\tau)x_0'(\tau)]\mathrm{d}\tau$. λ and f represent the wavelength and the focal length of the Fourier lens, respectively. ρ is a constant, and m is the phase gradient parameters. For the closed PBs, the phase accumulation is $2\pi m$ and the PGP can be understood as the TC. To generate the 3D PBs using a phase-only SLM, we employed the complex-amplitude coding algorithm reported by Bolduc [22]. Based on this algorithm, the hologram addressed to the SLM is written as

$$H(x, y) = M\big(\phi_{\mathrm{relg}}(x, y) - \pi M\big), \qquad (4)$$

where $M = 1 + \mathrm{sinc}^{-1}[A_{\mathrm{relg}}(x, y)]/\pi$ is the modulation function, $\varphi_{\mathrm{relg}}(x, y)$ is a total relative phase, $A_{\mathrm{relg}}(x, y)$ is the relative field amplitude.

The SDI scheme is based on the interference between two PBs with the same intensity curve, but different PGP. The target beam has the expected PGP values, and the reference beam, however, has the PGP of zero and is slightly defocused. The Fresnel lens phase φ_{Lens} is used to control the convergence of the reference beam, written as

$$\varphi_{\mathrm{Lens}} = \frac{2\pi h(x^2 + y^2)}{\lambda f'} \qquad (5)$$

Here, λ is the wavelength, f' is the focal length of the Fresnel lens, h is the defocusing distance from the focal plane. By setting an appropriate value of h, the reference beam will be slightly defocused with respect to the target beam. As an illustration, we used a PB with a ring trajectory by setting the parameters of the target beam as follow: $x_0(t) = R_0\cos(t)$, $y_0(t) = R_0\sin(t)$, $R_0 = 300\mu m$, and $m = 10$ (**Figure 1E**), and verified the performance of the SDI method in determining the PGP by simulation. The interference field between the target and reference beams can be expressed by

$$E = \exp\big(i\varphi_{\mathrm{PB},m}\big) + C\exp\big(i\varphi_{\mathrm{PB},0} + i\varphi_{\mathrm{Lens}}\big). \qquad (6)$$

Here, C is a constant for adjusting the amplitude of the reference beam, $\varphi_{\mathrm{PB},m}$ and $\varphi_{\mathrm{PB},0}$ denote the complex amplitude-coded phase (**Figures 1A,B**) for generating the target ring-shaped beam with $m = 10$ (**Figure 1E**) and the reference ring-shaped beam with $m = 0$. The slightly defocused reference beam as shown in **Figure 1F**. By directly calculating the argument of the optical field E, i.e., Arg(E), the complex amplitude-coded phase holograms (**Figures 1C,D**) to be displayed on the SLM for generating the interference patterns with $m = 10$ (**Figure 1G**) and $m = -10$ (**Figure 1H**) are obtained. The slight defocusing enables the determination of the sign of the PGP. We can see that the interference patterns are divided into 10 fringes, equal to the magnitude of PGP of the target PB. **Figure 1I** shows the azimuthal intensity profiles of the interference patterns with the dotted lines in **Figures 1G,H** are the start point. The red and the blue curves (**Figure 1I**) both show periodic curves with a period of $2\pi/10$ for $m = 10$ and -10, respectively, proving that the magnitude of PGP is 10.

Particularly worth mentioning is that the sign of PGP can be obtained intuitively by observing the arrow-shaped fringes' direction. As indicated by the pink arrows shown in the inset of **Figures 1G,H**, when PGP > 0, the pointed end of the "arrow" is along the clockwise direction. In comparison, it is counterclockwise for PGP < 0. Therefore, by appropriately setting the parameter C and the lens phase φ_{Lens}, the sign of the PGP can be precisely determined.

EXPERIMENTAL SETUP

As shown in **Figure 1J**, a 532 nm laser first passed through a beam expander consisting of Lenses 1 and 2. Then the beam illuminated a phase-only SLM [the resolution is 1920 × 1080, Pluto-NIR-II (HOLOEYE Photonics AG Inc., Germany)]. The complex amplitude-coded phase hologram (**Figure 1J1**) was addressed on the SLM to modulate the input beam. The modulated beam was then reflected by the triangle reflector and relayed to the back focal plane of Lens 5 by the 4f system consisting of Lenses 3 and 4. A spatial filter (the aperture size is 2 mm) placed at the focal plane of Lenses 3 and 4 to block the other order diffractions except for the +first order, including the target beam and the slightly defocused reference beam. To register the results, we employed a camera (the resolution is 1280 × 1024 and the pixel size is 5.3 μm, DCC3240M (Thorlabs, America)) at the focal plane of Lens 5.
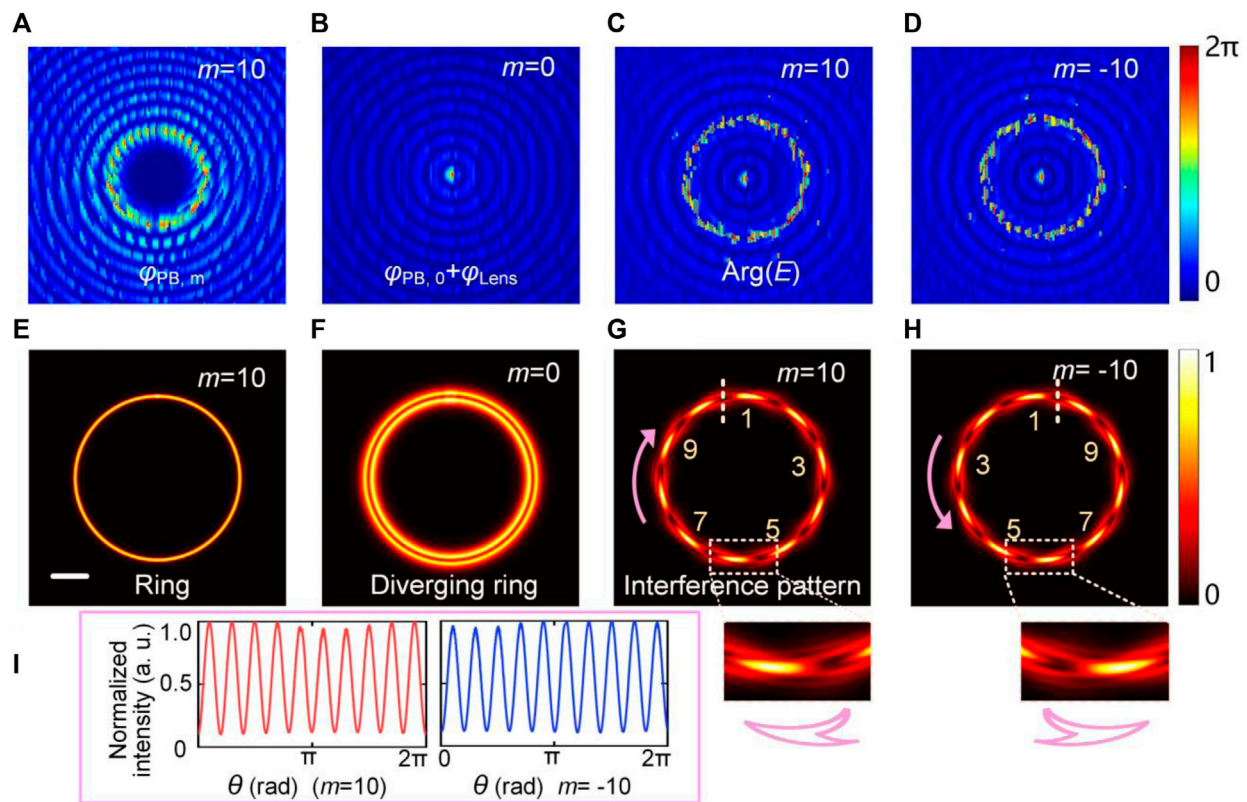
FIGURE 1 | Simulation results of determination of PGP of ring-shaped beams by the SDI method. **(A)** phase hologram for generation of a ring-shaped beam with $m = 10$. **(B)** phase hologram for generating a defocused ring-shaped beam with $m = 0$ through a Fresnel lens phase. **(C,D)** phase holograms for generating the interference patterns with $m = \pm 10$. **(E–H)** correspond to the simulated focal plane patterns generated in **(A–D)**. The insets in **(G,H)** show the detail of the interference fringes. **(I)** The azimuthal intensity profiles of the interference patterns in **(G,H)**. Scale bar: 100 μm. **(J)** The schematic of the experimental setup. **(J1)** The complex amplitude coded hologram. **(J2)** The interference pattern with $m = 10$.

RESULTS AND DISCUSSION

We first experimentally demonstrated the SDI method in determining the PGP of different integral 2D PBs as shown

Figure 2, including square-shaped beam ($x_0(t) = 3R_0\cos(t)+7R_0\cos(3t)/20$, $y_0(t) = 3R_0\sin(t)-7R_0\sin(3t)/20$, **Figure 2A**), ring-shaped beam ($x_0(t) = R_0\cos(t)$, $y_0(t) = R_0\sin(t)$, **Figure 2B**), star-like beam ($x_0(t) = r(t)R_0\cos(t)$, $y_0(t)$
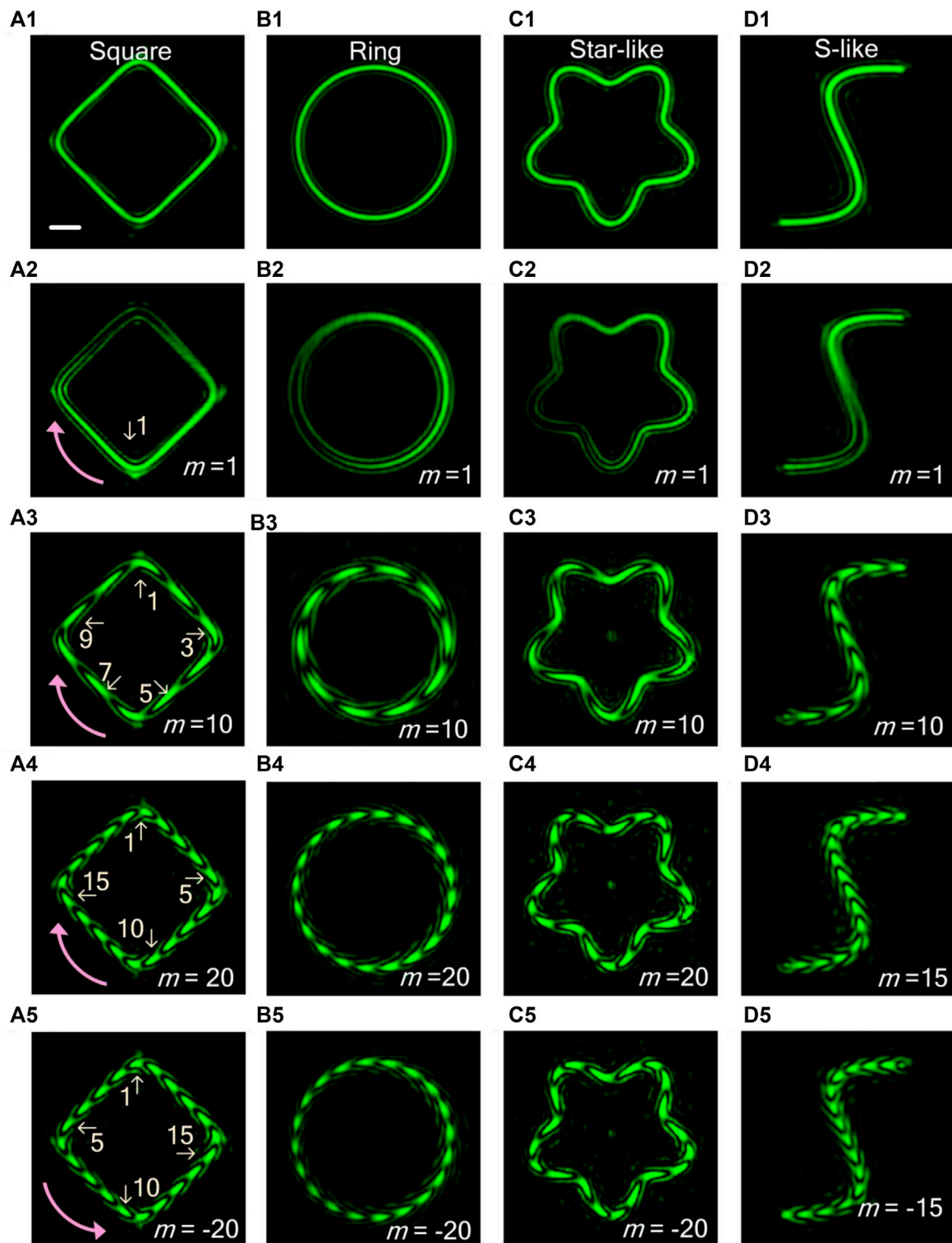
FIGURE 2 | Experimental results for determining the integral PGP of 2D PBs. The **(A1–D1)** in the figure respectively shows the intensity distribution of square-shaped beam, ring-shaped beam, star-like beam, and S-like beam. **(A2–D5)** are the interference patterns of PBs with m = 1, 10, 20, −20, R_0 = 300 μm, except for **(D4)** and **(D5)**, which are the interference patterns of the S-like beam with m = ±15. Scale bar: 100 μm.
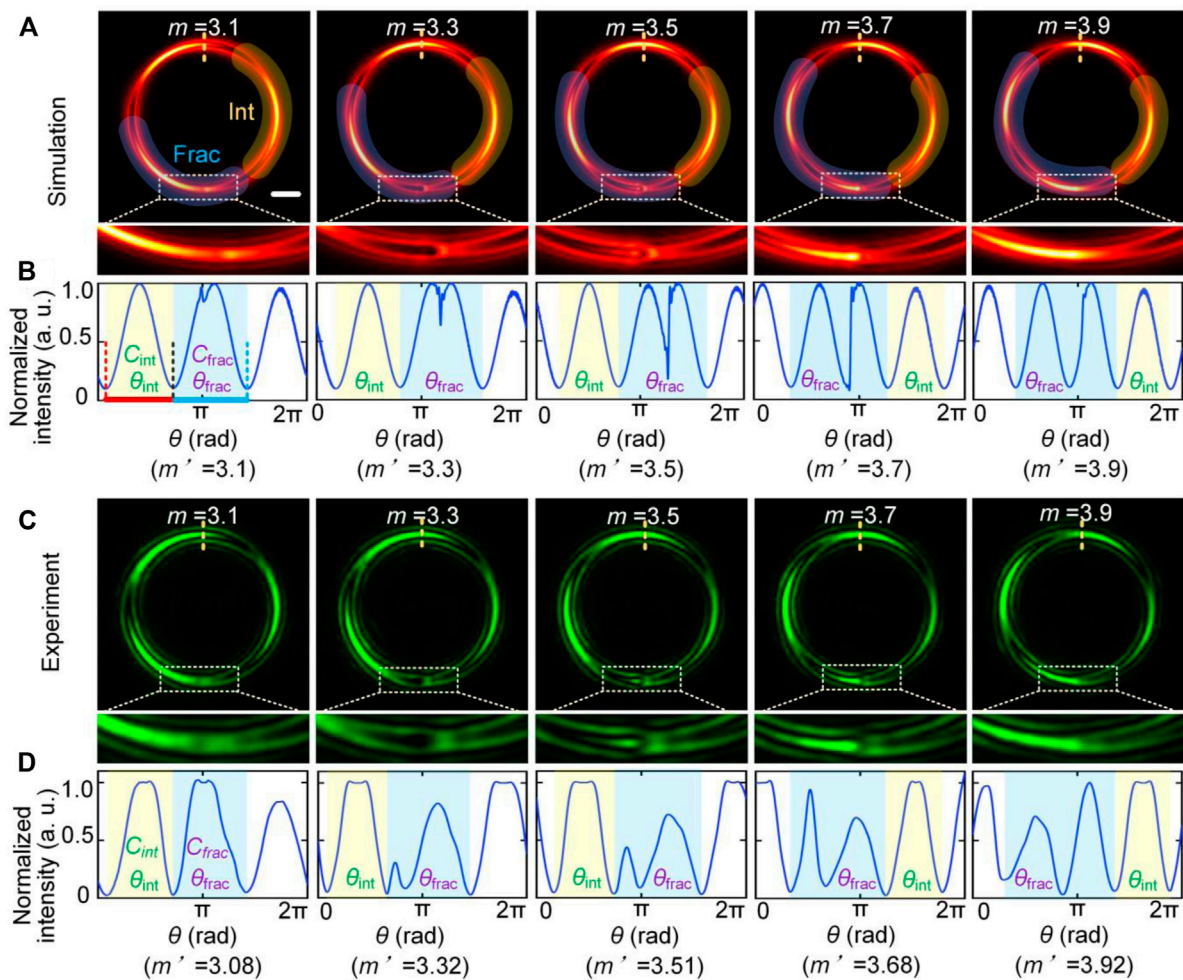
FIGURE 3 | Results for determining the fractional PGP. **(A)** are the evolution of the interference patterns of ring-shaped Beams with m = 3.1, 3.3, 3.5, 3.7 and 3.9. **(B)** Azimuthal intensity profiles of the interference patterns in **(A)**. **(C,D)** are the corresponding experiment results. Scale bar: 100 μm.

= $r(t)R_0\sin(t)$, $r(t) = 1 - \cos(4t)/4$, **Figure 2C**), and S-like beam (**Figure 2D**. When the curve is nonparametric, $c_3(t)$ can be approximated by a set of linked Bézier curves [23]). The experimentally measured intensity distributions of these four types of PBs are shown in the first row. The measured interference patterns for various PGP are presented in rows 2–5. For m = 1, 10, 15, −15, 20, and −20, the interference fringes exhibit respective 1, 10, 15, and 20 petals along the curve, respectively; the number of petals happens to be the absolute value of the corresponding PGP. From rows 4 and 5, we can find that the PGP of any two PBs in the same column has opposite signs, as indicated by the pink arrows. Each segment magically shows an "arrow" shape, just like a polymorphic snake, making the interference patterns explicitly spiral out in the anticlockwise direction (row 4, PGP > 0) or anticlockwise direction (row 5, PGP < 0). These features allow us to readily determine the sign of PGP. In addition, for non-closed beams with arbitrary trajectories, such as S-like PBs (**Figure 2D**), the SDI method still performs well in determining PGP.

The VBs with fractional PGP possess unique intensity distribution and more sophisticated orbital angular momentum modulation dimension [24, 25]. Therefore, it is of great significance to determine the fractional PGP. The simulation and experimental results using the SDI method have shown high quality, making the determination of fractional PGP a possible mission. **Figure 3** shows the numerically simulated (**Figures 3A,B**) and experimentally measured (**Figures 3C,D**) interference results of the ring-shaped beams with m = 3.1, 3.3, 3.5, 3.7 and 3.9 using the SDI method. When the PGP increases gradually, one of the fringes of the interference pattern breaks, and a fourth interference fringe gradually appears (as indicated by the insets in **Figures 3A,C**. **Figure 3B** is the one-dimensional azimuthal intensity profile curves along the trajectory of the interference patterns (**Figure 3A**). Denote by θ_{int} the angle subtended by the arc between two adjacent valleys of the curve (yellow shaded region in **Figure 3B** which corresponds to an unbroken fringe marked with "Int") and denote by θ_{frac} the angle associated with

TABLE 1 | Comparison of fractional PGP measured by simulation and experiment.

Simulation			Experiment		
m	$\theta_{frac}/\theta_{int}$	m'	m	$\theta_{frac}/\theta_{int}$	m'
3.1	1.1	3.1	3.1	1.08	3.08
3.3	1.3	3.3	3.3	1.32	3.32
3.5	1.5	3.5	3.5	1.51	3.51
3.7	1.7	3.7	3.7	1.68	3.68
3.9	1.9	3.9	3.9	1.92	3.92

the arc of broken the fringes (marked with "Frac") between two adjacent valleys of the curve (the blue shaded region in **Figure 3B**). The whole PGP can be deduced from $\theta_{frac}/\theta_{int}$ + 2, or $2\pi/\theta_{int}$.

The measured results of the arc length ratio $\theta_{frac}/\theta_{int}$ from **Figures 3B,D** are shown in **table 1**. For m = 3.1, 3.3, 3.5, 3.7 and 3.9, the simulated ratios $\theta_{frac}/\theta_{int}$ are 1.1, 1.3, 1.5, 1.7, and 1.9. Correspondingly the determined PGP are m' = 3.1, 3.3, 3.5, 3.7, and 3.9. The accuracy of the simulated results depends on the step size of the azimuthal intensity curve calculated by the program. In

our simulations, it was set to 10,000, making the measuring relative error smaller than 10^{-3}. In theory, the numerically measured PGP is equal to the designed PGP. The experimentally measured ratios $\theta_{frac}/\theta_{int}$ are 1.08, 1.32, 1.51, 1.68, and 1.92. Therefore, the determined PGP are m' = 3.08, 3.32, 3.51, 3.68, and 3.92, respectively. Compared with the simulation results, the experimental results showed small deviation from the theoretical values, which is attributed to the influence of background stray light, and the limited beam shaping resolution. However, the measuring error is less than 0.03, demonstrating the high feasibility of the SDI method.

Importantly, the SDI method can be applied to determining the PGP of the 3D PBs. The PBs with tilted-ring shape and waved-ring shape are taken as examples to demonstrate the determination of the PGP of 3D PBs. In **Figure 4**, columns 1 and 2 are the numerical simulation results of the 3D view of PBs and the interference intensity profiles with m = ±10, respectively. By moving the camera in the axial direction to scan the beam, we can record the 2D intensity images of the beam at a sequence of axial positions. The 3D patterns are constructed with these 2D images, as shown in columns 3 and 4. Column 5 provides the

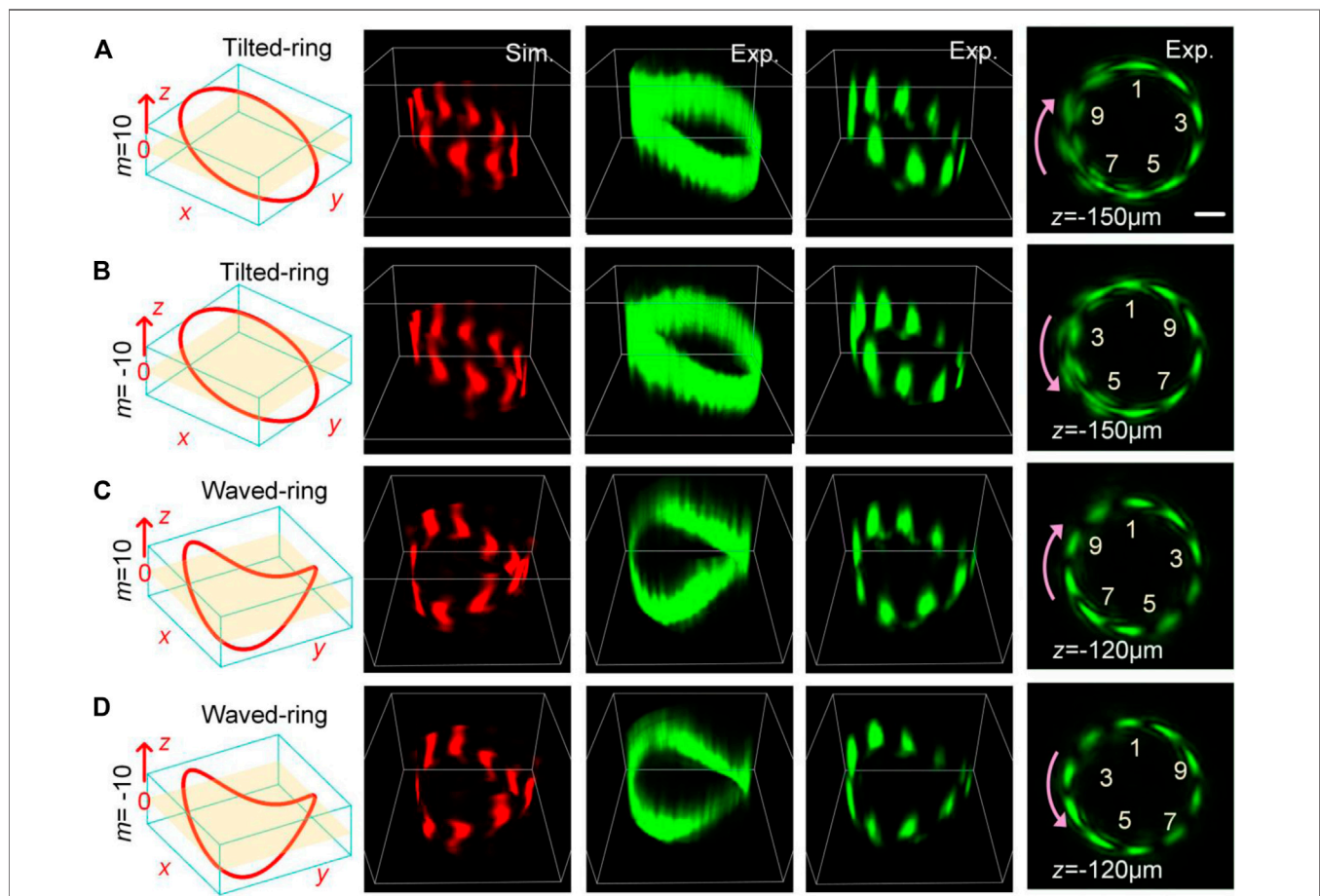**FIGURE 4** | Determination of PGP of 3D PBs. **(A,B)** Tilted-ring with m = ±10. **(C,D)** Waved-ring with m = ±10. Columns 1 and 2 are the numerical simulation results of the 3D view of PBs and the interference intensity profiles. Columns 3 and 4 are the corresponding experimental results. Column 5 displays the beam propagated before the focal plane. Scale bar: 100 μm.

cross-section intensities at different axial positions before the focal plane. Again, we can find that the light curves of the 3D PBs are divided into 10 fringes, equivalent to the value of the PGP. Notably, the sign is determined by the direction of the "arrows" of the interference fringes in column 5 as theoretically predicted. Moreover, the fractional PGP of 3D PBs can also be detected by analyzing the intensity profile curve of the maximum projection of the interference pattern in the z-direction.

CONCLUSION AND DISCUSSION

In conclusion, we have reported the SDI method for quantitatively determining the integral and fractional PGP of PBs with high accuracy. The experimental results are in good agreement with the theoretical predictions. The SDI method holds great promise to be a powerful tool for studying the properties of 3D PBs, and thus great potential in applying to various fields, such as optical tweezers, optical communications, etc.

Although the fractional PGP of 3D PBs with simple geometry can be detected by the SDI method, for more complex-shaped beams, such as the optical solenoid beam [26], the measurement of the fractional PGP is still limited due to the overlap of the light field projections in the z-direction. In future work, we will consider the multi-angle projection to detect the PGP of the complex-shaped beams. Recently, a deep learning method named "VortexNet" can accurately reveal the topological properties [27]. In view of the strong performance of this method, we plan to

combine the SDI method with the deep learning approach. In this way, we would expect to achieve a higher-precision measurement of the PGP.

DATA AVAILABILITY STATEMENT

The original contributions presented in the study are included in the article/Supplementary Material, further inquiries can be directed to the corresponding author.

AUTHOR CONTRIBUTIONS

ML and YL conceived and designed the study. XY and YL designed the system and collected data. XY and MH prepared the samples. All authors contributed to results interpretation. XY and YL drafted the manuscript, to which all authors contributed.

FUNDING

REFERENCES

1. Allen L, Beijersbergen MW, Spreeuw RJC, Woerdman JP. Orbital Angular Momentum of Light and the Transformation of Laguerre-Gaussian Laser Modes. *Phys Rev A* (1992) 45(11):8185–9. doi:10.1103/physreva.45.8185

2. Bozinovic N, Yue Y, Ren Y, Tur M, Kristensen P, Huang H, et al. Terabit-Scale Orbital Angular Momentum Mode Division Multiplexing in Fibers. *science* (2013) 340(6140):1545–8. doi:10.1126/science.1237861

3. Zhang K, Wang Y, Yuan Y, Burokur SN. A Review of Orbital Angular Momentum Vortex Beams Generation: From Traditional Methods to Metasurfaces. *Appl Sci* (2020) 10(3):1015. doi:10.3390/app10031015

4. Rodrigo JA, Alieva T. Polymorphic Beams and Nature Inspired Circuits for Optical Current. *Sci Rep* (2016) 6(1):35341–8. doi:10.1038/srep35341

5. Rodrigo JA, Alieva T, Abramochkin E, Castro I. Shaping of Light Beams along Curves in Three Dimensions. *Opt Express* (2013) 21(18):20544–55. doi:10.1364/oe.21.020544

6. Rodrigo JA, Angulo M, Alieva T. All-Optical Motion Control of Metal Nanoparticles Powered by Propulsion Forces Tailored in 3d Trajectories. *Photon Res* (2021) 9(1):1–12. doi:10.1364/prj.408680

7. Amaral AM, Falcão-Filho EL, de Araújo CB. Characterization of Topological Charge and Orbital Angular Momentum of Shaped Optical Vortices. *Opt Express* (2014) 22(24):30315–24. doi:10.1364/oe.22.030315

8. Fickler R, Campbell G, Buchler B, Lam PK, Zeilinger A. Quantum Entanglement of Angular Momentum States with Quantum Numbers up to 10,010. *Proc Natl Acad Sci U.S.A* (2016) 113(48):13642–7. doi:10.1073/pnas.1616889113

9. Ma H, Li X, Tai Y, Li H, Wang J, Tang M, et al. *In Situ* Measurement of the Topological Charge of a Perfect Vortex Using the Phase Shift Method. *Opt Lett* (2017) 42(1):135–8. doi:10.1364/ol.42.000135

10. Bianchetti A, Etchepareborda P, Federico A. Determining the Fractional Topological Charge Shifting in Perfect Vortices from Laser Speckle. *Opt Commun* (2019) 441:74–9. doi:10.1016/j.optcom.2019.02.051

11. de Araujo LEE, Anderson ME. Measuring Vortex Charge with a Triangular Aperture. *Opt Lett* (2011) 36(6):787–9. doi:10.1364/ol.36.000787

12. Alperin SN, Niederriter RD, Gopinath JT, Siemens ME. Quantitative Measurement of the Orbital Angular Momentum of Light with a Single, Stationary Lens. *Opt Lett* (2016) 41(21):5019–22. doi:10.1364/ol.41.005019

13. Kotlyar VV, Kovalev AA, Porfirev AP. Astigmatic Transforms of an Optical Vortex for Measurement of its Topological Charge. *Appl Opt* (2017) 56(14):4095–104. doi:10.1364/ao.56.004095

14. Amiri P, Mardan Dezfouli A, Rasouli S. Efficient Characterization of Optical Vortices via Diffraction from Parabolic-Line Linear Gratings. *J Opt Soc Am B* (2020) 37(9):2668–77. doi:10.1364/josab.398143

15. Rasouli S, Amiri P, Kotlyar VV, Kovalev AA. Characterization of a Pair of Superposed Vortex Beams Having Different Winding Numbers via Diffraction from a Quadratic Curved-Line Grating. *J Opt Soc Am B* (2021) 38(8):2267–76. doi:10.1364/josab.428390

16. Rasouli S, Fathollazade S, Amiri P. Simple, Efficient and Reliable Characterization of Laguerre-Gaussian Beams with Non-zero Radial Indices in Diffraction from an Amplitude Parabolic-Line Linear Grating. *Opt Express* (2021) 29(19):29661–75. doi:10.1364/oe.435116

17. Leach J, Padgett MJ, Barnett SM, Franke-Arnold S, Courtial J. Measuring the Orbital Angular Momentum of a Single Photon. *Phys Rev Lett* (2002) 88(25):257901. doi:10.1103/physrevlett.88.257901

18. Kumar P, Nishchal NK. Modified Mach-Zehnder Interferometer for Determining the High-Order Topological Charge of Laguerre-Gaussian Vortex Beams. *J Opt Soc Am A* (2019) 36(8):1447–55. doi:10.1364/josaa.36.001447

19. Cui S, Xu B, Luo S, Xu H, Cai Z, Luo Z, et al. Determining Topological Charge Based on an Improved Fizeau Interferometer. *Opt Express* (2019) 27(9):12774–9. doi:10.1364/oe.27.012774

20. Pan S, Pei C, Liu S, Wei J, Wu D, Liu Z, et al. Measuring Orbital Angular Momentums of Light Based on Petal Interference Patterns. *OSA Continuum* (2018) 1(2):451–61. doi:10.1364/osac.1.000451

21. Liang Y, Yan S, He M, Li M, Cai Y, Wang Z, et al. Generation of a Double-Ring Perfect Optical Vortex by the Fourier Transform of Azimuthally Polarized Bessel Beams. *Opt Lett* (2019) 44(6):1504–7. doi:10.1364/ol.44.001504

22. Bolduc E, Bent N, Santamato E, Karimi E, Boyd RW. Exact Solution to Simultaneous Intensity and Phase Encryption with a Single Phase-Only Hologram. *Opt Lett* (2013) 38(18):3546–9. doi:10.1364/ol.38.003546

23. Rodrigo JA, Angulo M, Alieva T. Dynamic Morphing of 3d Curved Laser Traps for All-Optical Manipulation of Particles. *Opt Express* (2018) 26(14):18608–20. doi:10.1364/oe.26.018608

24. Tao SH, Yuan X-C, Lin J, Peng X, Niu HB. Fractional Optical Vortex Beam Induced Rotation of Particles. *Opt Express* (2005) 13(20):7726–31. doi:10.1364/opex.13.007726

25. Zhang H, Zeng J, Lu X, Wang Z, Zhao C, Cai Y. Review on Fractional Vortex Beam. *Nanophotonics* (2022) 11(2):241–73. doi:10.1515/nanoph-2021-0616

26. Lee S-H, Roichman Y, Grier DG. Optical Solenoid Beams. *Opt Express* (2010) 18(7):6988–93. doi:10.1364/oe.18.006988

27. Wang H, Yang X, Liu Z, Pan J, Meng Y, Shi Z, et al. *Deep-Learning-Based Recognition of Multi-Singularity Structured Light*. Nanophotonics (2021). doi:10.1515/nanoph-2021-0489

Background Noise Suppression of Optical Sectioning Structured Illumination Microscopy *via* Fourier Domain Reconstruction

Shipei Dang [1,2], Jia Qian [1], Tong Peng [1], Chen Bai [1], Junwei Min [1], Haixia Wang [3], Baoli Yao [1,2]* and Dan Dan [1]*

[1]State Key Laboratory of Transient Optics and Photonics, Xi'an Institute of Optics and Precision Mechanics, Chinese Academy of Sciences, Xi'an, China, [2]University of Chinese Academy of Sciences, Beijing, China, [3]The Third Affiliated Hospital of Sun Yat-sen University, Guangzhou, China

Optical sectioning structured illumination microscopy (OS-SIM) has been attracting considerable interest in fast 3D microscopy. The reconstruction of optical sectioning images in the conventional method employs the root-mean-square (RMS) algorithm in the spatial domain, which is prone to residual background noise. To overcome this problem, we propose a Fourier domain based optical sectioning image reconstruction algorithm (termed Fourier-OS-SIM), which has an improved background noise suppression capability compared to the RMS algorithm. The experimental results verified the feasibility and the effectiveness of the algorithm. The improved performance of the Fourier-OS-SIM may find more applications in biomedical or industrial fields.

Keywords: structured illumination microscopy (SIM), optical sectioning, background noise suppression, image reconstruction, Fourier domain

INTRODUCTION

Optical sectioning structured illumination microscopy (OS-SIM) [1] has drawn much attention due to the compact wide-field architecture, fast speed, and optical sectioning capability, compared to the prominent laser scanning confocal microscopy (LSCM) [2]. With the structured illumination pattern, OS-SIM enables to discriminate the in-focus portion and gets rid of the out-of-focus portion of the depth of field (DOF) of the objective lens. The RMS (root mean square) algorithm is a usually used method to recover an optically sectioned image by using three fringe illuminated raw images with a phase shift interval of $2\pi/3$ [1, 3]. Firstly, every two of the three raw images subtract from each other. Then, these substractions are squared and summed up, and finally rooted to yield an optical sectioning image. It is worth noting that the RMS algorithm does not take noises into account. However, noises exist inevitably in the raw images, and they will cause a background noise after the RMS calculation. The background noise will become more evident when the raw SIM images have a low signal-to-noise ratio (SNR), which is usual in fluorescence imaging, where the weak signal from the labeled fluorophores is surrounded by strong background noise. OS-SIM is different from super-resolution SIM (SR-SIM) that aims to break the diffraction limit [4, 5]. Although OS-SIM and SR-SIM can perform on the same system, they are based on different principles and have distinct image reconstruction frameworks.

To mitigate the weakness of the RMS algorithm, some modified reconstruction methods have been proposed. Santos et al. introduced a HiLo microscopy using one uniform wide-field image

and another structured illumination image as inputs [6, 7]. High- and low-pass filters were applied to extract the high and low frequencies of the in-focus information, which are then synthesized into a sectioned image. However, the parameters of the high- and low-pass filters need to be determined empirically [8]. Patorski et al. proposed a two-shot OS-SIM with a phase shift of π *via* Hilbert-Huang processing [9]. The subtraction of the two-shot images is decomposed into a series of bi-dimensional intrinsic mode functions (BIMFs) through fast and adaptive bi-dimensional empirical mode decomposition (FABEMD) [10] and then filtered selectively. The sectioned image is reconstructed using a 2D spiral Hilbert transform from the filtered outcome. Although selective filtration can remove noise and bias to a certain extent, the decomposition and the 2D spiral Hilbert transformation are time-consuming. Subsequently, Zhou *et al.* presented a 1D Hilbert transform reconstruction that dramatically simplifies the Hilbert-Huang processing approach [11]. Another advantage is that the phase shift of the two shots can be arbitrary rather than constant π. Despite the simplicity of procedure and robustness in phase shifting, the 1D Hilbert transform reconstruction is lousy in background noise suppression since there is no noise-relevant operation involved in this method. Recently, deep learning has significantly boosted the OS-SIM reconstruction speed and reduced the number of raw images requested [12, 13]. However, it needs enormous training datasets and an excel reconstruction algorithm in advance. The robustness of the deep learning networks remains a challenge for different imaging situations.

In this paper, we propose a Fourier domain based optical sectioning image reconstruction algorithm (termed Fourier-OS-SIM) with background noise suppression capability. The Fourier-OS-SIM outperforms background noise suppression for the sectioned images compared to the conventional RMS-based OS-SIM reconstruction method. The performance of the Fourier-OS-SIM can be enhanced by using fruitful frequency filters to reduce the image background further.

PRINCIPLE OF FOURIER-OS-SIM

The intensity distribution of the illumination cosinusoidal fringe pattern employed in SIM is expressed as:

$$I(r) = I_0\left[1 + m\cos\left(2\pi k_0 r + \varphi\right)\right], \tag{1}$$

where r indicates the coordinate in the object plane; I_0, m, k_0, and φ represent the mean intensity, modulation depth, spatial frequency, and initial phase, respectively. In the linear regime, the intensity of the fluorescence signal is proportional to the excitation illumination intensity. The image intensity distribution recorded in the camera plane can be written as:

$$D(r) = [S(r)I(r)] \otimes PSF(r), \tag{2}$$

where S(r) represents the structure of the sample, PSF(r) is the point spread function of the imaging system, and the symbol $\otimes$

denotes the convolution operation. Substitution of **Eq. 1** into **Eq. 2** results in:

$$D(r) = I_0\{S(r)\left[1 + m\cos\left(2\pi k_0 r + \varphi\right)\right]\} \otimes PSF(r). \tag{3}$$

Making the Fourier transform for **Eq. 3**, we obtain the following equation in the frequency domain:

$$\tilde{D}(k) = I_0\big[\tilde{S}(k) + 0.5me^{-i\varphi}\tilde{S}(k + k_0)$$
$$+ 0.5me^{i\varphi}\tilde{S}(k - k_0)\big]OTF(k). \tag{4}$$

Here, the symbol ~ represents the corresponding Fourier spectrum, k denotes the spatial frequency, OTF(k) is the optical transfer function formed by taking the Fourier transform of the PSF(r). $\tilde{S}(k)$ refers to the conventional wide-field spectrum. $\tilde{S}(k + k_0)$ and $\tilde{S}(k - k_0)$ correspond to spectra with frequencies shifted by a distance of $\pm k_0$, respectively. Combining these three spectra into one will enlarge the object spectrum scope, indicating a resolution enhancement in the spatial domain.

To solve the three spectral items of $\tilde{S}(k)$, $\tilde{S}(k + k_0)$, and $\tilde{S}(k - k_0)$ in **Eq. 4**, the initial phase φ is generally varied three times through phase shifting. Specifically, three phase-shifting with an interval of $2\pi/3$ is common-used. Such phase-shifting results in three raw images, forming an equation set:

$$\begin{cases} \tilde{D}_1(k) = I_0\big[\tilde{S}(k) + 0.5me^{-i\varphi_1}\tilde{S}(k + k_0) + 0.5me^{i\varphi_1}\tilde{S}(k - k_0)\big]OTF(k) \\ \tilde{D}_2(k) = I_0\big[\tilde{S}(k) + 0.5me^{-i\varphi_2}\tilde{S}(k + k_0) + 0.5me^{i\varphi_2}\tilde{S}(k - k_0)\big]OTF(k), \\ \tilde{D}_3(k) = I_0\big[\tilde{S}(k) + 0.5me^{-i\varphi_3}\tilde{S}(k + k_0) + 0.5me^{i\varphi_3}\tilde{S}(k - k_0)\big]OTF(k) \end{cases} \tag{5}$$

where $\varphi_1 = \varphi_0$; $\varphi_2 = \varphi_0 + 2\pi/3$; $\varphi_3 = \varphi_0 + 4\pi/3$. The solution of **Eq. 5** is:

$$\begin{cases} \tilde{S}(k) = \dfrac{1}{3I_0}\big[\tilde{D}_1(k) + \tilde{D}_2(k) + \tilde{D}_3(k)\big]\Big/OTF(k) \\[2mm] \tilde{S}(k + k_0) = \dfrac{2e^{i\varphi_0}}{3mI_0}\big[\tilde{D}_1(k) + e^{i\frac{2\pi}{3}}\tilde{D}_2(k) + e^{i\frac{4\pi}{3}}\tilde{D}_3(k)\big]\Big/OTF(k). \\[2mm] \tilde{S}(k - k_0) = \dfrac{2e^{-i\varphi_0}}{3mI_0}\big[\tilde{D}_1(k) + e^{i\frac{4\pi}{3}}\tilde{D}_2(k) + e^{i\frac{2\pi}{3}}\tilde{D}_3(k)\big]\Big/OTF(k) \end{cases} \tag{6}$$

Making the inverse Fourier transform for **Eq. 6**, we get:

$$\begin{cases} S(r) \otimes PSF(r) = \dfrac{1}{3I_0}[D_1(r) + D_2(r) + D_3(r)] \\[2mm] FT^{-1}\{\tilde{S}(k + k_0)\} \otimes PSF(r) = \dfrac{2e^{i\varphi_0}}{3mI_0}\big[D_1(r) + e^{i\frac{2\pi}{3}}D_2(r) + e^{i\frac{4\pi}{3}}D_3(r)\big], \\[2mm] FT^{-1}\{\tilde{S}(k - k_0)\} \otimes PSF(r) = \dfrac{2e^{-i\varphi_0}}{3mI_0}\big[D_1(r) + e^{i\frac{4\pi}{3}}D_2(r) + e^{i\frac{2\pi}{3}}D_3(r)\big] \end{cases} \tag{7}$$

The first equation of **Eq. 7** indicates that the conventional wide-field image can be reconstructed by summating the three raw images. Most notably, on the right side of the second and third equations, the terms of the square brackets identically represent the OS image, according to the RMS algorithm from the first report of OS-SIM [1]:

FIGURE 1 | The schematic of the DMD-based LED-illumination SIM microscope.
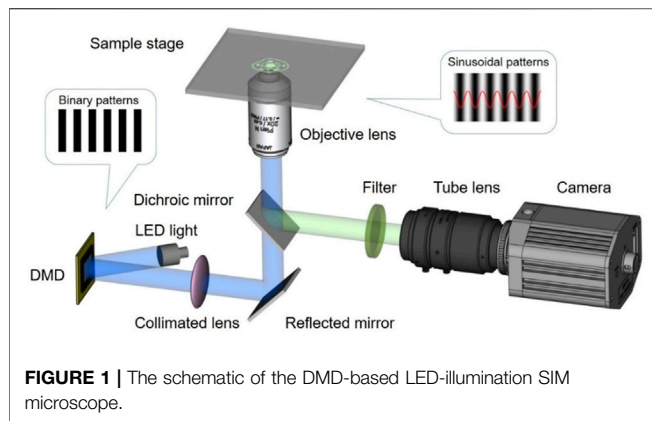
$$
\begin{aligned}
D_{os}(r) &= \left| D_1(r) + e^{i\frac{2\pi}{3}} D_2(r) + e^{i\frac{4\pi}{3}} D_3(r) \right| \\
&= \left| D_1(r) + e^{i\frac{4\pi}{3}} D_2(r) + e^{i\frac{2\pi}{3}} D_3(r) \right| \\
&= \frac{\sqrt{2}}{2} \sqrt{(D_2(r) - D_1(r))^2 + (D_3(r) - D_2(r))^2 + (D_1(r) - D_3(r))^2},
\end{aligned}
\tag{8}
$$

where the symbol $| \ |$ denotes the modulus operation. Combining **Eqs 7** and **8**, the OS image can be rewritten as:

$$
D_{os}(r) =
\begin{cases}
\left| \dfrac{3mI_0}{2e^{i\varphi_0}} FT^{-1} \left\{ \tilde{S}(k + k_0) \right\} \otimes PSF(r) \right|, \ or \\[2ex]
\left| \dfrac{3mI_0}{2e^{-i\varphi_0}} FT^{-1} \left\{ \tilde{S}(k - k_0) \right\} \otimes PSF(r) \right|
\end{cases}
. \tag{9}
$$

Since $\tilde{S}(k + k_0)$ and $\tilde{S}(k - k_0)$ are symmetric to the original point, the two equations in **Eq. 9** are equivalent. This implies the OS image is directly correlated to the acentric spectrum of $\tilde{S}(k + k_0)$ or $\tilde{S}(k - k_0)$. This provides an alternative way to reconstruct the OS image in the Fourier domain, which can apply filtering operation to reduce the background noise to enhance the performance of the OS image.

EXPERIMENTAL VERIFICATION

Experimental Setup

The experimental verification for the Fourier-OS-SIM is conducted in the home-built DMD-based LED illumination SIM microscope [14], whose scheme is illustrated in **Figure 1**. High brightness LED (center wavelength λ = 470 nm, LED4D251, Thorlabs, United States) is employed as the light source. After expanding and collimating, the LED beam incidents on the DMD chip (2,560 × 1,600 pixels, V-9001UV, ViALUX, Germany) at an angle of 24° with respect to the normal of the DMD panel. The rotation and phase-shifting of the fringe illumination are realized by rapidly refreshing the DMD patterns. In the binary pattern mode, the refreshing rate can reach 22 kHz. The objective lens (20×/NA0.45, Nikon, Japan) is used for fringe projection and imaging of samples. The sample is placed on an XYZ motorized translation stage for accurately positioning the observed target and axially scanning with a minimum step of 50 nm (M-405. DG,

Physik Instruments Inc., Germany). The excited fluorescence light passes through the dichroic beamsplitter (edge 473–491 nm, Semorock, United States), the filter (490 nm long-pass, Semorock, United States), the zoom lens (70–300 mm, F/4–5.6, Nikon, Japan), and is recorded by the scientific CMOS camera (2,048 × 2,048 pixels, 100 fps, Orca Flash 4.0, Hamamatsu, Japan). The Arduino Uno board [15] with C++ programming triggers all the electric components in sequence.

Background Noise Suppression *via* Fourier-OS-SIM

The experiment was performed with a mixed pollen grains specimen (Thermofisher). The autofluorescence signal was excited by the 470 nm LED light. The camera exposure time was 200 ms, and the field-of-view (FOV) area was measured to be $320 \times 320 \ \mu m^2$ by a micro ruler. We designed a 1D binary pattern with six pixels per period to produce the sinusoidal structured illumination fringe. The required three phase-shifts were realized by moving the fringe with a distance of two pixels for each step, corresponding to a $2\pi/3$ interval. With the f = 400 mm collimated lens and the 20× objective lens, the six pixels per period fringe (DMD pixel size 7.56 μm) were demagnified into 1.134 μm/period in the sample plane. The system has an optical resolution of about 0.522 μm (λ/2NA). The structured illumination frequency is nearly half of the cut-off frequency, meeting with the optimal condition of the OS-SIM theory [3].

Figure 2 shows the reconstruction results of the wide-field, RMS algorithm, and the Fourier-OS-SIM for the same input of three phase-shifted fringe images. For the Fourier-OS-SIM image, we first conducted the input in the reconstruction framework of SR-SIM and then fused the extended spectra of $\tilde{S}(k + k_0)$ and $\tilde{S}(k - k_0)$ in **Eq. 9**. It should be noted that the spectra fusion process does not involve the spectrum of $\tilde{S}(k)$ so as to eliminate the deterioration from the out-of-focus background. It can be seen that the contrasts of **Figures 2B,C** are much better than that of **Figure 2A**, demonstrating the optical sectioning capacity of the RMS algorithm and the Fourier-OS-SIM. From the zoom-in parts, we can see that the inner circle area, which indicates the background, **Figure 2C** is darker than **2B**, implying the background level of Fourier-OS-SIM is lower than that of RMS. The noise in **Figure 2F** is less intensive than **2E**; thus, **Figure 2F** is sharper and smoother than **2E**. The histograms of **Figures 2E,F** also reflect the noise degree, as shown in **Figures 2G,H**. The histogram of **Figure 2G** is more discrete and steeper than **2H**, which means the noise of Fourier-OS-SIM is more modest than the RMS algorithm.

Additional Background Noise Suppression by Filtering

One significant advantage of OS-SIM in the frequency domain is that plenty of filters can suppress the random electrical noise and photon shot noise or compound in an image. Here, we take the simplest Gaussian low-pass filter as an example to enhance the performance of Fourier-OS-SIM image. The radius of the Gaussian low-pass filter was set to two pixels, considering that
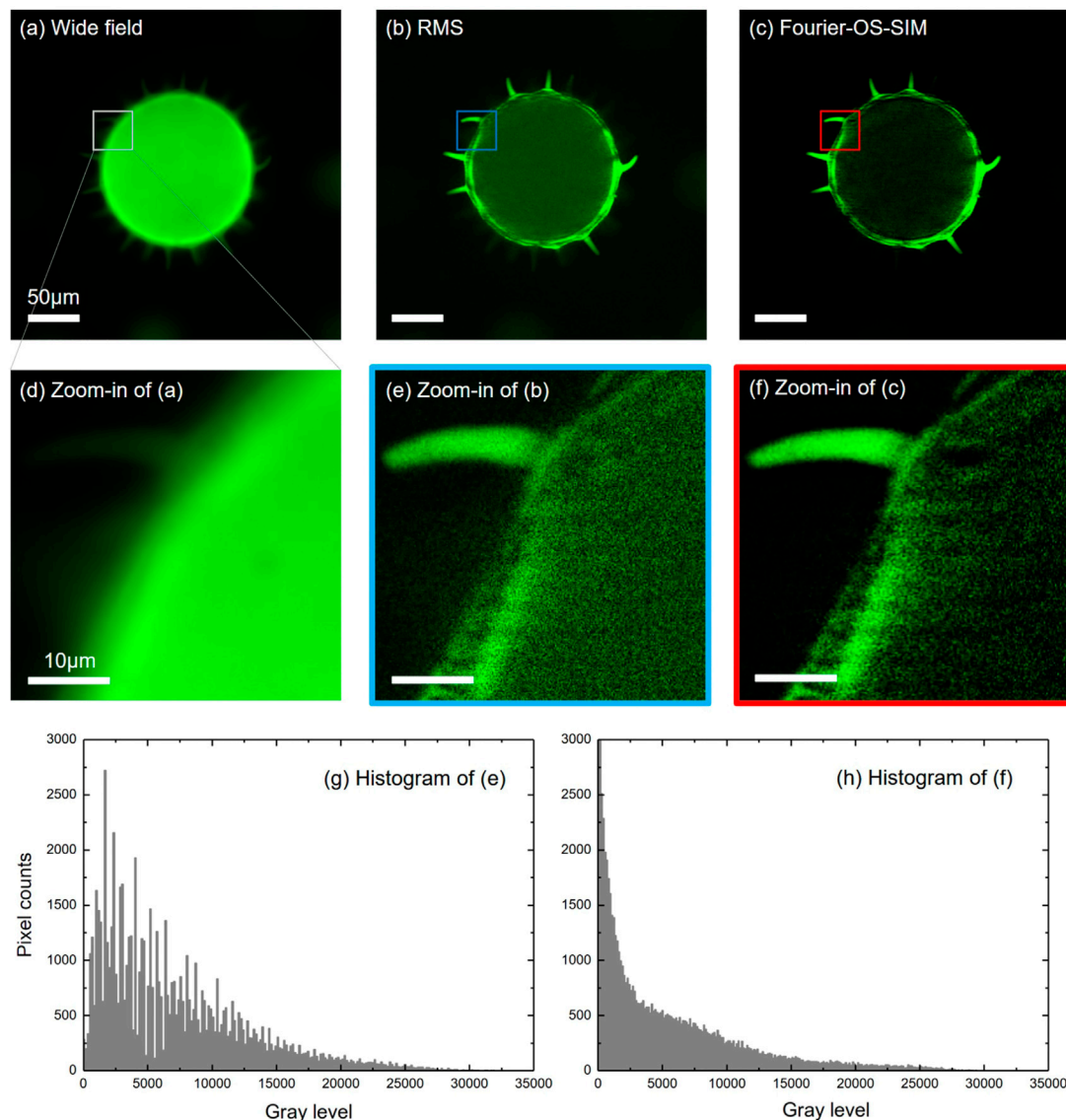
FIGURE 2 | Experimental results of the Fourier-OS-SIM in comparison with the Wide-field and RMS algorithm for imaging pollen grains. **(A–C)**: images of the Wide-field, RMS, and Fourier-OS-SIM, respectively. **(D–F)**: the zoom-in parts of the marked areas indicated in **(A–C)**. **(G–H)**: the histograms of **(E,F)**, respectively.

the imaging resolution is above six image pixels. Therefore, the filter does not harm the image signal. The filtered image of **Figure 3C** displays smoother than the original Fourier-OS-SIM image of **Figure 3B**; meanwhile, the details of **Figure 3B** are almost reserved. The SNR value was employed to evaluate the image quality. A reference image was pre-generated by subtracting the background of the wide-field image by using the ImageJ software (Biomedical imaging group, EPFL). The SNR value was calculated by using the SNR plugin of ImageJ. For comparison, a filtered RMS image is also presented in **Figure 3D**, which is applied with the same Gaussian filter. Although **Figure 3D** looks smoother than **Figure 3C**, the SNR of **Figure 3C** is much better than that of **Figure 3D**. From the SNR values in **Figures 3A–D**, we can see that the Fourier-OS-SIM

image (SNR 7.97 dB) is better than the RMS image (4.43 dB); and the Fourier-OS-SIM image is further improved by applying an exemplified Gaussian filter (SNR increases from 7.97 to 15.57 dB). The intensity profiles along the marked lines in RMS, Fourier-OS-SIM, filtered Fourier-OS-SIM, and filtered RMS images are plotted as in **Figures 3E–H**. The curves present that the SNR of the Fourier-OS-SIM is superior to the RMS algorithm, especially after the Gaussian low-pass filtering.

Image Reconstruction Accelerated by GPU

The drawback of the Fourier-OS-SIM is mainly related to the time-cost of the Fourier transform operation. To address this problem, we adopted the advanced GPU acceleration technology to boost the computational speed of Fourier transforms. An
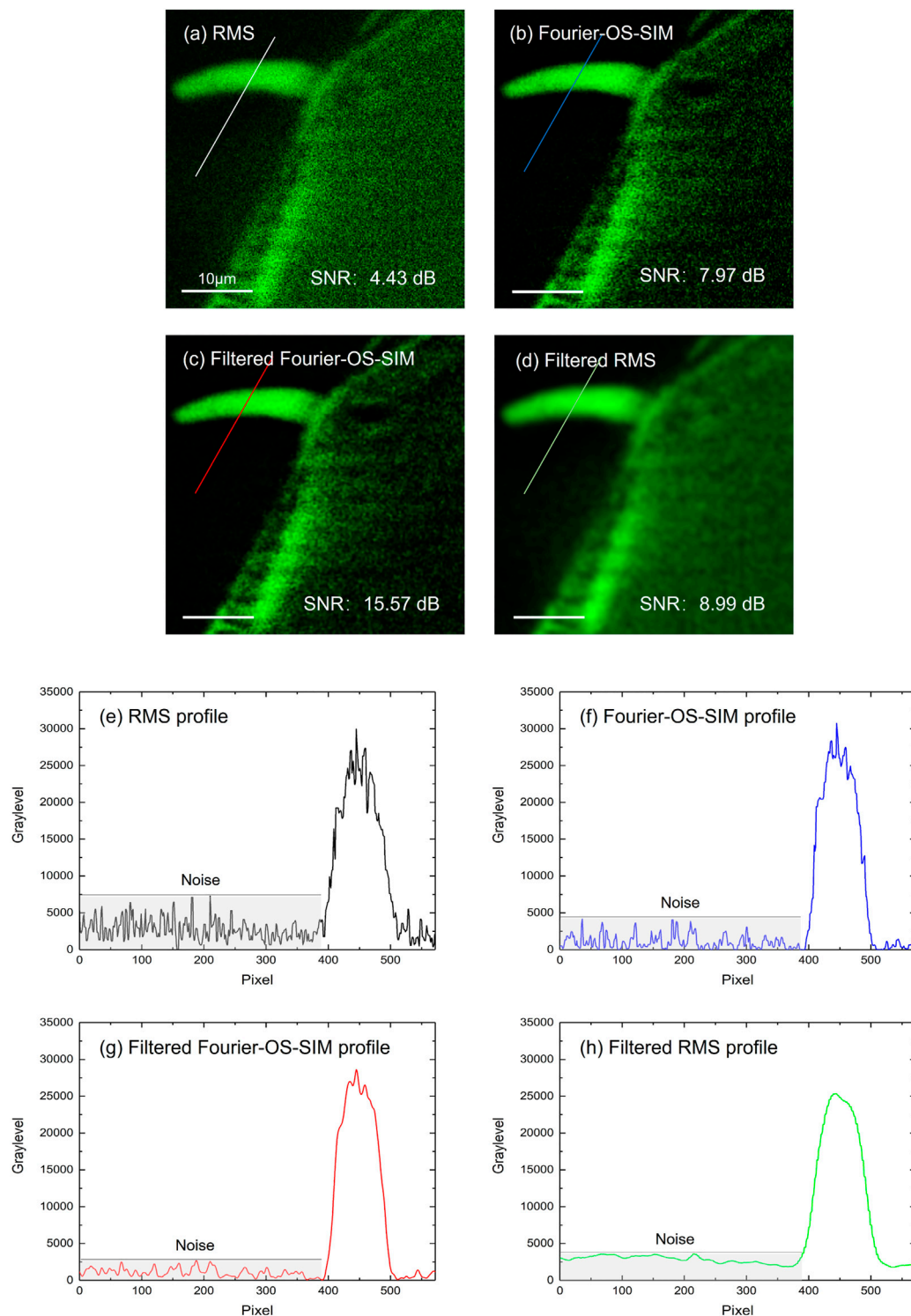
FIGURE 3 | Fourier-OS-SIM images before and after Gaussian low-pass filtering compared to the RMS image. **(A–D)**: images of the RMS, Fourier-OS-SIM before and after filtering, and the filtered RMS, respectively. **(E–H)**: the intensity profiles along the marked lines in **(A–D)**.

open-source library OpenCV [16] with Nvidia CUDA [17] support, was used to simplify the GPU acceleration. Three phase-shifted structured illumination images with 2,048 ×

2,048 pixels were employed as the same input for Fourier-OS-SIM and RMS scripts. The scripts were written in C++ and operated in a workstation computer (Intel Xeon Silver 4114 CPU,

FIGURE 4 | The MIPs of 3D images from the Fourier-OS-SIM and the RMS sectioned slice stacks. **(A,D)**: the MIPs of the RMS and the Fourier-OS-SIM slice stacks visualized by 3D volume rendering, respectively. **(B,E)**: the zoom-in images of the ROI in RMS and Fourier-OS-SIM 3D images. **(C,F)**: the intensity profiles along the cut-lines in **(B,E)**.
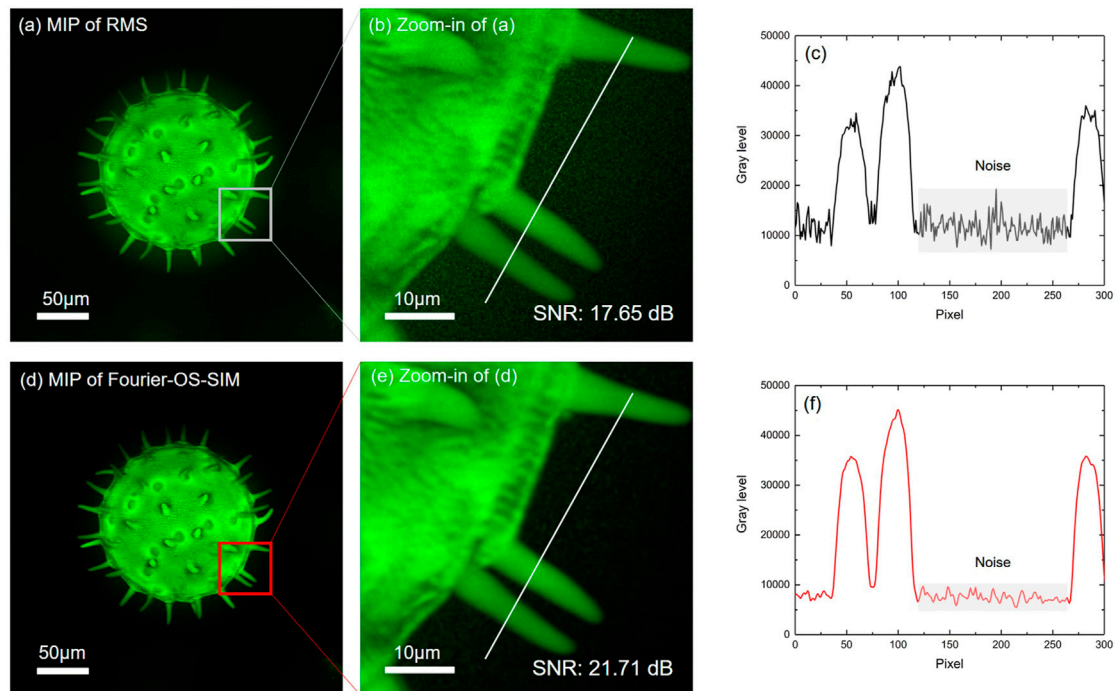
128GB RAM, Nvidia GeForce RTX 2080Ti graphic card, Windows 10 64 bit operation system). We iteratively ran the Fourier-OS-SIM, the accelerated Fourier-OS-SIM, and the RMS scripts 150 times, respectively, to record the reconstruction time. After acceleration, the Fourier-OS-SIM cost-time drops to 0.323 s from 1.591 s, achieving a nearly five folds boost. Although the accelerated Fourier-OS-SIM consuming time is still greater than RMS (0.026 s), the time gap is narrowed through GPU acceleration.

The Resultant 3D Imaging

3D imaging is reconstructed from the series of axially-scanned optically sectioned images. The optical sectioning enhancement efforts studied above can improve the performance of 3D images. We scanned the pollen sample by a step of 0.2 μm axially and sectioned 144 slices. **Figures 4A,D** present the maximum intensity projections (MIP) of the RMS and the Fourier-OS-SIM slice stacks visualized through 3D volume rendering, respectively. To demonstrate the superiority of the Fourier-OS-SIM more clearly, we zoomed in a rectangle ROI labeled in **Figures 4A,D**, as shown in **Figures 4B,E** accordingly. The intensity profiles along the same location lines in **Figures 4B,E** were plotted in **Figures 4C,F**. By comparing the two curves, we can see that the Fourier-OS-SIM curve is much smoother than the RMS, demonstrating a significant background noise suppression. The SNR values of **Figures 4B,E** support that the Fourier-OS-SIM algorithm is superior to the RMS algorithm.

CONCLUSION

We have proposed a Fourier reconstruction scheme for optical sectioning SIM, termed Fourier-OS-SIM. In theory, an equivalent expression of the common-used RMS reconstruction algorithm has been deduced in light of the SR-SIM principle in the Fourier domain. In contrast to the RMS reconstruction approach, experimental results show that the Fourier-OS-SIM is more advanced at background noise suppression. More importantly, suppressing image background in the Fourier domain is more accessible and effective than in the spatial domain in general instances, because the Fourier-OS-SIM intrinsically operates in the Fourier domain, a frequency filter can be straightforwardly applied to suppress noise further. Thus, the Fourier-OS-SIM provides a new possibility that specific background noise suppression filters can be involved in this pipeline to suppress background noise further. The improved performance of Fourier-OS-SIM may find more applications in biomedical or industrial fields.

DATA AVAILABILITY STATEMENT

The original contributions presented in the study are included in the article/Supplementary Material, further inquiries can be directed to the corresponding authors.

AUTHOR CONTRIBUTIONS

BY conceived and supervised the project. SD, HW, and DD performed experiments. DD Wrote the programming scripts. JQ, TP, CB, and JM assisted to data analysis. SD and DD wrote the manuscript. All the authors contributed to discuss and revise the manuscript.

REFERENCES

1. Neil MAA, Juškaitis R, Wilson T. Method of Obtaining Optical Sectioning by Using Structured Light in a Conventional Microscope. *Opt Lett* (1997) 22: 1905–7. doi:10.1364/OL.22.001905

2. Bayguinov PO, Oakley DM, Shih C-C, Geanon DJ, Joens MS, Fitzpatrick JAJ. Modern Laser Scanning Confocal Microscopy. *Curr Protoc Cytometry* (2018) 85:e39. doi:10.1002/cpcy.39

3. Dan D, Yao B, Lei M. Structured Illumination Microscopy for Super-resolution and Optical Sectioning. *Chin Sci Bull* (2014) 59:1291–307. doi:10.1007/s11434-014-0181-1

4. Gustafsson MGL. Surpassing the Lateral Resolution Limit by a Factor of Two Using Structured Illumination Microscopy. *J Microsc* (2000) 198:82–7. doi:10.1046/j.1365-2818.2000.00710.x

5. Gao P, Yuan C. Resolution Enhancement of Digital Holographic Microscopy via Synthetic Aperture: a Review. *Light Adv. Manuf.* (2022) 3:1. doi:10.37188/lam.2022.006

6. Santos S, Chu KK, Lim D, Bozinovic N, Ford TN, Hourtoule C, et al. Optically Sectioned Fluorescence Endomicroscopy with Hybrid-Illumination Imaging through a Flexible Fiber Bundle. *J Biomed Opt* (2009) 14:030502. doi:10.1117/1.3130266

7. Lim D, Chu KK, Mertz J. Wide-field Fluorescence Sectioning with Hybrid Speckle and Uniform-Illumination Microscopy. *Opt Lett* (2008) 33:1819–21. doi:10.1364/ol.33.001819

8. Shi R, Kong L. Evaluating Structured-Illumination Patterns in Optimizing Optical-Sectioning of HiLo Microscopy. *J Phys D: Appl Phys* (2021) 54:414001. doi:10.1088/1361-6463/ac153b

9. Patorski K, Trusiak M, Tkaczyk T. Optically-sectioned Two-Shot Structured Illumination Microscopy with Hilbert-Huang Processing. *Opt Express* (2014) 22:9517–27. doi:10.1364/OE.22.009517

10. Bhuiyan SMA, Adhami RR, Khan JF. A Novel Approach of Fast and Adaptive Bidimensional Empirical Mode Decomposition. In: IEEE International Conference on Acoustics, Speech and Signal Processing (ICASSP 2008). Las Vegas, NV, USA: IEEE (2008). doi:10.1109/ICASSP.2008.4517859

11. Zhou X, Lei M, Dan D, Yao B, Qian J, Yan S, et al. Double-exposure Optical Sectioning Structured Illumination Microscopy Based on Hilbert Transform Reconstruction. *PLoS One* (2015) 10:e0120892. doi:10.1371/journal.pone.0120892

12. Chai C, Chen C, Liu X, Lei Z. Deep Learning Based One-Shot Optically-Sectioned Structured Illumination Microscopy for Surface Measurement. *Opt Express* (2021) 29:4010–21. doi:10.1364/OE.415210

13. Bai C, Qian J, Dang S, Peng T, Min J, Lei M, et al. Full-color Optically-Sectioned Imaging by Wide-Field Microscopy via Deep-Learning. *Biomed Opt Express* (2020) 11:2619–32. doi:10.1364/BOE.389852

14. Dan D, Lei M, Yao B, Wang W, Winterhalder M, Zumbusch A, et al. DMD-based LED-Illumination Super-resolution and Optical Sectioning Microscopy. *Sci Rep* (2013) 3:1116. doi:10.1038/srep01116

15. Arduino Uno. *Arduino UNO* (2022). Available from: https://www.arduino.cc/en/Main/arduinoBoardUno> (Accessed March 20, 2022).

16. Open Source Computer Vision Library. *Open Source Computer Vision Library* (2022). Available from: https://opencv.org/(Accessed March 20, 2022).

17. Sanders J, Kandrot E. *CUDA by Example: An Introduction to General-Purpose GPU Programming*. Boston: Addison-Wesley Professional (2010).

FUNDING

High Spatio-Temporal Resolution Condenser-Free Quantitative Phase Contrast Microscopy

Ying Ma[1,2†], Lin Ma[1†], Juanjuan Zheng[1,3], Min Liu[1], Zeev Zalevsky[4] and Peng Gao[1]*

[1]*School of Physics and Optoelectronic Engineering, Xidian University, Xi'an, China,* [2]*Precision Machinery & Precision Instrumentation, University of Science and Technology of China, Hefei, China,* [3]*State Key Laboratory of Transient Optics and Photonics, Xi'an Institute of Optics and Precision Mechanics, Chinese Academy of Sciences, Xi'an, China,* [4]*Bar-Ilan University, Faculty of Engineering and Nano Technology Center, Ramat-Gan, Israel*

Quantitative phase-contrast microscopy (QPCM) provides an effective approach for label-free detection of transparent samples. In this study, we propose a condenser-free quantitative phase-contrast microscopy (CF-QPCM), in which several light-emitting diodes (LEDs) distributed on a ring are used for direct ultra-oblique illumination. Such condenser-free design greatly simplifies the system's structure and releases the space for installing samples. Quantitative phase maps are reconstructed by retarding the unscattered components of the object waves for a series of phases 0, $\pi/2$, π, and $3\pi/2$ through a high-speed spatial light modulator (SLM). With this system, quantitative phase imaging of live cells has been achieved at a spatial resolution of 231 nm (lateral) and a frame rate of 250 Hz. We believe that the proposed CF-QPCM can contribute to biomedical, industrial, chemistry fields, etc.

Keywords: quantitative phase imaging, phase contrast, ultra-oblique illumination, label-free, non-invasive

INTRODUCTION

The invention of microscope triggered a revolution in science and cognition, and it also greatly promoted the development of life sciences. Electron microscopes have sub-nanometer spatial resolution and play an incomparable value in structural biochemistry research [1, 2], however, the complex sample preparation hinders the application of electron microscopy in live cells. On the contrary, fluorescence microscopy has been acting as one of the mainstream techniques in life science due to the feature of being non-invasive and the capability to selectively visualize the bio-structures of interest by fluorescence labeling [3–6]. Nevertheless, the application of fluorescence microscopy is hindered by the phototoxicity and photobleaching of fluorophores used.

Being a label-free and non-invasive imaging technique, quantitative phase microscopy (QPM) can quantitatively access the thickness or refraction index (RI) distributions of samples [7, 8]. Digital holography microscopy (DHM) can perform high-accuracy phase measurements of transparent samples by utilizing the interference between an object wave and an off-axis reference wave [9–11]. Common-path configurations were used in DHM to enhance the immunity of the system to environmental disturbances [12]. Researchers further improved the spatial resolution and realized 3D tomographic imaging by mechanically scanning the illumination [13, 14]. Nevertheless, 240 angles scanning within an annular quasi-2π range are required and limit the imaging speed below 0.8 frames per second (FPS).

Single-beam QPM approaches, in terms of ptychographic iterative engine (PIE) [15] and Fourier ptychographic microscope (FPM) [16–18] have been developed rapidly in recent years, providing the
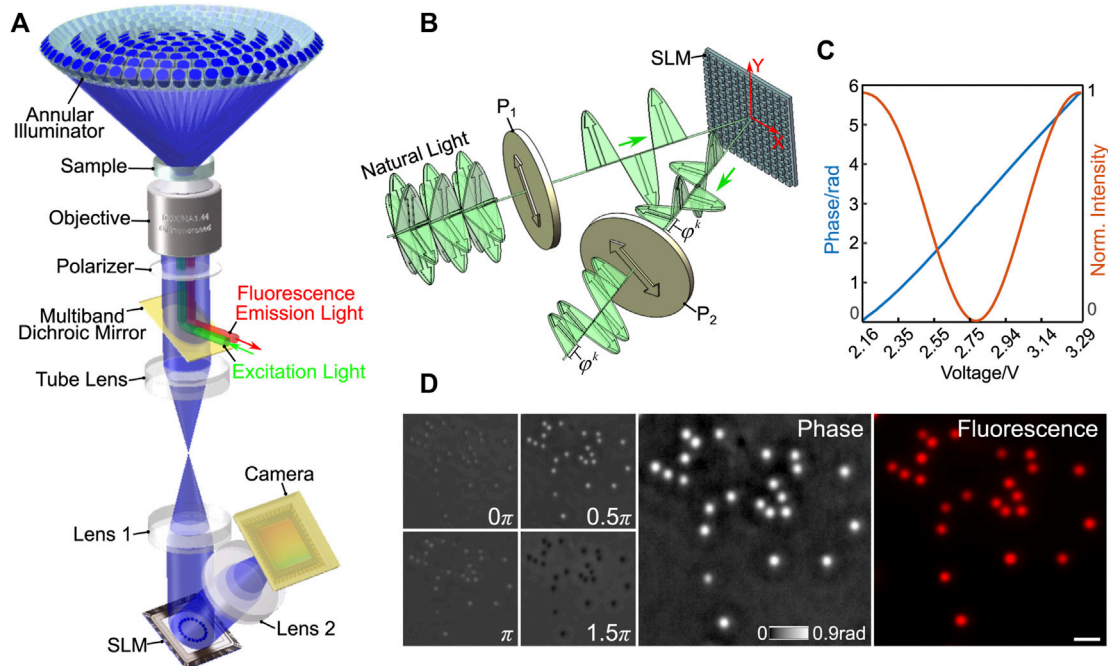
FIGURE 1 | (A) The schematic diagram of CF-QPCM. **(B)** The schematic setup for SLM calibration. **(C)** Calibration curves: the measured intensity (orange) and the modulated phase (blue) versus the loaded voltage. **(D)** Phase and fluorescence images of fluorescent polystyrene spheres (diameter: 300 nm). The left is the raw intensity images obtained during the four-step phase-shifting operation, and the right is the reconstructed phase image and the fluorescence image. Scale bar in **(D)** represents 1 μm.

complex amplitude information of samples by recording a series of diffraction patterns under different illumination positions/directions, or other physical constraints. It is worth noting that the reconstruction of a high-resolution image with these methods requires recording hundreds of low-resolution diffraction patterns, and hence their imaging speed is greatly limited. QPM based on asymmetrical illumination [19] and transport of intensity equation (TIE) [20] can also retrieve the phase mapping of a sample using a relatively-complicated recovery process. Popescu and his co-workers proposed gradient light interference microscopy (GLIM), realizing 3D imaging of optically thick embryos, however it is not suitable for discontinuous samples due to its differential interference contrast essence [21]. Alternatively, phase-contrast imaging, initially proposed by Zernike in the 1940s, can convert the phase distribution of a transparent object into intensity modulation and, therefore, has also been playing an important role in life science [22]. Further, condenser-free Zernike phase-contrast microscopy using annularly-arranged or radially-scanned LEDs was proposed, simplifying the configuration and easing sample installation [23]. As an evolution from qualitative phase imaging to quantitative phase imaging, spatial light interference microscopy (SLIM) uses a spatial light modulator (SLM) instead of the conventional phase plate to perform quantitative phase imaging at temporal and spatial resolutions of 0.6 s and 350 nm, respectively, [24, 25]. Recently, the oblique angle of the annular illumination in SLIM was enlarged, forming the ultra-oblique SLIM, which enhanced the

lateral resolution to 270 nm at an imaging speed of 250 Hz [26], and which identified mitochondria inside live cells by combining a neural network with SLIM [27]. It should be noted that the annular illumination module in SLIM system is either complicated or costly since they require a water-immersed objective lens with a high numerical aperture (NA) to provide ultra-oblique illumination (~70°). Moreover, the condenser in the illumination module narrows the space where samples can be installed and hence induce the inconvenience of loading samples.

In this study, we propose condenser-free quantitative phase microscopy, termed CF-QPCM. High spatio-temporal resolution QPM imaging is performed by combining the oblique illumination from annularly-distributed LEDs and the concept of the Zernike phase contrast. The proposed system greatly simplifies the architecture, releases the complexity of sample installation, and avoids the cell contamination caused by a water-immersed condenser objective lens. CF-QPCM can be combined with various fluorescence microscopies to perform multi-modality imaging, providing complementary information for the same sample.

METHODS

Principle of CF-QPCM

CF-QPCM is expediently constructed in a wide-field fluorescence microscope frame, where a dichroic mirror wheel is equipped for integrating fluorescence imaging modality, as shown in

Figure 1A. An illuminator is comprised of dozens of LEDs, which are distributed in several concentric rings. The LEDs on different rings can be chosen independently, so that they can illuminate a sample at different angles. All LEDs used are identical and have a narrow spectrum band (470 ± 10 nm, central wavelength ± half-width). For CF-QPCM imaging, only the LEDs on one ring are lit up simultaneously to achieve off-axis illuminations. The emitted light from the LEDs directly illuminates the sample, which is placed at the front focal plane of the objective lens (Leica, ×100/1.44 Oil Immersion, WD-0.17, Germany). After passing through the sample, an object wave is formed, which carries the structural and compositional information of the sample. The object wave can be divided into scattered and unscattered waves. The scattered and unscattered waves are Fourier transformed by the objective lens and further imaged to a high-speed SLM (Meadowlark Optics, MSP1920-400-800-HSP8, United States) by a telescope system (shown in **Figure 1A**). A polarizer is placed before the SLM to maximize the phase modulation efficiency of the SLM. To perform quantitative phase imaging of CF-QPCM, the spectra of unscattered waves, which are apparently the images of all the LEDs, are retarded in phase for 0, 0.5π, π, and 1.5π by the SLM, as seen in **Figure 1A**. For simplicity, the sample to be studied is described with the transmittance function $t(x, y) = A(x, y) \cdot exp(j\phi(x, y))$, where (x, y) are the coordinates on the sample plane, $A(x, y)$ and $\varphi(x, y)$ are the transmittance and phase modulation of the sample on the illumination light. Then, a series of phase-contrast images that are essentially the interference between the scattered and unscattered waves are successively recorded by the camera (Andor, Zyla 4.2, United Kingdom):

$$I(x, y, \delta\varphi) = I_0(x, y) \cdot (1 + \beta^2(x, y) + 2\beta(x, y) \cdot \cos[\Delta\varphi(x, y) + \delta\varphi]) \quad (1)$$

Here, $I_0(x, y)$ is the intensity distribution of the unscattered waves, $\Delta\varphi(x, y)$ and $\beta(x, y)$ are the phase difference and amplitude ratio between the scattered and unscattered waves, respectively. And $\delta\varphi = m \cdot \pi/2$ ($m = 0,1,2,3$) is the phase retarding value to the unscattered ones. With $\delta\varphi$ being switched four times, the phase distribution of the sample can be easily recovered by:

$$\varphi(x, y) = \tan^{-1}\left(\frac{\beta(x, y) \cdot \sin(\Delta\varphi(x, y))}{1 + \beta(x, y) \cdot \cos(\Delta\varphi(x, y))}\right) \quad (2)$$

Here $tan^{-1}\{\cdot\}$ denotes the arctangent function. Obviously, the temporal resolution of the system is determined by the maximal frame rate of the sCMOS camera and the SLM (the lower one of the two). Considering four frames are needed to reconstruct a quantitative phase image, the temporal resolution of the system is 4 ms. Ulteriorly, the temporal resolution of the system can reach up to 250 FPS by reusing the raw phase-shifting images [28].

SLM Calibration

SLM is the key component in CF-QPCM, whose nonlinear optical response of liquid crystal to loaded voltage needs to be calibrated for a linear response between the applied voltage and the generated phase. We propose a simple method to calibrate the

SLM accurately, which allows for measuring the response property of each pixel and avoiding the wavefront curvature induced by externally induced devices. The schematic diagram of the proposed SLM calibration is shown in **Figure 1B**. By nature, the liquid crystal in SLMs only respond to the light with the polarization orientation along the y direction (Y-axis), while it has no response to the light with the polarization orientation along the x direction (X-axis). Therefore, we set two polarizers, P_1 and P_2, with their polarization direction 45° with respect to the x-direction. After traversing through the first polarizer P_1 and modulated by the SLM, the resulted light beams can be written as

$$\begin{cases} E^x_{m,n} = A^x_{m,n} \cdot \exp(j \cdot \theta_{m,n}) \\ E^y_{m,n} = A^y_{m,n} \cdot \exp\left[j \cdot \left(\theta_{m,n} + \varphi^k_{m,n}\right)\right] \end{cases} \quad (3)$$

Here, m and n represent the pixel coordinates on the SLM along the x and y directions. $\varphi^k_{m,n}$ ($k = 1,2...255$) is the generated phase on a certain pixel when the kth voltage is applied. Then, the final light intensity generated at each pixel after passing through the second polarizer P_2 is calculated as:

$$I^k_{m,n} = 0.5 \cdot \left(A^x_{m,n}\right)^2 + 0.5 \cdot \left(A^y_{m,n}\right)^2 + A^x_{m,n} \cdot A^y_{m,n} \cdot \cos\left(\varphi^k_{m,n}\right) \quad (4)$$

The dc term $0.5 \cdot (A^x_{m,n})^2 + 0.5 \cdot (A^y_{m,n})^2$ and the modulation depth $A^x_{m,n} \cdot A^y_{m,n}$ can be determined when applying the voltage from 0 to the maximal voltage allowed and determining the maximal and minimal intensities for the intensity series obtained. Then the relation between the $\varphi^k_{m,n}$ and the voltage can be obtained with the $\cos^{-1}\{\cdot\}$ function, as is shown with the orange curve in **Figure 1C**. To verify the accuracy of the SLM calibration, a four-step phase measurement by CF-QPCM was performed on 300 nm fluorescent polystyrene spheres (RF300C, Huge Biotechnology), as shown in **Figure 1D**. Notably, the phase and fluorescence imaging were performed simultaneously, and the results are shown in **Figure 1D**-right. Considering the refractive indices of polystyrene (n) and the nutrient solution (n_m) are, respectively, 1.55 and 1.33, the induced maximum phase value by an individual polystyrene sphere can be estimated as $2\pi \cdot (n - n_m) \cdot d/\lambda = 2\pi \cdot (1.55 - 1.33) \cdot 300/470 = 0.88\ rad$, which is consistent with the measured value of 0.9 rad in the center of a sphere.

EXPERIMENTS AND RESULTS

Spatial Resolution Verification of CF-QPCM

In the CF-QPCM system, we use an annular illuminator circled by 24 LEDs, generating oblique illuminations (NA_{illu} = 0.7) to achieve higher spatial resolution. Under such illumination, a sample is imaged by an oil-immersed objective lens (×100/1.44, Leica). According to the principle of partially coherent imaging, the theoretical lateral resolution of the system is $\delta = \lambda/(NA_{imag} + NA_{illu})$ = 220 nm under the oblique illuminations and 326 nm under on-axis plane wave illumination, respectively. Then, we use 200 nm diameter fluorescent polystyrene spheres (RF200C, Huge Biotechnology) to measure the lateral resolution of the CF-QPCM system. **Figure 2** shows the images of the
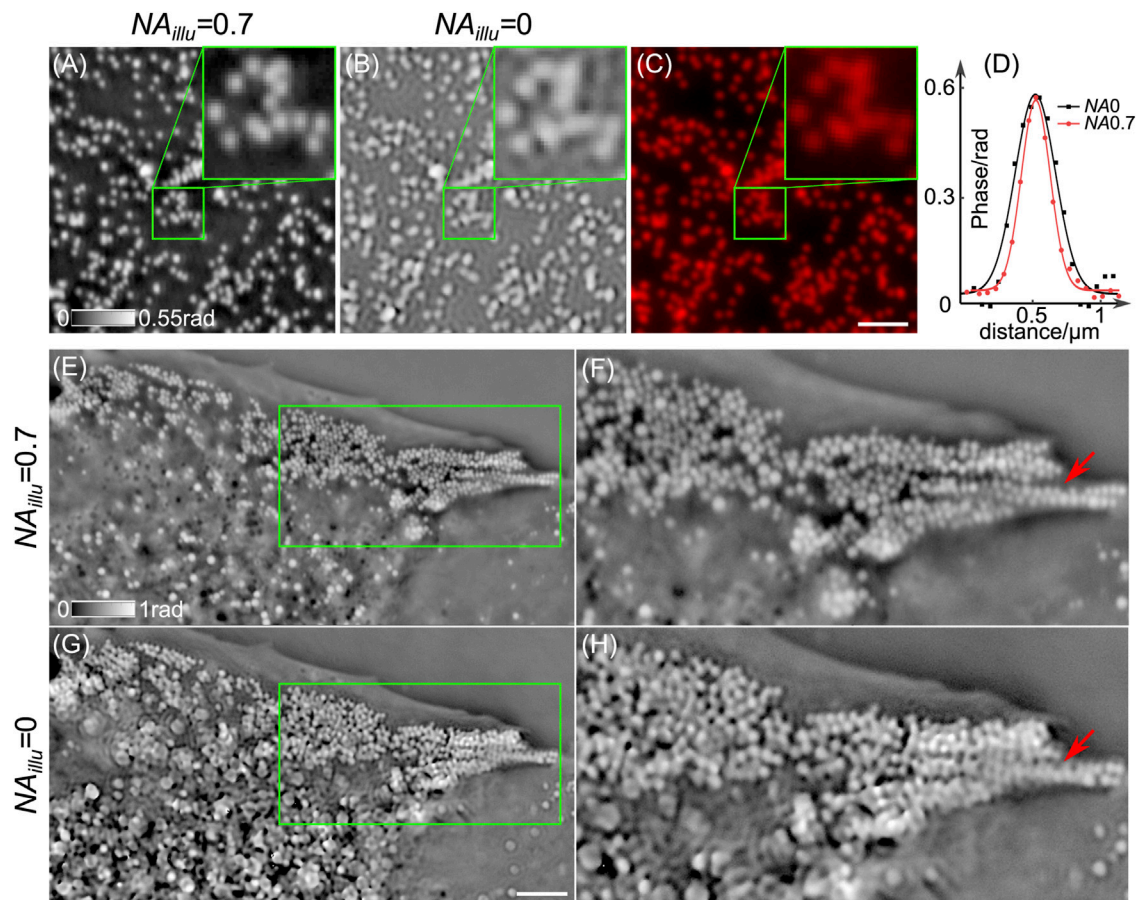
FIGURE 2 | CF-QPCM imaging of polystyrene spheres and lipid droplets inside live Cos7 cells. **(A,B)** The phase images of 200-nm diameter polystyrene spheres using CF-QPCM with annular illuminations (NA_{illu} = 0.7) and on-axis plane wave illumination (NA_{illu} = 0). **(C)** The fluorescence image of the polystyrene spheres. **(D)** The profiles along the lines crossing the centers of a sphere in **(A,B)**. **(E)** and **(G)** The phase images of live a Cos7 cell obtained by CF-QPCM with annular illumination (NA_{illu} = 0.7) and on-axis plane wave illumination (NA_{illu} = 0). **(F)** and **(H)** The enlarged views in the green boxes in **(E)** and **(G)** show the superiority of NA_{illu}-0.7 illumination over NA_{illu}-0 illumination on resolving minute structures of samples. Scale bars in **(C)** and **(G)**: 2 and 4 μm.

polystyrene spheres obtained with CF-QPCM in comparison with fluorescence imaging (**Figure 2C**). Specifically, **Figures 2A,B** are the phase images of the polystyrene spheres obtained with annular illumination (NA_{illu} = 0.7) and on-axis plane wave illumination (NA_{illu} = 0). The phase distributions along the line that crosses the center of the same individual sphere in **Figures 2A,B** were extracted and fitted with Gaussian functions in **Figure 2D**. It is apparent that the prior one has a higher spatial resolution than the later one. When dozens of spheres were analyzed like the way shown in **Figure 2D**, the statistics reveal that the measured lateral resolutions (in terms of full width at half maximum, FWHM) are $231 \pm 5\,nm$ and 330 ± 10 nm (mean ± standard deviation) for NA_{illu}-0.7 and NA_{illu}-0 illumination cases. The enlarged views in **Figures 2A,D** show the superiority of NA_{illu}-0.7 illumination over NA_{illu}-0 illumination on resolving minute structures of samples. Moreover, we also used the decorrelation analysis [29] to quantitively determine the lateral resolution of **Figures 2A,B**, and the results are 239 ± 10 nm and 319 ± 10 nm for the two illumination cases. The measured resolution is a little lower than

the theoretical resolution, as the imaging system is unavoidably accompanied by optical aberration. Further, we imaged lipid droplets inside live Cos7 cells with the above two illumination angles, as shown in **Figures 2E–H**. It is clear from **Figures 2F,H** that lipid droplets can be separated under NA_{illu}-0.7 illumination while failed under NA_{illu}-0 illumination. The comparison further confirms that the proposed CF-QPCM under oblique illumination renders the higher resolution images for fine structures inside live cells, compared with the QPCM with plane-wave illumination.

Dual-Modality Imaging of Live Cells

CF-QPCM can visualize fine structures of sub-cellular organelles inside live cells once for all with high contrast and high resolution, but it lacks the specificity of organelles. As a remedy, we integrated both the CF-QPCM module and fluorescence imaging module into a microscope frame to obtain complementary information simultaneously for the same organelles, as shown in **Figure 3**. First, we demonstrated phase and fluorescence dual-modality imaging on mitochondria in live
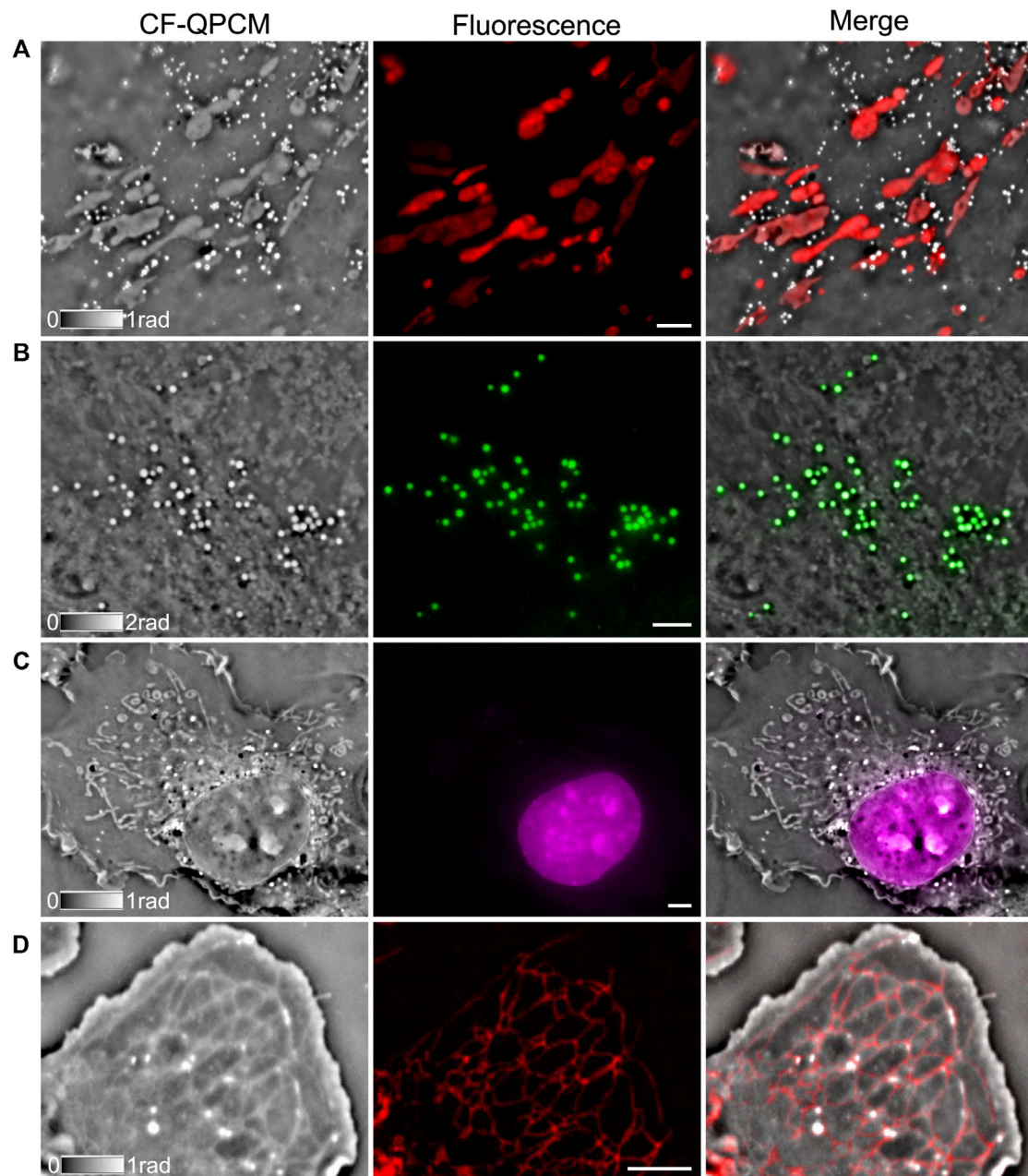
FIGURE 3 | Dual-modality images of live Cos7 cells obtained by combining CF-QPCM with a wide-field fluorescence imaging module. CF-QPCM (gray images) and wide-field fluorescence images (color images) of mitochondria **(A)**, lipid droplets **(B)**, cell nucleus with thin membrane **(C)**, and ER **(D)**. Scale bars in **(A–D)** represent 4 μm.

Cos7 cells stained with fluorescent dye (Thermo Fisher, MitoTracker 7512, United States), and the results are shown in **Figure 3A**. The merged image indicates that CF-QPCM can perform high-contrast imaging of mitochondria together with the surrounding organelles without fluorescent labeling. Second, we performed phase and fluorescence dual-modality imaging on lipid droplets in live Cos7 cells labeled with specific dye (Thermo Fisher, HCS LipidTOX, United States), as shown in **Figure 3B**. The phase images of the lipid droplets have high

contrast as their inner refractive index is quite different from the cytoplasm. Third, we performed phase and fluorescence dual-modality imaging on cell nucleus in live Cos7 labeled with desired dye (Biotium, NucSpot® Live 650 Nuclear Stain, United States), as shown in **Figure 3C**. The cell nucleus is often easily recognized since it has a clear membrane. The comparison between CF-QPCM and fluorescence images of the nucleus indicates that CF-QPCM can distinguish the nucleus from other surrounding organelles, such as mitochondria. Lastly, we performed phase

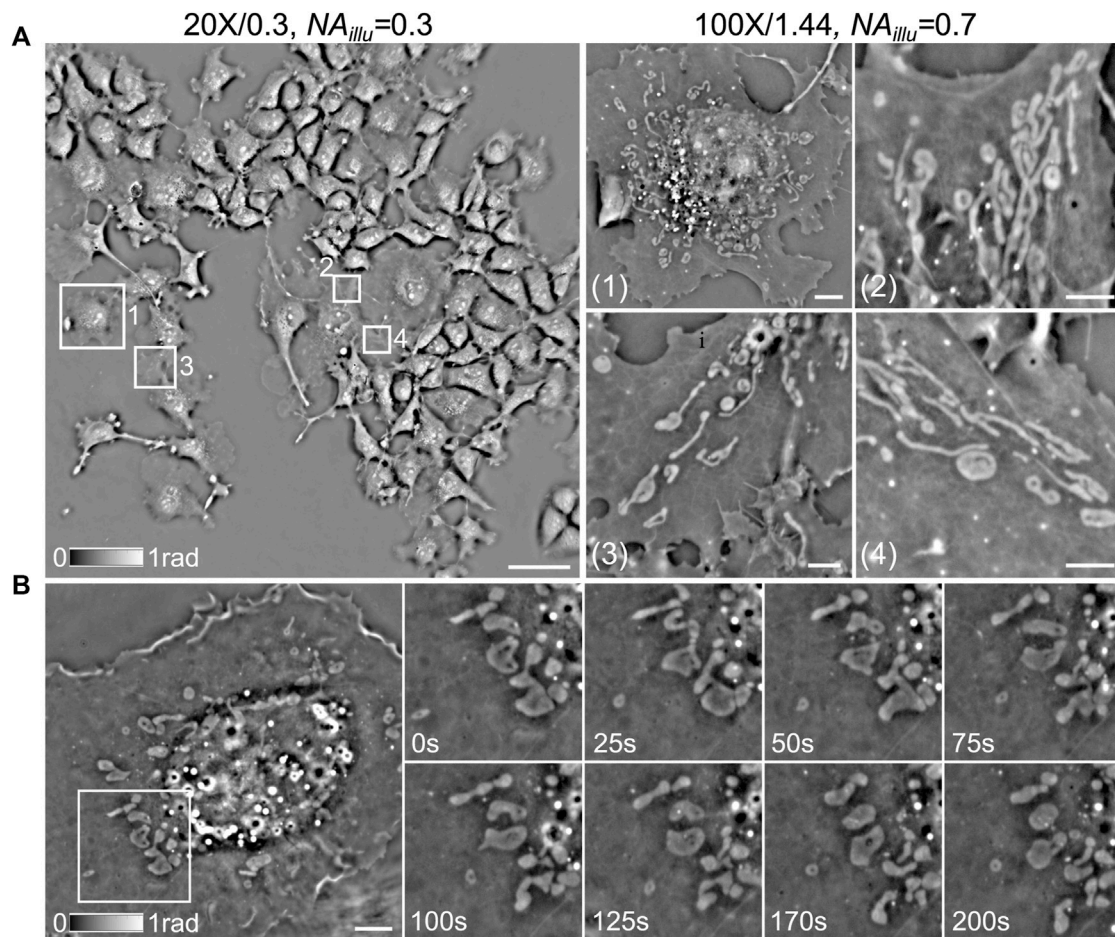**FIGURE 4 |** Phase imaging of live Cos7 cells with CF-QPCM under different configurations. **(A)** left: phase image of live Cos7 cells obtained with the large-FOV imaging mode; right: phase images of several sub-regions marked with white boxes on the left, obtained with the small-FOV imaging mode. **(B)** left: phase image of a live Cos7 cell obtained with the small-FOV imaging mode; right: time series of mitochondrial fission in the white box on the left. Scale bars in **(A)**-left, **(A)**-right, and **(B)** are 65 μm, 4 μm, and 6 μm, respectively.

and fluorescence dual-modality imaging on endoplasmic reticulum (ER) in live Cos7 cells labeled with ER Tracker (Thermo Fisher, ER Tracker E34250, United States), as shown in **Figure 3D**. Similar structures of ERs can be visualized in both the phase image and the fluorescence image. It is confirmed from the above experiments that CF-QPCM has the power to image organelles without fluorescent labeling and is compatible with other imaging modalities to provide complementary information.

Biological Dynamics Captured by CF-QPCM

As mentioned before, the LEDs on the rings with different diameters can be chosen to generate different illumination angles, according to different field of view (FOV) of CF-QPCM imaging. For the large-FOV imaging mode, an objective (×20/0.3) and the LEDs on a ring with a smaller diameter (yielding NA_{illu} = 0.3) are selected to match the phase ring on the SLM. For the small-FOV imaging mode, an oil-immersed objective (×100/1.44) is used, and the LEDs on a ring with a larger diameter (yielding NA_{illu} = 0.7) are selected to

match the phase ring on the SLM. The large-FOV imaging mode allows us to study the overall confluency and distribution of cells, as well as the interaction between different cells in a large FOV, while the small-FOV imaging mode enables us to investigate the structure and dynamics of internal organelles with high resolution without fluorescent labeling. Live Cos7 cells were used as the sample to demonstrate the two imaging modes of CF-QPCM in the following.

To demonstrate the first imaging mode of CF-QPCM, **Figure 4A**, left) shows a phase image of live Cos7 cells in a FOV of 500 × 500 μm² captured with the objective (×20/0.3) and NA_{illu} = 0.3. Dozens of cells can be observed in the large FOV once for all, which helps us to search for the sub-regions of interest. With the same setting, we captured the flow process of red blood cells (RBCs) as well in the blood vessels of zebrafish (**Supplementary Video S1**) with a temporal resolution of 100 frames per second (FPS). It can be found that RBCs flow in the blood vessels one by one, and the flow speed is different at different locations. To demonstrate the second imaging mode of

CF-QPCM, the sub-regions of interest (about $25 \times 25\ \mu m^2$), e.g., those marked with 1, 2, 3, 4, can be further visualized with high resolution using oil-immersed objective (×100/1.44) and NA_{illu} = 0.7, as shown in **Figure 4A**, right). Furthermore, CF-QPCM was used to image mitochondria, which play a key role in energy metabolism and are involved in cell aging and death. **Figure 4B** shows the time series of mitochondrial fission captured with CF-QPCM, and the dynamic process can be seen in **Supplementary Video S2**. In addition, the dynamic processes (notably the interactions) of ER, mitochondria, and lipid droplets in a live Cos7 cell can be found in **Supplementary Video S3**. The results indicate that the proposed CF-QPCM can perform high-quality phase imaging for different scales of samples to meet different application requirements.

CONCLUSION AND DISCUSSIONS

In this paper, we have demonstrated a high-resolution, condenser-free quantitative phase-contrast microscopy (CF-QPCM) by combining partially coherent annular illumination with quantitative phase-contrast microscopy (QPCM). In CF-QPCM, the transparent samples are directly illuminated with circularly distributed LEDs, greatly simplifying the system configuration, easing the sample installation, and avoiding the cell contamination caused by the water-immersed condenser objective lens. CF-QPCM has a very high spatial resolution of 231 nm (lateral) and a temporal resolution of 250 Hz for 2D imaging, and it can capture the dynamics of organelles inside live cells under normal survival conditions ($37°C$ and 5% CO_2) without fluorescent labeling. In the future, if higher spatial resolution is required, oblique illumination with an even larger angle could be used, although this may reduce the space between the sample and illuminator. CF-QPCM can be combined with various fluorescence microscopies to form the multi-modality imaging system. Due to its common path interference configuration, CF-QPCM has a strong immunity to external disturbances, which is very suitable for long-term observation of live samples. And in the proposed CF-QPCM, the annular illumination angle of LEDs can be expediently adjusted through electrical control according to different applications, providing complementary information for the same sample. Of note, the application of CF-QPCM to organelle-specific phase-contrast image can be enhanced by using a neural network, trained with phase and fluorescence image pairs of the same organelles [27]. There are also many label-free QPCM method to provide phase-contrast images for visualizing organelles inside live cells, such as optical diffraction tomography (ODT) with annular quasi-2π illumination [13, 14]. While, CF-QPCM only needs three or four phase-shifted raw images to reconstruct a quantitative phase image and hence has a much faster imaging speed, more suitable for observing the dynamics and interactions of live organelles. Meanwhile, a circularly distributed LEDs illuminator provides a superior spatial resolution to visualize tiny structures of organelles. The quantitative phase imaging capability of CF-QPCM also opens a gate for inspection of industrial devices, like MEMS or microlens arrays. Compared with the traditional approaches, such as digital holographic microscopy (DHM), CF-QPCM has a superior phase stability and sensibility due to its common-path configuration. CF-QPCM can also be applied to chemistry field, for example, to sense the composition of different solvents or to discriminate different substrate materials since different chemical constituent have different refractive index. We believe such a simple and versatile apparatus will be widely applied for biomedical fields and life science.

DATA AVAILABILITY STATEMENT

The original contributions presented in the study are included in the article/**Supplementary Material**, further inquiries can be directed to the corresponding author.

ETHICS STATEMENT

The animal study was reviewed and approved by Animal Experiment Ethics Committee of Xidian University.

AUTHOR CONTRIBUTIONS

PG conceived and supervised the project. YM and LM Performed experiments and data analysis. JZ, ML, and ZZ contributed to data analysis. YM wrote the draft of the manuscript. All the authors edited the manuscript.

FUNDING

SUPPLEMENTARY MATERIAL

The Supplementary Material for this article can be found online at: https://www.frontiersin.org/articles/10.3389/fphy.2022.892529/full#supplementary-material

REFERENCES

1. Yuan W., Zhu B., Li X.-Y., Hansen T. W., Ou Y., Fang K, et al. Visualizing H 2 O Molecules Reacting at TiO 2 Active Sites with Transmission Electron Microscopy. *Science* (2020) 367:428–30. doi:10.1126/science.aay2474

2. Kumar A., Baker J. N., Bowes P. C., Cabral M. J., Zhang S., Dickey E. C, et al. Atomic-resolution Electron Microscopy of Nanoscale Local Structure in lead-based Relaxor Ferroelectrics. *Nat. Mater.* (2021) 20:62–67. doi:10.1038/s41563-020-0794-5

3. Shao L., Kner P., Rego E. H., Gustafsson M. G. L. Super-resolution 3D Microscopy of Live Whole Cells Using Structured Illumination. *Nat. Methods* (2011) 8:1044–1046. doi:10.1038/nmeth.1734

4. Hell S. W., Wichmann J. Breaking the Diffraction Resolution Limit by Stimulated Emission: Stimulated-Emission-Depletion Fluorescence Microscopy. *Opt. Lett.* (1994) 19:780–782. doi:10.1364/OL.19.000780

5. Betzig E., Trautman J. K., Harris T. D., Weiner J. S., Kostelak R. L. Breaking the Diffraction Barrier: Optical Microscopy on a Nanometric Scale. *Science* (1991) 251:1468–1470. doi:10.1126/science.251.5000.1468

6. Rust M. J., Bates M., Zhuang X. Sub-diffraction-limit Imaging by Stochastic Optical Reconstruction Microscopy (STORM). *Nat. Methods* (2006) 3: 793–796. doi:10.1038/nmeth929

7. Micó V., Zheng J., Garcia J., Zalevsky Z., Gao P. Resolution Enhancement in Quantitative Phase Microscopy. *Adv. Opt. Photon.* (2019) 11:135–214. doi:10.1364/AOP.11.000135

8. Gao P., Yuan C. Resolution Enhancement of Digital Holographic Microscopy via Synthetic Aperture: a Review. *gxjzz* (2022) 3:1–16. doi:10.37188/lam.2022.006

9. Park Y., Choi W., Yaqoob Z., Dasari R., Badizadegan K., Feld M. S. Speckle-field Digital Holographic Microscopy. *Opt. Express* (2009) 17:12285–92. doi:10.1364/OE.17.012285

10. Zheng J., Pedrini G., Gao P., Yao B., Osten W. Autofocusing and Resolution Enhancement in Digital Holographic Microscopy by Using Speckle-Illumination. *J. Opt.* (2015) 17:085301. doi:10.1088/2040-8978/17/8/085301

11. Gao P., Pedrini G., Osten W. Structured Illumination for Resolution Enhancement and Autofocusing in Digital Holographic Microscopy. *Opt. Lett.* (2013) 38:1328–30. doi:10.1364/OL.38.001328

12. Zhang M., Ma Y., Wang Y., Wen K., Zheng J., Liu L, et al. Polarization Grating Based on Diffraction Phase Microscopy for Quantitative Phase Imaging of Paramecia. *Opt. Express* (2020) 28:29775–87. doi:10.1364/OE.404289

13. Dong D., Huang X., Li L., Mao H., Mo Y., Zhang G, et al. Super-resolution Fluorescence-Assisted Diffraction Computational Tomography Reveals the Three-Dimensional Landscape of the Cellular Organelle Interactome. *Light Sci. Appl.* (2020) 9:1–15. doi:10.1038/s41377-020-0249-4

14. Cotte Y., Toy F., Jourdain P., Pavillon N., Boss D., Magistretti P, et al. Marker-free Phase Nanoscopy. *Nat Photon* (2013) 7:113–117. doi:10.1038/nphoton.2012.329

15. Godden T. M., Suman R., Humphry M. J., Rodenburg J. M., Maiden A. M. Ptychographic Microscope for Three-Dimensional Imaging. *Opt. Express* (2014) 22:12513–12523. doi:10.1364/OE.22.012513

16. Zhang H., Jiang S., Liao J., Deng J., Liu J., Zhang Y, et al. Near-field Fourier Ptychography: Super-resolution Phase Retrieval via Speckle Illumination. *Opt. Express* (2019) 27:7498–512. doi:10.1364/OE.27.007498

17. Alexandrov S. A., Hillman T. R., Gutzler T., Sampson D. D. Synthetic Aperture Fourier Holographic Optical Microscopy. *Phys. Rev. Lett.* (2006) 97:168102. doi:10.1103/physrevlett.97.168102

18. Ou X., Horstmeyer R., Zheng G., Yang C. High Numerical Aperture Fourier Ptychography: Principle, Implementation and Characterization. *Opt. Express* (2015) 23:3472–91. doi:10.1364/OE.23.003472

19. Ledwig P., Robles F. E. Quantitative 3D Refractive index Tomography of Opaque Samples in Epi-Mode. *Optica* (2021) 8:6–14. doi:10.1364/OPTICA.410135

20. Zuo C., Li J., Sun J., Fan Y., Zhang J., Lu L, et al. Transport of Intensity Equation: a Tutorial. *Opt Lasers Eng* (2020) 135:106187. doi:10.1016/j.optlaseng.2020.106187

21. Nguyen T. H., Kandel M. E., Rubessa M., Wheeler M. B., Popescu G. Gradient Light Interference Microscopy for 3D Imaging of Unlabeled Specimens. *Nat. Commun.* (2017) 8:1–9. doi:10.1038/s41467-017-00190-7

22. Zernike F. Phase Contrast, a New Method for the Microscopic Observation of Transparent Objects Part II. *Physica* (1942) 9:974–986. doi:10.1016/S0031-8914(42)80035-X10.1016/s0031-8914(42)80079-8

23. Webb K. F. Condenser-free Contrast Methods for Transmitted-light Microscopy. *J Microsc* (2015) 257:8–22. doi:10.1111/jmi.12181

24. Wang Z., Millet L., Mir M., Ding H., Unarunotai S., Rogers J, et al. Spatial Light Interference Microscopy (SLIM). *Opt. Express* (2011) 19:1016–26. doi:10.1364/OE.19.001016

25. Zhang J. K., He Y. R., Sobh N., Popescu G. Label-free Colorectal Cancer Screening Using Deep Learning and Spatial Light Interference Microscopy (SLIM). *APL Photon* (2020) 5:040805. doi:10.1063/5.0004723

26. Ma Y., Guo S., Pan Y., Fan R., Smith Z. J., Lane S, et al. Quantitative Phase Microscopy with Enhanced Contrast and Improved Resolution through Ultra-oblique Illumination (UO-QPM). *J. Biophotonics* (2019) 12:e201900011. doi:10.1002/jbio.201900011

27. Guo S., Ma Y., Pan Y., Smith Z. J., Chu K. Organelle-specific Phase Contrast Microscopy Enables Gentle Monitoring and Analysis of Mitochondrial Network Dynamics. *Biomed. Opt. Express* (2021) 12:4363–4379. doi:10.1364/BOE.425848

28. Ma Y., Li D., Smith Z. J., Li D., Chu K. Structured Illumination Microscopy with Interleaved Reconstruction (SIMILR). *J. Biophotonics* (2017) 11: e201700090. doi:10.1002/jbio.201700090

29. Descloux A., Grußmayer K. S., Radenovic A. Parameter-free Image Resolution Estimation Based on Decorrelation Analysis. *Nat. Methods* (2019) 16:918–924. doi:10.1038/s41592-019-0515-7

Holographic Imaging Using an Imperfect Plane Wave Illumination With a Background Phase

Rujia Li, Feng Yang and Liangcai Cao*

State Key Laboratory of Precision Measurement Technology and Instruments, Department of Precision Instruments, Tsinghua University, Beijing, China

Aberrations in the optical components and misalignments in the optical system cause a background phase in the coherent illumination. To reconstruct the object phase, the background phase illuminating the object must be measured and subtracted. For diffraction imaging and in-line holography, the traditional phase retrieval method reconstructs the phase diffracting from clear edges. However, it falls into stagnation when solving a background phase slowly varying in the spatial domain. In this study, we propose to solve the background phase using a modulation-based phase retrieval method. Alternative structured phase modulation (ASPM) can be the phase constraint to avoid stagnation when solving the background phase without clear edges. With ASPM, the background phase in the experiment can be efficiently retrieved when 16 phase patterns are employed. The ASPM acts as a phase grating to concentrate the intensities and provides robustness to noise. Compared to the conventional random phase modulations, the ASPM method had a smaller error value in the reconstruction iterations, which leads to a better reconstruction quality. After measuring and subtracting the background phase, the object phase was retrieved using a coherent diffraction imaging system. A phase plate can be accurately reconstructed under three different background phases.

Keywords: phase retrieval, holography, background subtraction, phase modulation, spatial light modulator

INTRODUCTION

Aberrations and misalignments are inevitable in the optical setups of various phase imaging techniques, including interferometric methods [1–5] and diffraction-based methods [6–9]. To measure the complex amplitude, an object is illuminated with a coherent wave. The plane wave [10] or quasi-plane [11, 12] wave is widely used for illumination. With ideal plane-wave illumination, the transmitted wavefront represents the complex amplitude of the object. Typically, in the experiments, there are unavoidable aberrations and misalignments [13–15]. The illumination on the object has an undesirable background phase slowly varying in the spatial domain. The transmitted wavefront is the complex amplitude product of the object and illumination. To acquire the object phase, the background phase must be measured and subtracted.

Various methods have been proposed for the background phase compensation in the interferometric methods, such as off-axis holography techniques [16]. The compensation can be executed numerically during the reconstruction. The background phase can be compensated by generating a virtual phase from the hologram [17, 18] or using polynomial fitting [19, 20]. The

aberration compensation can also be mimicked by the computation of a numerical parametric lens [21]. Apart from the numerical method, measuring and subtracting the background phase is a straightforward approach [22]. Complete information on system aberration is calculated from three laterally shifted phase images using spiral phase integration [23]. In angular scanning digital holography setup, pupil aberrations are recovered by utilizing the cross-spectral density between optical fields at various incident angles [24]. For off-axis digital holography, the background phase can be measured directly. The phase of an object is acquired after background elimination [25]. In phase-shifting methods, the background phase is measured directly [26] or eliminated by numerical methods [27]. The aberrations can also be compensated using Zernike polynomials [28].

In diffraction imaging methods, iterative phase retrieval methods are used to retrieve the phase [29, 30]. The basic procedure of the algorithm is the alternating propagation of the estimated wavefront between the planes of interest and the recorded intensity. There is conjugated noise while propagating the intensity. Traditional phase retrieval methods used constraints to eliminate the conjugated noise. The Gerchberg-Saxton (GS) algorithm [31] used the amplitude of the wavefront of interest to be a strong constraint. Then, Fienup modified the GS algorithm by using a loose non-negative constraint [32] or support constraint [33]. A support constraint was widely used as a priori information for phase retrieval [34, 35]. The support region was artificially created by coherently illuminating a finite region of an extended object or a large scene [36]. The wavefront inside the support region was reconstructed iteratively. The noise outside the support region was weakened or abandoned [37].

In a diffraction imaging setup, there is no reference beam while recording the diffracted hologram. The background phase compensation is hard to execute using the aforementioned numerical methods. The background phase needs to be measured. The traditional phase retrieval method performs well when solving the phase diffracting from clear edges. Using simulated data, the phase inside the support region can be rapidly reconstructed [37]. When solving the background phase without clear edges, the reconstruction algorithm stagnates [36]. In the experiment, the intensity data was with environmental noise. The background phase is unsolvable based on its intensity pattern with noise using traditional phase-retrieval methods. Diversities in the diffraction intensities need to be detected adequately for retrieving a smooth background phase [38, 39].
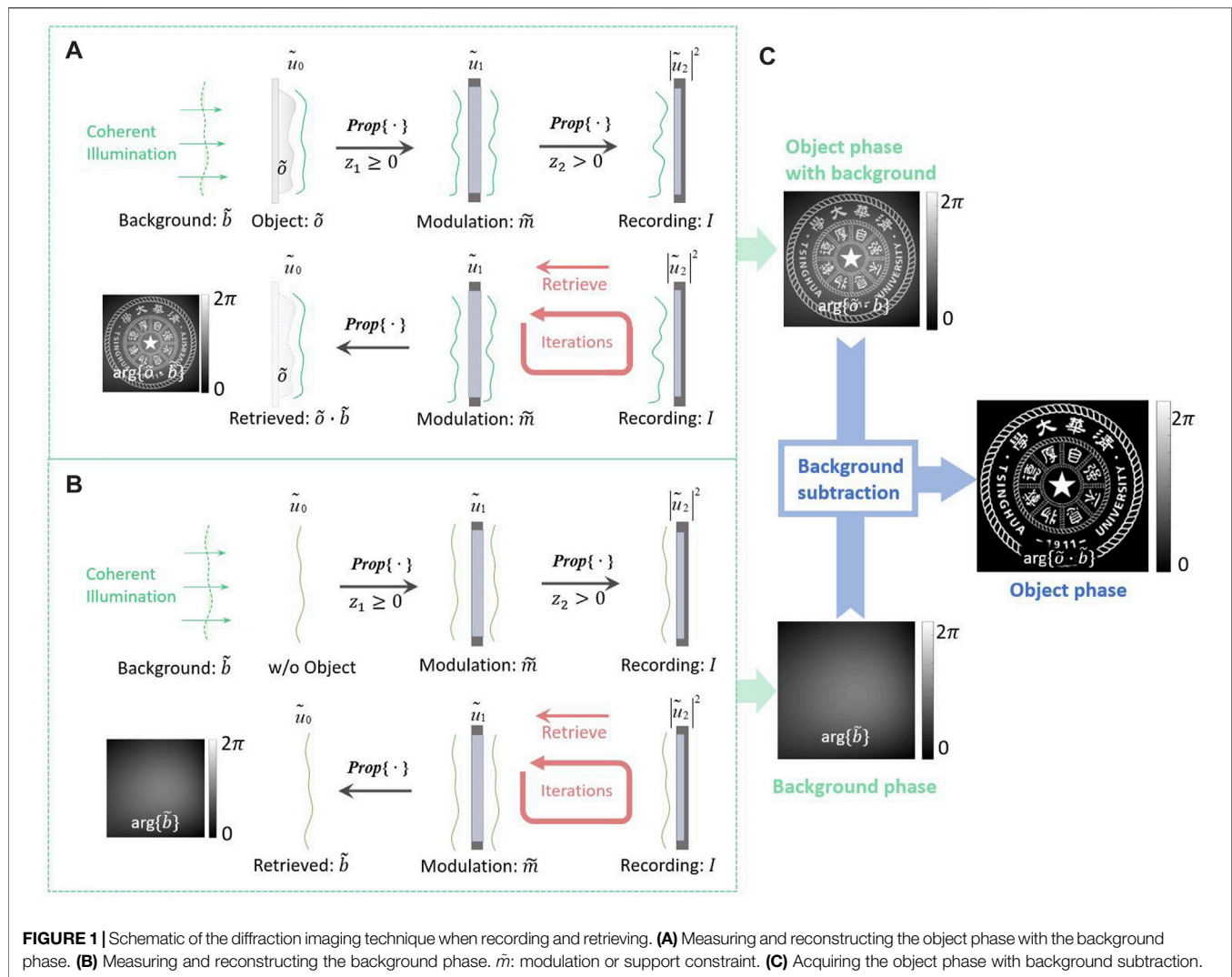
Modulations can also be used as modulation constraints to achieve successful phase retrieval. With multiple phase modulations, the wavefront can be fully reconstructed without finite support constraints [40]. Using shifting illumination, a large area of the specimen can be reconstructed at high resolution [41–43]. A novel topological modulation provides an effective dynamic range in the recorded intensities [44]. The two-dimensional circular grating array is designed for the simultaneous acquisition of scattering images in all possible directions using a single shot [45]. With a phase-stepping process, phase retrieval can be made with a high signal-to-noise

ratio (SNR) with a low dose x-ray illumination [46]. Progress in holographic imaging is made with random phase modulation using metasurface. A reference-free holographic image sensor can be made with a random diffuser [47]. High-precision quantitative phase gradient imaging can be made with a single shot using two coded metasurface layers [48]. With phase modulations, phase retrieval methods can be applied to building a novel wavefront sensor. Traditional wavefront sensor such as the Shack-Hartmann wavefront sensor has a lateral resolution limited by the size of micro-lens [49]. The wavefront sensing is made with a 10-megapixel lateral resolution using random phase modulations (RPM) on a spatial light modulator (SLM) [50]. To reduce the modulation defects on an SLM [51], the alternative structured phase modulations (ASPM) were designed for providing a reliable phase modulation on the SLM and increasing the robustness of data acquisition [52]. The structured phase modulation can also be used to shift the high spatial frequency terms into the diffraction-limited imaging setup, which is an effective approach to enhance the resolution of holographic microscopy [53, 54] or phase-shifting interferometry [55, 56].

In this study, we propose to solve the background phase using a modulation-based phase retrieval method. The ASPM can be the phase constraint to avoid stagnation when solving the background phase slowly varying in the spatial domain. The structured phase modulation patterns consisted of periodic phase bars. Two adjacent patterns were orthogonally placed to form one pair of ASPM patterns. The measured wavefront was perturbed by the ASPM patterns, and the modulated intensities were recorded correspondingly. Then, a modified GS algorithm was performed for reconstruction. The modulated intensities are concentrated by the phase gratings, which makes the method robust to noise. The algorithm rapidly converged in 100 iterations when solving the background phase in an experimental setup. After background phase subtraction, the object phase can be reconstructed accurately. A phase plate was experimentally studied and reconstructed using illumination with three background phases. The RPM patterns in ref. 39 [50] were also evaluated by measuring a phase object in the same experimental setup. The root means square error (RMSE) curves showed that the ASPM method had a smaller error value in the reconstruction iterations, which leads to a better reconstruction quality. The ASPM method is reliable for background subtraction and measuring an object's phase.

RETRIEVE THE OBJECT PHASE IN A DIFFRACTION IMAGING SYSTEM

A schematic of the diffraction imaging setup used to measure the phase object is shown in **Figure 1A**. The investigated object had a complex amplitude, where A_o and ϕ_o represent the amplitude and phase component of the object, respectively, x_o, y_o represent the Cartesian coordinates on the object plane and represent the complex function. When the illumination on the object is a coherent plane wave, it can be expressed as $\tilde{b} = 1$. The wavefront emitted from the object is $\tilde{u}_o = \tilde{b} \cdot \tilde{o} = \tilde{o}$.

FIGURE 1 | Schematic of the diffraction imaging technique when recording and retrieving. **(A)** Measuring and reconstructing the object phase with the background phase. **(B)** Measuring and reconstructing the background phase. $\tilde{m}$: modulation or support constraint. **(C)** Acquiring the object phase with background subtraction.

The illumination has a phase distribution, especially when there are some misalignments and aberrations in the setup. As shown in **Figure 1A**, the illumination on the object plane is $\tilde{b} = A_b(x_o, y_o)e^{i\phi_b(x_o, y_o)}$ where A_b and represents the amplitude and phase components of illumination, respectively. The wavefront emitted from the object is $\tilde{u}_o = \tilde{b} \cdot \tilde{o}$. After freely propagating at a distance of z_1, the complex wavefront $\tilde{u}_1$ arriving at the modulation plane can be calculated based on the angular spectrum method (ASM) as follows:

$$\tilde{u}_o(x_1, y_1) = Prop\{\tilde{u}_o(x_0, y_0)\}_{z1}$$

$$= \mathcal{F}^{-1}\left\{\mathcal{F}\{\tilde{u}_o(x_0, y_0)\}\exp\left[ikz\sqrt{1 - (\lambda f_x)^2 - (\lambda f_y)^2}\right]\right\} \quad (1)$$

where $Prop\{\cdot\}$ represents the propagation calculator, $\mathcal{F}\{\cdot\}$ represents the Fourier transform x_1, y_1 represents the coordinates on the modulation plane, and λ represents the wavelength of the illumination. On the modulation plane, modulation or support constraints were applied on $\tilde{u}_1$, which is

$\tilde{u}_1 \cdot \tilde{m}$. Then, the constrained wavefront was propagated to the recording plane at a distance of z_2. The intensity of the propagated wavefront $\tilde{u}_2$ was recorded as the intensity constraint. Note that z_2 must be larger than zero and the phase terms can be coded into the diffraction intensity [57, 58].

A schematic of the retrieval of the object phase is shown in **Figure 1A**. In the reconstruction process, the phase-retrieval algorithm proceeded between the modulation plane and the recording plane. Using the support or modulation constraint and the recorded intensity constraint $|\tilde{u}_2|^2$, the wavefront $\tilde{u}_1$ was iteratively reconstructed using phase retrieval algorithms. Then, $\tilde{u}_o$ was retrieved by numerically propagating $\tilde{u}_1$ back to the object plane.

The background phase must be measured and subtracted from $\tilde{u}_o$ and the object phase can be reconstructed. In diffraction imaging, $\tilde{u}_1$ was retrieved from $|\tilde{u}_2|^2$. After propagating $\tilde{u}_o$ to $\tilde{u}_1$ and $\tilde{u}_2$, the object $\tilde{o}$ and illumination $\tilde{b}$ terms were convoluted with the additional terms, as shown in **Eq. 1**. $\tilde{b}$ could not be eliminated using a linear operation on $|\tilde{u}_2|^2$. The operation
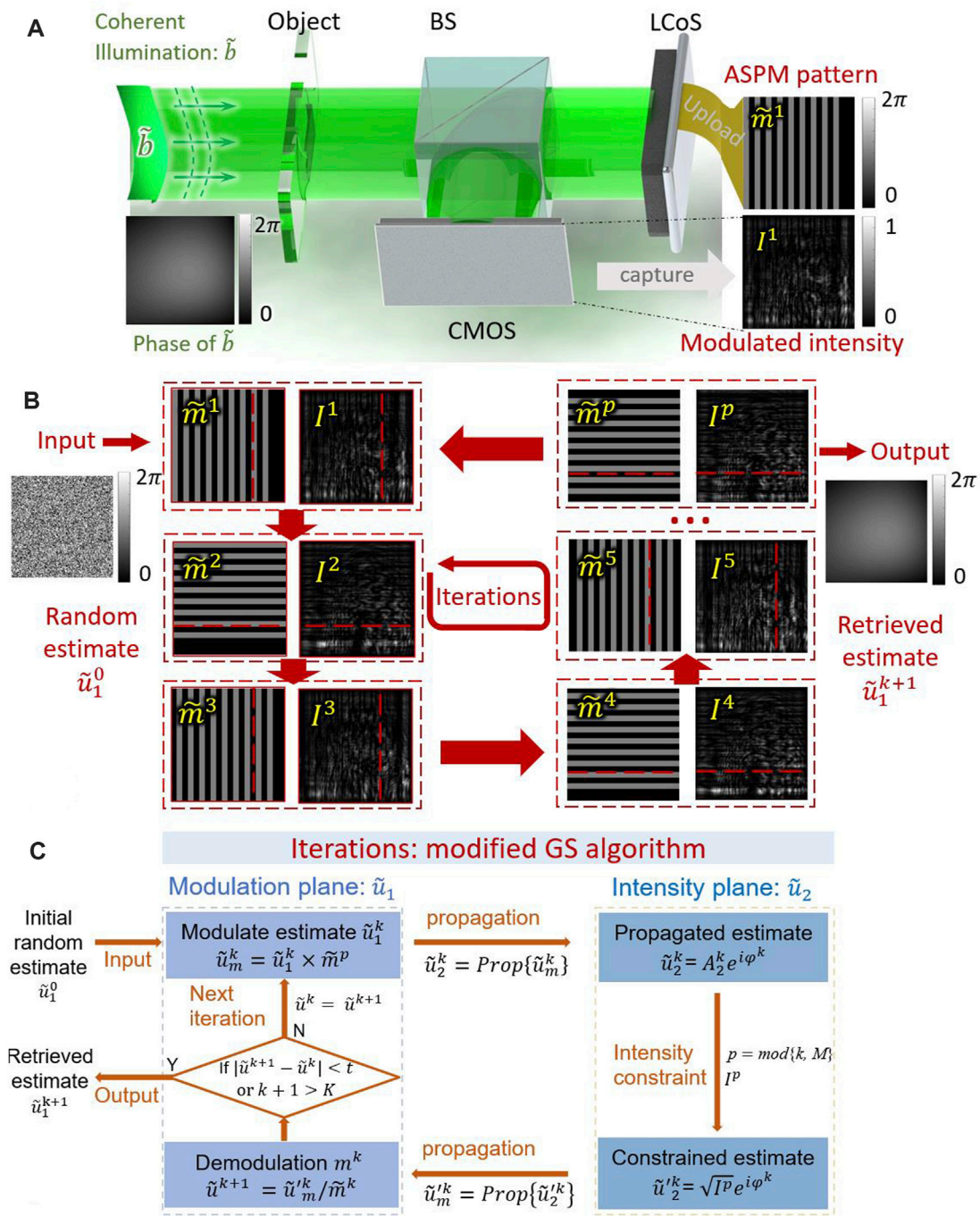
FIGURE 2 | (A) Schematic of diffraction imaging using the ASPM method. **(B)** Uploaded ASPM patterns on the LCoS and corresponding modulated intensities. **(C)** Flowchart of the iterations using ASPM method. $\tilde{m}^1$: the first ASPM modulation pattern. I^1: the first modulated intensity; k: number of iterations; p: number of modulations; M: total number of the constraints; $mod\{\cdot\}$ is the operator to calculate the remainder after division; t: the preferable value of the calculation error; K: a set maximum number of iterations.

commonly used in in-line holography is $|\tilde{u}_2|^2/|Prop\{\tilde{b}\}_{z_1+z_2}|^2$. With the linear operation on the diffraction intensity, the reconstruction was performed with an enhancement of the object outline, instead of acquiring the object phase. The same is true for diffraction imaging. For proper

reconstruction of $\tilde{o}$, the background $\tilde{b}$ also must be measured and reconstructed, as shown in **Figure 1B**. The investigated object can then be calculated as $\tilde{o} = \tilde{u}_o/\tilde{b}$. In this study, the illumination background $\tilde{b}$ was reconstructed using the ASPM method.

RETRIEVING A BACKGROUND PHASE USING THE ALTERNATIVE STRUCTURED PHASE MODULATION METHOD

Reconstruct a Complex Wavefront Using the Alternative Structured Phase Modulation Method

A schematic of the ASPM method is shown in **Figure 2A**. A phase object was illuminated as $\tilde{b}$. Then, the emitted complex wavefront was freely propagated to a liquid crystal on silicon (LCoS), which is a reflective phase-only spatial light modulator. The ASPM patterns were uploaded to the LCoS for phase modulation. The intensities of the modulated wavefronts were recorded using a CMOS sensor. Multiple modulations and intensities were the modulation and intensity constraints for the reconstruction iterations. A modified GS algorithm was used for phase retrieval.

As shown in **Figure 2**(and, an ASPM pattern is composed of bars and forms a structured phase modulation $\tilde{m}$ when uploaded on a phase-only LCOS. The modulated phase with phase bars is a binary-phase grating. For the ASPM in the x-direction, the normalized transmission function of the modulation is expressed as follows:

$$\tilde{m}_x(x,\ y) = \left[e^{i\phi_g} - 1 \right] \cdot rect\left(\frac{2x}{\Delta} \right) \otimes comb\left(\frac{x+s}{\Delta} \right) + 1, \quad (2)$$

where ϕ_g represents the modulated phase, Δ represents the period of the phase grating, $\otimes$ represents the convolution operation, and s represents the shift factor after one modulation. For the ASPM in the x-direction, the amplitude and phase terms of the object were modulated in the x-direction. The modulation constraints were applied in the x-direction. To measure an object that covers the x- and y-directions, structured phase modulation was alternatively applied in both directions. After one modulation, the modulated wavefront $\tilde{u}_m = \tilde{u}_1 \cdot \tilde{m}$ was propagated to the camera plane at a distance of z_2. The modulated wavefront after propagation is as follows:

$$\tilde{u}_2(x_2, y_2) = Prop\{\tilde{m}(x_1, y_1) \cdot \tilde{u}_1(x_1, y_1)\}_{z_2}, \quad (3)$$

The intensity $|\tilde{u}_2|^2$ is the intensity constraint recorded by the camera. As the modulation is a phase grating, the modulated wavefront is transmitted on the diffraction orders of the grating. Based on the principle of diffraction gratings, the diffraction angle α can be calculated from the period of the grating Δ, which is $\sin\alpha = m\lambda/\Delta$, where m is an integer representing the diffraction orders. The first order containing most of the diffraction energy is considered, and m is set to one. If the physical size of $\tilde{u}_1$ is $X_1 \cdot Y_1$, the size of $\tilde{u}_1$ after propagation is diffracted as $(X_1 + z_2\tan\alpha) \cdot (Y_1 + z_2\tan\alpha)$. The physical size of the camera $X_c \cdot Y_c$ should be sufficiently large to capture the modulated intensity.

$$X_c \geq (X_1 + z_2\tan\alpha),\ Y_c \geq (Y_1 + z_2\tan\alpha), \quad (4)$$

A modified GS algorithm was used for the ASPM method. A flowchart of the algorithm is presented in **Figure 2C**. The algorithm alternately propagates the estimated wavefront between the modulation and intensity planes. Conjugate noise was eliminated by the constraints on the two planes. An initial random estimate of the measured wavefront $\tilde{u}_1^0$ was first modulated by the ASPM $\tilde{m}^0$. The modulation-constrained wavefront, $\tilde{u}_m^0 = \tilde{u}_1^0 \cdot \tilde{m}^0$, was propagated to the intensity plane. Then, the propagated wavefront $\tilde{u}_2^0$ was intensity-constrained by replacing its amplitude with the recorded intensity I^0. The intensity-constrained wavefront $\tilde{u}_2'^0$ was back-propagated to the modulation plane and refresh the modulation-constrained wavefront $\tilde{u}_m'^0$. Demodulation was applied as $\tilde{u}_1^1 = \tilde{u}_m'^0/\tilde{m}^k$ to acquire the estimated wavefront $\tilde{u}_1^1$, which is the input for the next iteration and correction. M pairs of modulations and intensity constraints were sequentially applied to the estimates. In the kth iteration, the pth pair of constraints were applied. p is decided as $p = mod\{k, M\}$, where $mod\{\cdot\}$ calculates the remainder after division.

After one iteration, the conjugated terms were suppressed with constraints. After k iterations, the refreshed estimated wavefront $\tilde{u}_1^k$ was closer to the ground truth of the $\tilde{u}_1$. The iterations could be terminated if the calculation error between two iterations is preferable or the maximum number of iterations is achieved. The error evaluation is performed on the phase component using the root mean square error (RMSE):

$$RMSE = \sqrt{\frac{1}{X_1 Y_1} \sum_{x,y} \left| \phi_1^{k+1}(x_1, y_1) - \phi_1^k(x_1, y_1) \right|^2}. \quad (5)$$

In the ASPM method, the multiple phase modulations are made by shifting and rotating the phase grating perpendicular to the optical axis. There is significant variance in the captured intensities from the modulations. The diversities in the multiple intensities provide sufficient constraints for good convergence of iterations. More constraints result in a solution closer to the ground truth.

Simulation of Retrieving a Background Phase Using the Alternative Structured Phase Modulation Method

A simulation was performed for retrieving a background phase using the ASPM method. A 200×200-pixel concave wavefront was measured as the ground truth, as shown in **Figure 3A**. The phase component had a maximum value of 0.5 π rad, and the amplitude component had a uniform value of one. The illuminating wavelength was 532 nm. The measured wavefront was modulated using the ASPM method and then numerically propagated at a distance of 20 mm. The numerical propagation was calculated using the angular spectrum method (ASM) in the discrete form:

$$Prop\{u[\alpha,\beta]\}_{ASM} = DFT\left\{ IDFT\{u[\alpha,\beta]\} \cdot \exp\left[-iz\frac{2\pi}{\lambda}\sqrt{1 - \left(\frac{\lambda\xi}{\delta X_\alpha}\right)^2 - \left(\frac{\lambda\eta}{\delta X_\beta}\right)^2} \right] \right\}, \quad (6)$$
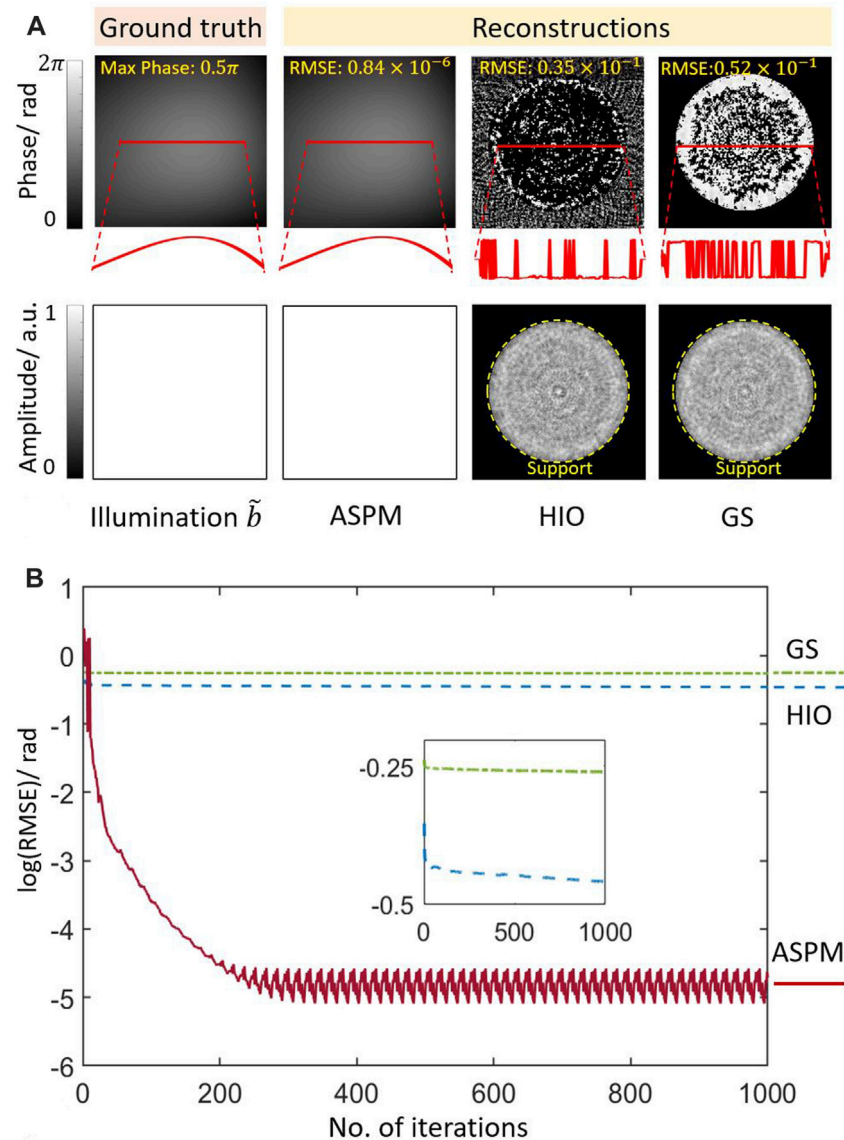
FIGURE 3 | (A) Ground truth of the wavefront and reconstructed phase and amplitude components using the ASPM, HIO, and GS methods. **(B)** The logarithm of the RMSE of the ASPM, GS, and HIO methods with 1000 iterations. *log*(RMSE): logarithm of the RMSE of the calculated phase and the ground truth.

where α, β and ξ, η are the indices of the samples in spatial domain and Fourier domain. X_α and X_β are the size of the wavefront, X_α, X_β = 200. δ represents the sampling period of the numerical calculation, δ = 3.8μm. *DFT*{·} and *IDFT*{·} are the two-dimensional discrete Fourier transform and inverse discrete Fourier transform.

The concave smooth wavefront in **Figure 3A** was modulated with eight groups of ASPM patterns. The period of each group of the ASPM patterns was from 2 to 16 pixels, with a duty ratio of 50%. After the modulation in both the *x*- and *y*- directions, the pattern was shifted with one pixel. A modified GS algorithm was then used to work with the constraints for reconstruction. The logarithm of the RMSE between the ground truth and the calculated phase during the iterations is shown in **Figure 4**. A

total of 1000 iterations were performed during the reconstruction process. When there are 2 or 4 modulations, the reconstruction cannot be made. There are three unknowns in the phase retrieval problem, which are the phase of the diffracted wavefront, phase and amplitude of the measured wavefront. At least three pairs of modulations in *x*- and *y*- directions are needed for reconstruction. As the number of modulations increases from 6, the concave smooth phase can be reconstructed successfully. Structured phase patterns are modulation constraints. The corresponding recorded modulated intensities were the intensity constraints. Multiple modulations provide sufficient constraints for noise elimination. The convergence of the iterations and the accuracy of the reconstruction are increased with the number
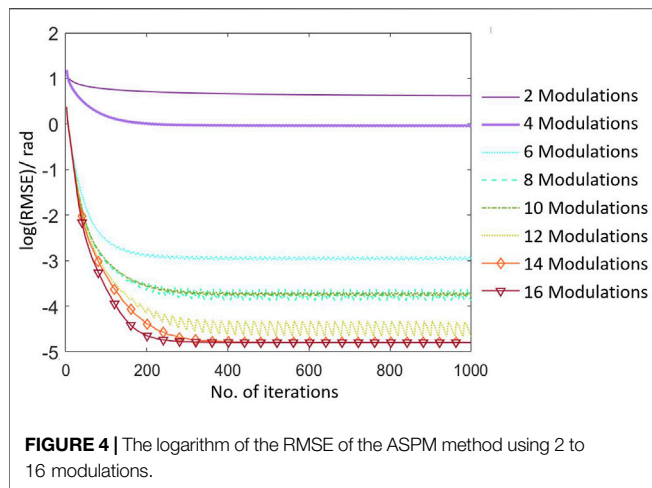
FIGURE 4 | The logarithm of the RMSE of the ASPM method using 2 to 16 modulations.

of modulations. In the following simulations and experiments, 16 modulations are used for a good result.

With 16 modulations, The ASPM pattern was shifted eight times in both the *x-* and *y-directions*. As shown in **Figure 3B**, during the first 100 iterations, the algorithm converges rapidly, which shows the efficiency of the ASPM method for error elimination. After 300 iterations, the algorithm converges to the final result. Compared to the ground truth, the RM phase component reached approximately 0.84×10^{-6} after 300 iterations. The RMSE on the amplitude component is approximately 0.65×10^{-5}. In **Figure 3B**, the RMSE value of the ASPM is oscillatory. There are some residual errors in different iterations or using different constraints. As 16 modulations are sequentially used for reconstruction, the RMSE values oscillate at a period of 16.

The classical GS and hybrid-input-output (HIO) [13] algorithms were also used to measure the concave wavefront. The measured wavefront was the same as that in the ASPM method. To apply the GS and HIO method, the wavefront was constrained with a support region, which was a round central pass filter with a radius of 80 pixels. In the GS algorithm, the wavefront inside the support region was completely passed, and outside the region was blocked. In the HIO algorithm, the wavefront inside the support region was completely passed and outside the region was suppressed by a factor of 0.07 in every iteration. Both the GS and HIO algorithms failed to solve the background phase $\arg\{\tilde{b}\}$. Compared to the efficient ASPM method, the convergence of the GS and HIO algorithms was marginal in this simulation, as shown in **Figure 3B**. The HIO algorithms performed better than the GS algorithm on the simulated intensity data. However, in the experiment, the intensity data were recorded with inevitable noise, which may lead to a failure when using the classical method for reconstructing the background wavefront.

In the classical GS and HIO method, the recording and retrieving can be described by **Eqs. 7, 8**. There is a support region C on the measured complex wavefront $\tilde{u}$. P is the propagation operator. After free propagation, one intensity pattern I is recorded. The retrieval is made by solving the optimization problem and searching for an optimal solution

$\tilde{u}^*$ that minimize the error, as shown in **Eq. 8**. The GS method is based on alternatively propagating the estimation $\tilde{u}'$ between the support C and intensity plane I. For a rough measured phase, there is effective diversity in the diffraction intensity during propagation. The conjugated noise falls out of the support region. In every propagation, the estimation is closer to the optimal solution with an effective support constraint. For a smooth background phase, there is insufficient diversity during the propagation. Support C fails to constrain the estimation in the iterations, which leads to low convergence or stagnation.

$$I = |PC\tilde{u}|^2, \tag{7}$$

$$\tilde{u}^* = \mathrm{argmin}_{\tilde{u}'}\left\| I - \left|PC\tilde{u}'\right|^2 \right\|_2. \tag{8}$$

In the ASPM method, the recording and retrieving can be described by **Eqs. 9, 10**. The measured complex wavefront $\tilde{u}$ is modulated by M_n and then be recorded as I_n after propagation. Multiple modulations and recordings provide redundant constraints to solve the optimization problem. As the recorded intensities vary with modulations, there is sufficient diversity for reconstruction. The smooth background phase can be retrieved with good convergence.

$$I_n = |PM_n\tilde{u}|^2, n = 1, 2, 3\ldots, \tag{9}$$

$$\tilde{u}^* = \mathrm{argmin}_{\tilde{u}'} \sum_n \left\| I_n - \left|PM_n\tilde{u}'\right|^2 \right\|_2, \; n = 1, 2, 3\ldots. \tag{10}$$

EXPERIMENTS ON RECONSTRUCTING AN OBJECT PHASE USING THE ALTERNATIVE STRUCTURED PHASE MODULATION

Calibrating the Phase Modulation of a Spatial Light Modulator

In the ASPM method, the designed phase patterns are the modulation constraints in the reconstruction iterations. The modulated phase is a priori information for eliminating conjugated terms. Quantitative phase modulation is required for successful reconstruction. In addition, the ASPM method requires multiple modulations and measurements to guarantee the convergence of the algorithm and robustness to noise. Phase calibration of the LCoS modulation benefits the acquisition of good experimental results.

In this study, phase modulations were made using an LCoS (Holoeye GAEA-2-vis). LCoS is a pixelated digital device that can quantitatively modulate the phase. Owing to the limited manufacturing process and nonlinear optical response of the liquid crystal [59], the LCoS must be calibrated before being used. Many calibration methods have been proposed [60–62]. In this study, the LCoS was calibrated using an efficient and convenient self-referenced calibration method [63, 64]. Using a blazed-grating pattern [65], the phase modulation was measured with an accuracy of 0.06 π in the setup of diffraction imaging. The modulation curves before and after calibration are shown in **Figure 5A**. Using the cubic polynomial fitting method, the phase modulation of the LCoS can be predicted with an error less than the measurement error, as shown in **Figure 5B**. The
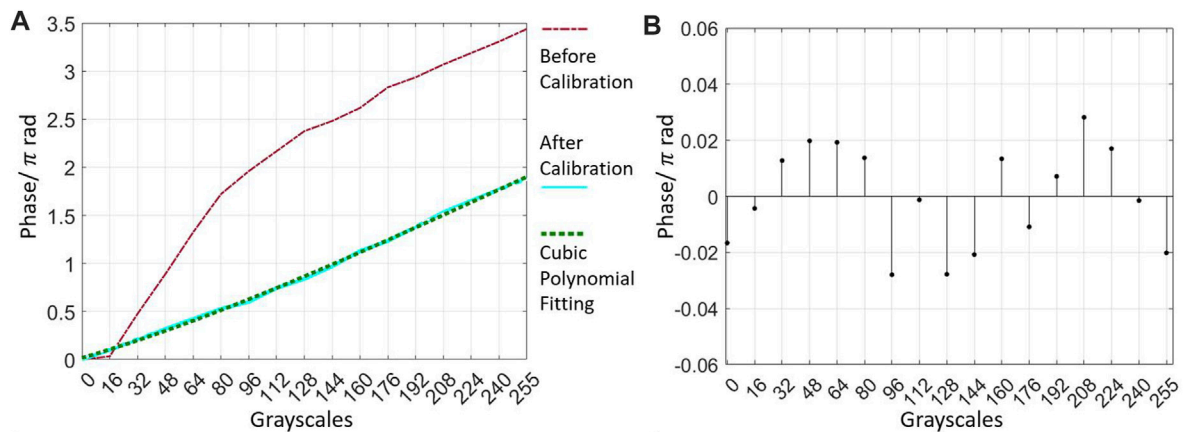
FIGURE 5 | (A) Modulation curves of the LCoS before and after calibration and curve using the cubic polynomial fitting method. **(B)** Residuals of the fitted curve.
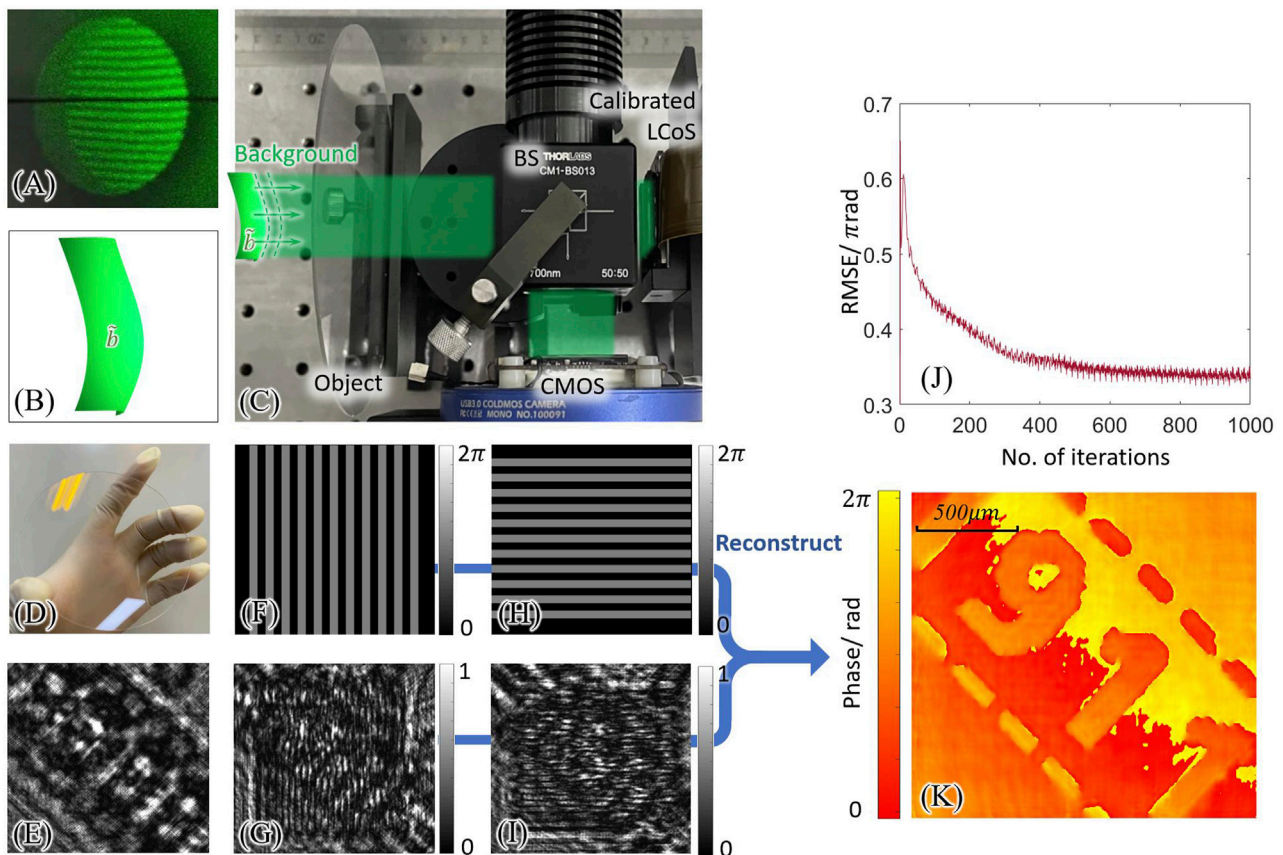
FIGURE 6 | Measuring a phase object using illumination with background phase. **(A)** The fringe pattern on a shearing interferometer (Thorlabs SI254) for measuring the background wavefront. **(B)** Schematic of the illumination with a background phase. **(C)** Schematic of a coherent diffraction imaging setup. **(D)** Picture of the object, a phase plate. **(E)** Diffraction pattern of the measured object. **(F,H)**: Two of the ASPM patterns in *x*- and *y*- direction. **(G,F)**: Captured intensities of the modulated wavefront. **(J)** The curve of the RMSE between the calculated wavefronts of adjacent iterations. **(K)** The reconstructed phase of the object with distortion in the illumination.

FIGURE 7 | (A) Reconstructed phase of the illumination in the experiment using the ASPM method. **(B)** RMSE during reconstruction. **(C)** The reconstructed phase of the object with an illumination background. **(D)** Object phase with background subtraction.

modulated phase ϕ_g related to the uploaded grayscale g can be predicted using cubic polynomial fitting as follows:

$$\phi_g = \left(-1.75 \times 10^{-8} g^3 + 1.24 \times 10^{-5} g^2 + 5.32 \times 10^{-3} g \right.$$
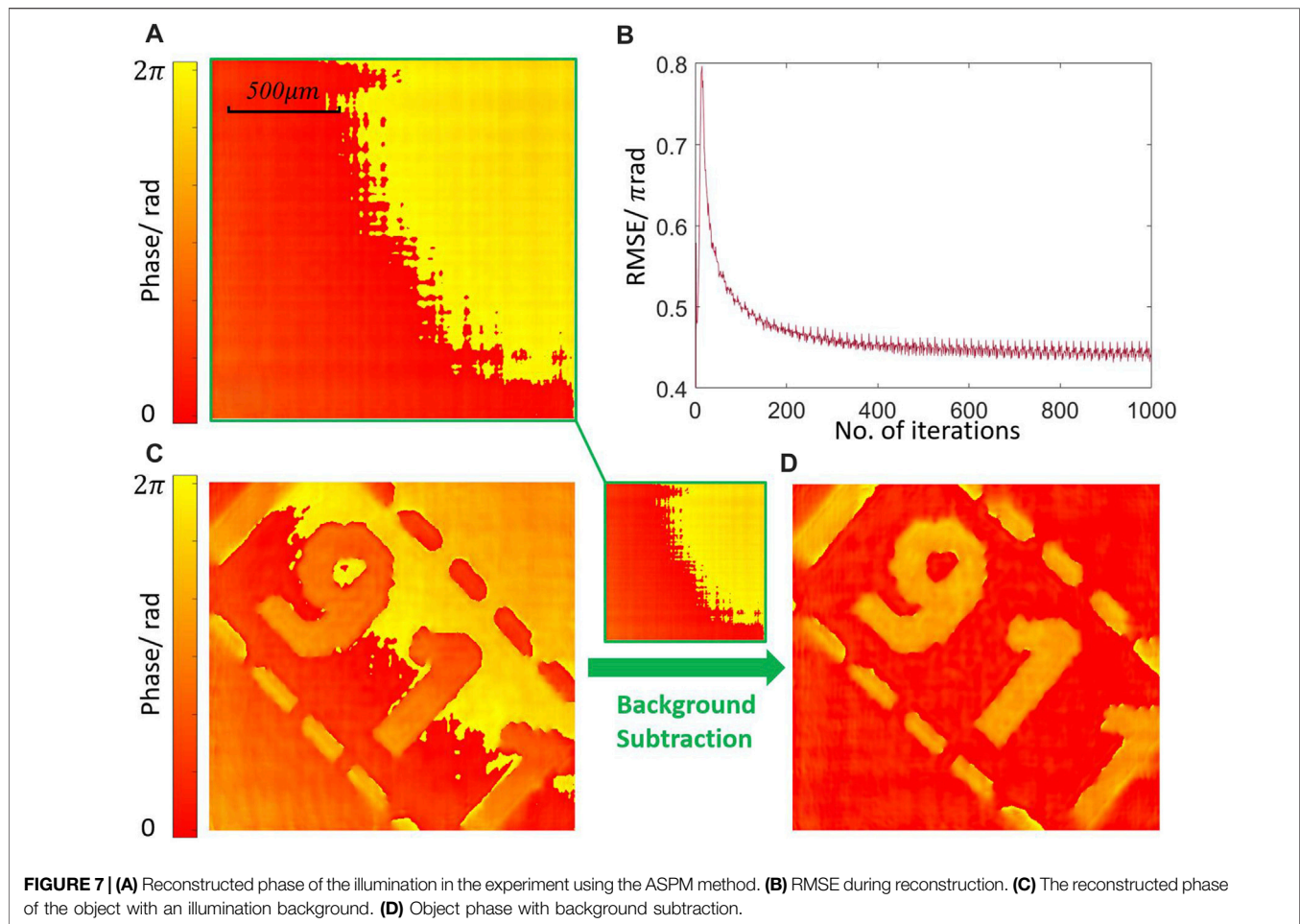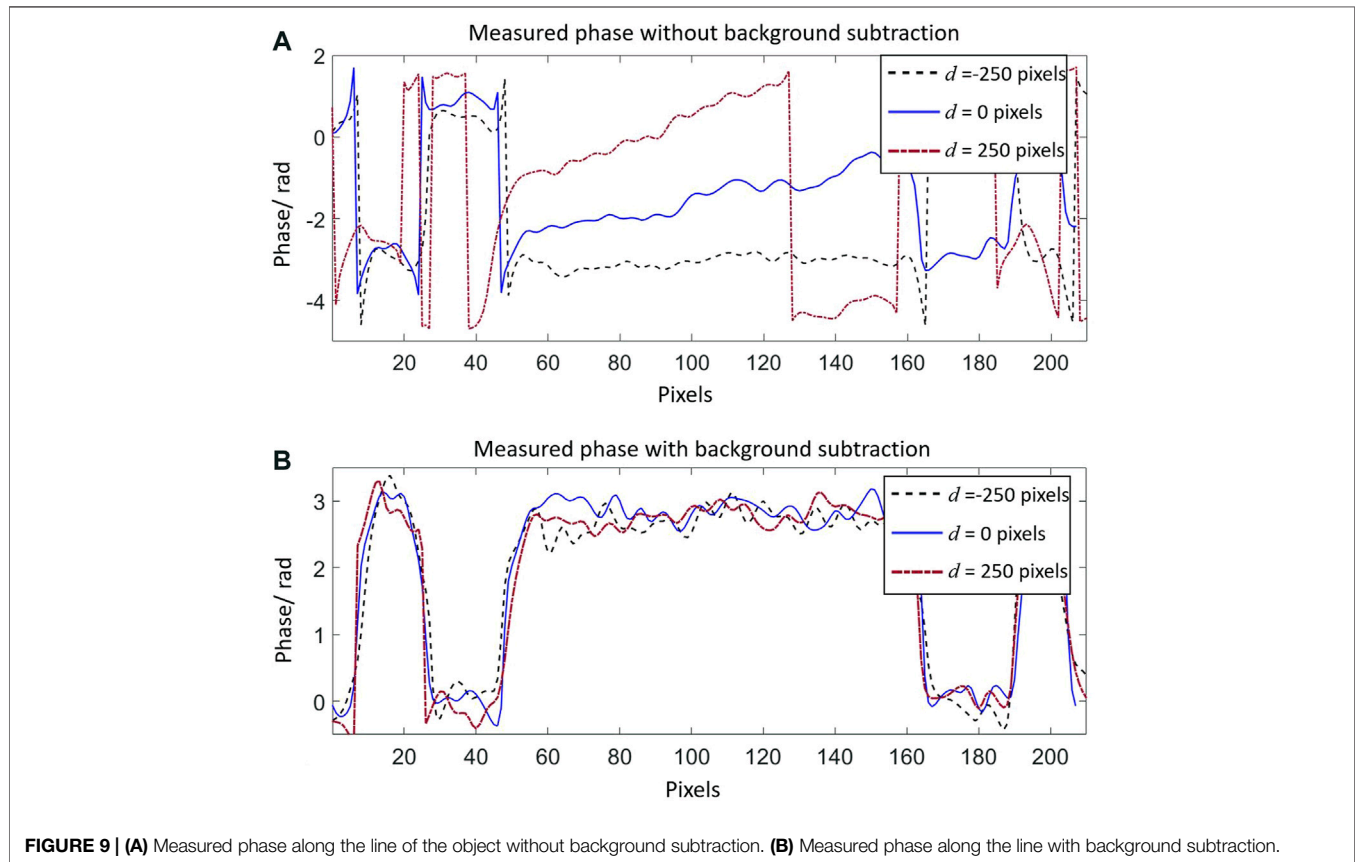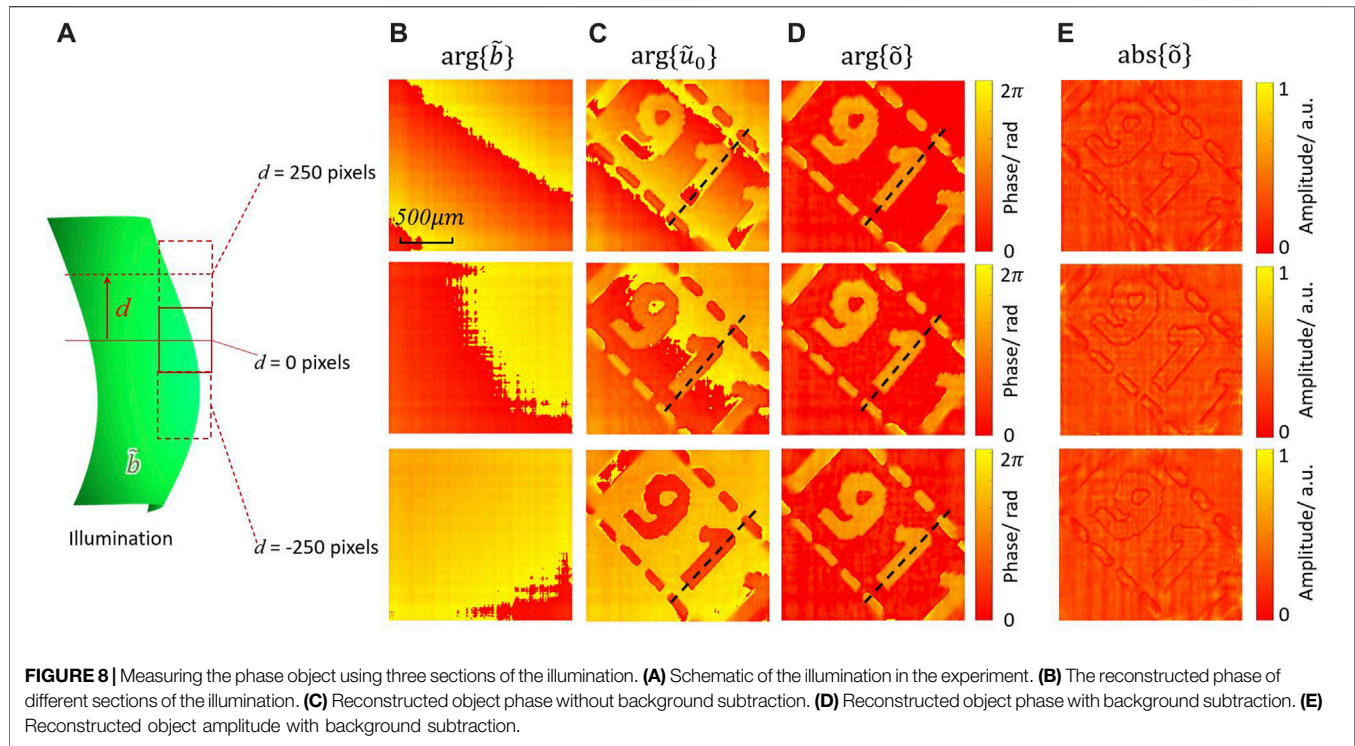$$\left. -1.66 \times 10^{-2} \right) \times \pi. \tag{11}$$

Measuring the object phase with background subtraction.

A phase plate was experimentally studied using the ASPM method. The setup was illuminated at $532\ nm$ wavelength. The polarization of the laser was adjusted by a $\lambda/2$ wave plate. The illumination was experimentally adjusted to be collimated but it was still not a perfect plane wave. The interferogram of the illumination was measured using a shear interferometer (Thorlabs, SI254), as shown in **Figure 6A**. The fringe pattern shows that the illumination $\tilde{b}$ had a background phase. A phase plate was measured as the object. The intensity pattern of the diffracted wavefront from the object is shown in **Figure 6E**. The diffracted wavefront was modulated using the ASPM method to reconstruct the phase of the object. The ASPM patterns were uploaded to the calibrated LCoS (Holoeye GAEA-2, 3.a 8 μm) at 60 Hz refreshing rate. As the LCoS is a birefringent device and the polarization of the incident beam has a great impact on the

modulation [66, 67]. The illumination was filtered by a linear polarizer to match the long display axis of the LCoS. The intensities of the modulated wavefront were captured with a CMOS camera (QHY 163, pixel size 3.8 μm) with 0.01 s exposure time. The period of the ASPM patterns was set to 40 pixels, and the modulated phase was π. After modulation in both directions, the pattern was shifted by five pixels for the next modulation. Sixteen modulations and captures were made for measuring a wavefront. Sixteen modulations and captures can be made in 0.27 s. Two of the modulation patterns and captured intensities are shown in **Figures 6F–I**.

The complex wavefront $\tilde{u}_1$ on the modulation plane was reconstructed using the ASPM method. The RMSEs of the adjacent iterations are shown in **Figure 6J**. The algorithm converged rapidly in 400 iterations and reached the final result after approximately 800 iterations. The complex wavefront $\tilde{u}_o$ emitted from the phase object was calculated by back-propagating $\tilde{u}_1$ to the object plane. As shown in **Figure 6K**, the phase can be distinguished as a character of '1911', which is the founding year of Tsinghua University. However, the wavefront $\tilde{u}_o$ is the multiple products of $\tilde{o}$ and $\tilde{b}$, $\tilde{u}_o = \tilde{b} \cdot \tilde{o}$. The phase of $\tilde{u}_o$ does not represent the object phase. The phase term of illumination $\tilde{b}$ must be measured and subtracted.

FIGURE 8 | Measuring the phase object using three sections of the illumination. **(A)** Schematic of the illumination in the experiment. **(B)** The reconstructed phase of different sections of the illumination. **(C)** Reconstructed object phase without background subtraction. **(D)** Reconstructed object phase with background subtraction. **(E)** Reconstructed object amplitude with background subtraction.

FIGURE 9 | (A) Measured phase along the line of the object without background subtraction. **(B)** Measured phase along the line with background subtraction.
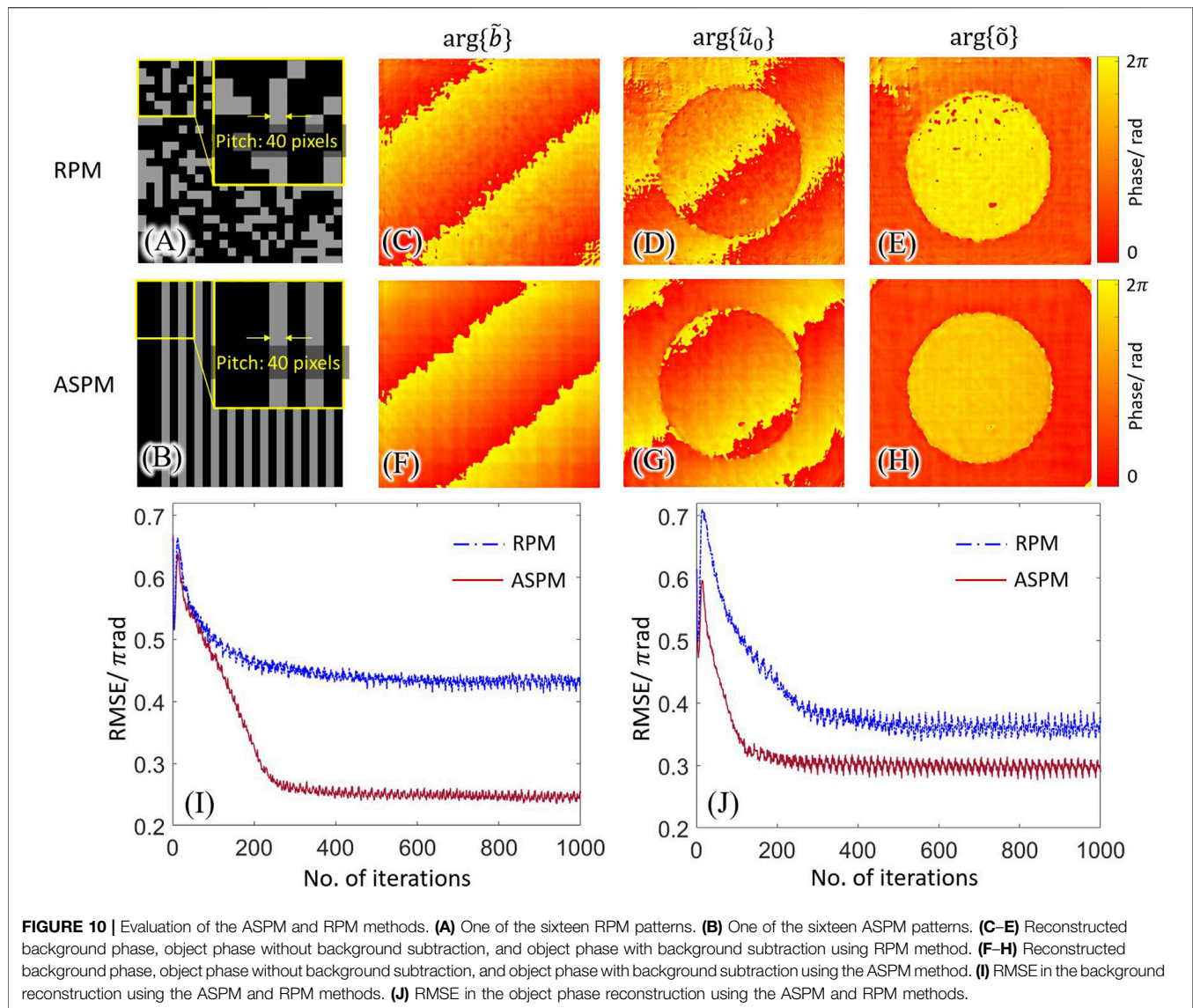
FIGURE 10 | Evaluation of the ASPM and RPM methods. **(A)** One of the sixteen RPM patterns. **(B)** One of the sixteen ASPM patterns. **(C–E)** Reconstructed background phase, object phase without background subtraction, and object phase with background subtraction using RPM method. **(F–H)** Reconstructed background phase, object phase without background subtraction, and object phase with background subtraction using the ASPM method. **(I)** RMSE in the background reconstruction using the ASPM and RPM methods. **(J)** RMSE in the object phase reconstruction using the ASPM and RPM methods.

Using the ASPM method, illumination $\tilde{b}$ was measured individually during the experiment. As shown in **Figure 7A**, the phase of $\tilde{b}$ indicates that the illumination on the object was slightly oblique and nonuniform in the experiment. The RMSE values during the reconstruction iterations are shown in **Figure 7B**. The ASPM method has good convergence in solving the background phase using the experimental data with noise. To calculate $\tilde{o}$, the illumination $\tilde{b}$ must be subtracted from the measured $\tilde{u}_o$. The phase of the object after subtraction is shown in **Figure 7D**. The average phase difference of the character was measured to be approximately 2.9 rad, which matched the designed value of the phase plate.

In the experiment, the illumination was expanded, and a schematic of the phase profile of the illumination is shown in **Figure 8A**. The phase plate was measured experimentally using three sections of illumination. After modulations and captures using the central section of the illumination, the next sections

at an interval of 250 pixels were used to illuminate the object. Using the ASPM method, the wavefronts of the three illumination sections were reconstructed. The background phases of the illumination sections are shown in **Figure 8B**. After subtracting the phase under illumination, the phase of the object was measured under the three illumination sections. The phase profiles before and after subtraction are shown in **Figures 8C, D**. The phase values along the dotted line in **Figures 8C, D** are plotted in **Figures 9A, B**. Before the subtraction, the phase was visually distinguished, but difficult to evaluate quantitatively. The strong background phases destroyed the investigated phase from the object. The phase profile of the reconstructed wavefront could not represent the object phase. After subtraction, the phase values along the line were quantitatively evaluated. The measured phase values under different illuminations matched well.

Evaluation of the Alternative Structured Phase Modulation and RPM Methods

The ASPM and RPM methods were experimentally evaluated. Sixteen ASPM patterns with a period of 40 pixels were used for modulation. For comparison, sixteen RPM patterns with a pitch size of 40 pixels were used for modulation. One of the RPM and ASPM patterns is shown in **Figures 10A, B**. Using the setup in **Figures 6A, C** phase object illuminated with a background phase was studied using the ASPM and RPM methods, respectively. Using the two methods, the phase of the background and object can be iteratively reconstructed, as shown in **Figures 10C–H**. The RMSEs curves of the two methods during iterations are shown in **Figures 10I, J**, which shows that the ASPM method has a smaller error during the reconstruction for a background phase and object phase. Compared to the RPM method, the ASPM method has a better reconstruction quality for the background phase and object phase.

In the proposed method, the spatial light modulator is used for phase modulation. SLM is a digitalized device and has a limited modulation bandwidth. The phases in the RPM are randomly distributed in a high spatial complexity, which makes the RPM hard to be accurately modulated using an available SLM. The phases in the ASPM are the same in one direction and vary periodically in the other direction. Compared to the RPM, the ASPM have lower complexity and is friendly for SLM modulation. Besides, there us environmental noise during the experiment. The ASPM patterns act as the phase gratings and concentrate the modulated intensities, which provides robustness to noise.

CONCLUSION

In this study, the ASPM method was used to retrieve the background phase in the illumination. Three statics background phases were reconstructed in a diffraction imaging setup, which is difficult to use in traditional phase-retrieval methods. A phase plate was investigated under three background illuminations, and the object phase was reconstructed. The ASPM method can retrieve the complex wavefront gathered from a lens set. With the ASPM method, various wavefront sensing techniques can be used for quantitative phase imaging. The method is also capable of measuring an object with a phase slowly varying in the spatial domain. The background phases in various types of imaging setups, such as in-line holography, can be retrieved and compensated using the ASPM method. In this work, the modulations were made with an SLM working at a 60 Hz refreshing rate. Sixteen acquisitions for measuring a background phase can be made in 0.27 s. The acquisition time can be reduced by using a faster modulation device, such as ferroelectric SLM.

DATA AVAILABILITY STATEMENT

The raw data supporting the conclusions of this article will be made available by the authors, without undue reservation.

AUTHOR CONTRIBUTIONS

LC and FY conceived and supervised the project. RL performed experiments and data analysis. FY, RL, and LC contributed to data analysis. RL and LC wrote the draft of the manuscript; All the authors edited the manuscript.

FUNDING

REFERENCES

1. Zhou W, Yu Y, Asundi A. Study on Aberration Suppressing Methods in Digital Micro-holography. *Opt Lasers Eng* (2009) 47(2):264–70. doi:10.1016/j.optlaseng.2008.04.026

2. Javidi B, Carnicer A, Anand A, Barbastathis G, Chen W, Ferraro P, et al. Roadmap on Digital Holography [Invited]. *Opt. Express* (2021) 29(22): 35078–118. doi:10.1364/OE.435915

3. Yan F, Yan H, Yu Y, Zhou W, Asundi A. The Suppression of Phase Error by Applying Window Functions to Digital Holography. *Opt Lasers Eng* (2016) 86: 206–15. doi:10.1016/j.optlaseng.2016.05.022

4. Sheridan JT, Kostuk RK, Gil AF, Wang Y, Lu W, Zhong H, et al. Roadmap on Holography. *J Opt* (2020) 22(12):123002. doi:10.1088/2040-8986/abb3a4

5. Paturzo M, Pagliarulo V, Bianco V, Memmolo P, Miccio L, Merola F, et al. Digital Holography, a Metrological Tool for Quantitative Analysis: Trends and Future Applications. *Opt Lasers Eng* (2018) 104:32–47. doi:10.1016/j.optlaseng.2017.11.013

6. Miao J, Charalambous P, Kirz J, Sayre D. Extending the Methodology of X-Ray Crystallography to Allow Imaging of Micrometre-Sized Non-crystalline Specimens. *Nature* (1999) 400(6742):342–4. doi:10.1038/22498

7. Zuo C, Li J, Sun J, Fan Y, Zhang J, Lu L, et al. Transport of Intensity Equation: A Tutorial. *Opt Lasers Eng* (2020) 135:106187. doi:10.1016/j.optlaseng.2020.106187

8. Latychevskaia T, Longchamp J-N, Fink H-W. When Holography Meets Coherent Diffraction Imaging. *Opt. Express* (2012) 20(27):28871–92. doi:10.1364/OE.20.028871

9. Wang K, Di J, Li Y, Ren Z, Kemao Q, Zhao J. Transport of Intensity Equation from a Single Intensity Image via Deep Learning. *Opt Lasers Eng* (2020) 134: 106233. doi:10.1016/j.optlaseng.2020.106233

10. Gao Y, Cao L. High-Fidelity Pixel-Super-Resolved Complex Field Reconstruction via Adaptive Smoothing. *Opt. Lett.* (2020) 45(24):6807–10. doi:10.1364/OL.409697

11. Ozcan A, McLeod E. Lensless Imaging and Sensing. *Annu. Rev. Biomed. Eng.* (2016) 18(1):77–102. doi:10.1146/annurev-bioeng-092515-010849

12. Rivenson Y, Zhang Y, Günaydın H, Teng D, Ozcan A. Phase Recovery and Holographic Image Reconstruction Using Deep Learning in Neural Networks. *Light Sci Appl* (2018) 7(2):17141. doi:10.1038/lsa.2017.141

13. Migukin A, Agour M, Katkovnik V. Phase Retrieval in 4f Optical System: Background Compensation and Sparse Regularization of Object with Binary Amplitude. *Appl. Opt.* (2013) 52(1):A269–A80. doi:10.1364/AO.52.00A269

14. Min J, Yao B, Gao P, Ma B, Yan S, Peng F, et al. Wave-Front Curvature Compensation of Polarization Phase-Shifting Digital Holography. *optik* (2012) 123:1525–9. doi:10.1016/j.ijleo.2011.09.018

15. He X, Tao H, Pan X, Liu C, Zhu J. High-Quality Laser Beam Diagnostics Using Modified Coherent Phase Modulation Imaging. *Opt. Express* (2018) 26(5): 6239–48. doi:10.1364/OE.26.006239

16. Cuche E, Marquet P, Depeursinge C. Spatial Filtering for Zero-Order and Twin-Image Elimination in Digital off-Axis Holography. *Appl. Opt.* (2000) 39(23):4070–5. doi:10.1364/AO.39.004070

17. Seo KW, Choi YS, Seo ES, Lee SJ. Aberration Compensation for Objective Phase Curvature in Phase Holographic Microscopy. *Opt. Lett.* (2012) 37(23): 4976–8. doi:10.1364/OL.37.004976

18. Di J, Zhao J, Sun W, Jiang H, Yan X. Phase Aberration Compensation of Digital Holographic Microscopy Based on Least Squares Surface Fitting. *Opt Commun* (2009) 282(19):3873–7. doi:10.1016/j.optcom.2009.06.049

19. Yu H, Jia S, Dong J, Huang D, Xu S. Phase Curvature Compensation in Digital Holographic Microscopy Based on Phase Gradient Fitting and Optimization. *J. Opt. Soc. Am. A* (2019) 36(12):D1–D6. doi:10.1364/JOSAA.36.0000D1

20. Miccio L, Alfieri D, Grilli S, Ferraro P, Finizio A, De Petrocellis L, et al. Direct Full Compensation of the Aberrations in Quantitative Phase Microscopy of Thin Objects by a Single Digital Hologram. *Appl. Phys. Lett.* (2007) 90(4): 041104. doi:10.1063/1.2432287

21. Colomb T, Montfort F, Kühn J, Aspert N, Cuche E, Marian A, et al. Numerical Parametric Lens for Shifting, Magnification, and Complete Aberration Compensation in Digital Holographic Microscopy. *J. Opt. Soc. Am. A* (2006) 23(12):3177–90. doi:10.1364/JOSAA.23.003177

22. Jianglei D, Jianlin Z, Qi F, Hongzhen J, Weiwei S. Phase Correction of Wavefront Reconstruction in Digital Holographic Microscopy. *Acta Optica Sinica* (2008) 28(1):56–61. doi:10.3788/aos20082801.0056

23. Choi I, Lee K, Park Y. Compensation of Aberration in Quantitative Phase Imaging Using Lateral Shifting and Spiral Phase Integration. *Opt. Express* (2017) 25(24):30771–9. doi:10.1364/OE.25.030771

24. Baek Y, Hugonnet H, Park Y. Pupil-Aberration Calibration with Controlled Illumination for Quantitative Phase Imaging. *Opt. Express* (2021) 29(14): 22127–35. doi:10.1364/OE.426080

25. Stadelmaier A, Massig JH. Compensation of Lens Aberrations in Digital Holography. *Opt. Lett.* (2000) 25(22):1630–2. doi:10.1364/OL.25.001630

26. Liu Q, Wang Y, He J, Ji F. Phase Shift Extraction and Wavefront Retrieval from Interferograms with Background and Contrast Fluctuations. *J. Opt.* (2015) 17(2):025704. doi:10.1088/2040-8978/17/2/025704

27. Yatabe K, Ishikawa K, Oikawa Y. Simple, Flexible, and Accurate Phase Retrieval Method for Generalized Phase-Shifting Interferometry. *J. Opt. Soc. Am. A* (2017) 34(1):87–96. doi:10.1364/JOSAA.34.000087

28. RF Oliver, S Johannes, B Albrecht, S Horst, editors. *Measurement of the Wave Aberrations of Holographic Optical Lens Elements*. Prague, Czech Republic: ProcSPIE (1993).

29. Brady DJ, Choi K, Marks DL, Horisaki R, Lim S. Compressive Holography. *Opt. Express* (2009) 17(15):13040–9. doi:10.1364/OE.17.013040

30. Huang Z, Memmolo P, Ferraro P, Cao L. Dual-Plane Coupled Phase Retrieval for Non-prior Holographic Imaging. *PhotoniX* (2022) 3(1):3. doi:10.1186/s43074-021-00046-w

31. Gerchberg RWA. Practical Algorithm for the Determination of Phase from Image and Diffraction Plane Pictures. *Optik* (1971) 35(2):237

32. Fienup JR. Reconstruction of an Object from the Modulus of its Fourier Transform. *Opt. Lett.* (1978) 3(1):27–9. doi:10.1364/OL.3.000027

33. Fienup JR. Reconstruction of a Complex-Valued Object from the Modulus of its Fourier Transform Using a Support Constraint. *J. Opt. Soc. Am. A* (1987) 4(1):118–23. doi:10.1364/JOSAA.4.000118

34. Zhang F, Chen B, Morrison GR, Vila-Comamala J, Guizar-Sicairos M, Robinson IK. Phase Retrieval by Coherent Modulation Imaging. *Nat Commun* (2016) 7(1):13367. doi:10.1038/ncomms13367

35. Wang B, Wang Q, Lyu W, Zhang F. Modulator Refinement Algorithm for Coherent Modulation Imaging. *Ultramicroscopy* (2020) 216:113034. doi:10.1016/j.ultramic.2020.113034

36. Paxman RG, Fienup JR, Clinthorne JT. The Effects of Tapered Illumination and Fourier Intensity Errors on Phase Retrieval. *Proc SPIE* (1988) 0828. doi:10.1117/12.942098

37. Fienup JR. Phase Retrieval Algorithms: A Comparison. *Appl. Opt.* (1982) 21(15):2758–69. doi:10.1364/AO.21.002758

38. Almoro PF, Pham QD, Serrano-Garcia DI, Hasegawa S, Hayasaki Y, Takeda M, et al. Enhanced Intensity Variation for Multiple-Plane Phase Retrieval Using a Spatial Light Modulator as a Convenient Tunable Diffuser. *Opt. Lett.* (2016) 41(10):2161–4. doi:10.1364/OL.41.002161

39. Almoro PF, Waller L, Agour M, Falldorf C, Pedrini G, Osten W, et al. Enhanced Deterministic Phase Retrieval Using a Partially Developed Speckle Field. *Opt. Lett.* (2012) 37(11):2088–90. doi:10.1364/OL.37.002088

40. Zhang F, Pedrini G, Osten W. Phase Retrieval of Arbitrary Complex-Valued Fields through Aperture-Plane Modulation. *Phys. Rev. A* (2007) 75(4):043805. doi:10.1103/PhysRevA.75.043805

41. Rodenburg JM, Faulkner HML. A Phase Retrieval Algorithm for Shifting Illumination. *Appl. Phys. Lett.* (2004) 85(20):4795–7. doi:10.1063/1.1823034

42. Zheng G, Horstmeyer R, Yang C. Wide-Field, High-Resolution Fourier Ptychographic Microscopy. *Nat Phot* (2013) 7(9):739–45. doi:10.1038/nphoton.2013.187

43. Konda PC, Loetgering L, Zhou KC, Xu S, Harvey AR, Horstmeyer R. Fourier Ptychography: Current Applications and Future Promises. *Opt. Express* (2020) 28(7):9603–30. doi:10.1364/OE.386168

44. Li R, Cao L. Complex Wavefront Sensing Based on Coherent Diffraction Imaging Using Vortex Modulation. *Sci Rep* (2021) 11(1):9019. doi:10.1038/s41598-021-88523-x

45. Kagias M, Wang Z, Villanueva-Perez P, Jefimovs K, Stampanoni M. 2d-Omnidirectional Hard-X-Ray Scattering Sensitivity in a Single Shot. *Phys. Rev. Lett.* (2016) 116(9):093902. doi:10.1103/PhysRevLett.116.093902

46. Wang Z, Huang Z, Chen Z, Zhang L, Jiang X, Kang K, et al. Low-Dose Multiple-Information Retrieval Algorithm for X-Ray Grating-Based Imaging. *Nucl Instrum Methods Phys Res Sect A Accel Spectrom Detect Assoc Equip* (2011) 635(1):103–7. doi:10.1016/j.nima.2011.01.079

47. Lee K, Park Y. Exploiting the Speckle-Correlation Scattering Matrix for a Compact Reference-free Holographic Image Sensor. *Nat Commun* (2016) 7(1): 13359. doi:10.1038/ncomms13359

48. Kwon H, Arbabi E, Kamali SM, Faraji-Dana M, Faraon A. Single-Shot Quantitative Phase Gradient Microscopy Using a System of Multifunctional Metasurfaces. *Nat. Photonics* (2020) 14(2):109–14. doi:10.1038/s41566-019-0536-x

49. Platt BC, Shack R. History and Principles of Shack-Hartmann Wavefront Sensing. *J Refract Surg* (2001) 17(5):S573–7. Epub 2001/10/05. doi:10.3928/1081-597X-20010901-13

50. Wu Y, Sharma MK, Veeraraghavan A. WISH: Wavefront Imaging Sensor with High Resolution. *Light Sci Appl* (2019) 8(1):44. doi:10.1038/s41377-019-0154-x

51. Zhang Z, You Z, Chu D. Fundamentals of Phase-Only Liquid Crystal on Silicon (Lcos) Devices. *Light Sci Appl* (2014) 3:e213. doi:10.1038/lsa.2014.94

52. Li R, Cao L. Complex Wavefront Sensing Based on Alternative Structured Phase Modulation. *Appl. Opt.* (2021) 60(4):A48–A53. doi:10.1364/AO.405630

53. Gao P, Pedrini G, Osten W. Structured Illumination for Resolution Enhancement and Autofocusing in Digital Holographic Microscopy. *Opt. Lett.* (2013) 38(8):1328–30. doi:10.1364/OL.38.001328

54. Zheng J, Gao P, Yao B, Ye T, Lei M, Min J, et al. Digital Holographic Microscopy with Phase-shift-free Structured Illumination. *Phot. Res.* (2014) 2(3):87–91. doi:10.1364/PRJ.2.000087

55. Gao P, Pedrini G, Osten W. Phase Retrieval with Resolution Enhancement by Using Structured Illumination. *Opt. Lett.* (2013) 38(24):5204–7. doi:10.1364/OL.38.005204

56. Ma Y, Wen K, Liu M, Zheng J, Chu K, Smith ZJ, et al. Recent Advances in Structured Illumination Microscopy. *J. Phys. Photonics* (2021) 3(2):024009. doi:10.1088/2515-7647/abdb04

57. Zhang J, Sun J, Chen Q, Zuo C. Resolution Analysis in a Lens-free On-Chip Digital Holographic Microscope. *IEEE Trans. Comput. Imaging* (2020) 6: 697–710. doi:10.1109/TCI.2020.2964247

58. Fan Y, Li J, Lu L, Sun J, Hu Y, Zhang J, et al. Smart Computational Light Microscopes (Sclms) of Smart Computational Imaging Laboratory (Scilab). *PhotoniX* (2021) 2(1):19. doi:10.1186/s43074-021-00040-2

59. Cirtoaje C, Petrescu E. The Influence of Single-Walled Carbon Nanotubes on the Dynamic Properties of Nematic Liquid Crystals in Magnetic Field. *Materials* (2019) 12(24):4031. doi:10.3390/ma12244031

60. DeMars LA, Mikuła-Zdańkowska M, Falaggis K, Porras-Aguilar R. Single-Shot Phase Calibration of a Spatial Light Modulator Using Geometric Phase Interferometry. *Appl. Opt.* (2020) 59(13):D125–D30. doi:10.1364/AO.383610

61. Arias A, Paniagua-Diaz AM, Prieto PM, Roca J, Artal P. Phase-Only Modulation with Two Vertical Aligned Liquid Crystal Devices. *Opt. Express* (2020) 28(23):34180–9. doi:10.1364/OE.410429

62. Shen Y, Hu Z, Wu D, Ma C, Liu Y. An Open-Source, Accurate, and Iterative Calibration Method for Liquid-Crystal-Based Spatial Light Modulators. *Opt Commun* (2021) 495:127108. doi:10.1016/j.optcom.2021.127108

63. Li R, Gao Y, Cao L. *In Situ* Calibration for a Phase-Only Spatial Light Modulator Based on Digital Holography. *Opt. Eng.* (2020) 59(5):1–10. doi:10.1117/1.OE.59.5.053101

64. Gao Y, Li R, Cao L. Self-Referenced Multiple-Beam Interferometric Method for Robust Phase Calibration of Spatial Light Modulator. *Opt. Express* (2019) 27(23):34463–71. doi:10.1364/OE.27.034463

65. Márquez A, Martínez-Guardiola F, Francés J, Neipp C, Ramírez M, Calzado E, et al. Analytical Modeling of Blazed Gratings on Two-Dimensional Pixelated Liquid Crystal on Silicon Devices. *Opt Eng* (2020) 59(4):041208. doi:10.1117/1.OE.59.4.041208

66. Falldorf C, von Kopylow C, Bergmann RB. Wave Field Sensing by Means of Computational Shear Interferometry. *J. Opt. Soc. Am. A* (2013) 30(10):1905–12. doi:10.1364/JOSAA.30.001905

67. Agour M, Falldorf C, Bergmann RB. Investigation of Composite Materials Using Slm-Based Phase Retrieval. *Opt. Lett.* (2013) 38(13):2203–5. doi:10.1364/OL.38.002203

![frontiers] Frontiers in Physics

Check for updates

Coherent noise suppression in digital holographic microscopy based on label-free deep learning

Ji Wu[1,2], Ju Tang[2], Jiawei Zhang[2] and Jianglei Di[1,2]*

[1]Advanced Institute of Photonics Technology, School of Information Engineering, and Guangdong Provincial Key Laboratory of Information Photonics Technology, Guangdong University of Technology, Guangzhou, China, [2]MOE Key Laboratory of Material Physics and Chemistry Under Extraordinary Conditions, and Shaanxi Key Laboratory of Optical Information Technology, School of Physical Science and Technology, Northwestern Polytechnical University, Xi'an, China

Deep learning techniques can be introduced into the digital holography to suppress the coherent noise. It is often necessary to first make a dataset of noisy and noise-free phase images to train the network. However, noise-free images are often difficult to obtain in practical holographic applications. Here we propose a label-free training algorithms based on self-supervised learning. A dilated blind spot network is built to learn from the real noisy phase images and a noise level function network to estimate a noise level function. Then they are trained together via maximizing the constrained negative log-likelihood and Bayes' rule to generate a denoising phase image. The experimental results demonstrate that our method outperforms standard smoothing algorithms in accurately reconstructing the true phase image in digital holographic microscopy.

KEYWORDS

digital holography, noise suppression, self-supervised learning, label-free, digital holographic microscopy (DHM)

Introduction

Digital holographic microscopy (DHM) is a non-invasive, highly precise and real-time quantitative phase measurement technology, and it has important applications in the fields of microsurface topography measurement, flow field measurement, biological cell measurement, and so on [1–4]. However, under high coherent illumination, uneven surfaces such as dust and scratches on the specimen will introduce random amplitude and phase fluctuations, and finally form speckle noise in the reconstructed holographic image [5]. And furthermore, the undesired diffraction and multiple reflections include the phase noise. They are all coherent noise because of the high coherence of optical field. Thus, the suppression of coherent noise is a key research subject, which is of great significance to improve the measurement accuracy and resolution of DHM.

The coherent noise suppression technologies can be classified into the optical approach and the digital image processing method. A light source with a low
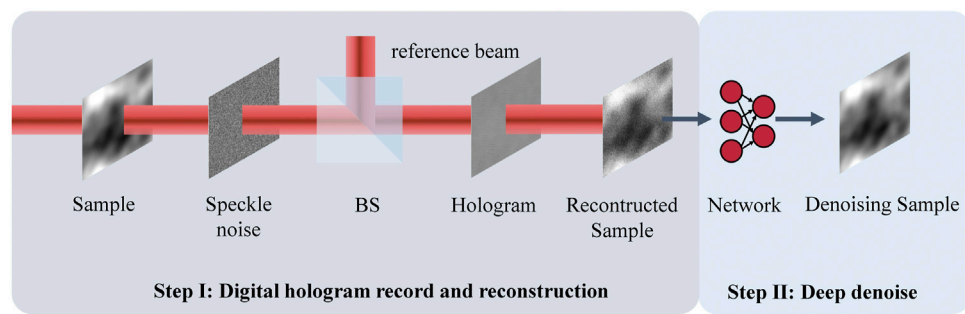
FIGURE 1
The schematic diagram for the label-free coherent noise suppression in digital holographic microscopy.

coherence length can prevent noise outside the coherence length from being imaged on the hologram, thus lowering the coherent noise [6, 7]. Multiple holograms with different incident angles [8, 9], polarization states [10] or wavelengths [11] can be collected and then superimposed to average the speckle noise. However, this increases the complexity of optical system, and can't process holograms offline. In digital image processing, the median filtering and mean filtering are usually used for speckle noise suppressing, but high frequency details will inevitably be lost. The wiener filtering, blind convolution method and Block-matching and 3D filtering (BM3D) can also be used with the disadvantage that the parameter selection is difficult to determine [12]. The frequency-domain denoising assumes that the noise belongs to high-frequency information, so the denoising is accomplished by suppressing high-frequency information, such as windowed Fourier transform, wavelet transform, and so on [13]. The third type of digital image processing methods convert the denoising problem into an unconstrained optimization problem by building an optimization function such as a convex optimization form [14].

In recent years, the deep learning-based denoising methods have emerged. The work of Wang et al. demonstrated that the neural network can adapt to coherent noise on its own [15]. In most deep learning based coherent noise suppression methods, the training data pairs of noisy and noise-free phase images are first constructed using the noise model. The training data pairs are utilized to train a neural network capable mapping both the noisy and noise-free phase images [16–20]. However, these methods require paired data to train the neural network, which is difficult in practical holographic applications. Yin *et al.* used neural networks to learn common information from paired noisy phase images without noise-free data and achieved neural network denoising for noisy phase images [21]. However, this method still needs to obtain multiple noisy phase images while ensuring the consistency of the underlying sample.

We propose a label-free coherent noise suppression method based on deep learning, which realizes the self-supervised

learning between the noise generation and suppression models by establishing the negative log-likelihood function of noise. The noise-free phase images are not necessary as labels, only the noisy phase images are needed to complete the network training. The trained network can achieve noise suppression for various noisy phase images, and the algorithm has remarkable generalization ability, which is of great significance for dynamic holographic imaging.

Methods

Physical generation of speckle noise

Assuming that the coordinates of the holographic recording plane is (x, y), the off-axis digital holographic intensity $I(x, y)$ is expressed as [22].

$$I(x, y) = |O(x, y)|^2 + |R(x, y)|^2 + O(x, y)R^\star(x, y) \\ + O^\star(x, y)R(x, y) + n(x, y) \quad (1)$$

Where, $O(x, y)$ and $R(x, y)$ are the object wavefront and reference wavefronts at the recording plane, respectively. The third and fourth terms can be used to reconstruct the amplitude and phase of object wavefront, and the fifth term is speckle noise. For any scattering point source p of the imaging system, the coherent noise $n(x, y)$ can be expressed as [5].

$$n(x, y) = \left| \sum_1^N a(x_p, y_p) \exp\left[j\varphi(x_p, y_p) \right] \exp\left[j\varphi(x, y) \right] \right|^2 \quad (2)$$

Where, $a(x_p, y_p)$ is the random intensity fluctuation, $\varphi(x_p, y_p)$ is the random phase fluctuation, and $\varphi(x,y)$ is the propagation phase of the light.

In the numerical reconstruction of the digital hologram, the reconstructed complex amplitude $U(\xi, \eta)$ can be obtained by using the angular spectrum method [23]. Then, the phase of the sample can be calculated through

FIGURE 2
The framework for the label-free holographic phase noise suppression.
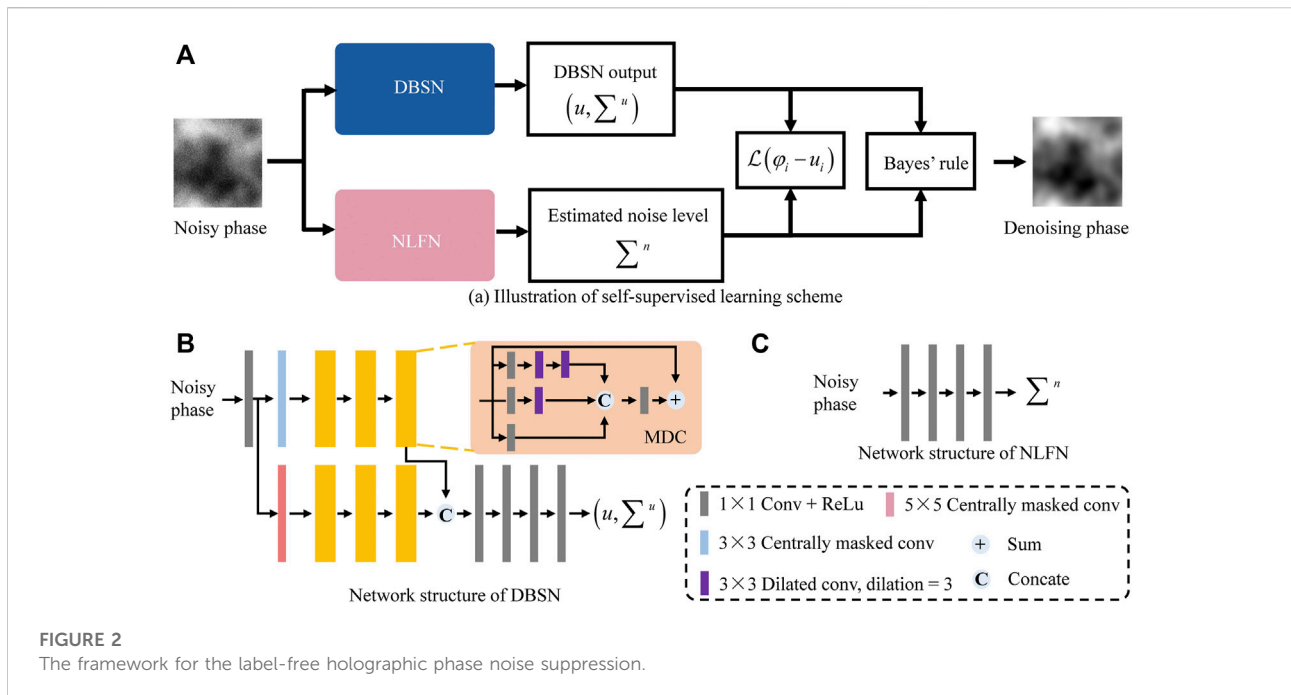
$$\varphi(\xi, \eta) = \arctan \frac{\text{Im}[U(\xi, \eta)]}{\text{Re}[U(\xi, \eta)]} \ (\text{mod} \ 2\pi) \qquad (3)$$

Where, Im ( ) and Re ( ) represent the operations of taking the complex imaginary part and the real part, respectively. Then the real phase of the sample can be obtained through the unwrapping operation. However, the obtained phase image will inevitably contain noise. Assuming that the noisy phase image can be expressed as

$$\varphi(\xi, \eta) = \tilde{\varphi}(\xi, \eta) + n(\xi, \eta) \qquad (4)$$

Where, $n(\xi, \eta)$ denotes the noise in $\varphi(\xi, \eta)$, $\tilde{\varphi}(\xi, \eta)$ is the underlying noise-free phase image [24]. Assuming that the phase $\varphi(\xi, \eta)$ is spatially correlated, the noise $n(\xi, \eta)$ is a pixel-independent and signal-dependent Gaussian noise [25]. And then, the noise variance of pixel i var (n_i) is only determined by the underlying noise-free pixel value $\tilde{\varphi}_i$ of pixel i. The noise variance var (n_i) can be regarded as a noise level function (NLF) $g(\tilde{\varphi}_i)$, which can be expressed as

$$\text{var}(n_i) = g(\tilde{\varphi}_i). \qquad (5)$$

Label-free coherent noise suppression

The label-free coherent noise suppression method is composed of two steps, shown in Figure 1. In the first step, the object beam passes through the sample and the simulated coherent noise screen successively, and then interferes with the reference beam after the beam splitting prism (BS) to form the

digital hologram. In this step, the coherent noise is introduced and a real holographic recording system is simulated. In the simulation process, the model of speckle-noise involves only phase distribution of object waves. The simulated coherent noise screen modulates the object beam in the form of an exponential term to simulate the random phase fluctuation of digital holography. In the second step, the noisy phase images will be processed by the trained neural network to reconstruct the clean phase images.

DBSN and NLFN

As shown in Figure 2A, the main structure is composed of the dilated blind spot network (DBSN) and the noise level function network (NLFN) [26]. Then, a self-supervised loss function is introduced to jointly train DBSN and NLFN by maximizing the constrained log-likelihood. For a given noisy phase image, DBSN and NLFN cooperate to produce a clean denoising phase image under a Bayes' rules.

The structure of DBSN in Figure 2B is based on the blind spot network. DBSN starts with a 1 × 1 convolutional layer followed by two network branches. A 3 × 3 center-masked convolutional layer and six multi-dilated convolutional (MDC) modules make up each branch. The feature maps of the two branches are then concatenated, followed by the deployment of four 1 × 1 convolutional layers to yield the network output. The MDC module in Figure 2B utilizes a residual structure involving three sub-branches. In these branches, zero, one, and two 3 × 3 dilated convolutional layers are stacked on top of 1 × 1 convolutional
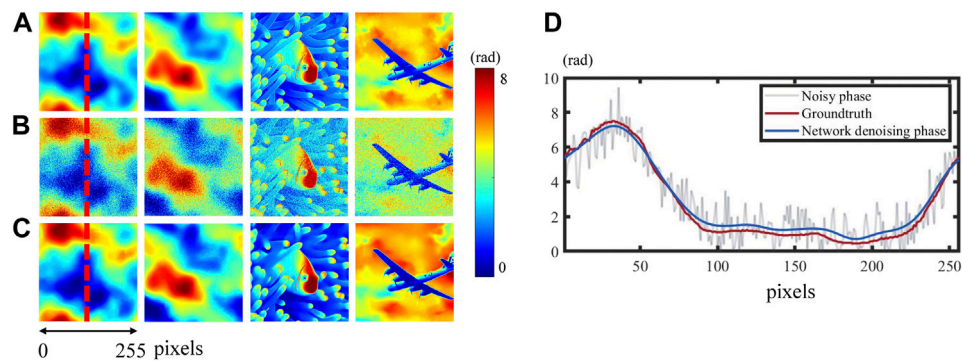
FIGURE 3
Neural network coherent noise suppression results on simulation data. **(A)** The noise-free phase images; **(B)** The noisy phase images reconstructed by a DHM; **(C)** The network denoising phase images; **(D)** The profile map along with the red lines.
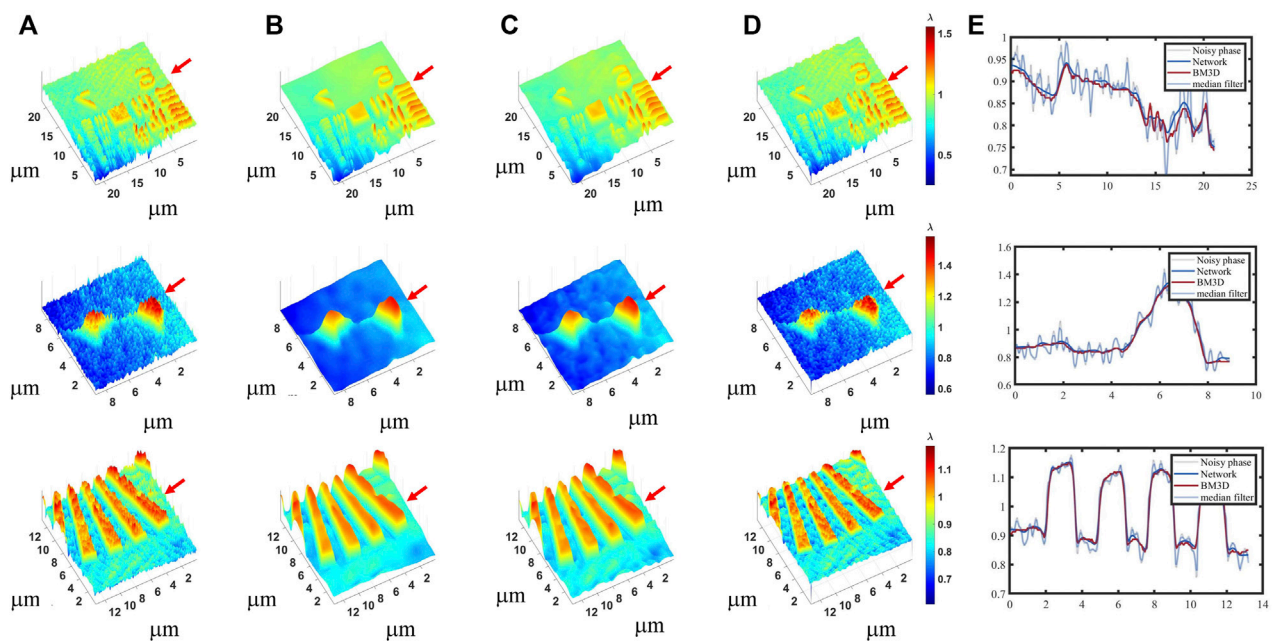

FIGURE 4
Comparison of noise suppression results on cell phase. The upper and lower rows are different cells. **(A)** The phase images of the resolution board, HT22 cell and line board; **(B)** The noise suppression phase by the network; **(C)** The noise suppression phase by median filter in a 6-by-6 neighborhood; **(D)** The noise suppression phase by BM3D with noise variance of 0.02; **(E)** The profile map along with the red at the red arrow.

layers, respectively. These branches' outputs are then concatenated, followed by another 1×1 convolutional layer, and summed with the input of the MDC module. Finally, four 1×1 convolutional layers are further applied to produce the DBSN output by concatenating the feature maps from the two network branches.

To enhance the model's flexibility, the noise is assumed as a signal-dependent multivariate Gaussian noise [25], with each noisy phase image being NLF-specific. The noise level will always be determined by input values at the same location. In the self-supervised learning, only noisy reconstructed phase images can be utilized. So NLFN learns NLF to approximate $g(\tilde{\varphi}_i)$ from the noisy phase image. The NLFN comprises five 1×1 convolutional

layers with 16 channels, as shown in Figure 2C. Except for the final layer, the activation function ReLU applies to all convolutional layers.

In the proposed unpaired learning algorithms, the underlying noise-free image $\tilde{\varphi}$ and the NLF are not available. Therefore, self-supervised learning is used to train DBSN and NLFN. For a given position i, μ is set to be the clean image predicted directly by DBSN, which is closer to $\tilde{\varphi}_i$ than φ_i. Then the assumption can be expressed as

$$\begin{cases} \varphi_i = \tilde{\varphi}_i + n_i, \ n_i \sim N\left(0, \sum_i^n\right) \\ \mu_i = \tilde{\varphi}_i + n_i^\mu, \ n_i^\mu \sim N\left(0, \sum_i^u\right) \\ \left|\sum_i^n\right| \gg \left|\sum_i^u\right| \approx 0 \end{cases} \quad (6)$$

Among them, φ_i, $\tilde{\varphi}_i$, n_i is constant. And further assume that n_i and μ_i are independent. Considering that $\tilde{\varphi}_i$ is not available, the self-supervised loss function employs the negative log-likelihood of $\varphi_i - u_i$, which can be written as [26]

$$L\left(\varphi_i - u_i\right) = \sum_i \frac{1}{2}\left(\varphi_i - u_i\right)^T \left(\sum_i^n + \sum_i^u\right)^{-1} \left(\varphi_i - u_i\right) + \log\left|\sum_i^n\right|$$
$$+ \operatorname{tr}\left(\left(\sum_i^n\right)^{-1} \sum_i^u\right)$$
$$(7)$$

where, u_i, $\sum_i^u$ can be estimated from the output of the DBSN at location i, and $\sum_i^n$ can be estimated from the output of the NLFN network at location i. After self-supervised learning, the denoising phase image can be obtained using the Bayes' rule for each pixel

$$\phi_i = \left(\sum_i^n + \sum_i^u\right)^{-1} \left(\sum_i^n u_i + \sum_i^u \varphi_i\right) \quad (8)$$

The following are the specifics of DBSN and NLFN self-supervised training. Noise-free phase images were obtained via using the power spectrum inversion method [27] to generate 10,000 images with 256 × 256 pixels. The holographic phase noise model in Figure 1 is used to generate noisy phase images. The test dataset consists of actual noisy phase images reconstructed from a DHM. The network is initialized with pre-trained parameters [26] throughout training and terminated after 100 epochs. DBSN and NLFN are trained using the Adam optimizer with a learning rate of 3×10^{-4}. The underlying noise-free image is first computed using DBSN, and then its noise level is estimated by NLF. Then, the loss function is calculated using Eq. 7, and then the parameters of DBSN and NLF are updated sequentially using the optimizer. The network is implemented by Pytorch 1.7 based on Python 3.7.1, which is performed on a PC with an Intel Core i7-10700K CPU, 32 GB of RAM, using NVIDIA GeForce GTX 2080Ti GPU.

Results and conclusion

The test dataset consists of 1,000 phase images from the real-world dataset [28] and 1,000 phase images simulated by the power spectrum inversion method [27]. Noisy phase images with atmospheric turbulence, fish and airplane patterns are shown in Figure 3A. The phase variation varies from 0 to 8 rad. The noisy phase images in Figure 3B are generated by the simulation method in Figure 1, simulating the phase reconstruction results of a DHM. It is worth emphasizing that the ground truth doesn't participate in the network's training process. It is simply utilized for comparing outcomes. A total of three sets of findings are shown in Figure 3. The mean relative phase error between denoising results and the real phase is 2.08%, which shows the self-supervised learning neural network can effectively suppress the noise of noisy phase images. The exact phase distribution at the red line on the left is shown in Figure 3D. The profile of network denoising result is shown by the red curve, while the profile of noise-free phase is represented by the blue curve. The two curves have a mean deviation error of 0.2838 rad, less than 0.1 wavelength. It demonstrates that the network denoising results accurately portray the samples' real phase distribution.

The noise suppression test is conducted on the testing sample once finishing the network training. A series of digital holograms were recorded by using a DHM with a common-path and a wavelength of 532 nm [29, 30]. The phase images of the resolution board, HT22 cell and line board are numerically reconstructed in Figure 4A. Here, it is evident for the impact of coherent noise on quantitative phase measurements. To compare the noise suppression effect, median filter in a 6-by-6 neighborhood and BM3D with noise variance of 0.02 are employed. As shown in Figure 4, the proposed label-free self-supervised learning technique produces a smoother phase image with superior noise suppression than the BM3D and median filtering methods. Furthermore, the robustness of the proposed method may be proved since the feature space of phase images from a DHM and simulated turbulent phase images, which is the train dataset differ from each other significantly.

In summary, we propose a label-free coherent noise suppression method based on self-supervised learning. The proposed method has excellent coherent noise suppression performance and good robustness. By constructing a negative log-likelihood loss function, we can complete the training of the denoising network without noise-free phase data. The mean relative phase error between denoising results and the real phase is 2.08%.

Data availability statement

The original contributions presented in the study are included in the article/Supplementary Material, further inquiries can be directed to the corresponding author.

Author contributions

JW wrote the draft of the manuscript and contributed to data analysis. JW, JT, and JZ performed experiments. JD conceived and supervised the project. All the authors edited the manuscript.

Conflict of interest

The authors declare that the research was conducted in the absence of any commercial or financial relationships that could be construed as a potential conflict of interest.

Publisher's note

All claims expressed in this article are solely those of the authors and do not necessarily represent those of their affiliated organizations, or those of the publisher, the editors and the reviewers. Any product that may be evaluated in this article, or claim that may be made by its manufacturer, is not guaranteed or endorsed by the publisher.

References

1. Wang K, Dou J, Kemao Q, Di J, Zhao J. Y-Net: A one-to-two deep learning framework for digital holographic reconstruction. *Opt Lett* (2019) 44:4765. doi:10.1364/OL.44.004765

2. Di J, Li Y, Xie M, Zhang J, Ma C, Xi T, et al.Dual-wavelength common-path digital holographic microscopy for quantitative phase imaging based on lateral shearing interferometry. *Appl Opt* (2016) 55:7287. doi:10.1364/AO.55.007287

3. Sun W, Zhao J, Di J, Wang Q, Wang L. Real-time visualization of karman vortex street in water flow field by using digital holography. *Opt Express* (2009) 17: 20342. doi:10.1364/OE.17.020342

4. Wang K, Zhang M, Tang J, Wang L, Hu L, Wu X, et al.Deep learning wavefront sensing and aberration correction in atmospheric turbulence. *PhotoniX* (2021) 2:8. doi:10.1186/s43074-021-00030-4

5. Goodman JW. *Speckle phenomena in optics: Theory and applications*. Bellingham, Washington, United States: SPIE (2020).

6. Bhaduri B, Pham H, Mir M, Popescu G. Diffraction phase microscopy with white light. *Opt Lett* (2012) 37:1094. doi:10.1364/OL.37.001094

7. Shan M, Kandel ME, Majeed H, Nastasa V, Popescu G. White-light diffraction phase microscopy at doubled space-bandwidth product. *Opt Express* (2016) 24: 29033. doi:10.1364/OE.24.029033

8. Feng P, Wen X, Lu R. Long-working-distance synthetic aperture fresnel off-axis digital holography. *Opt Express* (2009) 17:5473. doi:10.1364/OE.17.005473

9. Wang Y, Meng P, Wang D, Rong L, Panezai S. Speckle noise suppression in digital holography by angular diversity with phase-only spatial light modulator. *Opt Express* (2013) 21:19568–78. doi:10.1364/OE.21.019568

10. Rong L, Xiao W, Pan F, Liu S, Li R. Speckle noise reduction in digital holography by use of multiple polarization holograms. *Chin Opt Lett* (2010) 8: 653–5. doi:10.3788/col20100807.0653

11. Turko NA, Eravuchira PJ, Barnea I, Shaked NT. Simultaneous three-wavelength unwrapping using external digital holographic multiplexing module. *Opt Lett* (2018) 43:1943. doi:10.1364/ol.43.001943

12. Dabov K, Foi A, Katkovnik V, Egiazarian K. Image denoising by sparse 3-d transform-domain collaborative filtering. *IEEE Trans Image Process* (2007) 16: 2080–95. doi:10.1109/TIP.2007.901238

13. Kemao Q. Windowed Fourier transform method for demodulation of carrier fringes. *Opt Eng* (2004) 43:1472. doi:10.1117/1.1759333

14. Rudin LI, Osher S, Fatemi E. Nonlinear total variation based noise removal algorithms. *Physica D: Nonlinear Phenomena* (1992) 60:259–68. doi:10.1016/0167-2789(92)90242-F

15. Wang K, Li Y, Kemao Q, Di J, Zhao J. One-step robust deep learning phase unwrapping. *Opt Express* (2019) 27:15100. doi:10.1364/OE.27.015100

16. Jeon W, Jeong W, Son K, Yang H. Speckle noise reduction for digital holographic images using multi-scale convolutional neural networks. *Opt Lett* (2018) 43:4240. doi:10.1364/OL.43.004240

17. Tahon M, Montresor S, Picart P. Towards reduced cnns for de-noising phase images corrupted with speckle noise. *Photonics* (2021) 8:255. doi:10.3390/photonics8070255

18. Yan K, Yu Y, Sun T, Asundi A, Kemao Q. Wrapped phase denoising using convolutional neural networks. *Opt Lasers Eng* (2020) 128:105999. doi:10.1016/j.optlaseng.2019.105999

19. Yan K, Chang L, Andrianakis M, Tornari V, Yu Y. Deep learning-based wrapped phase denoising method for application in digital holographic speckle pattern interferometry. *Appl Sci* (2020) 10:4044. doi:10.3390/app10114044

20. Jung K-J, Mandija S, Kim J-H, Ryu K, Jung S, Cui C, et al.Improving phase-based conductivity reconstruction by means of deep learning–based denoising of phase data for 3T MRI. *Magn Reson Med* (2021) 86:2084–94. doi:10.1002/mrm.28826

21. Yin D, Gu Z, Zhang Y, Gu F, Nie S, Feng S, et al.Speckle noise reduction in coherent imaging based on deep learning without clean data. *Opt Lasers Eng* (2020) 133:106151. doi:10.1016/j.optlaseng.2020.106151

22. Goodman JW. *Introduction to fourier optics*. New York, United States: McGraw-Hill (1968).

23. Di J, Zhao J, Sun W, Jiang H, Yan X. Phase aberration compensation of digital holographic microscopy based on least squares surface fitting. *Opt Commun* (2009) 282:3873–7. doi:10.1016/j.optcom.2009.06.049

24. Krull A, Buchholz T-O, Jug F. Noise2void - learning denoising from single noisy images. In: IEEE/CVF Conference on Computer Vision and Pattern Recognition (CVPR); 5 Apr 2019; Dresden, Germany (20192019). p. 2124–32. doi:10.1109/CVPR.2019.00223

25. Foi A, Trimeche M, Katkovnik V, Egiazarian K. Practical poissonian-Gaussian noise modeling and fitting for single-image raw-data. *IEEE Trans Image Process* (2008) 17:1737–54. doi:10.1109/TIP.2008.2001399

26. Wu X, Liu M, Cao Y, Ren D, Zuo W. Unpaired learning of deep image denoising. In: A Vedaldi, H Bischof, T Brox, J-M Frahm, editors. *Computer vision – eccv 2020*. Cham: Springer International Publishing (2020). p. 352–68.

27. Kaushal H, Kaddoum G. Optical communication in space: Challenges and mitigation techniques. *IEEE Commun Surv Tutorials* (2017) 19:57–96. doi:10.1109/COMST.2016.2603518

28. Roth S, Black MJ. Fields of experts. *Int J Comput Vis* (2008) 82:205–29. doi:10.1007/s11263-008-0197-6

29. Zhang J, Dai S, Ma C, Xi T, Di J, Zhao J, et al. A review of common-path off-axis digital holography: Towards high stable optical instrument manufacturing. *gxjzz* (2021) 2:1. doi:10.37188/lam.2021.023

30. Di J, Wu J, Wang K, Tang J, Li Y, Zhao J, et al.Quantitative phase imaging using deep learning-based holographic microscope. *Front Phys* (2021) 9. doi:10.3389/fphy.2021.651313

Frontiers in Physics

Label-free observation of morphological alteration of irradiated-urothelial bladder carcinoma cells through digital holographic microscopy

Xi Xiao[1†], Leiping Che[2†], Yinjia Li[3,4], Ran Peng[1], Mingqing Wang[1], Wen Xiao[2], Feng Pan[2]* and Hao Wang[1,5]*

[1]Department of Radiation Oncology, Peking University Third Hospital, Beijing, China, [2]Key Laboratory of Precision Opto-Mechatronics Technology of Ministry of Education, School of Instrumentation Science and Optoelectronics Engineering, Beihang University, Beijing, China, [3]Center of Basic Medical Research, Peking University Third Hospital Institute of Medical Innovation and Research, Beijing, China, [4]Medical Research Center, Peking University Third Hospital, Beijing, China, [5]Cancer Center, Peking University Third Hospital, Beijing, China

Radiotherapy is an effective treatment for certain patients with muscle-invasive bladder cancer and radio-sensitivity detection plays a vital role during bladder cancer radio treatment because radiotherapy responses have profound influences on a patient's prognosis. Although several potential biomarkers were investigated to assess the radio-response of bladder cancer, studies on detecting radio-sensitivity based on morphological characteristics of cancer cells at the single-cell level are rare. In fact, morphological parameters are vital characteristics of cells that could provide direct information to infer the physiological statuses of cells and evaluate the response of cells to the external stimulations. In this study, digital holographic microscopy was applied to quantify morphological parameters of bladder cancer cells (HT-1376) at the single-cell level and their alterations after exposure to four different radiation doses, i.e., 0 Gy (control), 4, 8, and 12 Gy. Based on the reconstructed phase images, four morphological parameters of cells, namely, cell phase volume (CPV), cell projected area (CPA), cell average phase height (CAPH), and cell maximum phase height (CMPH), were quantitatively calculated. The results show that the change rates of CPV, CAPH, and CMPH were increased with the radiation dose rising, while the change rate of CPA was decreased with the radiation dose increasing. Moreover, the change rates of CPV, CPA, CAPH, and CMPH were different between control group and 12 Gy treated group. The results demonstrate that morphological characteristics have the potential to be utilized to estimate the radio-sensitivity of bladder cancer cells, and it may provide new perspectives to establishing label-free methods to detect radio-sensitivity and guide radiotherapy in bladder cancer.

1 Introduction

Bladder cancer (BC) is the 10th most common cancer worldwide, with an estimated 200,000 deaths in 2018 GLOBOCAN statistics [1]. For muscle-invasive BC (MIBC), which occupies approximately 25% of all cases, radiotherapy is an alternative treatment for patients who demand bladder preservation or with unresectable lesions [2]. However, the heterogeneity of BC response to radiotherapy results in inconsistent treatment outcomes. Exploiting a predictive strategy to improve the accuracy of radiotherapy delivery is an urgent clinical problem to be solved. Several potential biomarkers were studied to access the radio-response of BC, but all failed to guide clinical decision-making due to unrevealed clinical validation and correlation [3]. At present, the choice of radiotherapy still depends on the preference of patients and the clinical experience of radiologists. Therefore, prospectively and precisely predicting the radio-response of BC to assist clinical decision-making is a practical issue the clinician faced.

Ionizing radiation, as well as some other chemical drugs, could largely influence the cellular status and biological function. Meanwhile, comprehensive studies verified that the changes in biological alternation, including cell growth [4], intercellular communication [5], transcriptome, and proteome [6], were associated with cellular morphological phenotypes. Some specific morphological manifestations were even coordinated with the cell fate decisions [7]. These indicate that the response of cells to radiation may be evaluated *via* quantitative morphological observation.

Digital holographic microscopy (DHM) is a novel optical microscopic imaging technique that combined qualities found in optical microscopy and digital holography with the capability of quantitative phase microscopic imaging [8]. As a quantitative phase imaging method, DHM images the sample by measuring the optical path length delays introduced by the sample. Thus, no labeling or staining is necessary for living cell observation. This also means that the three-dimensional morphology of a living cell could be objectively quantified using optical path length, and thus multiple morphological parameters could be deduced based on the phase image of the living cell to describe its morphology quantitatively. As the optical path length delays introduced by the living cell is the product of the geometric length of the living cell and the refractive index difference between the sample and the medium, the phase image encodes the refractive index information of the living cell. Also, the refractive index of a living cell is linearly proportional to dry mass density [9]. Therefore, the biochemical parameters of a living cell could be inferred from the phase image, such as cellular dry mass and cellular dry mass density. Furthermore, DHM arranged in an off-axis configuration is capable of recording the phase image of the living cell in a single exposure with nanoscale sensitivity. Due to great advantages in living cell measurement, DHM has been widely applied in biomedical research, especially for measuring on morphological parameter changes in living cells [10].

In this study, we aimed to establish a method based on DHM to detect the radio-response of bladder cancer cells. DHM was applied to obtain the phase images of the cells and to retrieve the changes in cell morphological parameters, which were used to evaluate the radio-response of cells irradiated by different radiation dose. Cell morphological parameters including CPV, CPA, CAPH, and CMPH were quantitatively calculated from the reconstructed phase images. The change rates of morphological parameters manifest a closed relationship with radiation doses, where the change rates of CPV, CAPH, and CMPH were increased with the radiation doses rising, while the change rates of CPA were decreased with the radiation doses increasing. Moreover, the change rates of CPV, CPA, CAPH, and CMPH were different between control group and 12Gy treated group.

2 Methods

2.1 Cell culture and treatments

The human urothelial bladder cancer cell line HT-1376 (CRL-1472) was purchased and validated from Beijing Biotides Biotechnology Co., Ltd. Cells were grown in Eagle's Minimum Essential (EME) Medium (Gibco, #11095080) supplemented with 10% fetal bovine serum (FBS) (Gibco, #10099141) and 1% penicillin streptomycin (Gibco, #15140122) at 37°C in 5% CO_2 humidified incubator (Thermo HERAcell150i). Monthly, mycoplasma tests ensured Mycoplasma-negative cultures (TransDetect, FM311-01). The Automated Cell Counter named Countess™ II FL (Invitrogen, #AMQAF1000) was used for live-cell counting. Cells ($1.5–3\times10^6$/dish) were seeded in 30-mm glass-bottom cell culture dishes (NEST Scientific #801001) and incubated for 12 h, followed by radiation using a Varian Trilogy (SSD = 100 cm). For the treatment group, the cells were exposed to different dose of 6-MV X-rays at a dose rate of 300 cGy/min. The irradiated cells were then used for further DH microscope or biology analyses.

2.2 Biological characteristics of HT-1376 bladder cancer cell lines irradiated by different doses

2.2.1 Determining the viability of HT-1376 bladder cancer cell lines treated with different radiation doses

The HT-1376 cells were cultured and irradiated as mentioned above, followed by the cell viability detection using the cell counting kit (CCK-8 kit). Three doses of irradiation (4, 8, and 12 Gy) and a control group were included in this experiment. After irradiation, cells should be cultured for 48-h and reseeded in clear bottom 96-well plates at the optimum concentration, followed by culturing again for 12-h till they grow adhering. All the steps were performed according to the manufacturer's
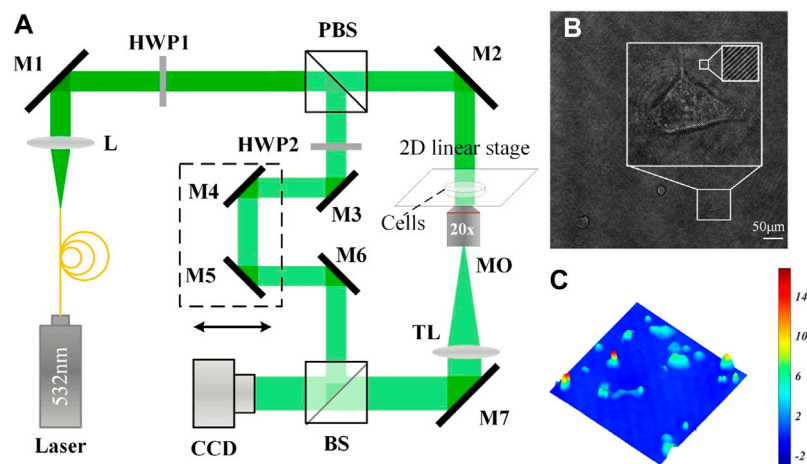
FIGURE 1
(A) Schematic of the DH microscope; **(B)** a single hologram with a dimension of 1024 × 1024 pixels captured by **(A)**; and **(C)** a reconstructed pseudo-three-dimensional phase map from **(B)**.

instructions (CCK8 Dojindo CK04-05) and finally quantified on the microplate reader.

2.2.2 Determining proliferation ability of HT-1376 bladder cancer cell lines treated with different radiation doses

The HT-1376 cells were seeded and incubated in 6-well plates until adherent. After 8 Gy of X-ray radiation treatment, as described before, the cells were trypsinized to single-cell suspensions and seeded into 6-well plates in triplicate. At 14 days after seeding, colonies were stained with 0.5% crystal violet (Solarbio, #G1062), and the colonies with >50 cells were counted.

2.2.3 Determining migration ability of HT-1376 bladder cancer cell lines treated with different radiation doses

The HT-1376 cells were also seeded and incubated in 6-well plates. After 8 Gy of X-ray radiation treatment as described before, a 10 μl pipette tip was used to scrape a wound on the cell monolayers, images of the wound region were taken, and distance was measured by ImageJ software.

2.3 Digital holographic microscopy setup and data processing

2.3.1 Digital holographic microscopy setup

In this study, holograms of HT-1376 cells were recorded by the DH microscope setup sketched in Figure 1A. This setup is built in an afocal configuration, where the back focal plane of the microscope objective (MO) coincides with the front focal plane of the tube lens (TL), with the object placed at the front focal plane of the MO. A

solid-state laser (532 nm, 100 mW, single-mode fiber output) is adopted and emits a coherent light that propagates through a collimating lens (L) to produce a plane wave. The polarizing beam splitter (PBS) splits this wave into two beams, one beam acts as the reference beam R, and the other beam is used as an illumination beam. In the object arm, the object beam O is formed after the illumination beam transmits through the condenser lens (CL), the object, the MO (Olympus UPLFLN, 20X, NA = 0.50), and the TL sequentially. A half-wave plate (HPW1) is positioned in front of the PBS to adjust the intensity ratio between R and O. Another half-wave plate (HPW2) is placed in the reference arm to make the polarization direction of O and R consistent. In the reference arm, a variable optical delay line (DL) is adopted to match both arms of the optical path precisely. After passing through the DL and being reflected by the mirror (M6) and the beam splitter (BS), R interferes with O with a small tile angle set by the M6. Thus, an off-axis hologram is formed and recorded by a charge-coupled device (CCD, 1024 × 1024 pixels, 5.86 μm, PointGrey, Canada). Figure 1B presents a hologram of HT-1376 cells captured by the DH microscope of Figure 1A, where high contrast interference fringes were observed. Figure 1C shows the reconstructed pseudo-three-dimensional phase maps of Figure 1B, it can be seen that CAPH varies in a very large range of about a few to dozen rad, manifesting the high heterogeneity of morphology of HT-1376 cells.

2.3.2 Hologram recording and phase reconstruction

To reveal the morphological alteration of HT-1376 cells introduced by different Ionizing radiation doses, i.e., 0 Gy (control), 4, 8, and 12 Gy, each group was observed once before and after radiation. Each group was first observed using a DH microscope and then taken to the radiation

instrument to receive Ionizing radiation. After radiating, each group was brought back and placed under DH microscope to perform the second observation. The time interval of each group from the first observation to receive Ionizing radiation was about 30 min, and it also took about 30 min to bring back each group to perform the second observation. All observations were performed in cell culture dishes (NEST Scientific #801001).

In the hologram reconstruction process, the hologram's zero-order and twin term was eliminated by the spatial-frequency domain filtering method [11], and the refocusing distance was automatically detected by the Tamura criterion [12]. The phase images were then reconstructed by the angular spectrum method, and the phase aberrations introduced by the off-axis geometry and optical elements were removed by the background phase fitting method [13]. After phase unwrapping, a phase offset operation was finally performed on the obtained phase images to make the average background phase value near the zero lines. The single-cell was extracted from the reconstructed phase images by the Otsu threshold segmentation algorithm [14], and the marker-based watershed segmentation algorithm was further applied when cells adhered together.

2.4 Calculation and analysis of cellular morphological parameters

2.4.1 Calculation of morphological parameters

To quantitatively describe the change in cell morphology, four parameters were taken into consideration and calculated from the reconstructed phase images, including CPV, CPA, CAPH, and CMPH.

DHM is a powerful quantitative phase imaging method that measures the optical phase delays to describe the sample quantitatively. In DHM, the sample is expressed by phase shift and could be written as:

$$\Delta\varphi(x, y) = \frac{2\pi}{\lambda} [n_c(x, y) - n_m] h(x, y) \tag{1}$$

where λ is the wavelength of the laser source, $n_c(x, y)$ is the average cellular refractive index in the spatial position (x, y), n_m is the refractive index of the cellular culture medium, and $h(x, y)$ is cell height along observation direction. Phase shift at (x, y) is referred to as cell phase height at (x, y). It can be seen that cell phase height at (x, y) is determined by both the average cellular refractive index at (x, y) and the cell height at (x, y). Usually, the cellular refractive index changes slightly so that the change of cell phase height could reliably reflect the change of cell height. Since the phase shift of several nanometers could be sensed by interference, DHM could provide a highly precise way to detect the change along observation direction, that is, not achievable for traditional optical microscopes. Based on the phase image of cells, the four parameters, i.e., CPV, CPA, CAPH, and CMPH could be deduced as follows:

$$CPV = \sum_{(x,y) \in s_c} \Delta\varphi(x, y) \tag{2}$$

$$CPA = S_p \times N \tag{3}$$

$$CAPH = \frac{CPV}{CPA} \tag{4}$$

$$CMPH = \frac{1}{50} \sum Select\{Sort(\Delta\varphi(x, y)), 50\} \tag{5}$$

In these four equations, S_c denotes the occupied region of the cell in the phase image, S_p denotes the real area of one pixel of the CCD camera, N denotes the total number of pixels in S_c, $Sort(\cdot)$ denotes the sort operation and $Select\{\cdot\}$ denotes the operation of selecting the top 50 largest numbers of a sequence. CPV, CPA, and CAPH could reflect the 3D, transverse and vertical morphology of living cell, respectively, while CMPH could reflect the vertical morphology of the cellular nucleus.

2.4.2 Change rate calculation

To quantitatively compare the morphological changes among different radiation doses, the change rates of CPV, CPA, CAPH, and CMPH of every cell are calculated. The change rate of the parameter is defined as the ratio of the change of the parameter before and after radiation to the parameter before radiation, which are expressed as:

$$CR_{CPV} = \frac{CPV_A - CPV_B}{CPV_B} \tag{6}$$

$$CR_{CPA} = \frac{CPA_A - CPA_B}{CPA_B} \tag{7}$$

$$CR_{CAPH} = \frac{CAPH_A - CAPH_B}{CAPH_B} \tag{8}$$

$$CR_{CMPH} = \frac{CMPH_A - CMPH_B}{CMPH_B} \tag{9}$$

In these four equations, CR denotes change rate, subscript A denotes the parameter calculated after radiation, and subscript B denotes the parameter measured before radiation.
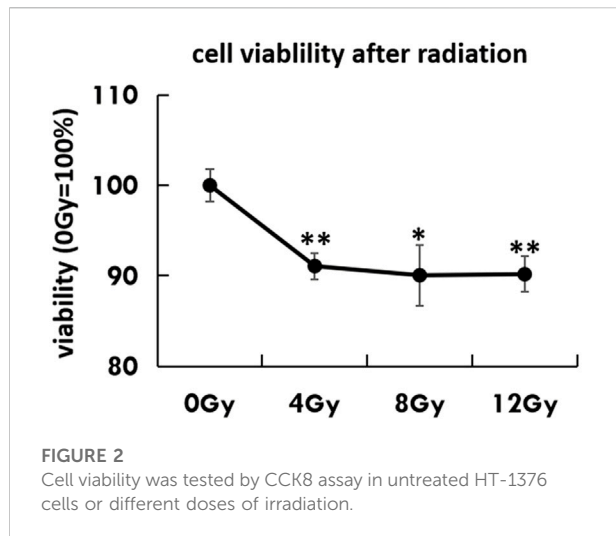
2.4.3 Statistical analysis

Data were analyzed by GraphPad Prism 8 (GraphPad Software, Califnia, LLC) and displayed as a mean ± 95% confidence interval. The comparisons between the two groups were analyzed by Student's t-test. The level of significant difference was set as two-tailed $p < 0.05$ (**$p < 0.01$, *$p < 0.05$).

3 Results

3.1 Changes of the viability of HT-1376 bladder cancer cell lines treated with different radiation doses

To establish the optimal radiation dose-response for the urothelial bladder carcinoma cell line, HT-1376 was treated

FIGURE 2
Cell viability was tested by CCK8 assay in untreated HT-1376 cells or different doses of irradiation.

FIGURE 3
The irradiated cells were reseeded at a low density (400 cells/ well) in a petri dish (D = 3 cm). The Coomassie-staining and colonies (≥50 cells) counting were performed after 2 weeks. Representative photographs of colonies and the colony fraction were shown.

with different doses of radiation. The cell viability was determined 48 h later by CCK8 assay. Radiation significantly inhibited the viability of HT-1376 in a dose-dependent manner, as the cell number strongly decreased (Figure 2).

3.2 Changes of proliferation ability of HT-1376 bladder cancer cell lines treated with different radiation doses

Moreover, as the cytotoxic effect of radiation was the DNA-double strand breakage, we investigated the alteration of cancer stem cell features *via* colony formation. The irradiated cells had a dramatically low colony-forming capacity when compared to the untreated group ($p < 0.01$) (Figure 3).

3.3 Changes of migration ability of HT-1376 bladder cancer cell lines treated with different radiation doses

As we had captured the phenomenon of cell movement under the DH microscope, we thus examined the migration ability of irradiated cells by wound-healing assay. The mean width of the wound remained unchanged in the radiation group after 24 h, while significantly decreased in the untreated group ($p = 0.05$) (Figure 4).

3.4 Changes in morphological parameters of HT-1376 bladder cancer cell lines treated with different radiation doses

HT-1376 cells were individually exposed to 0, 4, 8, and 12 Gy, where 0 Gy group acted as the control. All groups were measured
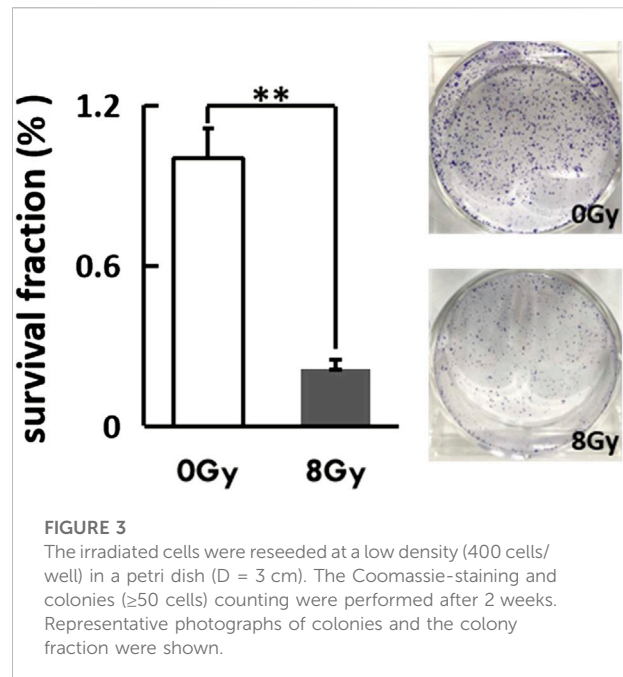
once under the same environmental condition before and after radiation. As shown in Figure 5, a set of holographic phase images and their pseudo-three-dimensional images before and after radiation for 0, 4, 8, and 12 Gy were displayed in the first two columns and later two columns, respectively. Phase images before and after radiation of each group were displayed with a unified color map, and color bars of each group were located on the right. The white line in Figure 5B indicates the scale of the phase images. According to Figure 5, no obvious change in phase height and cellular shape was observed in 0 Gy group, while phase height increase could be seen in 4, 8, and 12 Gy groups.

The distributions of CPV, CPA, CAPH, and CMPH of each group before and after radiation were first qualitatively compared. Figure 6 presents the histograms of CPV, CPA, CAPH, and CMPH of each group before and after radiation. The number of cells in 0Gy group, 4Gy group, 8Gy group, and 12Gy group are 94, 93, 67, 79, respectively. The histograms indicated by the blue color show the distributions of parameters before radiation, while the histograms indicated by the green color show the distributions of parameters after radiation. As can be seen in Figures 6C,D, the histograms of CPV, CAPH, and CMPH after radiation seen slightly shift right compared with those before radiation, while the histograms of CPA slightly shift left compared with those before radiation, which indicates that the morphology of cells is changed after radiation.

The changes in CPV, CPA, CAPH, and CMPH of each group were quantitatively examined. Since higher radiation dose carries larger energy and would cause more severe damage to cells, increased changes in CPV, CPA, CAPH, and CMPH were expected with the rise of radiation doses. The change rates of these four parameters of each group were presented in Figure 7.
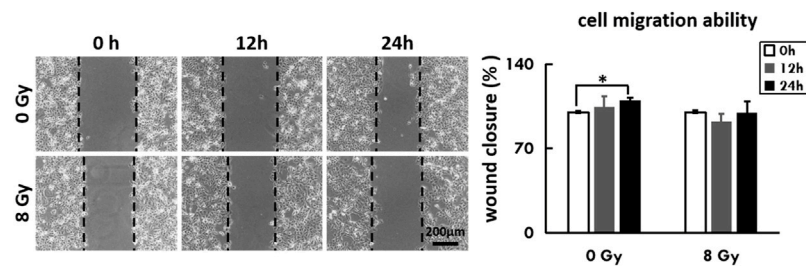
FIGURE 4
The irradiated cells were recultured to 90% confluence with adherence status, followed by a scratching assay. Closure of the wounded region was evaluated by light-microscopy every 3 h. The percentage of the healing area was evaluated *via* ImageJ software and displayed as a diagram.
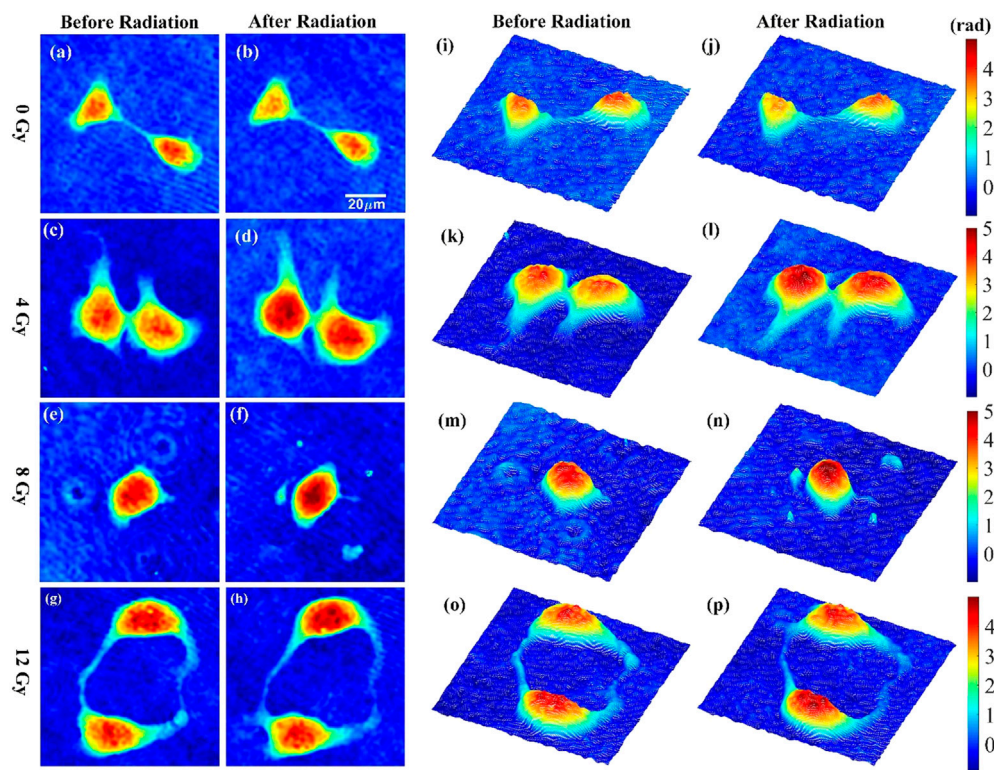

FIGURE 5
Phase images and corresponding pseudo-three-dimensional images of HT-1376 cells before and after radiation for 0, 4, 8, and 12 Gy.

As can be seen, the change rates of CPV, CAPH, and CMPH show increased trends with the radiation dose rising, while the change rate of CPA was decreased with the radiation increase. As shown in Figure 7A, the change rate of the CPV of 12 Gy group increased significantly (4.49% vs. 2.28%, $p = 0.0079$) compared to the 0 Gy group, while 4 Gy group and 8 Gy group did not show a significant increase (3.08% vs. 2.28%, $p = 0.3447$ and 3.19% vs. 2.28%, $p = 0.3178$, respectively). As shown in Figure 7B, the change rate of the CPA of 12 Gy group decreased significantly (−

1.92% vs. 0.98%, $p = 0.0378$) compared to the 0 Gy group, while 4 Gy group and 8 Gy group did not show a significant decrease (0.86% vs. 0.98%, $p = 0.9222$ and −0.21% vs. 0.98%, $p = 0.3598$, respectively). As shown in Figure 7C, the change rate of the CAPH of 12 Gy group and 8 Gy group increased significantly (4.74% vs. 0.95%, $p = 0.0007$ and 3.17% vs. 0.95%, $p = 0.0239$, respectively) compared to the 0 Gy group, while 4 Gy group did not show a significant increase (1.96% vs. 0.95%, $p = 0.2767$). Moreover, the change rate of the CAPH of 12 Gy group increased
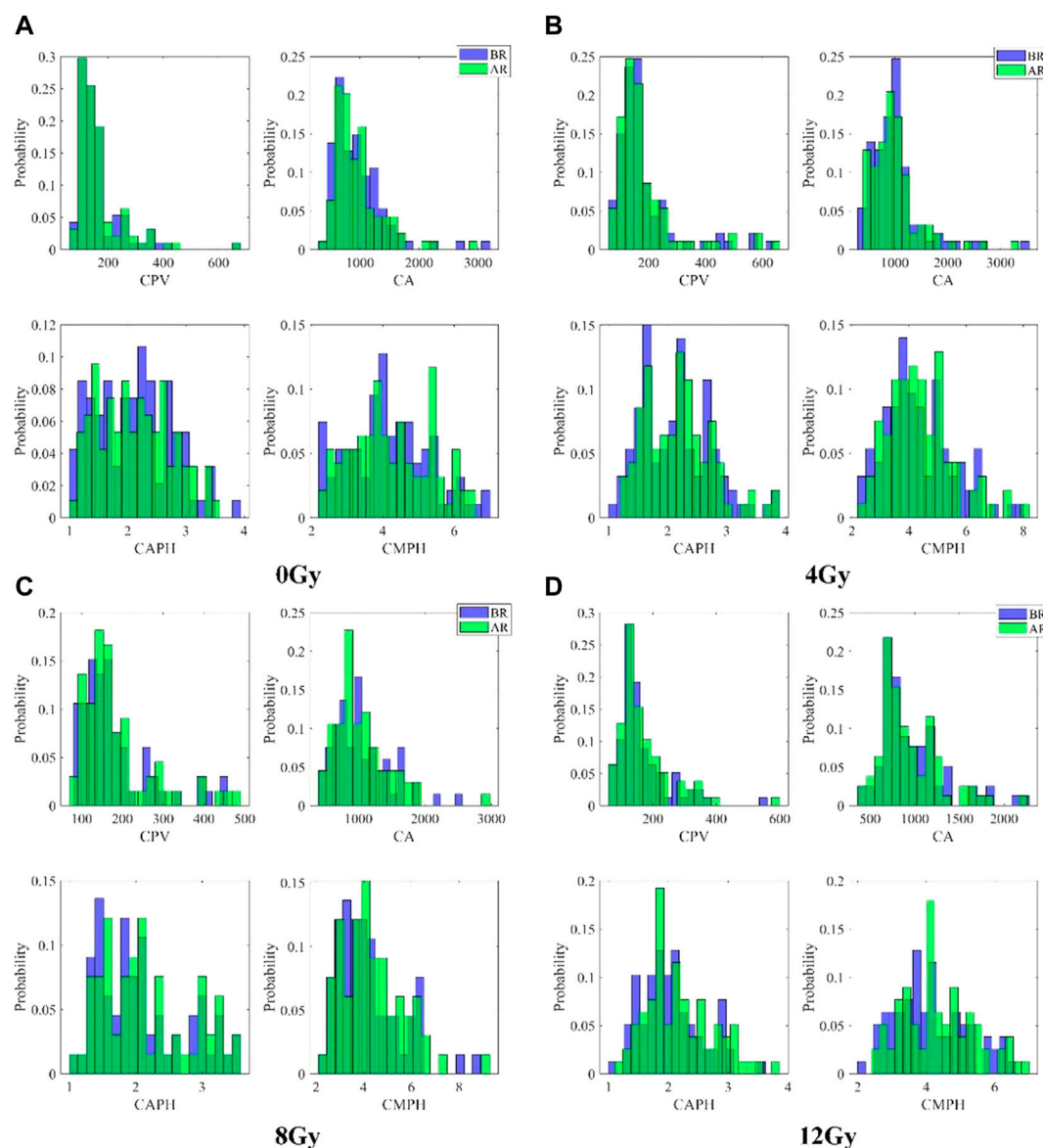
FIGURE 6
The distributions of CPV, CPA, CAPH, and CMPH of each group before and after radiation.

significantly (4.74% vs. 1.96%, *p* = 0.0168) compared to the 4 Gy group. As shown in Figure 7D, the change rate of CMPH in 12 Gy group increased significantly (6.60% vs. 3.22%, *p* = 0.0390) compared to the 0 Gy group, while 4 Gy group and 8 Gy group did not show significant (0.86% vs. 2.89%, *p* = 0.8407 and 5.43% vs. 2.89%, *p* = 0.1080, respectively) decrease.

4 Discussion

Radiotherapy is one of the routine methods for tumor treatment. However, research on the relationship between radiation and cell morphology is rare, especially the dynamic and quantitative morphological changes after radiation. This study, to our knowledge, is the first record that observes and characterizes the cancer cell's morphological changes after radiation based on phase imaging strategy *via* DH microscope.

In experiments, bladder cancer cells were treated with three doses of radiation and imaged by the DH microscope. We have demonstrated that radiation could impair the growth and migration of cancer cells and thus cause remarkable morphological changes. Meanwhile, irradiation could not only attack the cell itself but also break the intercellular junctions and destroy cell communication. (PMID: 30570385, 34688032,
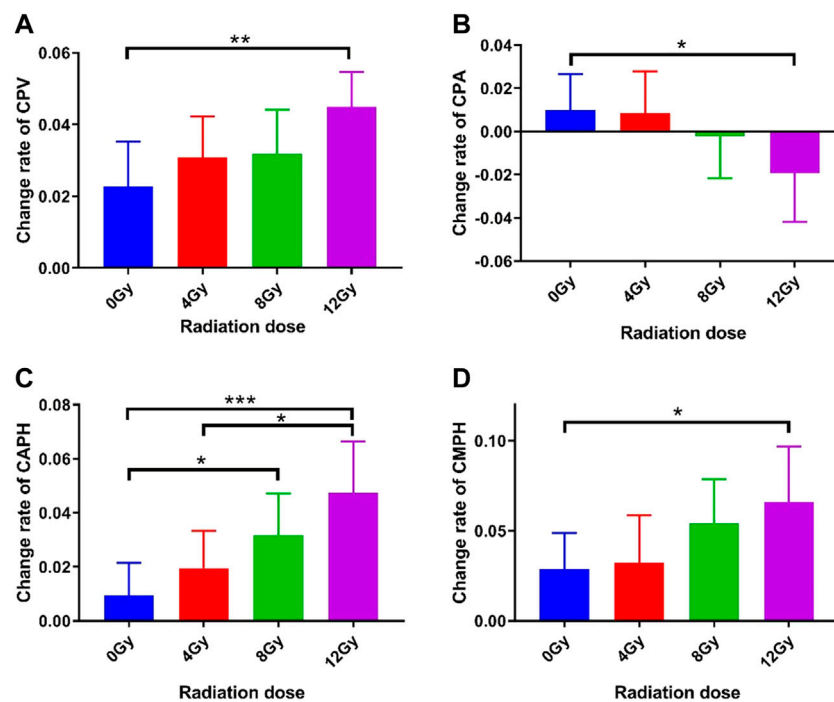
FIGURE 7
The change rates in CPV, CPA, CAPH and CMPH of each group.

11149936, 33416428) In our experiment, we observed those two types of morphological phenomena for irradiated cells, which are cellular regulation and intercellular regulation. Single-cell response to radio-stimulation by self-alteration was defined as cellular regulation, including cell division, cell death, and the disappearance of cytoplasmic vacuolization. The cell-to-cell interaction response to radio-stimulation was defined as intercellular regulation, including cell communication, cell migration, endocytosis, and exocytosis. Notably, intercellular junctions are highly sensitive to ionizing radiation, and previous studies observed the irradiated cells increasing in size and cellular roundness due to cell-to-cell adhesion loss. (PMID: 30570385) This phenomenon is consistent with what we observed, that some cells separated quickly from a tight touched status and changed in shape after irradiation, as shown in Figure 5C. Although those phenomena we observed might not all be radio-specific, we noticed tremendous shape changes of cells in a short period leading to a rapid increase in phase height and, ultimately, cell death.

Moreover, we obtained several parameters of irradiated cells, including phase height, cluster shade, and phase variance based on refractive index measurements. The average phase height for the confluent monolayer cells after gradient radiation presented a good steady rising trend, which can be attributed to the shortage of pseudopodium and damage to adhesion ability. Correspondingly, the change rate of cell cluster shade rose over gradient radiation,

indicating that the surface of cells bends and folds after radiation. Unfortunately, we only observed the radiological dose-dependent manner of cell viability and cell morphological change but not a time-dependent manner. Therefore, contrary to some studies before [15–17], there was no unique parameter under the DH microscope that could stand for post-radiation morphological features. However, despite the nonspecific morphological parameter, the DH microscope has several advantages over the light microscopes, including the collection of informative 3D-morphology data, observation with nondestructive addition, and most importantly, tracing cells with the dynamic real-time view.

To our knowledge, morphology data describing treatment for cancer cells is limited. Kemper et al. reported the first case of drug influence on the morphology changes of pancreatic cancer cells *via* DH microscope. They treated the pancreatic cancer cells with Latrunculin B, which led to a decrease in their phase values and cell thickness [15]. Yunxin et al. identified that the low concentration of methanol (12%–25%) reduced the optical stickiness of cervical cancer cells, while the high concentration (50%) of methanol fixed the cells immediately with tiny shape change [18]. Furthermore, chemotherapy etoposide improved the cell volume of prostate cancer cells [16], while cisplatin was unable to alter the cell volume of endometrial cancer cells [17]. As a result, the effect of chemical or physical interventions on the cell morphological change might depend on the treatment-specific properties and the cytotoxic sensitivity of cells.

Therefore, the DH microscope parameter alone might not be sufficient enough to distinguish the type of treatment.

Our observation has some limitations. Firstly, no radiation-related morphological parameter of cells was obtained due to the nonspecific shape alteration was captured. Secondly, only one type of cancer cell line was tested. Despite the limitations, our research has a specific significance for the single irradiated-cell continuous monitoring and their 3D shape data obtaining.

5 Conclusion

In conclusion, our study is the first observation that deeply investigated the irradiated cancer cells based on the quantitative phase imaging strategy using a quantitative tool, i.e., DH microscopy. We not only verified that the irradiated-related biological phenomena can be captured and identified *via* DH microscopy but also obtained the pattern of cell morphological change in a radiological dose-dependent manner. More importantly, our results open the way for further studies focused on exploring the treatment-specific cell morphology or distinguishing the cell response *via* the previously discovered or reported quantitative morphology biomarkers.

Data availability statement

The raw data supporting the conclusions of this article will be made available by the authors, without undue reservation.

Author contributions

The Author Contributions section is mandatory for all articles, including articles by sole authors. If an appropriate statement is not provided on submission, a standard one will be inserted during the production process. The Author Contributions statement must describe the contributions of individual authors referred to by their initials, and in doing so, all authors agree to be accountable for the content of the work. Please see here for full authorship criteria.

Funding

Conflict of interest

The authors declare that the research was conducted in the absence of any commercial or financial relationships that could be construed as a potential conflict of interest.

Publisher's note

All claims expressed in this article are solely those of the authors and do not necessarily represent those of their affiliated organizations, or those of the publisher, the editors and the reviewers. Any product that may be evaluated in this article, or claim that may be made by its manufacturer, is not guaranteed or endorsed by the publisher.

References

1. Bray F, Ferlay J, Soerjomataram I, Siegel RL, Torre LA, Jemal A. Global cancer statistics 2018: GLOBOCAN estimates of incidence and mortality worldwide for 36 cancers in 185 countries. *CA: A Cancer J Clinicians* (2018) 68(6):394–424. doi:10.3322/caac.21492

2. El-Achkar A, Souhami L, Kassouf W. Bladder preservation therapy: Review of literature and future directions of trimodal therapy. *Curr Urol Rep* (2018) 19(12):108. doi:10.1007/s11934-018-0859-z

3. Song YP, McWilliam A, Hoskin PJ, Choudhury A. Organ preservation in bladder cancer: An opportunity for truly personalized treatment. *Nat Rev Urol* (2019) 16(9):511–22. doi:10.1038/s41585-019-0199-x

4. Goranov AI, Gulati A, Dephoure N, Takahara T, Maeda T, Gygi SP, et al. Changes in cell morphology are coordinated with cell growth through the TORC1 pathway. *Curr Biol* (2013) 23(14):1269–79. doi:10.1016/j.cub.2013.05.035

5. Hughes BR, Mirbagheri M, Waldman SD, Hwang DK. Direct cell-cell communication with three-dimensional cell morphology on wrinkled microposts. *Acta Biomater* (2018) 78:89–97. doi:10.1016/j.actbio.2018.07.053

6. Nassiri I, McCall MN. Systematic exploration of cell morphological phenotypes associated with a transcriptomic query. *Nucleic Acids Res* (2018) 46(19):e116. doi:10.1093/nar/gky626

7. Tatapudy S, Aloisio F, Barber D, Nystul T. Cell fate decisions: Emerging roles for metabolic signals and cell morphology. *EMBO Rep* (2017) 18(12):2105–18. doi:10.15252/embr.201744816

8. Javidi B, Carnicer A, Anand A, Barbastathis G, Chen W, Ferraro P, et al. Roadmap on digital holography [Invited]. *Opt Express* (2021) 29(22):35078–118. doi:10.1364/oe.435915

9. Popescu G, Park Y, Lue N, Best-Popescu C, Deflores L, Dasari RR, et al. Optical imaging of cell mass and growth dynamics. *Am J Physiology-Cell Physiol* (2008) 295(2):C538–C544. doi:10.1152/ajpcell.00121.2008

10. Depeursinge C, Marquet P, Pavillon N. Application of Digital Holographic Microscopy in Biomedicine[J]. In: *Handbook of biomedical Optics*. Editors D. A. Boas, C. Pitris, N. Ramanujam (2011): 614–647.

11. Cuche E, Marquet P, Depeursinge C. Spatial filtering for zero-order and twin-image elimination in digital off-axis holography. *Appl Opt* (2000) 39(23):4070–5. doi:10.1364/ao.39.004070

12. Memmolo P, Distante C, Paturzo M, Finizio A, Ferraro P, Javidi B. Automatic focusing in digital holography and its application to stretched holograms. *Opt Lett* (2011) 36(10):1945–7. doi:10.1364/OL.36.001945

13. Leiping C, Xiao W, Xiaoping L, Liu J, Pan F, Ferraro P. Automatic removal of phase aberration in holographic microscopy for drug sensitivity detection of ovarian cancer cells. *OSA Continuum* (2020) 3(7):1856–68. doi:10.1364/OSAC.391773

14. Khan W. Image segmentation techniques: A survey. *Joig* (2014) 1:166–70. doi:10.12720/joig.1.4.166-170

15. El-Schich Z, Mölder A, Tassidis H, Härkönen P, Falck Miniotis M, Gjörloff Wingren A. Induction of morphological changes in death-induced cancer cells monitored by holographic microscopy. *J Struct Biol* (2015) 189(3):207–12. doi:10.1016/j.jsb.2015.01.010

16. Kemper B, Carl D, Schnekenburger J, Bredebusch I, Schäfer M, Domschke W, et al. Investigation of living pancreas tumor cells by digital holographic microscopy. *J Biomed Opt* (2006) 11(3):034005. doi:10.1117/1.2204609

17. Yao T, Cao R, Xiao W, Pan F, Li X. An optical study of drug resistance detection in endometrial cancer cells by dynamic and quantitative phase imaging. *J Biophotonics* (2019) 12(7):e201800443. doi:10.1002/jbio.201800443

18. Wang Y, Yang Y, Wang D, Ouyang L, Zhang Y, Zhao J, et al. Morphological measurement of living cells in methanol with digital holographic microscopy. *Comput Math Methods Med* (2013) 2013:1–7. doi:10.1155/2013/715843

Advantages of publishing in Frontiers

OPEN ACCESS
Articles are free to read for greatest visibility and readership

FAST PUBLICATION
Around 90 days from submission to decision

HIGH QUALITY PEER-REVIEW
Rigorous, collaborative, and constructive peer-review

TRANSPARENT PEER-REVIEW
Editors and reviewers acknowledged by name on published articles

Frontiers
Avenue du Tribunal-Fédéral 34
1005 Lausanne | Switzerland

Visit us: www.frontiersin.org
Contact us: frontiersin.org/about/contact

REPRODUCIBILITY OF RESEARCH
Support open data and methods to enhance research reproducibility

DIGITAL PUBLISHING
Articles designed for optimal readership across devices

FOLLOW US
@frontiersin

IMPACT METRICS
Advanced article metrics track visibility across digital media

EXTENSIVE PROMOTION
Marketing and promotion of impactful research

LOOP RESEARCH NETWORK
Our network increases your article's readership